

Depositional and Structural History of the Pavian and Kudu Nappes in the Naukluft Mountains, Namibia

Thesis by
Freya Kurt Morris

In Partial Fulfillment of the Requirements for
the degree of
Doctor of Philosophy in Geology

The Caltech logo, featuring the word "Caltech" in a bold, orange, sans-serif font, centered within a light yellow rectangular background.

CALIFORNIA INSTITUTE OF TECHNOLOGY
Pasadena, California

2024
(Defended July 11, 2023)

© 2024

Freya K. Morris
ORCID: 0000-0003-4765-9286

ACKNOWLEDGEMENTS

I am immensely grateful to the three field partners that made all this work possible: Cecilia Sanders (2018), Emilie Henry (2019), and Joshua Anadu (2021). I appreciate the assistance of all the members of the 2018 Agouron Institute Geobiology field course, especially the geologic context and logistical support provided by Judy Pu, Roger Swart, Daven Quinn, and Jason Indongo. I thank Anna Nguno for permitting and logistical support within Namibia along with the Namibian Ministry of Environment and Tourism, Ministry of Mines and Energy, and the town of Solitaire. I am grateful to the landowners Ralf Hansen, Ernst Sauber, Jan, Akas, and Moses for generous permission to study the geology of their farms. I also thank Janice Grancich, Mark Garcia, and Jay Dickson for logistical and technical support. Many thoughtful discussions with Paul Myrow are appreciated. I thank Andrew Merdith for generously providing the paleogeographic reconstructions we used for the sea-level models and Jessica Creveling for support in developing the topographic and ice sheet models. This work was financially supported by the National Science Foundation Graduate Research Fellowship Program (NSF GRFP), the Agouron Foundation, and the Simons Foundation.

I appreciate the research mentorship of my primary advisor John Grotzinger and am extremely grateful that he provided me the opportunity and flexibility to conduct and process the incredible field campaigns we did in the Naukluft Mountains. I thank Tamara Pico as my unofficial second advisor who gave me the skillset and confidence to explore a computational project based on the results of my field work. I also appreciate the guidance and assistance of my other committee members, Woody Fischer and Jean-Philippe Avouac.

ABSTRACT

The termination of the Marinoan Snowball Earth glacial epoch was one of the most extreme climate events in Earth history. Yet, the transition from global glaciation to an ice-free warmer climate is still poorly constrained. The Naukluft Nappe Complex of south-central Namibia contains several stratigraphic formations that record the environmental and tectonic transitions of the Neoproterozoic, including glaciogenic deposits and basal-Ediacaran cap carbonate of the Marinoan Snowball Earth. This stratigraphic record has the potential to provide a critical record of the climate, sea-level history, ocean chemistry, and time frames across the climate transition of the Marinoan Snowball deglaciation.

We first show a detailed study of the sedimentology and stratigraphy of the upper Blässkranz Formation and Tsabisis Formation cap carbonate to develop an environmental and sequence stratigraphic history spanning and following the deglaciation. In downdip areas Marinoan diamictite transitions upward into dolostone intermixed with sandstone and extrabasinal clasts that is gradually overlain by fine grained laminated dolostone. Updip localities show the diamictite is overlain by intercalated sandstones, gravels, and shales before an abrupt change to laminated dolostone of the cap carbonate. A succession of stromatolites, which become strongly elongate upward, prograde into the laminated dolostone in the updip localities. The stromatolites are overlain by laminated dolostone that grades upward into rhythmite with intercalations of shale. Near the top of the cap, rhythmites may be reworked into tabular intraclast conglomerate, locally intercalated with hummocky cross stratified sandstone, which passes upward into the shale and limestone members of the Tsabisis Formation. The lateral and vertical distribution of facies indicate a retreat of the shoreline and glacially sourced siliciclastics near the base of the cap carbonate, a shallowing succession to fair-weather wave base at the top of the stromatolite facies, and a second shallowing succession to storm wave base near the top of the cap carbonate. Maximum flooding occurred soon after the initiation of carbonate deposition and two sequence boundaries mark higher stratigraphic levels within the cap carbonate. With a sea-level history and chronological framework inferred from the sequence

stratigraphy we can consider different mechanisms of sea-level change, which may reflect the timescale and synchronicity of deglaciation.

Next, we consider the structural and stratigraphic relationships between the Neoproterozoic units of the Naukluft Mountains to define and contextualize the extent of the terminal Marinoan geologic record. We show that the Northern Pavian Nappe, which includes the Marinoan-associated Blässkranz and Tsabisis formations, is stratigraphically succeeded by the dolostone dominated Kudu Nappe and is not correlated or genetically related to the nearby Southern Pavian Nappe. Additionally, the modified stratigraphic and structural relationships allow for a simplified nappe emplacement history that reduces the magnitude of shortening associated with convergence along the Damara Orogen.

Finally, we use sea-level modeling of the Naukluft Marinoan record to constrain the duration of global deglaciation. Using a range of reconstructed synchronous and continuous deglaciation models, we evaluate if the observed sea-level patterns of the Naukluft can be fully explained by glacial isostatic mechanisms driven by the deglaciation. Short Snowball deglaciation durations, on the order of ~ 2 kyr, result in exclusive sea-level rise, or sea-level rise followed by sea-level fall, but cannot drive two distinct phases of sea-level fall. However, for longer duration snowball deglaciations, of ~ 10 - 30 kyr, we can drive two distinct intervals of sea-level rise and fall across much of the width of a continental margin, consistent with the stratal patterns observed in Naukluft Mountains cap carbonate succession. Our spatially varying sea-level predictions resulting from longer duration deglaciations may be applicable in interpreting stratal patterns of other cap carbonate successions. Furthermore, this work underlines the need for better constraints on the areal distribution and volume of Marinoan ice sheets, including improved understanding of plausible deglacial durations using updated global climate models.

PUBLISHED CONTENT AND CONTRIBUTIONS

Freya K. Morris, John P. Grotzinger, (2023) Facies and stratigraphy of the basal Ediacaran cap carbonate, Naukluft Mountains, Namibia, *Precambrian Research*, v. 394, 107113, ISSN 0301-9268, <https://doi.org/10.1016/j.precamres.2023.107113>.

F. K. Morris lead the conceptualization, methodology, field analysis and investigation, and writing of the manuscript

TABLE OF CONTENTS

Acknowledgements.....	iii
Abstract	v
Published Content and Contributions.....	vii
Table of Contents.....	viii
Chapter I: Introduction	3
Chapter I References	15
Chapter II: Facies and Stratigraphy of the Basal Ediacaran Cap Carbonate Naukluft Mountains, Namibia.....	20
Introduction.....	21
Geologic Background.....	23
Methods	28
Facies and Paleoenvironments	31
Platform Morphology and Evolution.....	46
Sequence Stratigraphy	52
Carbon and Oxygen Isotope Geochemistry	54
Discussion.....	56
Supplementals & References	63
Chapter III: Structural and Lithostratigraphic Framework of the Naukluft Nappe Complex	78
Introduction.....	79
Geologic Background.....	81
Methods	94
Nappe Lithostratigraphy.....	96
Structural Expression.....	112
Geochemistry	119
Discussion.....	124
Supplementals & References	133
Chapter IV: Melting the Marinoan Snowball Earth: Impact of Deglaciation Duration on the Sea-Level History of Continental Margins	153
Introduction.....	154
Model Set-Up	158
Results.....	160
Discussion.....	168
Conclusions.....	172
Supplementals & References.....	173

Chapter 1

INTRODUCTION

The Neoproterozoic era represents a critical time in Earth history as tectonic and climatic events induced fundamental changes in the Earth's environment and which contributed to the emergence of complex metazoan life (Fig. 1.1). Central to these changes are the two 'Snowball Earth' events, the older Sturtian and the younger Marinoan (terminating at ~635 Ma; Fig. 1.1), that represent glaciations of global scale lasting for several millions of years (e.g. Kirschvink 1992; Hoffman et al. 1998; Hoffman et al. 2017). The Snowball Earth events are particularly interesting because they represent an extreme end-member of Earth's climate system that may have stimulated widespread rise of macroscopic animals, yet the causality between these events and the mechanisms behind them continues to be an open question.

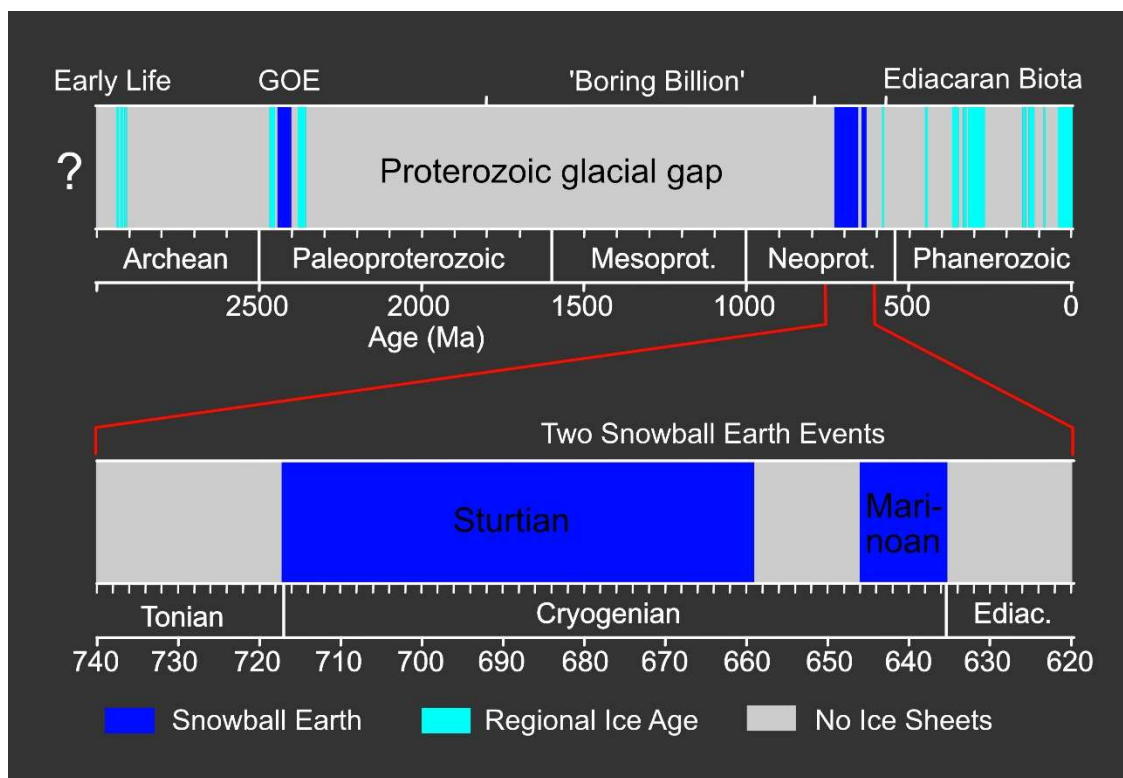


Fig. 1.1 Geologic timescale showing the timing of regional ice ages and global Snowball Earth glaciations from the Archean to the present. Inset highlights the two Neoproterozoic Snowball Earth events. Modified after Hoffman et al. 2017.

Prior to the Neoproterozoic Snowball Earth events there is no evidence for widespread glaciation in the rock record since the Huronian Glaciations, associated with the Great Oxygenation Event, over a billion years prior in the early Proterozoic (Hoffman et al. 2013; Hoffman et al. 2017; Zakharov et al. 2017). Much of the intervening time is known as the ‘Boring Billion’, when the tectonic and climatic systems appeared to have been relatively stable, and while there were important evolutionary developments, microorganisms dominated the planet (Roberts 2013; Mukherjee et al. 2018; Xiao & Tang 2018). The perturbations that knocked the Earth out of its stability and lead to the dramatic Neoproterozoic glaciations have been largely tied to the rifting and breakup of the tectonically stable supercontinent of Rodinia and the eruption of large igneous provinces (Hoffman et al. 2017; Macdonald & Wordsworth 2017; Pu et al. 2022). This appears to have led to an increase in the Earth’s albedo as the continents were shifted closer to the equator and driven a drawdown of CO₂ by the extensive weathering of mafic rocks, facilitating the run-away ice-albedo feedback and pulling the planet into a global glaciation. The pan-glacial state was eventually terminated only after millions of years due to the glaciation itself limiting most carbon sinks while volcanic CO₂ accumulated in the atmosphere (Kirschvink 1992; Hoffman et al. 1989; Hoffman & Schrag 2002; Hoffman et al. 2017). Then, initiated by the accumulated greenhouse effect, melting of the ice sheets would have activated the ice-albedo feedback in reverse resulting in a deglaciation that would presumably occur over a geologically short period of time (Hoffman & Schrag 2002; Hoffman et al. 2007; Hoffman et al. 2017). Following the Snowball deglaciation, the Earth was largely ice free, though the climatic history and whether there were later regional glaciations in subsequent early Ediacaran time remains ambiguous (Jiang & Christe-Blick 2003; Allen & Leather 2006; Hebert et al. 2010; Bold et al. 2016; Xiao et al. 2016; Sui et al. 2018) until the well-documented mid-Ediacaran regional Gaskiers Glaciation (~580 Ma; Myrow & Kaufman 1999; Pu et al. 2016; Rooney et al. 2020). Relatively soon after the Gaskiers Glaciation, the first Ediacaran metazoans appear in the rock record (~574 Ma; Rooney et al. 2020; Grotzinger et al., 1995) and within a few 10s of millions of years, these organisms were succeeded by the rise of the canonical shelly organisms through the end of the Ediacaran and

into the Cambrian radiation (Droser et al. 2017; Boag et al. 2018; Darroch et al. 2018; Grotzinger et al., 1995).

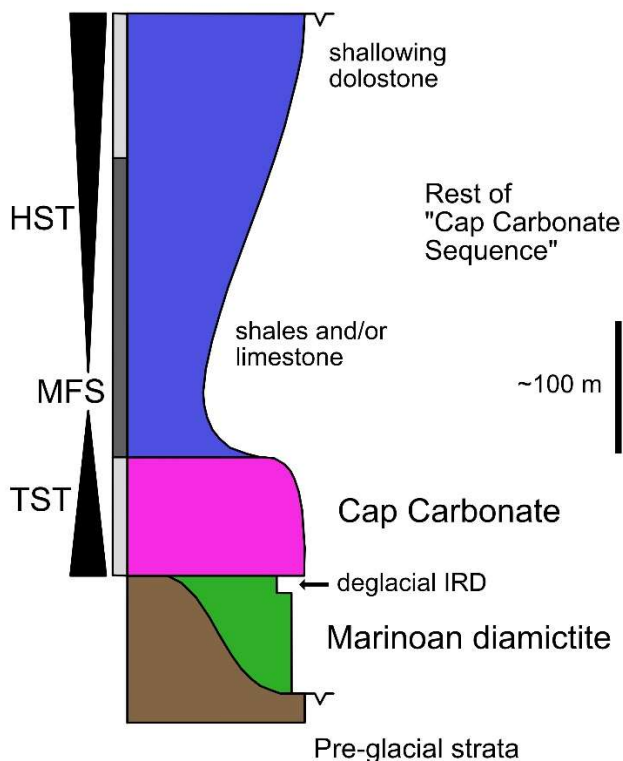


Fig. 1.2. Generalized sequence stratigraphic framework of cap carbonates commonly applied in the literature. Modified after Hoffman et al. 2017. Though sea-level regressions have been reported in the literature at the base of some cap carbonates and near the top of others, cap carbonates are frequently still generalized as being distinctly transgressive. Appreciating the nuances of their sequence stratigraphic/sea-level history, and the variability of these fluctuations between cap carbonates, is essential to understanding the mechanisms and temporal framework of the environmental changes recorded in terminal Marinoan deposits. TST – Transgressive systems tract (deepening sea-level), MFS – maximum flooding surface (maximum deepening), HST – highstand systems tract (shallowing sea-level), IRD – ice rafted debris such as dropstones that provide important evidence for glacial activity.

Neoproterozoic evidence for widespread glaciation, such as diamictites (with an abundance of carbonate fragments), dropstones, and varves found across multiple continents was long an enigmatic feature of the Precambrian rock record (e.g. Harland 1964; Williams 1975; Kirschvink 1992). Early explanations revolved around either rapid successive continental drift through polar regions (Crawford & Daily 1971; Eyles & Januszczak 2004) or phases of extremely high obliquity that could have shifted the regions of low and high temperatures (Williams 1975). However, paleomagnetic tests on the varved sediments in the Elatina

Formation of South Australia show that extensive sea-level deposits of continental glaciers reached within a few degrees of the equator (Kirschvink 1992). Work since then has followed through on the proposed tests of Kirschvink (1992), showing that the initiation and termination of the glaciations were broadly synchronous in two distinct Snowball episodes (Fig. 1.1), there is an association of banded iron formations with glacial deposits that indicate an inhibition of deep ocean oxygenation, and global lithological similarities between Snowball deposits (Hoffman et al. 1998; Hoffman & Schrag 2002; Macdonald et al. 2010; Rooney et al. 2015; Cox et al. 2016; Hoffman et al. 2017).

A key feature that showed lithological similarity across Snowball deposits are the distinctive cap carbonates that typically overlie the glaciogenic deposits (e.g. Fig. 1.2). Cap carbonates of the latter Marinoan Snowball Earth are relatively thick (up to 10s of meters) and typically composed of dolostone (e.g. Kennedy 1996; Hoffman et al. 1998; James et al. 2001; Hoffman & Schrag 2002; Higgins & Schrag 2003; Hoffman et al. 2017). Cap carbonates were long considered paradoxical as they indicate an abrupt transition from widespread glacial conditions to tropical environments (Williams 1979; Fairchild 1993). However, with the development of the Snowball Earth hypothesis and recognition of a variety of unusual sea-floor cements (Grotzinger, 1989; Grotzinger and James, 2000) these deposits indicate a phase of extreme carbonate oversaturation (Grotzinger and Knoll, 1995) of the oceans associated with rapid weathering of the exposed continents and development of a melt-water lid (Fabre & Berger 2012; Yang et al. 2017; Hoffman et al. 2017). Stratigraphically speaking, Marinoan cap carbonates (or ‘cap dolostones’ used by some workers) are considered to distinctly represent the transgressive systems tract, primarily associated with deglacial sea-level rise, that are then overlain by a single highstand system tract to complete a ‘cap-carbonate sequence’ (Fig. 1.2; Hoffman & Schrag 2002; Hoffman et al. 2007; Hoffman & Macdonald 2010; Hoffman et al. 2017). Though there are numerous examples of sea-level regressions at the base or top of cap carbonates (Fig. 1.3; e.g. Bertrand-Sarfati 1997; Shields et al. 2007; Hoffman & Macdonald 2010; Zhou et al. 2010; Hoffman 2011; Gan et al. 2022) these fluctuations are typically not described within sequence stratigraphic framework and the concept of cap carbonates as distinctly transgressive deposits has persisted (Fig. 1.2).

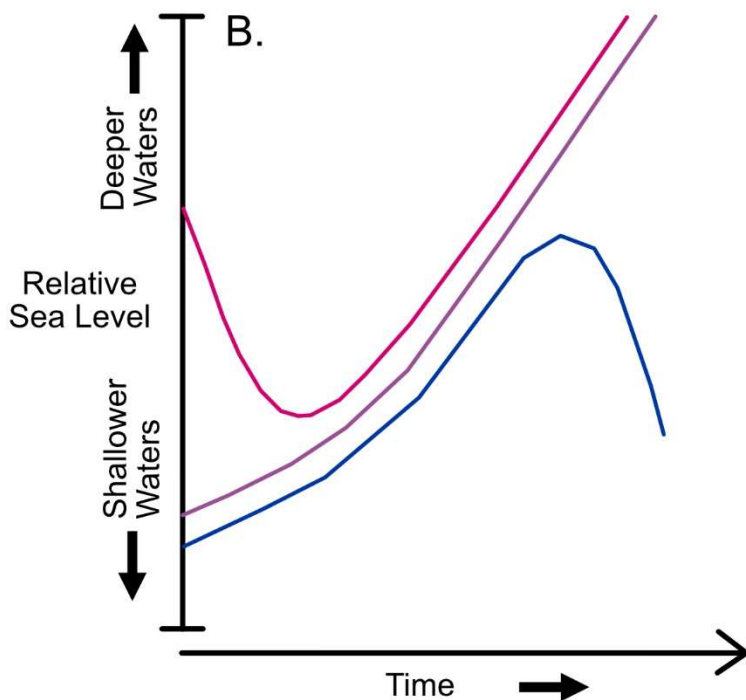


Fig. 1.3. Commonly reported sea-level histories for cap carbonates and terminal Marinoan deposits in general. See text for references.

The sequence stratigraphic framework of cap carbonates is particularly relevant for considering the timescale of global deglaciation and cap carbonate deposition. The duration of deglaciation is critical for understanding the scale and nature of the extreme climate transition, yet deglaciation has remained poorly constrained due to the lack of direct radiometric ages. The duration of the Marinoan deglaciation has been estimated by global climate models of Hyde et al. (2000), which predicted a timespan of ~ 2 kyr or less, however these models very limited in the parameter space exploration of deglacial duration. Therefore, workers have attempted to estimate the timescale of cap carbonate deposition and tie it to physical or chemical processes associated with the global deglaciation, which could then potentially elucidate the temporal framework of the climate transition (Trindade et al. 2003; Hoffman et al. 2007; 2011; 2017; Font et al. 2010; Hoffman & Macdonald 2010; Kennedy & Christie-Blick 2011; Yang et al. 2017; Nordsvan et al. 2019; Fairchild et al. 2022). However, these effort have yet to prove conclusive, with estimates for the timescale of cap carbonate deposition ranging from extremely short ~ 2 kyr (by coupling to above

deglacial duration of Hyde et al. 2000; Hoffman & Schrag 2002; Hoffman et al. 2007; Hoffman & Macdonald 2010; Hoffman 2011), to the scale of a few 10s of kyr (by coupling to ocean mixing timescale; Yang et al. 2017; Hoffman et al. 2017), up to several 100s of kyr (by paleomagnetic reversal evidence; Trindade et al. 2003; Font et al. 2010; Nordsvan et al. 2019). One potential avenue to explore the temporal framework of cap carbonates is to discern sea-level changes in the stratigraphy, which may be driven by glacial isostatic adjustment – a physical process that can be mathematically modeled. The feasibility of this approach has been explored (Hoffman & Macdonald 2010; Creveling & Mitrovica 2014; Hoffman et al. 2017; Irie et al. 2019), yet the persistence of a distinctly transgressive model for the sequence stratigraphic framework of cap carbonate has limited the usefulness and viability of this approach (Fig. 1.2; Fig. 1.3; Hoffman et al. 2017).

The significance of the Snowball Earth events as end-member climate states and their implications for the evolution of early life depends largely on the severity of the glaciations at their maximum, and the intensity of their initiation and termination. The present work focuses on exploring the nature of the deglaciation of the latter Marinoan Snowball Earth by studying sedimentological and sequence stratigraphic framework of the terminal Marinoan glaciogenic deposits and overlying cap carbonate that crops out in the Naukluft Mountains of Namibia.

The Neoproterozoic successions of the Naukluft Mountains of south-central Namibia were thrust southward during the central Namibian Damara Orogeny to form the Naukluft Nappe Complex (NNC; ~555 Ma; Gray et al. 2008; Miller et al. 2008; Goscombe et al. 2017). The basal thrust décollement of the NNC has been studied extensively due to its superb exposure and easy access at lower elevations (Korn & Martin 1959; Hartnady 1978; Martin 1983; Viola et al. 2006; Miller et al. 2008; Rowe et al. 2012; Fagereng et al. 2014). In contrast, the strata that make up the nappe complex include several, relatively unstudied, siliciclastic and carbonate Neoproterozoic sedimentary formations. The carbonates have been particularly underappreciated, with most prior work simply describing them by little more than their color (Korn & Martin 1959; Hartnady 1978). However, specific facies that include coarse grained siliciclastic rocks have been directly correlated to the Marinoan age glacial epoch. These rocks include diamictites of the Blässkranz Formation and an overlying ‘cap carbonate’

constituting the basal portion of the Tsabisis Formation (Hoffmann 1989; Miller 2008). Above this cap carbonate the shales and limestones of the rest of the Tsabisis Formation are overlain by the sandy dolostone of the Noab Formation and record Ediacaran time that immediately follows the Marinoan deglaciation.

This thesis presents a detailed study of the sedimentology and stratigraphy of the terminal Marinoan deposits, followed by an analysis of the broader structure and lithostratigraphic context of the NNC. Field observations form the basis for both of these studies in which understanding of depositional and structural patterns was enabled by simultaneous consideration of the stratigraphy and structural geology, where each informed the understanding of the other. This was essential in the NNC where there is significant lateral variability in both facies and deformation patterns and was especially important when evaluating the number and extent of individual ‘nappes’ of the NNC. Nappes are defined as thrust sheets that have undergone a transport distance of several kilometers (Howell 1960), yet there can be ambiguity in areas that underwent spatially variable shear deformation as is the case in the NNC. We address this ambiguity when considering laterally variable unit contacts that range from fully stratigraphic transitions to localized, laterally discontinuous thrust faults or bedding-parallel shear zones.

Three chapters follow the present introduction (Chapter 1). Chapter 2 is a detailed study of the sedimentology and stratigraphy of the upper Blässkranz Formation and Tsabisis cap carbonate that establishes an environmental and sequence stratigraphic framework spanning and following Marinoan deglaciation. This framework yields constraints on the history and mechanisms of sea-level change, which may reflect the timescale and synchronicity of deglaciation. Chapter 3 explores the structural and stratigraphic relationships of the Blässkranz and Tsabisis formations and compares them to other stratigraphic and structural units of the Naukluft Mountains to establish the broader tectonic context of the NNC. Chapter 4 uses sea-level modeling to evaluate the sea-level record recorded by Marinoan cap carbonates of the Tsabisis formation, which informs the dynamics of Marinoan deglaciation.

Chapter 2 investigates the sedimentology and sequence stratigraphy of the units recording the Marinoan deglaciation and is particularly focused on the upper Blässkranz Formation

glaciogenic depositions and the basal cap carbonate of the overlying Tsabisis Formation, which we informally term the Tsondab member (Hoffmann 1989; Miller 2008). Over two dozen stratigraphic sections were measured, and lateral bed/unit tracing was conducted to delineate stratigraphic stacking patterns and regional facies changes. Along these lines we established that the facing direction of the platform was to the north – such that southern outcrops were continentward or ‘updip’ while northern outcrops were basinward or ‘downdip’. In downdip locations Marinoan diamictite transitions upward into dolostone intermixed with sandstone and extrabasinal clasts that is gradually overlain by fine grained laminated dolostone. Updip localities show the diamictite is overlain by intercalated sandstones, gravels, and shales before an abrupt change to laminated dolostone of the cap carbonate. A succession of stromatolites, which become strongly elongate upward, prograde into the laminated dolostone in the updip localities. The stromatolites are overlain by laminated dolostone that grades upward into rhythmite with intercalations of shale. Near the top of the cap, rhythmites may be reworked into tabular intraclast conglomerate, locally intercalated with hummocky cross stratified sandstone, which passes upward into the shale and limestone members of the Tsabisis Formation. The Tsabisis Formation is overlain by the Noab Formation with a laterally varying contact that often is expressed as a progressive transition to the laminated dolostone, but can locally show abrupt stratigraphic downcutting by sedimentary breccia. The bulk of the Noab Formation is dominated by dolostone intraclast breccias, laminated dolostone, and sandstone. The lateral and vertical distribution of the Blässkranz and Tsondab facies indicate retreat of the shoreline and glacially sourced siliciclastics near the base of the cap carbonate, a shallowing succession to fair-weather wave base at the top of the stromatolite facies, and a second shallowing succession to storm wave base near the top of the cap carbonate. Maximum flooding occurred soon after the initiation of carbonate deposition and two sequence boundaries mark higher stratigraphic levels within the cap carbonate. The sedimentary breccia and erosive downcutting marking the Tsabisis-Noab contact suggest that it may represent another sequence boundary and an increase in the influx of siliciclastics through the upper Noab Formation suggests that it predominantly represents a highstand systems tract that is terminated by a sequence boundary. The depositional patterns of the Tsondab member cap carbonate resemble that of other Precambrian mixed carbonate-siliciclastic platforms and shows multiple base-level

fluctuations that could be attributed to a range of mechanisms (in contrast with Fig. 1.2; Ahr 1973; McIlreath & James 1978; Read 1985; Grotzinger 1989; Burchette & Wright 1992; Grotzinger and James 2000; Whalen et al. 2000). It is feasible that both sequence boundaries within the Tsondab member cap carbonate could be directly coupled to events driven by a regionally asynchronous deglaciation (Hoffman & Macdonald 2010; Hoffman 2011; Hoffman et al. 2021). However, the facies and stratigraphic record of the Tsondab member may not be consistent with this model, and given the typically assumed short duration of deglaciation (~2 kyr, Hyde et al. 2000), the cap carbonate may be better explained by a combination of deglacial crustal rebound and conventional controls on accommodation space.

Chapter 3 presents a broad structural and lithostratigraphic study of the Naukluft Mountains and its nappe complex. The Naukluft Nappe Complex (NNC) of south-central Namibia contains several stratigraphic formations that record environmental and tectonic events of the Neoproterozoic. With our interest in the Marinoan Snowball Earth glaciogenic and cap carbonate deposits it is critical to establish the context and relative relationships of these units to the rest of the Naukluft stratigraphy. This can be challenging given the pervasive deformation resulting from Damara Orogen tectonic transport, coupled with the scarcity of independent radiometric age constraints to facilitate correlation and chronology (Korn & Martin 1959; Hartnady 1978; Miller 2008). In particular, we were interested in the relationship between the Northern Pavian Nappe, which includes the Marinoan-associated Blässkranz and Tsabisis formations, and the overlying sandy dolostone Noab Formation of the Kudu Nappe. The contact between these two nappes has been a source of debate in the literature, as indications of intense bedding parallel deformation along this horizon in limestones obscure the contact and has been used as part of a tectonic model for structural inversion – where an older Kudu Nappe was thrust over a younger Northern Pavian Nappe (Hartnady 1978; 1980). However, with more extensive mapping and more detailed appreciation of stratigraphic transitions we show that the contact varies spatially between localized younger-over-older thrust faults, erosive disconformities, and progressive conformable intercalation. As a result, we are confident that the Noab Formation of the Kudu Nappe represents a younger unit that follows stratigraphically from Marinoan-associated

rocks of the Northern Pavian Nappe. Another unit with ambiguous relationships was the Southern Pavian Nappe, which is composed of mixed carbonate-siliciclastic strata that includes a thick dolostone unit containing both tubestone (*sensu* Corsetti and Grotzinger 2005) and oolitic facies. Previous work in the literature suggested that this dolostone unit of the Southern Pavian Nappe could be laterally equivalent to the Northern Pavian Nappe cap carbonate (Korn & Martin 1959), which could be an appealing correlation as the tubestone facies found in the Southern Pavian Nappe is commonly associated with Marinoan cap carbonates (Cloud et al. 1974; Corsetti & Grotzinger 2005; Bosak et al. 2013). However, our field study showed that the Southern Pavian Nappe only intersects with the Northern Pavian Nappe by thrust fault contacts with no indication of transitional stratigraphy, along with indication that the Southern Pavian Nappe was thrust up from a lower structural level than the Northern Pavian Nappe. This is coupled with a lack of similarities in the sedimentary facies, the inability to correlate sequence stratigraphic surfaces between the dolostone units, and sizable differences in chemostratigraphic patterns which all indicate that rocks of the Southern Pavian Nappe are likely not correlative with rocks of the Northern Pavian Nappe. Rocks of the Southern Pavian Nappe also are not easily correlated with any other units of the Naukluft Nappe Complex. Collectively, we are therefore able to consider the combined units of the Northern Pavian and Kudu nappes to be a single stratigraphic succession that provides a valuable Cryogenian to Ediacaran stratigraphic record from the Kalahari margin. Additionally, the updated stratigraphic and structural relationships enable us to reconsider overly complex models of deformation and emplacement that have been proposed for the NNC (Hartnady 1978). Our work helps further simplify (Quinn thesis; Quinn et al., in prep) the tectonic model to feature just two episodes of deformation which imply that the prior basis for quantitative estimates (Hartnady 1978) of thrust displacements of the NNC may no longer be valid, and therefore the displacement distance may have been significantly less than 78 km.

Chapter 4 utilizes numerical simulation to explore the dynamics of two episodes of sea-level rise and fall recorded in the upper Blässkranz Formation and Tsondab member cap carbonate, which are unusual for terminal Marinoan deposits. We study a range of reconstructed synchronous and continuous deglaciation models to find that the observed sea-level patterns

of the Naukluft can be fully explained by glacial isostatic mechanisms driven by the deglaciation. The duration of deglaciation is poorly constrained due to a lack of direct radiometric geochronology and, despite various efforts to estimate the duration of cap carbonate deposition, the relative timing of global cap carbonate deposition and deglaciation remains uncertain (Trindade et al. 2003; Hoffman et al. 2007; 2017; Hoffman 2011; Font et al. 2010; Hoffman & Macdonald 2010; Kennedy & Christie-Blick 2011; Yang et al. 2017; Nordsvan et al. 2019; Fairchild et al. 2022). The only direct quantitative estimate for the duration of the Marinoan deglaciation is based on global climate model simulations of Hyde et al. (2000), which predicted a timespan of ~ 2 kyr or less, but these models emphasized other questions regarding Snowball Earth and were limited in their scope and parameter space exploration of the deglaciation duration. Exploring the spatial distribution with shoreline-perpendicular transects, our sea-level models show a range of sea-level histories for short duration deglaciations (~ 2 kyr), including exclusive sea-level rise in the distal regions and sea-level rise followed by sea-level fall in the proximal area; but cannot drive the two distinct phases of sea-level fall. In contrast, longer deglacial durations between ~ 10 and 30 kyr show these same patterns in more distal or proximal sites, but also have a spatial zone in between that records two intervals of sea-level rise and fall, consistent with the stratal patterns observed in Naukluft Mountains cap carbonate succession. Sensitivity tests show these patterns with two intervals of sea-level rise and fall do vary slightly with different model parameters, such as mantle viscosity and paleogeography, but are broadly robust along most continental margins so long as the duration of deglaciation remains long (~ 10 -30 kyr). Other globally-distributed Marinoan cap carbonates show a range of sea-level patterns that differ from the two intervals of sea-level rise and fall observed in the Naukluft (e.g. Kennedy 1996; Macdonald et al. 2009; Hoffman & Halverson 2011; Bertrand-Sarfati 1997; Shields et al. 2007; Zhou et al. 2010; Creveling et al. 2016; Gan et al. 2022), but given the shoreline-perpendicular spatial variability of sea-level pattern, these could also be accounted for by a long duration deglaciation. Most notably, sea-level histories that show exclusive sea-level rise or sea-level rise followed by fall are predicted for sites that are more distal than the marginal zone of Naukluft-style sea-level patterns, depending on proximity and size of the ice sheet. In the case of both intervals of sea-level rise and fall being directly driven by deglacial mechanisms of a long duration deglaciation (e.g. 20 kyr), we can also suggest an

estimate for the timespan of cap carbonate deposition to be ~25-30 kyr, which is an intermediate estimate relative to suggestions from the literature that range from 10^3 to 10^5 (Hoffman & Schrag 2002; Trindade et al. 2003; Hoffman et al. 2007; Font et al. 2010; Hoffman et al. 2017; Nordsvan et al. 2019). With the limited existing constraints on duration and synchronicity of deglaciation, this work highlights the importance of future work to better constrain the ice history and climate transition of the Marinoan Snowball Earth deglaciation.

CHAPTER 1 REFERENCES

- Ahr, W. M. (1973). Carbonate Ramp—Alternative to Shelf Model. *AAPG Bulletin*, 57(9), 1826-1826.
- Bertrand-Sarfati, J., Flicoteaux, R., Moussine-Pouchkine, A., & Ait Kaci, A. A. (1997). Lower Cambrian apatitic stromatolites and phospharenites related to the glacio-eustatic cratonic rebound (Sahara, Algeria). *Journal of Sedimentary Research*, 67(5), 957-974.
- Boag, T. H., Stockey, R. G., Elder, L. E., Hull, P. M., & Sperling, E. A. (2018). Oxygen, temperature and the deep-marine stenothermal cradle of Ediacaran evolution. *Proceedings of the Royal Society B*, 285(1893), 20181724.
- Bold, U., Smith, E. F., Rooney, A. D., Bowring, S. A., Buchwaldt, R., Dudás, F. Ó., ... & Macdonald, F. A. (2016). Neoproterozoic stratigraphy of the Zavkhan terrane of Mongolia: The backbone for Cryogenian and early Ediacaran chemostratigraphic records. *American Journal of Science*, 316(1), 1-63.
- Bosak, T., Mariotti, G., MacDonald, F. A., Perron, J. T., & Pruss, S. B. (2013). Microbial sedimentology of stromatolites in Neoproterozoic cap carbonates. *The Paleontological Society Papers*, 19, 51-76.
- Burchette, T. P., & Wright, V. P. (1992). Carbonate ramp depositional systems. *Sedimentary geology*, 79(1-4), 3-57.
- Cloud, P., Wright, L. A., Williams, E. G., Diehl, P., & Walter, M. R. (1974). Giant stromatolites and associated vertical tubes from the Upper Proterozoic Noonday Dolomite, Death Valley region, eastern California. *Geological Society of America Bulletin*, 85(12), 1869-1882.
- Corsetti, F. A., & Grotzinger, J. P. (2005). Origin and significance of tube structures in Neoproterozoic post-glacial cap carbonates: example from Noonday Dolomite, Death Valley, United States. *Palaios*, 20(4), 348-362.
- Cox, G. M., Halverson, G. P., Poirier, A., Le Heron, D., Strauss, J. V., & Stevenson, R. (2016). A model for Cryogenian iron formation. *Earth and Planetary Science Letters*, 433, 280-292.
- Crawford, A. R., & Daily, B. (1971). Probable non-synchronicity of Late Precambrian glaciations. *Nature*, 230(5289), 111-112.
- Creveling, J. R., & Mitrovica, J. X. (2014). The sea-level fingerprint of a Snowball Earth deglaciation. *Earth and Planetary Science Letters*, 399, 74-85.
- Creveling, J. R., Bergmann, K. D., & Grotzinger, J. P. (2016). Cap carbonate platform facies model, Noonday Formation, SE California. *GSA Bulletin*, 128(7-8), 1249-1269.
- Darroch, S. A., Smith, E. F., Laflamme, M., & Erwin, D. H. (2018). Ediacaran extinction and Cambrian explosion. *Trends in ecology & evolution*, 33(9), 653-663.
- Droser, M. L., Tarhan, L. G., & Gehling, J. G. (2017). The rise of animals in a changing environment: global ecological innovation in the late Ediacaran. *Annual Review of Earth and Planetary Sciences*, 45, 593-617.
- Eyles, N., & Januszczak, N. (2004). 'Zipper-rift': a tectonic model for Neoproterozoic glaciations during the breakup of Rodinia after 750 Ma. *Earth-Science Reviews*, 65(1-2), 1-73.
- Fabre, S., & Berger, G. (2012). How tillite weathering during the snowball Earth aftermath induced cap carbonate deposition. *Geology*, 40(11), 1027-1030.

- Fagereng, Å., Smith, Z., Rowe, C. D., Makhubu, B., & Sylvester, F. Y. (2014). Stress, strain, and fault behavior at a thrust ramp: Insights from the Naukluft thrust, Namibia. *Journal of Structural Geology*, 58, 95-107.
- Fairchild I. J. (1993). Balmy shores and icy wastes: The paradox of carbonates associated with glacial deposits in Neoproterozoic times, in *Sedimentology Review 1*, V. P. Wright, Ed. (Blackwell), pp. 1–16.
- Fairchild, I. J., Bao, H., Windmill, R., & Boomer, I. (2022). The Marinoan cap carbonate of Svalbard: Syngenetic marine dolomite with 17 O-anomalous carbonate-associated sulphate. *The Depositional Record*, Early-Access.
- Font, E., Nédélec, A., Trindade, R. I. F., & Moreau, C. (2010). Fast or slow melting of the Marinoan snowball Earth? The cap dolostone record. *Palaeogeography, Palaeoclimatology, Palaeoecology*, 295(1-2), 215-225.
- Gan, T., Zhou, G., Luo, T., Pang, K., Zhou, M., Luo, W., ... & Xiao, S. (2022). Earliest Ediacaran speleothems and their implications for terrestrial life after the Marinoan snowball Earth. *Precambrian Research*, 376, 106685.
- Goscombe, B., Foster, D. A., Gray, D., & Wade, B. (2017). Metamorphic response and crustal architecture in a classic collisional orogen: the Damara Belt, Namibia. *Gondwana Research*, 52, 80-124.
- Gray, D. R., Foster, D. A., Meert, J. G., Goscombe, B. D., Armstrong, R., Trouw, R. A. J., & Passchier, C. W. (2008). A Damara orogen perspective on the assembly of southwestern Gondwana. *Geological Society, London, Special Publications*, 294(1), 257-278.
- Grotzinger, J. P. (1989). Facies and evolution of Precambrian carbonate depositional systems: emergence of the modern platform archetype, In P. D. Crevello, J. L. Wilson, J. F. Sarg, J. F. Read *Controls on Carbonate Platforms and Basin Development*, *SEPM Special Publication 44*, (pp. 79-106).
- Grotzinger, J. P., Bowring, S. A., Saylor, B. Z., & Kaufman, A. J. (1995). Biostratigraphic and geochronologic constraints on early animal evolution. *Science*, 270(5236), 598-604.
- Grotzinger, J. P., & Knoll, A. H. (1995). Anomalous carbonate precipitates: is the Precambrian the key to the Permian?. *Palaios*, 578-596.
- Grotzinger, J. P., & James, N. P. (2000). Precambrian carbonates: evolution of understanding.
- Harland, W. B. (1964). Critical evidence for a great infra-Cambrian glaciation. *Geologische Rundschau*, 54, 45-61.
- Hartnady, C. J. H. (1978). The structural geology of the Naukluft Nappe Complex and its relationship to the Damara Orogenic Belt, South West Africa/Namibia. [Doctoral dissertation, University of Cape Town]. <http://hdl.handle.net/11427/18057>
- Hartnady, C. J. H. (1980). Geological map of the Naukluft area, *Precambrian Research Unit, University of Cape Town*.
- Hebert, C. L., Kaufman, A. J., Penniston-Dorland, S. C., & Martin, A. J. (2010). Radiometric and stratigraphic constraints on terminal Ediacaran (post-Gaskiers) glaciation and metazoan evolution. *Precambrian Research*, 182(4), 402-412.
- Higgins, J. A., & Schrag, D. P. (2003). Aftermath of a snowball Earth. *Geochemistry, Geophysics, Geosystems*, 4(3).
- Hoffmann, K. H. (1989). New aspects of lithostratigraphic subdivision and correlation of late Proterozoic to early Cambrian rocks of the southern Damara Belt and their correlation with the central and northern Damara Belt and the Gariiep Belt.

- Hoffman, P. F., Kaufman, A. J., Halverson, G. P., & Schrag, D. P. (1998). A Neoproterozoic snowball earth. *Science*, 281(5381), 1342-1346.
- Hoffman, P. F., & Schrag, D. P. (2002). The snowball Earth hypothesis: testing the limits of global change. *Terra Nova*, 14(3), 129-155.
- Hoffman, P. F., Halverson, G. P., Domack, E. W., Husson, J. M., Higgins, J. A., & Schrag, D. P. (2007). Are basal Ediacaran (635 Ma) post-glacial “cap dolostones” diachronous?. *Earth and Planetary Science Letters*, 258(1-2), 114-131.
- Hoffman, P. F., & Macdonald, F. A. (2010). Sheet-crack cements and early regression in Marinoan (635 Ma) cap dolostones: regional benchmarks of vanishing ice-sheets?. *Earth and Planetary Science Letters*, 300(3-4), 374-384.
- Hoffman, P. F. (2011). Strange bedfellows: glacial diamictite and cap carbonate from the Marinoan (635 Ma) glaciation in Namibia. *Sedimentology*, 58(1), 57-119.
- Hoffman, P. F., & Halverson, G. P. (2011). Chapter 36 Neoproterozoic glacial record in the Mackenzie Mountains, northern Canadian Cordillera. *Geological Society, London, Memoirs*, 36(1), 397-412.
- Hoffman, P. F. (2013). The Great Oxidation and a Siderian snowball Earth: MIF-S based correlation of Paleoproterozoic glacial epochs. *Chemical Geology*, 362, 143-156.
- Hoffman, P. F., Abbot, D. S., Ashkenazy, Y., Benn, D. I., Brocks, J. J., Cohen, P. A., ... & Warren, S. G. (2017). Snowball Earth climate dynamics and Cryogenian geology-geobiology. *Science Advances*, 3(11), e1600983.
- Howell, J.V. (Editor) 1960: *Glossary of geology and related sciences*. American Geological Institute, Washington D.C., 325 p.
- Hyde, W. T., Crowley, T. J., Baum, S. K., & Peltier, W. R. (2000). Neoproterozoic ‘snowball Earth’ simulations with a coupled climate/ice-sheet model. *Nature*, 405(6785), 425-429.
- Irie, Y., Nakada, M., Okuno, J. I., & Bao, H. (2019). Nonmonotonic postdeglacial relative sea level changes at the aftermath of Marinoan (635 Ma) snowball Earth meltdown. *Journal of Geophysical Research: Solid Earth*, 124(8), 9373-9394.
- James, N. P., Narbonne, G. M., & Kyser, T. K. (2001). Late Neoproterozoic cap carbonates: Mackenzie Mountains, northwestern Canada: precipitation and global glacial meltdown. *Canadian Journal of Earth Sciences*, 38(8), 1229-1262.
- Jiang, G., Sohl, L. E., & Christie-Blick, N. (2003). Neoproterozoic stratigraphic comparison of the Lesser Himalaya (India) and Yangtze block (south China): Paleogeographic implications. *Geology*, 31(10), 917-920.
- Kennedy, M. J. (1996). Stratigraphy, sedimentology, and isotopic geochemistry of Australian Neoproterozoic postglacial cap dolostones; deglaciation, delta 13 C excursions, and carbonate precipitation. *Journal of sedimentary Research*, 66(6), 1050-1064.
- Kennedy, M. J., & Christie-Blick, N. (2011). Condensation origin for Neoproterozoic cap carbonates during deglaciation. *Geology*, 39(4), 319-322.
- Kirschvink, Joseph L. (1992) Late Proterozoic Low-Latitude Global Glaciation: the Snowball Earth. In: J.W. Schopf, C. Klein, & D. Des Maris (eds), *The Proterozoic Biosphere: A Multidisciplinary Study*. Cambridge University Press, pp. 51-52.
- Korn, H., & Martin, H. (1959). Gravity tectonics in the Naukluft mountains of South West Africa. *Geological Society of America Bulletin*, 70(8), 1047-1078.
- Macdonald, F. A., Jones, D. S., & Schrag, D. P. (2009). Stratigraphic and tectonic implications of a newly discovered glacial diamictite–cap carbonate couplet in southwestern Mongolia. *Geology*, 37(2), 123-126.

- Macdonald, F. A., Schmitz, M. D., Crowley, J. L., Roots, C. F., Jones, D. S., Maloof, A. C., ... & Schrag, D. P. (2010). Calibrating the cryogenian. *Science*, 327(5970), 1241-1243.
- Macdonald, F. A., & Wordsworth, R. (2017). Initiation of Snowball Earth with volcanic sulfur aerosol emissions. *Geophysical Research Letters*, 44(4), 1938-1946.
- Martin, H., Porada, H., & Wittig, R. (1983). The root zone of the Naukluft Nappe Complex: geodynamic implications. In *Intracontinental Fold Belts: Case Studies in the Variscan Belt of Europe and the Damara Belt in Namibia* (pp. 679-698). Springer Berlin Heidelberg.
- Miller, R. M. (2008). Neoproterozoic and early Palaeozoic rocks of the Damara Orogen. *The Geology of Namibia*, 2, 13-1.
- McIlreath, I., and N. James. "Facies models 13. Carbonate slopes." *Geoscience Canada* 5.4 (1978): 189-199.
- Mukherjee, I., Large, R. R., Corkrey, R., & Danyushevsky, L. V. (2018). The Boring Billion, a slingshot for complex life on Earth. *Scientific reports*, 8(1), 4432.
- Myrow, P. M., & Kaufman, A. J. (1999). A newly discovered cap carbonate above Varanger-age glacial deposits in Newfoundland, Canada. *Journal of Sedimentary Research*, 69(3), 784-793.
- Nordsvan, A. R., Barham, M., Cox, G., Kirscher, U., & Mitchell, R. N. (2019). Major shoreline retreat and sediment starvation following Snowball Earth. *Terra Nova*, 31(6), 495-502.
- Pu, J. P., Bowring, S. A., Ramezani, J., Myrow, P., Raub, T. D., Landing, E., ... & Macdonald, F. A. (2016). Dodging snowballs: Geochronology of the Gaskiers glaciation and the first appearance of the Ediacaran biota. *Geology*, 44(11), 955-958.
- Pu, J. P., Macdonald, F. A., Schmitz, M. D., Rainbird, R. H., Bleeker, W., Peak, B. A., ... & Hamilton, M. A. (2022). Emplacement of the Franklin large igneous province and initiation of the Sturtian Snowball Earth. *Science Advances*, 8(47), eadc9430.
- Quinn, D. P., (2018). *Regional Structural Geology of Earth and Mars*. Dissertation (Ph.D.), California Institute of Technology. doi:10.7907/9enj-wn23.
- Quinn, D. P., (in prep). *Tectonostratigraphy of the Zebra Nappe, a structurally displaced Ediacaran passive margin in the southern Naukluft Mountains, Namibia*. *Gondwana Research*.
- Read, J. F. (1985). Carbonate platform facies models. *AAPG bulletin*, 69(1), 1-21.
- Roberts, N. M. (2013). The boring billion?—Lid tectonics, continental growth and environmental change associated with the Columbia supercontinent. *Geoscience Frontiers*, 4(6), 681-691.
- Rooney, A. D., Strauss, J. V., Brandon, A. D., & Macdonald, F. A. (2015). A Cryogenian chronology: Two long-lasting synchronous Neoproterozoic glaciations. *Geology*, 43(5), 459-462.
- Rooney, A. D., Cantine, M. D., Bergmann, K. D., Gómez-Pérez, I., Al Baloushi, B., Boag, T. H., ... & Strauss, J. V. (2020). Calibrating the coevolution of Ediacaran life and environment. *Proceedings of the National Academy of Sciences*, 117(29), 16824-16830.
- Rowe, C. D., Fagereng, Å., Miller, J. A., & Mapani, B. (2012). Signature of coseismic decarbonation in dolomitic fault rocks of the Naukluft Thrust, Namibia. *Earth and Planetary Science Letters*, 333, 200-210.
- Shields, G. A., Deynoux, M., Culver, S. J., Brasier, M. D., Affaton, P., & Vandamme, D. (2007). Neoproterozoic glaciomarine and cap dolostone facies of the southwestern Taoudéni Basin (Walidiala Valley, Senegal/Guinea, NW Africa). *Comptes Rendus Geoscience*, 339(3-4), 186-199.

- Sui, Y., Huang, C., Zhang, R., Wang, Z., Ogg, J., & Kemp, D. B. (2018). Astronomical time scale for the lower Doushantuo Formation of early Ediacaran, South China. *Science bulletin*, 63(22), 1485-1494.
- Trindade, R. I. F. D., Font, E., D'Agrella-Filho, M. S., Nogueira, A. C. R., & Riccomini, C. (2003). Low-latitude and multiple geomagnetic reversals in the Neoproterozoic Puga cap carbonate, Amazon craton. *Terra Nova*, 15(6), 441-446.
- Viola, G., Mancktelow, N. S., & Miller, J. A. (2006). Cyclic frictional-viscous slip oscillations along the base of an advancing nappe complex: Insights into brittle-ductile nappe emplacement mechanisms from the Naukluft Nappe Complex, central Namibia. *Tectonics*, 25(3).
- Whalen, M. T., Eberli, G. P., Van Buchem, F. S., Mountjoy, E. W., & Homewood, P. W. (2000). Bypass margins, basin-restricted wedges, and platform-to-basin correlation, Upper Devonian, Canadian Rocky Mountains: implications for sequence stratigraphy of carbonate platform systems. *Journal of Sedimentary Research*, 70(4), 913-936.
- Williams, G. E. (1975). Late Precambrian glacial climate and the Earth's obliquity. *Geological magazine*, 112(5), 441-465.
- Williams, G. E. (1979). Sedimentology, stable-isotope geochemistry and palaeoenvironment of dolostones capping late Precambrian glacial sequences in Australia. *Journal of the Geological Society of Australia*, 26(7-8), 377-386.
- Xiao, S., Narbonne, G. M., Zhou, C., Laflamme, M., Grazhdankin, D. V., Moczydlowska-Vidal, M., & Cui, H. (2016). Towards an Ediacaran time scale: problems, protocols, and prospects. *Episodes Journal of International Geoscience*, 39(4), 540-555.
- Xiao, S., & Tang, Q. (2018). After the boring billion and before the freezing millions: evolutionary patterns and innovations in the Tonian Period. *Emerging topics in life sciences*, 2(2), 161-171.
- Yang, J., Jansen, M. F., Macdonald, F. A., & Abbot, D. S. (2017). Persistence of a freshwater surface ocean after a snowball Earth. *Geology*, 45(7), 615-618.
- Zakharov, D. O., Bindeman, I. N., Slabunov, A. I., Ovtcharova, M., Coble, M. A., Serebryakov, N. S., & Schaltegger, U. (2017). Dating the Paleoproterozoic snowball Earth glaciations using contemporaneous subglacial hydrothermal systems. *Geology*, 45(7), 667-670.
- Zhou, C., Bao, H., Peng, Y., & Yuan, X. (2010). Timing the deposition of ¹⁷O-depleted barite at the aftermath of Nantuo glacial meltdown in South China. *Geology*, 38(10), 903-906.

*Chapter 2***FACIES AND STRATIGRAPHY OF THE BASAL EDIACARAN CAP CARBONATE, NAUKLUFT MOUNTAINS, NAMIBIA**

Authors: Freya K. Morris^{a*} and John P. Grotzinger^a

^a *Department of Geological and Planetary Sciences, California Institute of Technology, Pasadena, CA 91125, USA*

** Corresponding Author: morrisfreya15@outlook.com*

Abstract: The termination of the Marinoan Snowball Earth glaciation constitutes a dramatic interval of climate change. This field study seeks to investigate this climate transition by characterizing the basal-Ediacaran cap carbonate succession of the Tsabisis Formation overlying the Blässkranz Formation glacial deposits exposed in the Naukluft Mountains of Namibia by using sedimentologic and stratigraphic field observations supplemented by chemostratigraphic analyses. Measured sections and lateral bed/unit tracing delineate stratigraphic stacking patterns and regional facies changes. In downdip areas Marinoan diamictite transitions upward into dolostone intermixed with sandstone and extrabasinal clasts that is gradually overlain by fine grained laminated dolostone. Updip localities show the diamictite is overlain by intercalated sandstones, gravels, and shales before an abrupt change to the laminated dolostone of the cap carbonate. A succession of stromatolites, which become strongly elongate upward, prograde into the laminated dolostone in the updip localities. The stromatolites are overlain by laminated dolostone that grades upward into rhythmite with intercalations of shale. Near the top of the cap, rhythmites may be reworked into tabular intraclast conglomerate, locally intercalated with hummocky cross stratified sandstone, which passes upward into the shale and limestone members of the Tsabisis Formation. The Tsabisis Formation is overlain by the Noab Formation, dominated by sedimentary breccia, laminated dolostone, and sandstone. The lateral and vertical distribution of facies indicate a retreat of the shoreline and glacially sourced siliciclastics near the base of the cap carbonate, a shallowing succession to fair-weather wave base at the top of the

stromatolite facies, and a second shallowing succession to storm wave base near the top of the cap carbonate. Maximum flooding occurred soon after the initiation of carbonate deposition and two sequence boundaries mark higher stratigraphic levels within the cap carbonate. The depositional patterns of the Tsabisis Formation cap carbonate resemble that of other Precambrian mixed carbonate-siliciclastic platforms and shows multiple base-level fluctuations that could be attributed to a range of mechanisms. Some of the base-level changes may have been directly coupled to events driven by deglaciation but distinguishing these from conventional controls on accommodation space in the rock record is challenging and multiple depositional models are feasible.

Key Words: cap carbonate, Marinoan, deglaciation, Naukluft, Namibia

1. Introduction

The termination of the Marinoan Snowball Earth glacial epoch was one of the most extreme climate events in Earth history (e.g. Kirschvink 1992; Hoffman et al. 1998; Hoffman et al. 2017). Yet, the transition from global glaciation to an ice-free warmer climate is still poorly constrained. For example, Ediacaran cap carbonates (~635 Ma) overlie Marinoan glaciogenic strata and potentially provide a critical record of the climate, sea-level history, ocean chemistry, and time frames across this transition (Hoffman & Schrag 2002; Halverson & Shields-Zhou 2011; Hoffman et al. 2017; Wei et al. 2019). These cap carbonates are typically dolostone and characteristically host a large negative carbon isotope excursion and variety of unusual carbonate textures including tubestones, crystal fans, and giant wave ripples (Cloud et al. 1974; Kennedy 1996; Hoffman et al. 1998; James et al. 2001; Higgins & Schrag 2003; Allen & Hoffman 2005; Corsetti & Grotzinger 2005; Jerolmack & Mohrig 2005; Jiang et al. 2006; Macdonald et al. 2009; Hoffman & Macdonald 2010; Rose & Maloof 2010; Hoffman 2011; Lamb et al. 2012; Creveling et al. 2016; Hoffman et al. 2017; Hoffman et al. 2021). However, although their idiosyncratic facies and textures are frequently emphasized, detailed studies of more ordinary carbonate facies, including lateral facies distributions and platform morphology, are necessary to constrain relative sea-level histories and temporal evolution (Kennedy 1996; James et al. 2001; Jiang et al. 2006; Hoffman et al. 2007; Rose & Maloof 2010; Kennedy & Christie-Blick 2011; Creveling et al. 2016).

The terminal deglaciation from Snowball Earth by global ice-sheet melting has been estimated by a coupled ice-sheet-climate model to have been over a timespan of ~ 2 kyr or less (Hyde et al. 2000). The melting of grounded ice sheets would have caused substantial eustatic (global mean) sea-level rise (Hoffman et al. 2007; Hoffman 2011). Yet, this sea-level rise would intersect with several regionally dependent drivers of base-level change, including the loss of gravitational attraction of ice sheets upon seawater and isostatic adjustment triggered by the removal of the ice masses (Creveling & Mitrovica 2014; Irie et al. 2019), along with the conventional controls on accommodation space of sediment accumulation and tectonic subsidence (e.g. Schlager 1981). Previous work has found different cap carbonates around the world recording either exclusively transgression (Kennedy 1996; Macdonald et al. 2009; Rose & Maloof 2010), basal regression followed by transgression – the regression largely attributed to the loss of gravitational attraction from early ice melting (Hoffman & Macdonald 2010; Hoffman 2011), or transgression followed by regression (and commonly subaerial exposure) at the top of the cap carbonates – interpreted to be the result of isostatic crustal rebound (Bertrand-Sarfati 1997; Shields et al. 2007; Zhou et al. 2010; potentially Creveling et al. 2016; Gan et al. 2022). The timespan of cap carbonate deposition has proved difficult to determine – resolution limitations have prevented direct radiometric geochronology and though paleomagnetic reversal studies have proposed estimates of \sim a few 10^5 yrs (Trindade et al. 2003; Font et al. 2010), these are tenuous because constraints on the frequency of paleomagnetic reversals are absent for the Ediacaran and it may be difficult to distinguish reversals from geomagnetic excursions and noise given the limited number of datasets (Hoffman et al. 2017). Others have used theoretical arguments of exponentially decaying carbonate sedimentation rates (Penman & Rooney 2019), to posit a very rapid initial sedimentation rate that quickly decays through the cap carbonate (Fairchild et al. 2022). Therefore, determining the base-level history, the physical mechanisms that are controlling regional sea-level, and relative timing of events in cap carbonate successions may inform our understanding of the Marinoan deglaciation and provide a ways to estimate timeframes in strata that lack direct age constraints.

Work on cap carbonates has typically had a heavy emphasis on the idiosyncratic carbonate textures and accompanying negative carbon isotope excursion (e.g. Hoffman & Shrag 2002;

Allen & Hoffman 2005; Hoffman et al. 2007; Hoffman & Li 2009; Hoffman & Macdonald 2010; Hoffman et al. 2017), yet the resulting depositional models and sequence stratigraphic framework generally does not incorporate the observed regional differences in sea-level patterns (e.g. Hoffman & Schrag 2002; Hoffman et al. 2017; variability predicted by Creveling & Mitrovica 2014; Irie et al. 2019). From this, important questions arise – despite the idiosyncratic features, does the stratigraphic evolution of cap carbonate platforms resemble that of canonical platform archetypes (Read 1985; Grotzinger 1989; Burchette & Wright 1992)? What regional differences in depositional history and sea-level patterns exist in cap carbonates, and how might they inform our understanding of the deglaciation?

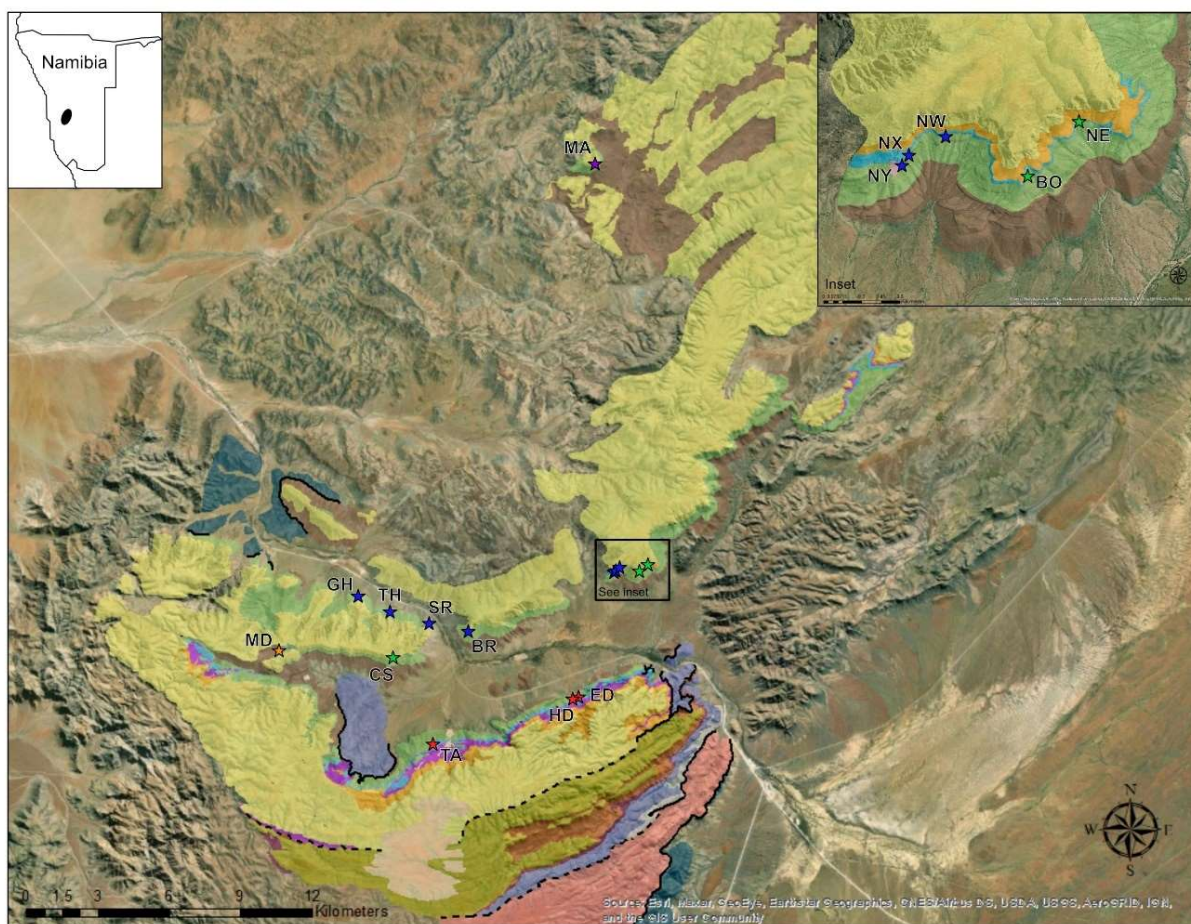
A suitable cap carbonate for a detailed sedimentological and stratigraphic study can be found in the Tsabisis Formation, exposed in the mountainous plateau of the Naukluft Mountains in south-central Namibia (Hoffmann 1989; Miller 2008). The present study seeks to constrain the facies distribution, stratigraphic architecture, and resulting sea-level history of the Naukluft cap carbonate. The sea-level and sequence stratigraphic history of the Tsabisis cap carbonate can then be compared with other models of cap carbonate deposition and mechanisms of sea-level change to evaluate the stratigraphic record and temporal evolution of this global deglaciation.

2. Geologic background

2.1 Tectonic and structural context

Neoproterozoic strata of the Naukluft Mountains are contained within a tectonic klippe known as the Naukluft Nappe Complex (NNC, Fig. 2.1). The NNC is a product of south-southeastward thrusting (Hartnady 1978; Martin et al. 1983; Quinn 2018) over the Nama foreland basin of the Kalahari craton during the ~590-505 Ma Damara Orogeny (Gray et al. 2008; Miller 2008; Goscombe et al. 2017). The root of the NNC was likely the northern margin of the Kalahari Craton. Structural levels above the basal decollement are represented by small-scale folds and thrust imbricates (Fig. 2.2B), within several large-scale nappe units (Korn & Martin 1959; Hartnady 1978; Hartnady 1980; Quinn 2018). Folds and thrusts generally show S-SE vergence, with SW vergence in the western Naukluft (Korn & Martin

1959; Hartnady 1978; Morris, in-progress thesis). The deformation of the sedimentary section throughout the NNC is accompanied by a lower greenschist metamorphic overprint (Korn & Martin 1959; Hartnady 1978); fortunately, primary fabrics are only rarely obscured.



Stratigraphic Units

Main Succession

- Noab Fm. upper mbr.
- Noab Fm. sedimentary breccia mbr.
- Tsabisis Fm. upper mbr.
- Tsabisis Fm. middle mbr.
- Tsabisis Fm. Tsondab mbr.
- Blasskrans Fm.
- Remhoogte Fm.

Legend

Southern Pavian Nappe Succession

- Adelt Fm. dolostone mbr.
- Adelt Fm. limestone mbr.
- Adelt Fm. shale mbr.
- Adelt Fm. tubestone mbr.
- Aushlucht Fm.

Other Regional Units

- Tufa & cover
- Nama Group (~Late Ediacaran)
- Bullsport Formation

Structure

- Thrust Fault
- Fault (uncertain)

Figure 2.1. Geologic map of the pertinent portions of the Naukluft Mountains. Upper-left regional map shows location of the Naukluft Mountains by the black oval in south-central Namibia. Colored stars in the geologic maps show the locations of the stratigraphic sections described in the text. The colors of the stars represent the interpreted platform positions of the localities – cooler colors (purple, blue) represent more downdip localities, while hotter colors (orange, red) represent more updip localities, green represents intermediate platform positions. The inset shows a more detailed view around the BO locality, an area where depositional strike trends ~SW to NE. The localities show by the stars indicate only the well exposed and representative sections for the relevant units shown in Fig. 2.3 and Supp. Fig. 2.1, depicting a sub-set of localities investigated for this study. Due to lithologic change within the Blässkranz Formation, and structural complexities, distinguishing between the Remhoogte Formation and Blässkranz Formation becomes challenging in the northernmost regions of the Naukluft Mountains. As such, outside of the well exposed MA locality, they are mapped together as Remhoogte Formation.

From lower to higher structural levels, the NNC is comprised of the Zebra, Dassie, Southern Pavian, Northern Pavian, and Kudu nappes (Korn & Martin 1959; Hartnady 1978; Hoffmann 1989; Quinn 2018). Most pertinent for the present study is the Northern Pavian Nappe, which contains the Remhoogte, Blässkranz, and Tsabisis formations, and the Kudu Nappe that includes that Noab Formation. Though there is locally intense shear deformation and minor thrusts around the contact between the Northern Pavian and Kudu nappes, there is no stratigraphic inversion represented by these structural units (*sensu* Korn & Martin 1959; Hoffmann 1989; Miller 2008; Morris, in-progress thesis; in contrast with Hartnady 1978). Therefore, we consider the Remhoogte, Blässkranz, Tsabisis, and Noab formations as a conformable stratigraphic succession. Different workers have considered the Southern Pavian Nappe to contain stratigraphic units equivalent to those in the Zebra Nappe, the Northern Pavian Nappe, and/or the Nama Group (Korn & Martin 1959; Hartnady 1978; Miller 2008). More recent mapping and lithostratigraphic correlations (Quinn 2018; Morris, in-progress thesis) suggest the Southern Pavian Nappe cannot be directly correlated to any of these units; it may be most comparable with the Buschmannsklippe Formation in east-central Namibia (Prave et al. 2011).

2.2 Lithostratigraphy

The present work is focused on the lower member of the Tsabisis Formation, here informally termed the Tsondab member, which comprises of cream to mauve colored dolostone up to 21 meters thick (Fig. 2.2; Hoffmann 1989; Miller 2008). The Tsondab member was deposited atop Blässkranz Formation glacial deposits and is overlain by the shale of the middle Tsabisis

member and mixed limestone-shale slope deposits of the upper Tsabis member. The Tsabis Formation is overlain by the Noab Formation, which here is informally divided into the stratigraphically discontinuous lower sedimentary breccia member and a laterally extensive mixed dolostone-clastic upper Noab member.

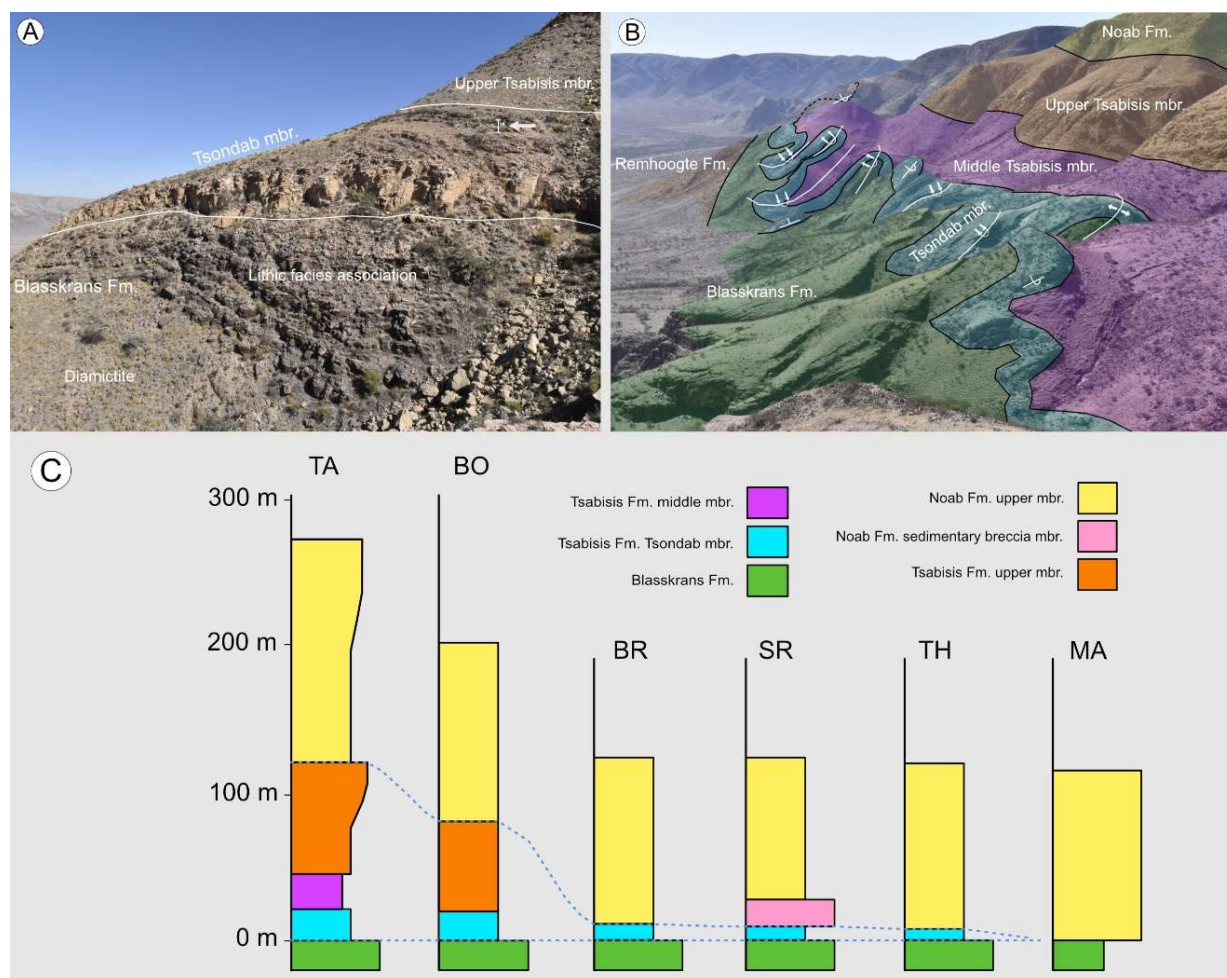


Figure 2.2. (A) Outcrop view of the light colored Tsondab member of the Tsabis Formation at the BO locality. Arrow points to ~2 m tall person for scale. The Blässkranz Formation shows the well bedded lithic facies association overlying the smooth slopes of the diamictite facies. Overlying the Blässkranz is the sharp lower contact of the Tsondab member (B) Outcrop view of the ED and HD localities (Supp. Fig. 2.1). Representative of the structural complexities encountered – the Tsondab member is often strongly folded, with tight to isoclinal angles and overturned orientations. Units colored to be consistent with legend in Fig. 2.2C. (C) Simplified stratigraphic columns showing the general units from the upper parts of the Blässkranz Formation through the Noab Formation. Sections are positioned from updip (left) to downdip (right). Blue dashed lines show the extent of the Tsabis Formation. The SR locality shows an example where the Tsondab member is only partly truncated by the sedimentary breccia member of the Noab Formation, in some other areas the Tsondab member is completely missing due to erosion represented by the sedimentary breccia member.

Post-Marinoan cap carbonates typically are dolostones that overlie Cryogenian glaciogenic strata (Hoffman & Schrag 2002; Hoffman et al. 2017). The sharp contact between the Tsondab member dolostone and the underlying glaciogenic Blässkranz Formation, along with regional correlations to units with radiometric age constraints, led to the Tsondab member to being interpreted as a Marinoan cap carbonate (Hoffmann 1989; Miller 2008)

The lowermost Remhoogte Formation is shale-dominated with minor subgreywacke and carbonate breccia (Korn & Martin 1959; Hartnady 1978), interpreted as a sedimentary *mélange* (Hartnady 1978) and deep-water turbiditic deposition (Miller 2008). The bulk of the Blässkranz Formation was described as a massive diamictite/breccia with carbonate clasts and dropstones in shale (Korn & Martin 1959; Hartnady 1978; Miller 2008). Miller (2008) noted that the clast suite was dominated by dark, commonly oolitic, limestone with minor components of grey dolostone, chert, quartzite, and basement granite – the latter correlated with the Gamsberg Granite and Piksteel Granodiorite. The upper Blässkranz contains volcanoclastic tuff interbedded with quartzite and shales (Hartnady 1978; Miller 2008). Miller (2008) recognizes a glacial origin for the Blässkranz via deep water mass flows and ice rafting.

Initial descriptions of the Tsabisis Formation were limited to noting a ‘white dolomite member’ overlain by purple shale and laminated limestone (Korn & Martin 1959; Hartnady 1978). Miller (2008) describes the Tsondab member as a light pink dolomite between 5 and 20 meters thick that shows a lower massive portion with wavy internal laminae and an upper part with dolomite interstratified with purple shale. This passes gradually into interbedded pink limestone and purple shale, with the top of the Tsabisis showing interbedded siltstones, dolomite, dolomitic limestone, and discordant breccia beds (Miller 2008). The Tsondab member is correlated with the Bildah Member of the Buschmannsklippe Formation in east-central Namibia, the basal dolomite of the Samara Formation in west-central Namibia, the Keilberg Member of the Maieberg Formation in northern Namibia, and the Dreigratberg member of the Holgat Formation in southern Namibia (Hoffmann 1989; Miller 2008; Macdonald et al. 2009). Overlying the Tsabisis Formation, the Noab Formation is generally reported as thick bedded to massive dolomite, sandy dolomite, and intercalated quartzite, which occasionally show current ripples (Korn & Martin 1959; Hartnady 1978; Miller 2008).

The vertical succession of facies and their paleogeographic distribution constrain the depositional history of the Tsondab member and related units. In the underlying Blässkranz Formation, glaciogenic diamictite facies in the south (Fig. 2.3) pass laterally into predominantly shales in the northern localities (Supp. Fig. 2.1D, MA). Similarly, the glacial outwash deposits of the “lithic facies association” in the Blässkranz Formation pinches out to the north (Fig. 2.3). The Tsondab member is at its thickest in the south, represented by the TA (Fig. 2.3) and ED (Supp. Fig. 2.1B) localities – all outcrops further south are comparable. The Tsondab member generally thins to the north and pinches out completely by the northern-most localities (Fig. 2.2C, Supp. Fig. 2.1D, MA). A succession of shallow-water stromatolite facies (see subsections 4.2.4, 4.2.5, and 5.2 below), that are laterally persistent in the southern Tsondab member pinch out northward by the intermediate localities (Fig. 2.3 TA, MD). The Tsondab member represents a gently sloping carbonate ramp (*sensu* Read 1985) with a northward facing direction (Fig. 2.1).

3. Methods

A lithofacies and sequence stratigraphic framework was developed for the Blässkranz, Tsabisis, and Noab formations of the Naukluft Mountains, with particular focus on the lower Tsondab member of the Tsabisis Formation. Three-dimensional outcrop trends (Fig. 2.2A, B) allowed lateral mapping of facies and many of their important transitions. Concurrently, bedding and cleavage attitudes were recorded along with fold and fault geometries to constrain the structural history and determine stratigraphic continuity. 25 detailed stratigraphic sections were measured (locations in Fig. 2.1; coordinates in Supp. Fig. 2.1A). Figure 3 shows seven of these sections that best represent the facies and their lateral changes from updip on the left to downdip on the right. Note that the TA and MD sections are composites of two and six closely spaced sections, respectively. Supplemental Figure 1 shows eight additional sections that pertain to the present discussion. Facies analysis was coupled with interpretations of stacking patterns to define systems tracts and depositional sequences (Mitchum et al. 1977; Vail et al. 1977; Van Wagoner 1988, 1990; Catuneanu 2009). Four sequences were identified across the Blässkranz, Tsabisis, and Noab formations.

Samples for facies analysis and C and O chemostratigraphy were collected while logging stratigraphic sections. Polished slabs and 82 thin sections were used to assist in lithofacies and diagenetic analysis. 254 samples were analyzed for chemostratigraphy, primarily to assist with the lithostratigraphic correlation of units. Dolostone and limestone without secondary veins or obvious alteration were targeted. Carbon and oxygen isotopes were analyzed using an automated carbonate preparation device (KIEL-III) coupled to a gas-ratio mass spectrometer (Finnigan MAT 252) at the University of Arizona Environmental Isotope Laboratory. Powdered samples were reacted with dehydrated phosphoric acid under vacuum at 70°C. The data of $\delta^{13}\text{C}$ and $\delta^{18}\text{O}$ were calibrated to VPDB (Vienna Pee Dee Belemnite) and external analytical precision is ± 0.08 ‰ (1σ) for $\delta^{13}\text{C}$ and ± 0.10 (1σ) for $\delta^{18}\text{O}$. Using published correction factors (Rosenbaum & Sheppard 1986; Swart et al. 1991), 1.4 ‰ was subtracted from the $\delta^{18}\text{O}$ values of dolomite samples to adjust for acid fractionation during analysis. No correction factors were necessary for $\delta^{13}\text{C}$ values.

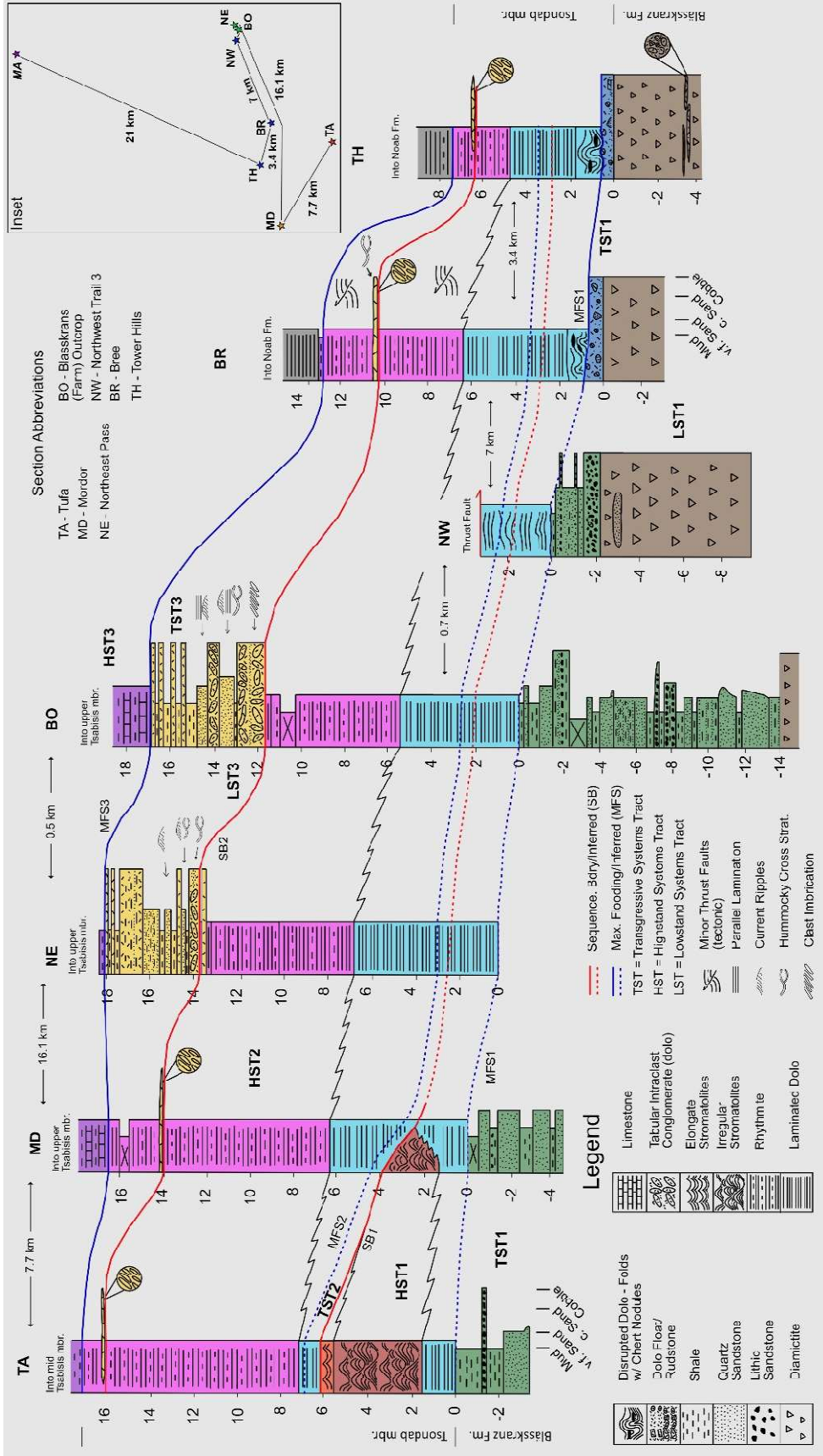


Figure 2.3. Measured sections of primarily the upper Blässkranz Formation and Tsondab member of the Tsabisis Formation with interpreted sequence stratigraphic correlations and systems tracts. Sections are positioned from updip (left) to downdip (right). Colors relate associated facies between sections. Lower green and brown colors show the upper portions of the Blässkranz Formation. The purple shales and limestone at the top of sections show the beginnings of the middle and upper members of the Tsabisis Formation, while the gray shaded facies represents the Noab Formation. The intervening stratigraphy represents the Tsondab member of the Tsabisis Formation, a Marinoan cap carbonate. Note the pinching out of the green colored lithic facies association between the BO, NW, and BR sections. The TA and MD sections show the prograding succession of stromatolites from updip positions. Though tabular intraclast conglomerate beds are found near the top of the Tsondab member in most regions, NE and BO sections show an expanded succession of intercalated tabular intraclast conglomerate, HCS sandstone, rhythmite, and shale. Inset shows the positions and distances between the sections of this figure along with the italicized MA section, which is not presented here but shown in Supp. Fig. 2.1D.

4. Facies and paleoenvironments

4.1 Blässkranz Formation

4.1.1 Diamictite

Description: The diamictite facies consists of matrix-supported and poorly-sorted clasts ranging from coarse sand to boulder in size (Fig. 2.4A). The matrix is greenish brown to dark maroon siliciclastic mudstone and does not show internal bedding, though clasts density varies laterally and vertically. Clast composition is dominated by tan dolostone and dark limestone, generally massive, but with abundant clasts of ooid grainstone. Rare quartzite and granitic clasts also are present. The diamictite facies contains thin to thick tabular beds of shale, massive quartz sandstone, and limestone-dominated clast-supported conglomerates.

Interpretation: The diamict texture is suggestive of an amalgamated mix derived from subglacial till pushed out of a glacier's grounding line. The front of glaciogenic material tends to be unstable and can become resedimented via debris flows that show a similar diamict texture as the till (Lønne 1995; Powell 1981; Lowe 1982; Shen et al. 2021). Though distinct dropstones are not observed, ice rafted debris dropped into outwash muds also can produce a diamict texture that can be difficult to distinguish from other glaciomarine facies (Lønne 1995; Powell 1981). Intermittent beds of shale and sandstone represent deposition from glacial outwash plumes as sediment gravity flows (Lønne 1995; Powell 1981; Shen et al. 2021). The predominance of carbonate clast composition suggests subglacial erosion of a

carbonate platform, though exact provenance is unknown. Similarly, the quartzite and granitic clasts indicates glacial erosion of extrabasinal cratonic sources. This facies is characteristic of ice-contact submarine fans (Lønne 1995).

4.1.2 Lithic facies association

This facies association is comprised of intercalated sandstones and shales, with uncommon interbeds of the diamictite facies.

4.1.2.1 Lithic pebbly sandstone

Description: These lithic fragment-rich sediments, along with rare dolostone clasts, mostly range in size from fine sand to pebble, with some clasts reaching up to boulder in size (Fig. 2.4B). Beds range in thickness from <1 cm to >1 m (Fig. 2.4C), although bed amalgamation is common. Beds tend to be tabular at outcrop scales though rarely there are lenses that pinch out laterally on a scale of meters. Grains tend to be subangular to angular, moderately to very-poorly-sorted, and clast-supported. Clasts of lithic fragments vary in color and texture. Some dark clasts show a distinctly vesicular texture and lithic fragments in thin section are dominated by elongate and angular plagioclase phenocrystic ‘laths’ within an amorphous matrix (Fig. 2.4B Inset). These textures are consistent with basaltic volcanic rock fragments (Scholle 1979). This facies occasionally contains a moderate proportion of fine to coarse rounded quartz grains. Beds show both normal and reverse grading, with contacts gradually transitioning between bounding shale beds (Fig. 2.4B).

4.1.2.2 Quartz sandstone

Description: Beds of gray sandstone, 5-100 cm thick, are composed predominantly of rounded, well-sorted quartz grains of very fine to very coarse size (Fig. 2.4C). Rarely, isolated pebble to cobble sized clasts of siliciclastic or carbonate lithologies are present. Massive bedding is most common, though planar lamination and current ripple trough cross lamination occurs in some beds. Most beds are tabular and up to 40 cm thick though some meter-width lenses of massive sandstone are present.

Current ripple sets range from 1.5 to 3 cm thick, with some examples of stoss-preservational climbing ripples. Both normal and reverse grading of grain sizes are present, though relatively rare.

4.1.2.3 Shale

Description: Siliciclastic mudstones, maroon, pale green, and rarely tan in color, form beds typically a few tens of centimeters thick (Fig. 2.4C). A well-developed cleavage related to tectonic deformation imparts a fissile appearance. Primary stratification is visible, however internal deformation and penetrative cleavage limit detailed observations.

Interpretation:

The lithic facies association represent fluctuations in energy level and sediment composition of a common overall depositional environment. Shales represent quiet-water background sedimentation of muds from suspension (Powell 1981; Shen et al. 2021). The lack of shallow water indicators including wave ripple stratification in the coarser facies suggest deposition below wave base. The sandstones lack well-developed Bouma-style turbidite successions (Bouma 1962), though planar laminated sandstones transitioning to current rippled sandstone may indicate deposition from waning turbidity currents. Climbing current ripples within the quartz sandstone suggest deposition by decelerating flows (Ashley et al. 1982). The sandstones with reverse and normal grading indicate deposition by wax-wane flows (Cheel & Rust 1982; Mulder et al. 2003; Lamb et al. 2008). Wax-wane flows can be produced by hyperpycnal flows tied to rising and falling discharge of a flooding fluvial system (Mulder et al. 2003; Lamb et al. 2008). Lithic sandstones are composed of volcanic rock fragments likely sourced from proximal volcanic material, then eroded and reworked into the marine environment by currents and sediment gravity flows. Together, the lithic and quartz sandstones represent deposition by sediment gravity flows, consistent with hyperpycnal and related turbiditic flows (Powell 1981). The oversized rock fragments and interbedded diamictite suggest the waning influence of glaciogenic ice rafted debris and ice advancement, respectively, though they could also be explained by remobilization of the underlying

diamictite (Powell 1981). Together this facies association suggests the prodelta environment of an ice-contact delta (Lønne 1995), where a proximal glacier and its recently deposited till still influenced deposition, but the processes were dominated by glacial outwash.

4.2 Tsabisis Formation, Tsondab member

The dolostone of the Tsondab member is heavily recrystallized to form an anhedral mosaic of crystals which have effectively overprinted any primary microtextures and limits the utility of thin section petrography.

4.2.1 Basal sandy dolostone

Description: Tan dolostone mixed with poorly-sorted silt to coarse sand-size quartz grains (~40-700 microns) dominates this facies. Extrabasinal clasts formed mostly of massive gray dolostone, and less commonly granitic, quartzite, and silicified oolite compositions, are found within the dolostone and sand matrix. Clasts are either dispersed within the dolostone matrix without point-to-point contact or distinct layering with a gradual lithologic transition of the matrix from the underlying diamictite (Fig. 2.4D), or they form clast-supported tabular beds ~15 cm thick abruptly overlying the diamictite facies (Fig. 2.4E). Clasts are granule to cobble in size and have angular to subrounded and equidimensional to elongate shapes. From a maximum proportion of ~50%, the facies consistently shows an upward decrease in quartz sand and silt content within the matrix. The facies is frequently cut by pervasive veins, filled with coarse dolomitic spar or silica.

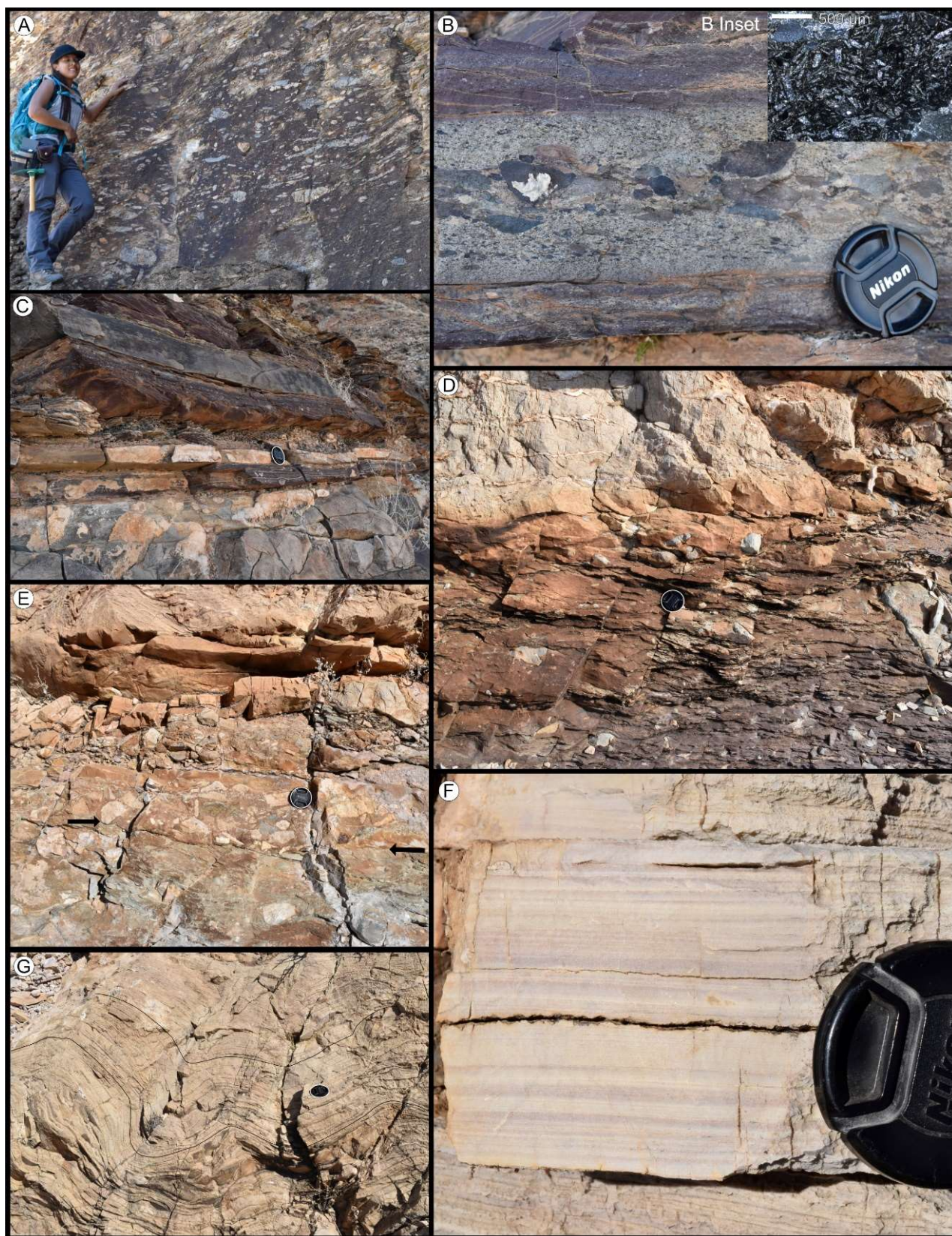


Figure 2.4. (A) Diamictite facies with large, poorly-sorted clasts of diverse composition, Blässkranz Formation. (B) Lithic sandstone with reverse and normal grading. Lens cap has a diameter of 5.5 cm. Inset shows thin section of lithic grains under plane-polarized light, 500 micron scale bar. Note elongate and angular plagioclase phenocrystic laths within a dark amorphous matrix. (C) Interbeds of gray quartz sandstone, shale, and thin beds of coarse lithic sandstone. Lens cap is 5.5 cm in diameter. (D) Gradual transition from dark-toned diamictite to overlying basal sandy dolostone with outsized clasts. Lens cap is 5.5 cm in diameter (E) Basal sandy dolostone facies with two clast-supported beds, arrows point to sharp contact with underlying diamictite. (F) Laminated dolostone facies with variable thickness of laminae. Lens cap is 5.5 cm in diameter. (G) Disrupted dolostone facies of folded laminated dolostone, with sheet cracks of spar and chert along the laminations and annotation highlighting the folded laminations. Lens cap is 5.5 cm in diameter.

Interpretation: The relatively massive nature of this facies makes interpretation difficult. Recrystallization of the dolostone inhibits carbonate grain recognition, and associated sedimentary structures are not observed. One hypothesis for the clast-supported beds is deposition by sediment gravity flows (Lowe 1982). The compositional similarity of the clasts with that of the underlying diamictite could indicate remobilization of the underlying glaciogenic deposits into mass flow deposits that evolved during the time of carbonate deposition. However, the examples with dispersed matrix-supported clasts and the gradual lithological transition of the matrix from siliciclastic muds of the diamictite facies to dolostone mixed with siliciclastic sands and silts, to dolostone lacking any siliciclastics, appears inconsistent with a series of discrete mass-flow deposits. An alternative hypothesis would feature accumulation of fine carbonate sediment from suspension mixed with sand and larger clasts as ice rafted debris (Lønne 1995; Powell 1981). Both depositional processes may have been concurrent across a ramp environment that was influenced by glacio-marine processes (Lønne 1995).

4.2.2 Laminated dolostone

Description: This facies consists of cream-colored very fine to finely crystalline dolostone (10-30 microns). The dolostone is thinly to very thinly laminated – 0.3 mm to 3 mm, with bundles of laminae commonly forming ~1 cm thick beds (Fig. 2.4F). Laminae generally are parallel and concordant, yet low angle truncations of sub-cm scale also are present. Rare medium silt-size quartz grains are dispersed throughout and show no concentration along laminae. Locally, the facies is more coarsely crystalline.

Interpretation: These thinly laminated fine grain sediments represent the delivery of allochthonous carbonate sediment from an updip source (McIlreath & James 1978; Grotzinger 1986). Sediment particles could have been deposited by gravitational suspension settling in hypopycnal plumes or directly from fine grained turbidites (Whalen et al. 2000; Creveling et al. 2016). Truncation surfaces may represent erosion of underlying sediments by traction currents. The absence of oscillatory sedimentary structures or exposure surfaces within very fine-grained sediments indicates deposition below wave base (Corkeron 2007). Together this indicates an outer-ramp and/or upper-slope environment for this facies (Ahr 1973; McIlreath & James 1978; Burchette & Wright 1992; Whalen et al. 2000; Creveling et al. 2016).

4.2.3 Disrupted dolostone

Description: Folding and brecciation via early post-depositional deformation overprint finely crystalline cream colored laminated dolostone (Fig. 2.4G). Folds reach up to 50 cm in wavelength and amplitude, in discontinuous, disharmonic shapes that rotate bedding up to vertical and with local overturning. Folding is most intense near the base of the unit (underlying strata lack these deformation features); folds progressively flatten upward into planar laminated dolostone. Diagenetic sheet cracks (Kennedy et al. 2001) run parallel to laminae and are filled with isopachous dolomitic spar with elongate crystals forming a ~3 mm-thick rim; thicker sheet cracks are filled with amorphous chert/silica within the spar rim. In other areas the laminated dolostone shows a fitted fabric of incipient brecciation in the absence of folding (Supp. Fig. 2.2). The void spaces within the fitted fabric are filled with equant brown sparry dolomite.

Interpretation: This facies was deposited in a manner similar to the laminated dolostone facies via accumulation of fines in a deep-water setting below wave base (McIlreath & James 1978). Following deposition, the partly cemented laminated dolostone underwent early deformation (Grotzinger 1986; Rossetti 1999). Most of the facies show convergent folds, with the unfolded fitted fabric representing extension during the formation of neptunian dikes (Grotzinger 1986; Berra & Felletti 2011). This type of early deformation is common on carbonate slopes – possible triggers include loading from overlying sediments, fluid

overpressure (Corkeron 2007), earthquakes (Berra & Felletti 2011), or gravitational instability. Whatever the cause, the facies shows early post-depositional downslope slumping and failure of the carbonate strata. The isopachous dolomitic spar, followed by silica, then filled the sheet cracks formed within the folded laminae.

4.2.4 Irregular stromatolites

Description: Irregular stromatolites are cream colored and have convex-upward laminae that define domes ranging from 4 to 15 cm in width, with 1 to 8 cm synoptic relief (Fig. 2.5A). Millimeter-scale laminae are composed of finely to medium crystalline (20-100 microns) dolostone with rare, interspersed silt-sized rounded quartz grains. These stromatolites lack strong inheritance of form vertically and vary in shape and size laterally. Some laminae are laterally linked across stromatolites, others converge and terminate against neighboring stromatolite domes. Domal forms do not show preferred orientation or elongation in plan view. Beds of irregular stromatolites have a flat geometry.

Interpretation: Irregular stromatolites lack subaerial exposure indicators, erosive features, intervening coarse sediment, and elongation. Together, this suggests a quiet depositional setting below the influence of wave or tidal energy (Logan 1974; Hoffman 1974; Ferronato et al. 2021). Most ancient stromatolites are interpreted to have formed within the photic zone by comparison to modern analogs (Sherman et al. 2000). Therefore, it is likely that the irregular stromatolites formed in relatively shallow subtidal water, though still deeper than fair-weather wave base (mid-ramp; Ahr 1973; Burchette & Wright 1992; Ferronato 2021).



Figure 2.5. (A) Irregular stromatolite facies, annotation highlighting wavy geometry of stromatolitic laminae. Lens cap is 5.5 cm in diameter (B) Cross sectional view of laterally-linked elongate stromatolites, annotations illustrate the inheritance of lamina form. Lens cap is 5.5 cm in diameter. Inset is a close-up of the stromatolites, showing the difference in color and shape between the troughs and peaks (C) Plan view of elongate stromatolites. Scale bar is graded by cm increments (D) Rhythmite facies – mauve dolostone beds parted by laminae of maroon shale. Lens cap is 5.5 cm in diameter. (E) Thin bed of tabular intraclasts. Lens cap is 5.5 cm in diameter. (F) Hummocky cross stratification in brown sandstone intermixed with gray dolostone. Lens cap is 5.5 cm in diameter. (G) Unsorted intraclasts of angular limestone. Large clast just above lens cap continues for ~1 meter to the left of the figure. Lens cap is 5.5 cm in diameter.

4.2.5 Elongate stromatolites

Description: Elongate stromatolites are cream colored and have convex-up laminae with cross-sectional morphologies ranging from domal to peaked with rounded troughs (Fig. 2.5B). Millimeter-scale laminae are composed of very fine to finely crystalline (10-40 microns) dolostone, with rare interspersed silt-sized rounded quartz grains. The width of domes and peaks ranges from 6-8 cm with a synoptic relief of ~2 cm. Laminae tend to display a modest inheritance of form, maintaining consistent shape and size vertically and laterally between stromatolites with continuous linked laminae (Fig. 2.5B). In plan view, the stromatolites form elongate parallel ridges (Fig. 2.5C). Bifurcations or intersection of ridges have not been observed. Direction of elongation, corrected for tectonic tilt, is generally oriented north-south throughout the field area (Fig. 2.6, Supp. Table 2.1). Beds of elongate stromatolite beds have a flat geometry.

Interpretation: The consistent elongate morphology of the stromatolites indicates sculpting by persistent wave or tidal current action (Logan 1974; Hoffman 1974; Grotzinger 1986). The elongation direction of stromatolites tends to develop parallel to current scour, which is generally perpendicular to the shoreline (Logan 1974; Grotzinger 1986; Hoffman & Grotzinger 1993). This suggests an east-west orientation of the paleoshoreline. Lack of exposure features indicates this facies was deposited in a subtidal environment, yet it was still shallow enough for waves/tidal currents to form consistent and extensive elongation. Therefore, these stromatolites formed in a shallow subtidal environment likely above fair-weather wave base (Grotzinger 1986; Grotzinger 1989; Creveling et al. 2016). This

presumably would have been a shallower inner ramp environment compared to the quiet-water environment of the irregular stromatolites (Burchette & Wright 1992).

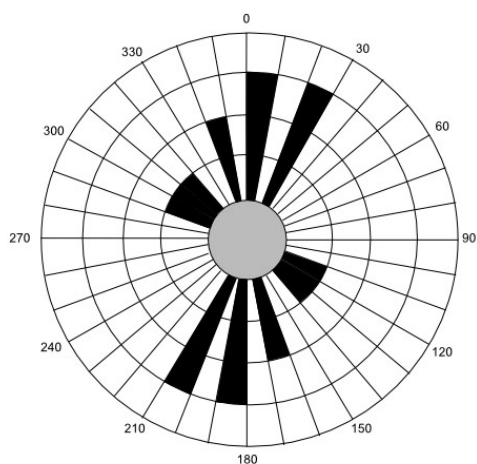


Figure 2.6. Rose diagram showing azimuths of elongate stromatolites corrected for tectonic tilt.

4.2.6 Rhythmites

Description: Rhythmites consist of mauve colored laminated dolostone intercalated with laminae of ~1 mm to ~3 cm thick maroon shale (Fig. 2.5D). The thinly bedded dolostone has planar millimeter to centimeter scale laminae that are composed of finely crystalline (20-40 microns) dolostone with intermixed siliciclastic mudstone. The frequency and thickness of the shale laminae tend to increase upwards through this facies.

Interpretation: The facies formed in a similar manner as the fine carbonate sediments of the laminated dolostone facies in deep waters below wave base (McIlreath & James 1978; Grotzinger 1986; Burchette & Wright 1992). The intermixing of siliciclastics within the dolostone indicates a greater influx of siliciclastics derived from terrestrial sources. Fluctuating pulses of fine carbonate and siliciclastic mud were brought to this outer-ramp environment via hypopycnal plumes or fine grained turbidites (McIlreath & James 1978; Burchette & Wright 1992; Whalen et al. 2000; Creveling et al. 2016).

4.2.7 HCS Sandstone

Description: This sandstone is rusty brown in color with grain size ranging from coarse silt to fine sand. It is composed mostly of quartz grains, with a minor mica component, intermixed with finely to medium crystalline dolostone (20-120 microns) in up to equal proportions. Hummocky cross stratification (HCS) is found in some beds where low-angle curved laminae and low-angle truncation surfaces form convex-up hummocks with wavelengths of ~40 cm (Fig. 2.5F). Other beds show abundant planar laminae and 2-3 cm thick current ripple sets. Current ripple sets commonly overlie planar laminae of the same bed. Beds tend to be ~2-20 cm in thickness and are generally lenticular with significant lateral variation in thickness. Beds of this facies are intercalated with the shale, rhythmite, and tabular intraclast conglomerate facies.

Interpretation: Hummocky cross stratification records deposition under the influence of storm waves (Southard et al. 1990; Duke et al. 1991; Myrow 1992; Myrow et al. 2008). The planar laminae and current ripples in the sandstone indicate traction flow as Bouma T_b – T_c successions showing decelerating unidirectional turbidity currents (Bouma 1962; Lowe 1982). This facies was deposited above storm wave base, with the intercalation of quiet-water shale and rhythmite indicating deposition largely below fair-weather wave base, consistent with a mid-ramp environment (Ahr 1973; Burchette & Wright 1992; Grammer et al. 2000).

4.2.8 Tabular intraclast conglomerate

Description: This facies is a pink/mauve colored rudstone that consists of tabular rounded dolostone intraclasts formed of finely recrystallized (20-60 microns) dolostone (Fig. 2.5E). The tabular intraclasts tend to be 0.5-2 cm thick and ~3-10 cm long. Intraclast orientations tend to be subhorizontal with common imbrication and some edgewise (~vertical) orientations. The matrix consists of fine to medium recrystallized (30-120 microns) dolostone intermixed with up to 30% quartz grains of silt to fine sand size. Beds tend to be lenticular and range up to ~0.5 meters in thickness and may be amalgamated. Basal scour, normal grading of clasts, and undulating top contacts are observed. Beds of this facies consistently form interbeds within rhythmite and are associated with shale and HCS sandstone.

Interpretation: The tabular intraclast conglomerates, with locally intercalated HCS sandstone, represent intermittent high energy events interspersed with shale and rhythmite that were deposited during quiet-water periods. Imbricated tabular intraclasts support deposition by traction currents with the edgewise orientations and undulating upper contacts of the beds indicating reworking by waves (Grotzinger 1986; Myrow et al. 2004). The composition and shape of the tabular intraclasts suggest they are rip ups of the thinly bedded rhythmite facies. These sedimentary structures and the locally associated HCS sandstone indicate erosion was likely related to storm wave and turbidity currents. This facies was deposited above storm wave base, with the intercalation of shale and rhythmite indicating deposition largely below fair-weather wave base, consistent with a mid-ramp environment (Ahr 1973; Grotzinger 1986; Burchette & Wright 1992; Grammer et al. 2000; Myrow et al. 2004).

4.3 Tsabisis Formation middle and upper members

4.3.1 Shale

The middle member of the Tsabisis Formation is composed of maroon shale. It was deposited by background settling from hypopycnal plumes or fine-grained turbidites in deep waters.

4.3.2 Limestone

Description: The upper member of the Tsabisis Formation is composed primarily of finely crystalline limestone (20-40 microns), commonly interbedded with dark shale. The facies commonly contains coarse, massive breccias formed of limestone and rare dolostone intraclasts that range from centimeter to meter in diameter (Fig. 2.5G).

Interpretation: This facies represents mixed carbonate-siliciclastic sedimentation in a distal deep-water slope setting (McIlreath & James 1978). The coarse intraclast deposits likely represent sediment gravity flows triggered by storms and/or slope failure (Lowe 1982; Hiscott & James 1985; Whalen et al. 2000). The finer grained carbonate and shale deposition shows lower energy allochthonous sedimentation by gravitational settling or turbidites from updip sources (McIlreath & James 1978; James 1981; Grotzinger 1986).

4.4 Noab Formation

4.4.1 Sedimentary breccia member

Description: The sedimentary breccia facies consists of clasts derived from the erosion of older strata that are both matrix and clast supported and range from centimeters to meters in diameter (Fig. 2.7A). The facies is internally massive and unsorted. Clast composition is dominated by angular and elongate cream-colored dolostone with internal parallel laminae. There are several clasts of cream and mauve colored rhythmite, and one clast shows cream-colored convoluted dolostone with sheet cracks. The facies also includes abundant clasts of silicified ooids and gray dolostone lacking internal textures, along with rare clasts of quartzite and granitic composition. The matrix is composed of variably intermixed recrystallized dolostone and quartz grains, ranging in size from silt to coarse sand. Beds tend to be amalgamated, but where distinct, beds are both tabular (20-60 cm thick) and lenticular (~30 cm thick and ~1.1 meter across).

Interpretation: The texture and clast size of the facies indicate deposition as debris flows (Crevello & Schlager 1980; Lowe 1982). Clast composition records reworking of underlying strata, including laminated dolostone, disrupted dolostone, and rhythmite. Clasts of silicified oolite and gray dolostone could be silicified and dolomitized versions of oolitic and textureless limestone clasts of the diamictite facies. Similarly, the granitic and quartzite clasts are comparable to those found in the diamictite and basal sandy dolostone. This facies likely represents large scale remobilization of the underlying Tsabisis and Blässkranz formations. This is consistent with slope failure where gravitational instabilities can result in volumetrically significant and erosive mass flows (McIlreath & James 1978; James 1981; Grotzinger 1986; Whalen et al. 2000).

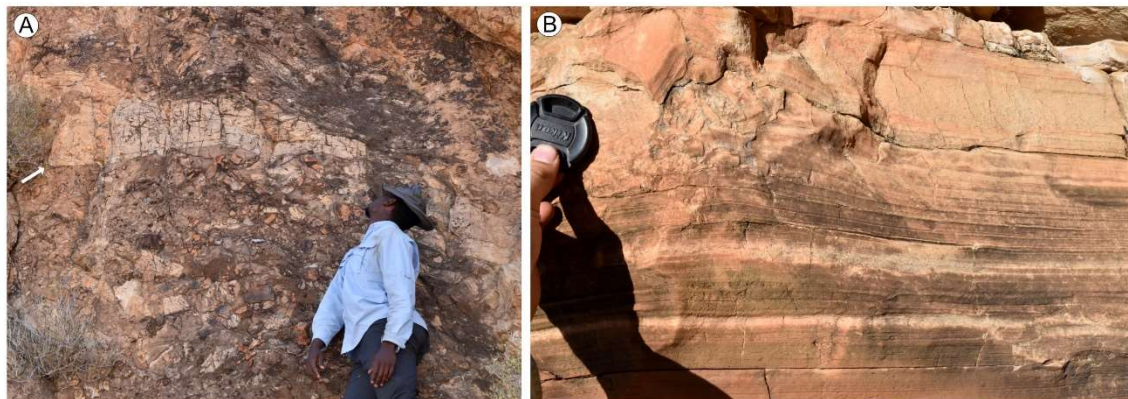


Figure 2.7. (A) Sedimentary breccia facies with up to meter-scale angular blocks of light-toned laminated dolostone and silicified oolite. This locality has breccia abruptly overlying diamictite of the Blässkranz Formation. Arrow points to the corner of a clast that reaches ~2 meters in length. This locality was not formally measured, but is located ~1.5 km to the west-northwest of the BR locality ($24^{\circ} 05' 34.44''$ S, $016^{\circ} 15' 20.95''$ E) (B) Laminated dolostone of the Noab Formation, with higher concentration of siliciclastic silts in the brown colored lower portions. Upper left shows incipient brecciation of the dolostone. Lens cap is 5.5 cm in diameter.

4.4.2 Upper Noab member

Description: Much of the upper Noab is composed of finely crystalline (20-60 microns) gray colored dolostone with millimeter-scale laminae (Fig. 2.7B). Silt to very coarse sand-size quartz grains increase in abundance upward in the member and towards its more northern outcrops. The quartz sandstone shows planar lamination and cm- to dm-scale cross bedding. Intraclasts ranging from centimeters to decimeters in diameter, form beds 20 cm to 4 m thick with common amalgamation. Beds show both matrix and clast support, with examples of fitted fabrics and incipient brecciation (Fig. 2.7B). Rare beds of maroon or green shale are intercalated within the dolostone.

Interpretation: The laminated fine-grained carbonates are likely derived from an updip carbonate source (McIlreath & James 1978; James 1981; Grotzinger 1986) and deposited below wave base via hypopycnal plumes or fine grained turbidites (Creveling et al. 2016). The breccia intraclasts, with common fitted fabrics, are indicative of local remobilization of the *in situ* laminated dolostone into debris flows (Lowe 1982; Grotzinger 1986). These features suggest a deep-water slope environment where the debris flows may be triggered by gravitational instability (McIlreath & James 1978; Whalen et al. 2000).

5. Platform morphology and evolution

The Tsondab member of the Tsabisis Formation is interpreted to represent a mixed carbonate-siliciclastic ramp overlying the glacio-marine strata of the Blässkranz Formation. The middle Tsabisis, upper Tsabisis, and Noab Formation represent evolution to a distally steepened ramp or slope environment (Read 1985; Fig. 2.8). We present the vertical and lateral stratigraphic evolution with an inferred chronological framework.

5.1 Ice proximal delta and carbonate initiation

The Tsondab member is deposited upon the glaciogenic Blässkranz Formation, which in updip paleogeographic positions shows an upward transition from diamictite to the lithic facies association (Fig. 2.3 BO, NW). Sections including the lithic facies association tend to have at least 10 cm of shale directly underlying the Tsondab dolostone (Fig. 2.3 TA, BO, likely MD). From a maximum thickness of ~23 m (Supp. Fig. 2.1B, ED) the lithic facies association generally thins in the downdip direction, progressively pinching out ~1 km to the northwest of the BO section (Fig. 2.1; Fig. 2.3 NW; Supp. Fig. 2.1C). In sections downdip of NY locality the Tsondab carbonates sit directly above diamictite (Fig. 2.3 BR, TH).

In updip localities (Fig. 2.3 TA, MD, NE, BO, NW), the basal Tsondab member is composed of the laminated dolostone facies with minor (~1-2%) siliciclastics that lie in sharp contact with the underlying lithic facies. In the downdip localities (Fig. 2.3 BR, TH) the basal sandy dolostone facies lies above the diamictite either abruptly as clast-supported beds (Fig. 2.4E; Supp. Fig. 2.1D, GH) or gradually with dispersed matrix-supported clasts (Fig. 2.3 TH; Fig. 2.4D). The basal sandy dolostone shows an upward decrease in the quartz sand content over a thickness of a few 10's of cm, though clasts continue through that transition interval. Convolute laminae of the disrupted dolostone facies abruptly overlie the last of the dolostone clasts. The disrupted dolostone facies is limited to the downdip sections (Fig. 2.3 BR, TH) and transitions upward into several meters of the undeformed laminated dolostone facies.

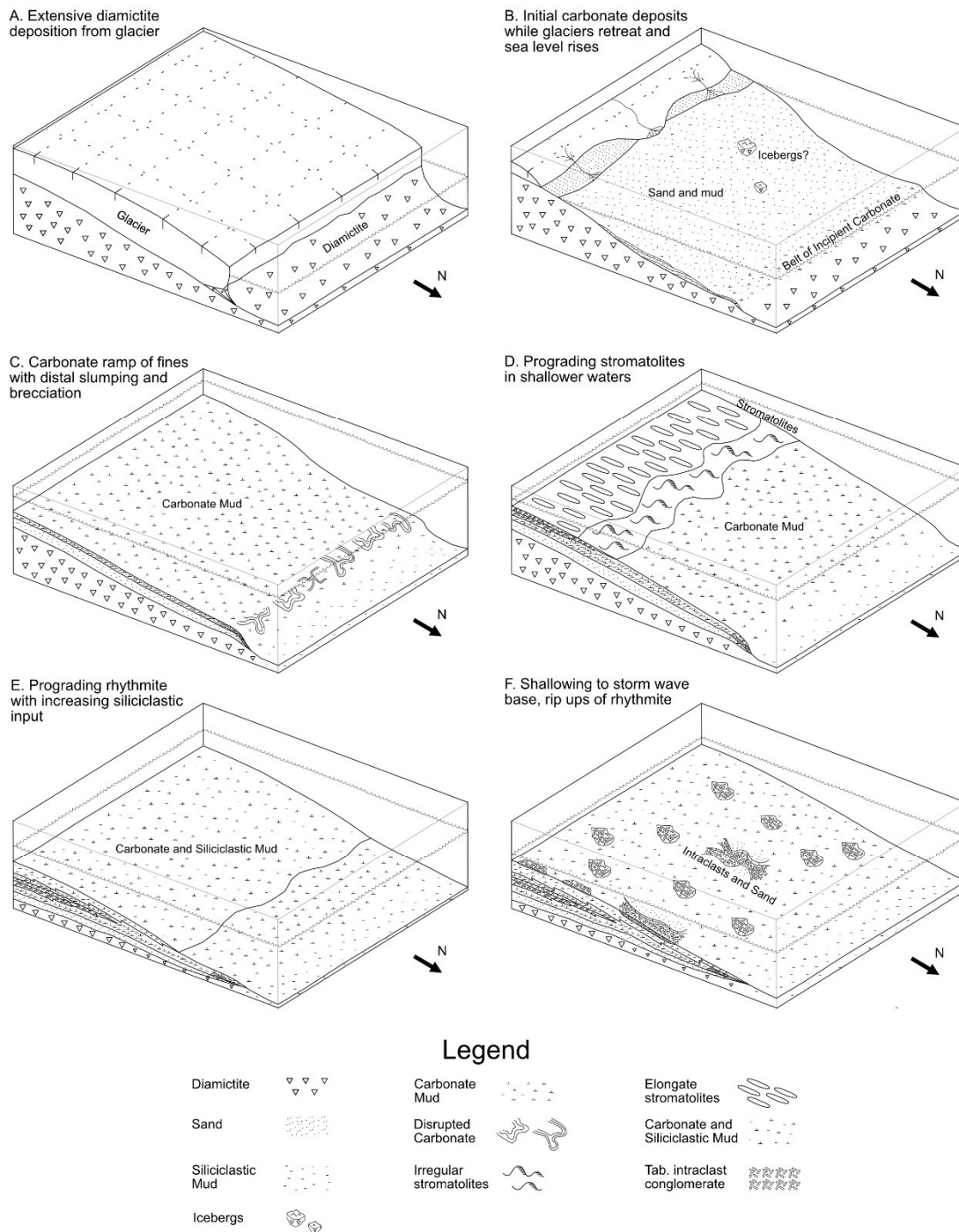


Figure 2.8. Schematic block diagrams of the stages of interpreted platform evolution showing both plan view and cross-sectional stratigraphic view. The black arrow points north, the apparent downdip direction of the platform. Legend shows the symbology used for the different facies. Dolostone versus limestone deposition is not distinguished here for simplicity. (A) Diamictite facies deposition recorded by the bulk of the Blässkranz Formation. (B) Deposition of the lithic facies association in

updip areas (upper Blässkranz Formation) while incipient carbonate precipitation begins in the downdip areas with the sandy basal dolostone facies (basal Tsondab member). (C) Lower Tsondab member deposition with laminated dolostone in deposition across the ramp, locally developing into disrupted dolostone in the downdip areas. (D) Lower-mid portion of the Tsondab member as the stromatolite facies prograde down the ramp. (E) Upper portion of Tsondab member with the prograding rhythmite facies. (F) Top of the Tsondab member when the rhythmite is ripped up into the tabular intraclasts conglomerate, intercalated with the HCS sandstone.

The vertical and the lateral downdip-updip facies transitions from the ice-contact submarine fan of the diamictite to the ice-contact pro-delta of the lithic facies association suggests a backstepping of the glacial influence and therefore likely the retreat of the proximal ice sheet, possibly in concert with relative sea-level rise (Fig. 2.8, A to B; Powell & Molnia 1989; Lønne 1995; Shen et al. 2021). Then, while the updip areas received outwash deposition from the backstepping ice-contact pro-delta (Lønne 1995), only a condensed flux of outwash sediments, remobilized diamictite, and possible ice rafted debris reached the distal downdip regions. The quartz sands and clasts at the base of the Tsondab member in the downdip areas suggest that clastic sediments were being transported to the distal areas at the time that carbonate production began (Fig. 2.8B). The upward decrease of quartz sands within the basal sandy dolostone is consistent with transgression and submergence of at least part of the siliciclastic source area (Loutit et al. 1988; Southgate et al. 1993). In updip areas, the shaly content of the uppermost decimeters of the Blässkranz Formation and the absence of clastics in the basal carbonates suggests that transgression of glacial sources had progressed enough to limit the influx of clastic sediments (Fig. 2.8C; Nordsvan et al. 2019; Shen et al. 2021). The bulk of the Blässkranz diamictite is interpreted as the pre-deglacial to earliest syn-deglacial low stand systems tract (*sensu* Fielding 2018; Ezpeleta et al. 2020). A maximum flooding surface (Fig. 2.3 MFS1) is interpreted at the top of the downdip sandy basal dolostone, which likely correlates to the base of the Tsondab member in the updip areas. In this context the laminated dolostone and disrupted dolostone facies represent early highstand and progradation of fine-grained carbonates (*sensu* Kendall & Schlager 1981; Hanford & Loucks 1993; Brown & Loucks 1993). The disrupted dolostone represents slumping of the prograding platform in downslope positions, potentially showing distal steepening of the ramp (Fig. 2.8C).

5.2 Stromatolites along carbonate ramp

In the most updip platform positions the laminated dolostone is overlain by stromatolitic carbonates (Fig. 2.3 TA). Planar laminated dolostone conformably transitions into ~4 meters of irregular stromatolites, progressively overlain by ~0.5 m of elongate stromatolites, which gradually decrease their synoptic relief over a few centimeters back into 1-1.2 meters of laminated dolostone. In downdip platform positions the elongate stromatolites pinch out and only irregular stromatolites are present, and in more distal positions (Fig. 2.3 MD) the irregular stromatolites pinch out laterally into the laminated dolostone, showing interfingering at the decimeter scale.

The stromatolite facies represent a shallower depositional environment than the enclosing laminated dolostone, with the elongate stromatolites forming above fair-weather wave base and possibly much shallower. The stratigraphic relationships of the irregular and elongate stromatolite facies indicates progradational stacking from the interpreted updip regions of the ramp into the basin depocenter (Logan 1974; Grotzinger 1986; Burchette & Wright 1992), likely associated with a relative sea-level fall (Fig. 2.8D). The return to laminated dolostone above the stromatolites suggests a phase of retrogradational stacking into deeper waters. No evidence of subaerial exposure including desiccation, dissolution, soil development, etc., is present at the base or top of the stromatolite-bearing interval. Therefore, a type 2 sequence boundary (Fig. 2.3 SB1) is interpreted near the top of the stromatolite facies (Schlager 1991). Given the context of the overlying rhythmite (discussed below) a second maximum flooding surface is inferred within the laminated dolostone that overlies the stromatolites (Fig. 2.3 MFS2). The equivalent sea-level changes, and resulting sequence boundary, are not visible in the downdip locations as the deeper waters along the ramp are less sensitive to shifts in water depth, so laminated dolostone deposition is uninterrupted.

5.3 Upper Tsondab transitions

Dolostone-shale rhythmites everywhere overlie the laminated dolostone/stromatolite facies. The contact is gradual and intercalated, with an increasing frequency and thickness of shale intercalations between dolostone beds and an increasing proportion of siliciclastic muds within the dolostone beds – shown in outcrop by a color transition from cream to mauve. This trend continues upward throughout the entire rhythmite facies.

Fine siliciclastic sediments from nearshore environments can readily be transported into deeper waters by storm generated currents (Mount 1984). Though the bulk of the rhythmite would continue to accumulate below wave base, the increasing flux of siliciclastics into the carbonate system implies increasing proximity of a siliciclastic source via regression of the shoreline (Fig. 2.8E; Kendall & Schlager 1981).

The tabular intraclast facies interfingers with the rhythmite facies. In most sections 1 to 3 lenticular beds up to 20 cm thick of tabular intraclast conglomerate are intercalated with rhythmite (Fig. 2.3 TA, MD, BR, TH). Above the last tabular intraclast bed, the rhythmite continues for ~1-2 meters before grading into the shales and limestones of the overlying Tsabisis members. In some intermediate platform positions the HCS sandstone and shale facies are intercalated within the tabular intraclast facies and rhythmite (Fig. 2.3 NE, BO). The underlying rhythmite facies is ripped up *in situ* into upward-thickening beds of imbricated and edgewise tabular intraclast conglomerate (Fig. 2.9). Sandstone beds with hummocky cross-stratification are intercalated most abundantly within stratigraphically lower tabular intraclast facies (Fig. 2.3 NE 13.4-14.6 m, BO 11.7-14.3 m). Above this, the tabular intraclast beds tend to thin and have smaller clasts, the sandstone beds lack hummocky cross stratification, and the proportion of shale increases upward (Fig. 2.3 NE 14.6-18 m, BO 14.3-17 m). This transitions progressively into the shales and limestones of the upper Tsabisis member.

These coarser facies near the top of the Tsondab member show increasing current activity and shallowing water depths that resulted in bed scouring of the rhythmite facies to produce intraclasts (Fig. 2.9, Myrow et al. 2004). The lower intercalations at the NE section (Fig. 2.9), suggest that this shallowing was progressive into the storm wave base depths indicated by the hummocky cross-stratification and tabular intraclasts with imbricated and edgewise orientations (Grotzinger 1986; Southard et al. 1990; Myrow et al. 2004, 2008). The greater thickness and variety of sedimentary features indicating strong sediment transport in the NE, BO, and CS sections (Fig. 2.3; Supp. Fig. 2.1C) suggest that these platform positions may have developed submarine channels cut normal to the shoreline by storm generated surges and relaxation currents, possibly during lowstand systems tract development (Fig. 2.8F; Field & Roy 1984; Myrow 1992; Amos et al. 2003; Pattison et al. 2007).

Stratigraphically higher, these sections show a progressive transition to greater shale accumulation coincident with the absence of current reworking, suggesting deeper water deposition of a transgressive systems tract (Southgate et al 1993; Myrow et al. 2004). In the other localities, the return to rhythmite deposition above the tabular intraclast beds also suggest a transgressive systems tract with deeper water deposition and backstepping carbonate production before passing upward to overlying shales and limestones. A type 2 sequence boundary is interpreted at the base the tabular intraclast beds (Fig. 2.3 SB2). A maximum flooding surface (MFS3) is interpreted at the top of the last tabular intraclast bed for the NE, BO, and CS sections and the top of the last rhythmite for the other localities (Schlager 1991).



Figure 2.9. Stratigraphy of section NE from approximately 13 to 14.5 meters (Fig. 2.3) showing the upper portion of the Tsondab member. (A) Upper end of the rhythmite that shows centimeter-scale intercalations of maroon shale. (B) Wavy rhythmite with thin partings of v.f. sand instead of shale. (C) *In situ* rip ups of the rhythmite into tabular intraclasts, inset shows close-up of well-defined examples. (D) Bed of wavy rhythmite. (E) Amalgamated bed of tabular intraclast conglomerate, arrow points to well defined examples of intraclasts. The sandstone lens with hummocky cross-stratification shown in Fig. 2.5F pinches out laterally into this amalgamated bed. (F) Shale bed. (G) Bed of sandstone with hummocky cross-stratification. Handle of rock hammer for scale, visible length ~20 cm.

5.4 Supra-Tsondab strata

The middle and upper Tsabisis members tend to thin downdip and the gray dolostone of the Noab Formation overlies the Tsabisis Formation throughout the field area (Fig. 2.2; Fig. 2.3 BR, TH). The sedimentary breccia member occurs at the base of the Noab Formation and has a complex relationship with underlying units. It is laterally discontinuous and appears to frequently downcut through the Tsabisis and even the upper Blässkranz Formation (Supp. Fig. 2.1D, SR).

The facies transitions of the upper Tsondab to the overlying middle Tsabisis indicates backstepping of the local carbonate system by rising sea-level into the deposition of distal shales (Kendall & Schlager 1981; Homewood & Eberli 2000). The allochthonous slope deposits of the upper Tsabisis member limestones represent the return of local carbonate deposition, likely by highstand progradation into the basin (Handford & Loucks 1993; Grammer et al. 1993; Whalen et al. 2000). The downdip thinning and absence of the middle and upper Tsabisis members is most likely a function of condensed sedimentation (Loutit et al. 1988). The sedimentary breccia along the Tsabisis-Noab contact suggests slope failure causing remobilization of the underlying stratigraphy. Such failure may be triggered by base-level fall across a carbonate platform during a lowstand (Handford & Loucks 1993; Grammer et al. 1993; Whalen et al. 2000), though the extent of relative sea-level change remains unclear given the lack of evidence for subaerial exposure. The upper Noab member shows similar slope deposition to the upper Tsabisis member, but with dolostone and a higher proportion of siliciclastic silts and sands that may indicate further highstand progradation of the siliciclastic source into the platform (Whalen et al. 2000).

6. Sequence stratigraphy

The Blässkranz, Tsabisis and Noab formations encompass four complete depositional sequences, with two sequence boundaries within the Tsondab member of the Tsabisis Formation (Fig. 2.3). The bulk of the Blässkranz diamictite represents a low stand systems tract of glacial deposition (LST1, where LST indicates low stand systems tract). Overlying the diamictite is the transgressive systems tract of the lithic facies association and

basal sandy dolostone (TST1) that show the backstepping of glacial deposition during base-level rise leading to a maximum flooding surface (MFS1). The subsequent laminated dolostone and disrupted dolostone record initial filling in of accommodation space during the early highstand systems tract (HST1). The progradational stacking pattern and fair-weather wave base deposition of the updip stromatolite succession indicates that late highstand carbonate production filled accommodation in the updip portions of the basin (HST1). This culminated in a sequence boundary near the top of the stromatolites that was not subaerially exposed within the study area (SB1). Retrogradational stacking between the stromatolite facies and the overlying laminated dolostone records an increase in accommodation during a transgressive systems tract (TST2) to an inferred maximum flooding surface within the laminated dolostone (MFS2).

The rhythmite then shows the progradational filling of accommodation space of a highstand systems tract (HST2) to the sequence boundary at the base of the tabular intraclast conglomerates. This sequence boundary (SB2) does not show subaerial exposure but does record *in situ* erosion of the rhythmite facies. The tabular intraclast conglomerate and HCS sandstone facies represents a lowstand systems tract as incised submarine channel fill across the carbonate ramp (LST3). Then a retrogradational stacking pattern of tabular intraclast conglomerate, sandstone, shale, and rhythmite form another transgressive systems tract (TST3) leading to a maximum flooding surface at the top of the Tsondab member (MFS3). The middle and upper members of the Tsabisis Formation then show the early and later stages of a prograding highstand systems tract filling in the accommodation space of the basin (HST3). The sedimentary breccia member of the Noab Formation represents a subsequent lowstand systems tract with substantial erosion of the underlying strata due to a base-level fall (LST4 over SB3). The bulk of the upper Noab member then records a final highstand systems tract for the regional stratigraphy (HST4).

Therefore, two sequence boundaries are present within the Tsondab member with the bulk of the stratigraphy recording highstand systems tracts. The lithic facies association of the Blässkranz Formation represents an extensive transgressive systems tract, but transgression within the Tsondab member is limited to thin backstepping intervals. Though episodes of substantial relative sea-level rise are observed through the upper Blässkranz Formation and

Tsondab member, the bulk of the Tsondab cap carbonate does not record transgression, but rather regression as the sediments fill in the accommodation space. This is common for sequence stratigraphic interpretations of conventional mixed carbonate-siliciclastic platforms, but as discussed below, contrasts with the sequence stratigraphic framework typically applied to Marinoan cap carbonates.

7. Carbon and oxygen isotope geochemistry

The $\delta^{13}\text{C}$ and $\delta^{18}\text{O}$ chemostratigraphy for the Tsondab member of the Naukluft Mountains is shown in Fig. 2.10. It shows five profiles corresponding to the respective stratigraphic columns of Fig. 2.3 and Supp. Fig. 2.1 through the Tsondab member, along with a full profile for the TA locality that shows values for the Tsondab and its overlying upper Tsabisis member limestone and Noab Formation dolostone. The profiles show that the bulk of the Tsondab member $\delta^{13}\text{C}$ values tend to be -2 ± 0.6 ‰. The TH Profile (Fig. 2.10) shows relatively positive $\delta^{13}\text{C}$ values at the base with the matrix of the basal sandy dolostone starting with a value of $\sim +2$ ‰, which rapidly converge to values ~ -2 ‰ for the rest of the Tsondab member. Though complete profiles were not taken due to thrust faults, samples of the sandy basal dolostone in the BR and NY localities (Fig. 2.3; Supp. Fig. 2.1) also show relatively positive $\delta^{13}\text{C}$ values between -1 ‰ and $+1$ ‰ (Supp. Table 2.2). The $\delta^{18}\text{O}$ values tend to show greater range and scatter, with the bulk of the Tsondab member ranging from -9 to -5 ‰ (Fig. 2.10). Cross-plots between $\delta^{18}\text{O}$ and $\delta^{13}\text{C}$ (Supp. Fig. 2.3) show that the Tsondab member profiles lack strong correlations, but the complete TA profile does show a positive correlation. This indicates that upper Tsabisis member and Noab Formation may have experienced significant diagenetic alteration (Swart 2015; Ahm et al. 2018), while the Tsondab member geochemistry appears viable.

The $\delta^{13}\text{C}$ values of the Tsondab member show steady and consistent trends within profiles and between localities. The relatively negative plateau of $\delta^{13}\text{C}$ values is broadly consistent with cap carbonates found elsewhere (e.g. Hoffman et al. 1998; Kennedy 1996; James et al. 2001; Jiang et al. 2003; Porter et al. 2004; Rose & Maloof 2010; Liu et al. 2018; Yu et al. 2020). Certain cap carbonate profiles (James et al. 2001, Redstone Section; Hoffman et al.

2007, slope sections 1-4; Hoffman & Macdonald 2010) also show the steep initial decline in $\delta^{13}\text{C}$ found in the TH Profile of the Tsondab member (Fig. 2.10).

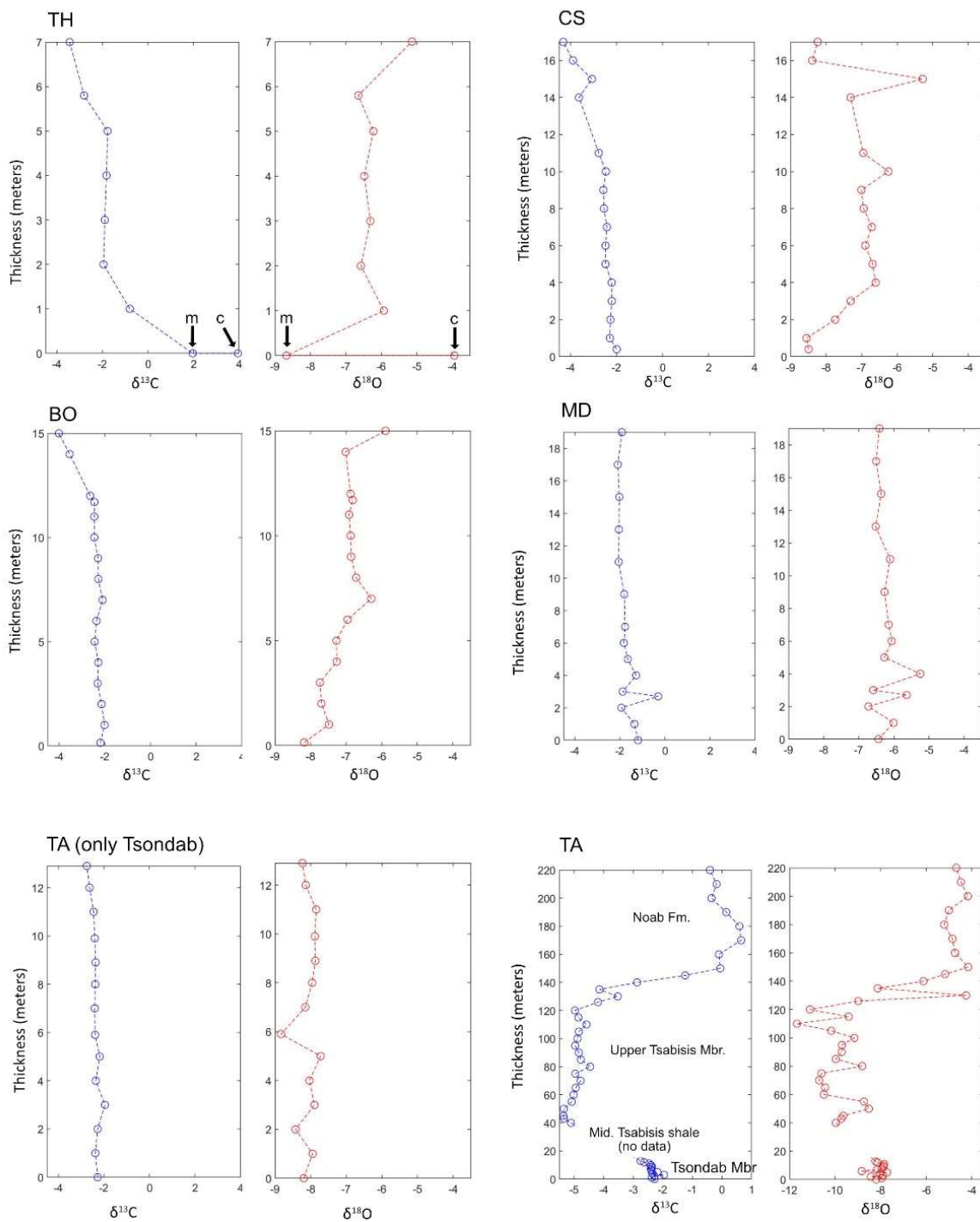


Figure 2.10. Carbon and oxygen isotope profiles for different localities (‰ VPDB). Note that profiles TH, CS, BO, MD, and the Tsondab-only section of TA keep the same scale for $\delta^{13}\text{C}$ and $\delta^{18}\text{O}$ with different vertical scales that correspond to the stratigraphic thickness shown in the sections of Fig. 2.3 and Supp. Fig. 2.1. The complete TA profile shows the Tsondab member at its base, along with the overlying upper Tsabisis member (40 - 130 meters) and the Noab Formation (130 – 220 meters), with a shifted scale for $\delta^{13}\text{C}$. At 0 meters the TH profile had both the dolomitic matrix (m) and a dolostone clast (c) sampled, as indicated by the arrows. The MD Section (Fig. 2.3) has a slightly different thickness from the MD Profile here due to being a composite stratigraphic section. See Supp. Fig. 2.3 for cross plots of $\delta^{13}\text{C}$ and $\delta^{18}\text{O}$.

The similarities with Marinoan-age cap carbonates elsewhere support the recognition of the Tsondab member as a basal-Ediacaran cap carbonate, consistent with previous lithostratigraphic correlations (Hoffmann 1989; Miller 2008.). The initial decline of $\delta^{13}\text{C}$ values found in slope/downdip localities and its absence in more updip localities was used by Hoffman et al. (2007) to interpret the basal downdip stratigraphy as the earliest cap carbonate deposition. This would be consistent with our sequence stratigraphic interpretation where the downdip sandy basal dolostone that shows the initial steep decline in $\delta^{13}\text{C}$ (Fig. 2.10, TH; Supp. Table 2.2, BR, NY) represents the oldest deposits of the Tsondab member, laid down during the initial transgressive systems tract.

8. Discussion

8.1 Cap carbonate

The Tsondab member of the Tsabisis Formation is a basal-Ediacaran cap carbonate that represents a wave-influenced mixed carbonate-siliciclastic ramp with a complex sea-level history (Fig. 2.8; Fig. 2.11). While the Tsondab member of the Tsabisis Formation shows some facies, like the finely laminated dolostone, disrupted dolostone, and elongate stromatolites that are seen in other cap carbonates, it lacks many of the more idiosyncratic features of Marinoan-age cap carbonates such as tubestones, giant wave ripples, barite layers, and crystal fans (Cloud et al. 1974; Kennedy 1996; Hoffman et al. 1998; James et al. 2001; Higgins & Schrag 2003; Allen & Hoffman 2005; Corsetti & Grotzinger 2005; Jerolmack & Mohrig 2005; Jiang et al. 2006; Macdonald et al. 2009; Hoffman & Macdonald 2010; Rose & Maloof 2010; Hoffman 2011; Lamb et al. 2012; Creveling et al. 2016; Hoffman et al. 2017; Hoffman et al. 2021) that are observed only rarely outside of cap carbonates

(Grotzinger, 1989; Grotzinger and James, 2000). The facies distribution of the Tsondab member and surrounding units show clear depositional gradients that are controlled by the changing physical environment – predominantly water depth, wave and current energy, and proximity to the shoreline. Hence, the depositional patterns of Tsondab member resemble that of other Precambrian (and Phanerozoic) mixed carbonate-siliciclastic platforms (Ahr 1973; McIlreath & James 1978; Read 1985; Grotzinger 1989; Burchette & Wright 1992; Grotzinger and James, 2000; Whalen et al. 2000). The primary distinction is that the Tsondab member lacks well-defined parasequences and has the unusual juxtaposition of a carbonate unit overlying glaciogenic strata.

A common sequence stratigraphic framework for ‘cap carbonate sequences’ has persisted that defines a single transgressive systems tract dominated by the cap carbonate followed by shallowing upward to a highstand systems for a single sequence boundary (Hoffman & Schrag 2002, Fig. 2.3; Hoffman et al. 2017, Fig. 24). Yet, previous work has indicated sea-level regressions at the base or top of cap carbonates (e.g. Bertrand-Sarfati 1997; Shields et al. 2007; Hoffman & Macdonald 2010; Zhou et al. 2010; Hoffman 2011; Gan et al. 2022) and our work has shown a maximum flooding surface near the base of the Tsondab cap carbonate, multiple smaller depositional sequences within the cap carbonate strata largely recording regression (Fig. 2.11), and a third sequence boundary at the top of the limestone upper Tsabisis member, before the final highstand systems tract of the succession is recorded in the upper Noab member. This suggests that the “cap carbonate sequence” is an incomplete framework to describe the sequence stratigraphic history of the Naukluft succession and several other cap carbonate examples around the world.

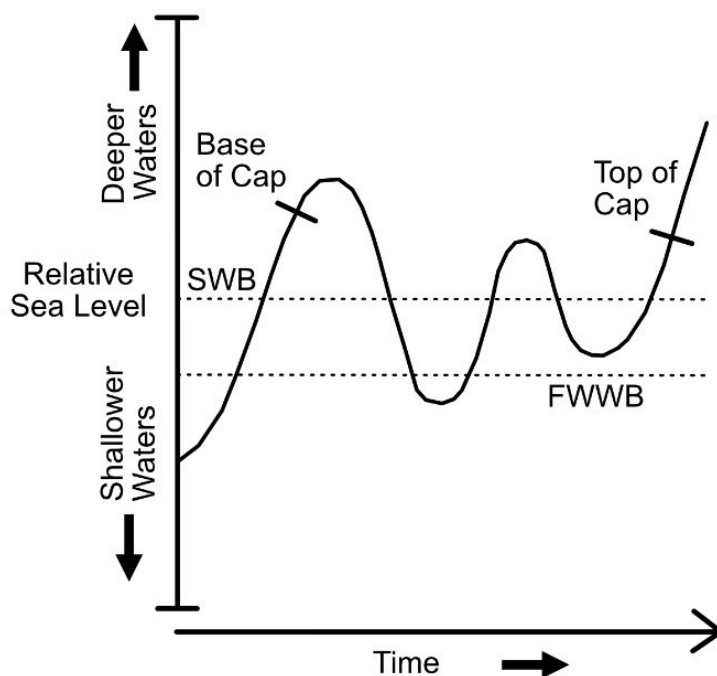


Figure 2.11. Qualitative illustration of the relative sea level history recorded in the Tsondab cap carbonate. This is not meant to represent global/eustatic sea level, but specifically the changing water depths represented by the facies and sequence stratigraphy through time in the Tsondab member. FWWB – fair weather wave base, SWB – storm wave base.

8.2 Sea-level history

Over the longest-term, strata of the Blässkranz, Tsabisis, and Noab formations record the filling of tectonically produced accommodation space of passive margin thermal subsidence created over the course of the Marinoan glacial epoch and its termination. The glacial epoch had a duration of several million years (Hoffman et al. 2017), which allowed for up to a few hundred meters of accommodation space along a subsiding passive margin (McKenzie 1978; Steckler & Watts 1978; Schlager 1981; Hoffman & Schrag 2002). The relative sea-level history at continental margins across the Marinoan deglaciation results from the competing balance of eustatic, isostatic, and gravitational factors produced by the melting of global glaciers, superimposed upon this existing tectonic subsidence (e.g. Farrell & Clark 1976; Creveling & Mitrovica 2014). Eustatic sea-level (global ocean volume, RSL_{est}) would drive substantial relative sea-level rise, that could be at least partly offset by the loss of gravitational attraction between ice sheets and seawater driving sea-level fall (RSL_{att}), and the isostatic effect from the viscoelastic response of the Earth to the ice sheet and seawater

loads (RSL_{iso} , combining ice sheet and seawater components) can drive relative sea-level fall or rise depending on spatially variable crustal rebound or peripheral bulge subsidence (e.g. Farrell & Clark 1976; Nakada & Lambeck 1987; Creveling & Mitrovica 2014; Irie et al. 2019). Both RSL_{esl} and RSL_{att} have instantaneous effects on sea-level and are zero in the post-deglacial phase. RSL_{iso} has both rapid and prolonged sea-level response related to the timescale of the viscoelastic mantle (which can be spatially variable depending on mantle properties, e.g. Zurbuchen & Simms 2019), with the potential to continue to have a significant impact on relative sea-level for a few 10 kyr into the post-deglacial phase (Creveling & Mitrovica 2014; Irie et al. 2019). In addition to these glacially driven changes, accommodation space is also dependent on the conventional mechanisms of sediment accumulation and continuing tectonic subsidence (RSL_{sed} and RSL_{tect}). The competing components can be represented by the equation: $RSL = RSL_{esl} + RSL_{att} + RSL_{iso} + RSL_{sed} + RSL_{tect}$. Thermal expansion of the ocean over the course of the deglaciation has also been suggested as a component of sea-level rise (Yang et al. 2017), but the magnitude has been considered relatively minor (Hoffman et al. 2017).

Conclusively distinguishing between these components in the rock record is difficult. Regressions near the base of certain cap carbonates, followed by extended transgressions, have been attributed to RSL_{att} fall overcoming RSL_{esl} in the early stages of deglaciation (Hoffman & Macdonald 2010; Hoffman 2011; Hoffman et al. 2021). However, modeling has shown that this is only a viable mechanism if global deglaciation was asynchronous with localized melting occurring ~exclusively in these specific regions prior to deglaciation of the rest of the globe (Creveling & Mitrovica 2014). This is a possible mechanism for phases of sea-level fall in cap carbonates that we will consider, yet independent geologic evidence for regional-scale asynchronous deglaciation is absent and what limited climate modeling exists for the Marinoan (Hyde et al. 2000) does not provide any constraints on the synchronicity of ice melting, so we must weigh other drivers for sea-level changes. Other examples of cap carbonates show shallowing (Shields et al. 2007) or exposure surfaces (Bertrand-Sarfati 1997; Zhou et al. 2010; potentially Creveling et al. 2016; Gan et al. 2022) at the top of the cap carbonates, which have been interpreted to represent sea-level fall driven by deglacial-driven crustal rebound following eustatic transgression. These regressions were interpreted

to have been driven by crustal rebound due to their high stratigraphic positions marking the end of recorded cap carbonate deposition and the longer timescale needed for the karstification of up to 2 meters relief than the instantaneous RSL_{att} mechanism can provide (Gan et al. 2022).

Considering the units found in the Naukluft, the glaciomarine lowstand is represented by the bulk of the Blässkranz diamictite (*sensu* Fielding 2018; Ezpeleta et al. 2020), the upper Blässkranz lithic facies association and Tsondab member basal sandy dolostone record a substantial transgression, which can likely be attributed to eustatic sea-level rise from the melting of ice sheets. However, the record of this initial transgression does not continue much beyond the base of the Tsondab cap carbonate, with the stromatolite succession showing a regressive highstand systems tract that leads to a sequence boundary (SB1, Fig. 2.3) within the lower half of the cap carbonate. The rhythmite, tabular intraclast conglomerate, and HCS sandstone record a second regression to the sequence boundary (SB2, Fig. 2.3) in the upper parts of the cap carbonate (Fig. 2.11). What might be the drivers for these multiple sea-level changes within a cap carbonate?

Given that RSL_{att} is expected to have an early effect in the case of regional asynchronous melting while RSL_{iso} has a slower signal, one feasible model would be that the SB1 regression of the stromatolites represents regional RSL_{att} sea-level fall and the upper SB2 regression was driven by later RSL_{iso} crustal rebound. This explanation would show some consistency with proposed evidence for RSL_{att} regressions near the base of the Keilberg Member cap carbonate of northern Namibia (Congo Craton, Hoffman 2011; Hoffman et al. 2021) and the Dreigratberg member cap carbonate of southern Namibia (Kalahari Craton, Hoffman & Macdonald 2010). Paleogeography would place both of these locations, especially that of the Dreigratberg member, relatively nearby during the time of cap carbonate deposition (e.g. Gray et al. 2008; Miller 2008; Goscombe et al. 2017; Merdith 2017; 2021), which could suggest all three were experiencing the same regional effects of RSL_{att} during early asynchronous melting of the nearby ice sheets. However, there are potentially important differences; the interpreted regressions of these correlated cap carbonates are located immediately at their base, preceding the major flooding recorded in the cap carbonate, and are commonly associated with a turbidite to grainstone transition

paired with a zone of sheet crack cements (Hoffman & Macdonald 2010). Meanwhile, the SB1 regression in the Tsondab member is recorded by a progressive succession from laminated dolostone into irregular and elongate stromatolites over at least ~5 meters (Fig. 2.3 TA) that overlies a major transgression represented by TST1, recorded in the upper Blässkranz Formation and basal Tsondab member. Sedimentation rates are difficult to estimate in cap carbonates, however the progressive development of shallower-water stromatolite morphotypes (Fig. 2.3 TA; subsection 5.2), along with downdip progradation and interfingering of irregular stromatolites with the laminated dolostone (Fig. 2.3 MD; subsection 5.2), and the lack of exposure surfaces overlying either stromatolite facies, suggests a more gradual signal of relative sea-level fall than would be expected for the instantaneous RSL_{att} effect (Hoffman & Macdonald 2010; Gan et al. 2022).

Alternatively, the SB1 regression in the Tsondab member may be consistent with the more gradual response of RSL_{iso} crustal rebound following transgression driven by RSL_{esl} ice melting (Bertrand-Sarfati 1997; Shields et al. 2007; Zhou et al. 2010; Creveling & Mitrovica 2014; Creveling et al. 2016; Gan et al. 2022). In this model, an earlier regression driven by RSL_{att} of initial ice melting is either indistinguishable within the largely massive Blässkranz Formation diamictite, or there was not sufficient early regional ice melting to overcome the global signal of RSL_{esl} sea-level rise (Creveling & Mitrovica 2014). If crustal rebound is driving the first regression (SB1), what is mechanism for the second regression within the Tsondab member (SB2)? Nonmonotonic postdeglacial changes driven by RSL_{iso} could result in a second pulse of crustal uplift following continuous and synchronous deglaciation (Irie et al. 2019). However, these second, isostatically driven regressions (Irie et al. 2019, Fig. 10n) rely on specific paleogeographic conditions, only initiate ~200,000 yrs after deglaciation, and have a muted magnitude of ~0.2-0.25 m/kyr (for comparison, carbonate platform sedimentation rates average 1 m/kyr and can reach up to 10 m/kyr, while tectonic subsidence rates on passive margins can reach 0.1 m/kyr; Adey 1978; McKenzie 1978; Steckler & Watts 1978; Schlager 1981; Hoffman & Schrag 2002). Without other mechanisms directly related to the deglaciation (RSL_{esl} , RSL_{att} , RSL_{iso}) that could have the magnitude to drive relative sea-level fall following the primary phase crustal rebound represented by SB1, the sea-level fluctuations recorded in the upper portions of the Tsondab

cap carbonate may have to be predominantly accounted for by the conventional controls on accommodation space – the balance between RSL_{sed} and RSL_{tect} .

Conclusively distinguishing between these two models for the mechanisms driving sea-level changes within the Tsondab cap carbonate may not be possible with the existing data and scope of the present work but could be valuable to refining our understanding of the Marinoan deglaciation. If future work could show that SB1 represents an early RSL_{att} effect and SB2 records RSL_{iso} crustal rebound, it would substantiate previous work suggesting RSL_{att} signals in other Namibian cap carbonates (Hoffman & Macdonald 2010; Hoffman 2011), potentially allow for the estimation of the timescale of cap carbonate deposition by using numerical models of crustal rebound to determine the age of SB2 relative to the deglaciation (e.g. Creveling & Mitrovica 2014), and be an example of a Marinoan cap carbonate that distinctly records both RSL_{att} and RSL_{iso} signals. On the other hand, if SB1 represents RSL_{iso} crustal rebound and SB2 cannot be directly attributed to one of the mechanisms tied to deglaciation, then it could remove the upper bound on the timeframe of cap carbonate deposition, at least by the physical mechanisms of sea-level changes. Alternative means of estimating cap carbonate timescale would then be necessary, like what has been proposed by correlation and modeling of geochemical ocean mixing horizons (Yang et al. 2017; Hoffman et al. 2017) or models of exponentially decaying carbonate sedimentation rates (Penman & Rooney 2019; Fairchild et al. 2022).

Future work to test the mechanisms for relative sea-level changes in cap carbonates will likely rely on judging the facies context (instantaneous versus gradual changes), lateral consistency, and stratigraphic positions of sea-level fluctuations on a regional scale. With the existing work on cap carbonates in northern Namibia (Hoffman 2011; Hoffman et al. 2021) and southern Namibia (Hoffman & Macdonald 2010; Macdonald et al. 2009), and now the Naukluft Mountains of south-central Namibia, we suggest that there may be important work to be done in less well-studied Marinoan cap carbonates on the Kalahari Craton and nearby Neoproterozoic margins. Most notable would be the Buschmannsklippe Formation of the Witvlei Group in east-central Namibia (Hoffmann 1989; Prave et al. 2011).

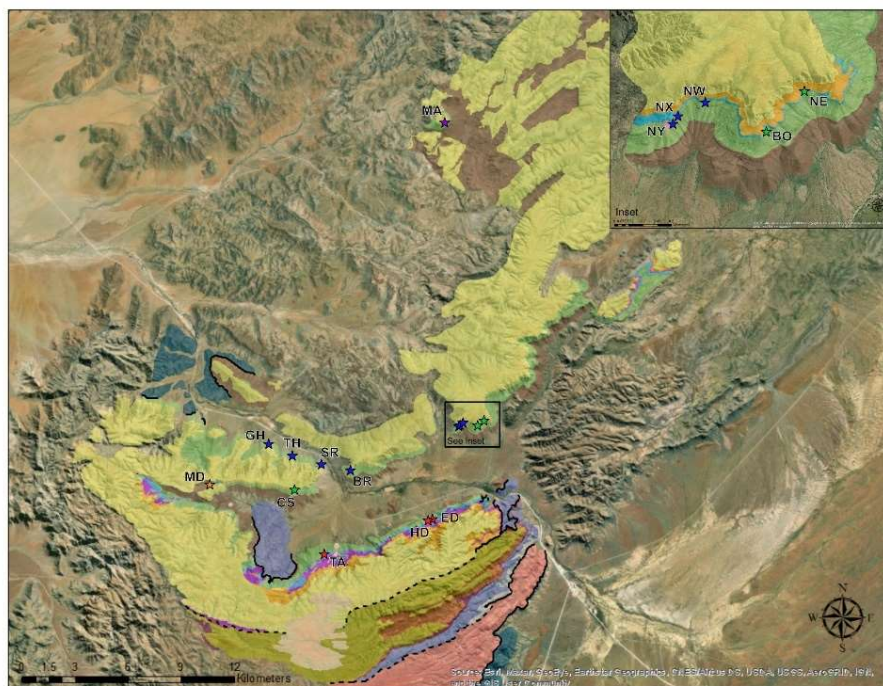
Chapter 2 supplementary data tables can be found at:

<https://doi.org/10.22002/9125q-yn792>

Supplemental Table 2.1. Azimuths of elongate stromatolites corrected for tectonic tilt with their coordinates in latitude/longitude.

Supplemental Table 2.2. Table for all $\delta^{13}\text{C}$ and $\delta^{18}\text{O}$ values shown in Fig. 2.10 and Supp. Fig. 2.3. Also included are the values for the BR and NY sections, which were less extensively sampled but show $\delta^{13}\text{C}$ values in the sandy basal dolostone consistent with those recorded in the TH section. Eight broadly spaced samples of the MA section are included as well.

Chapter 2 Supplementary Figures



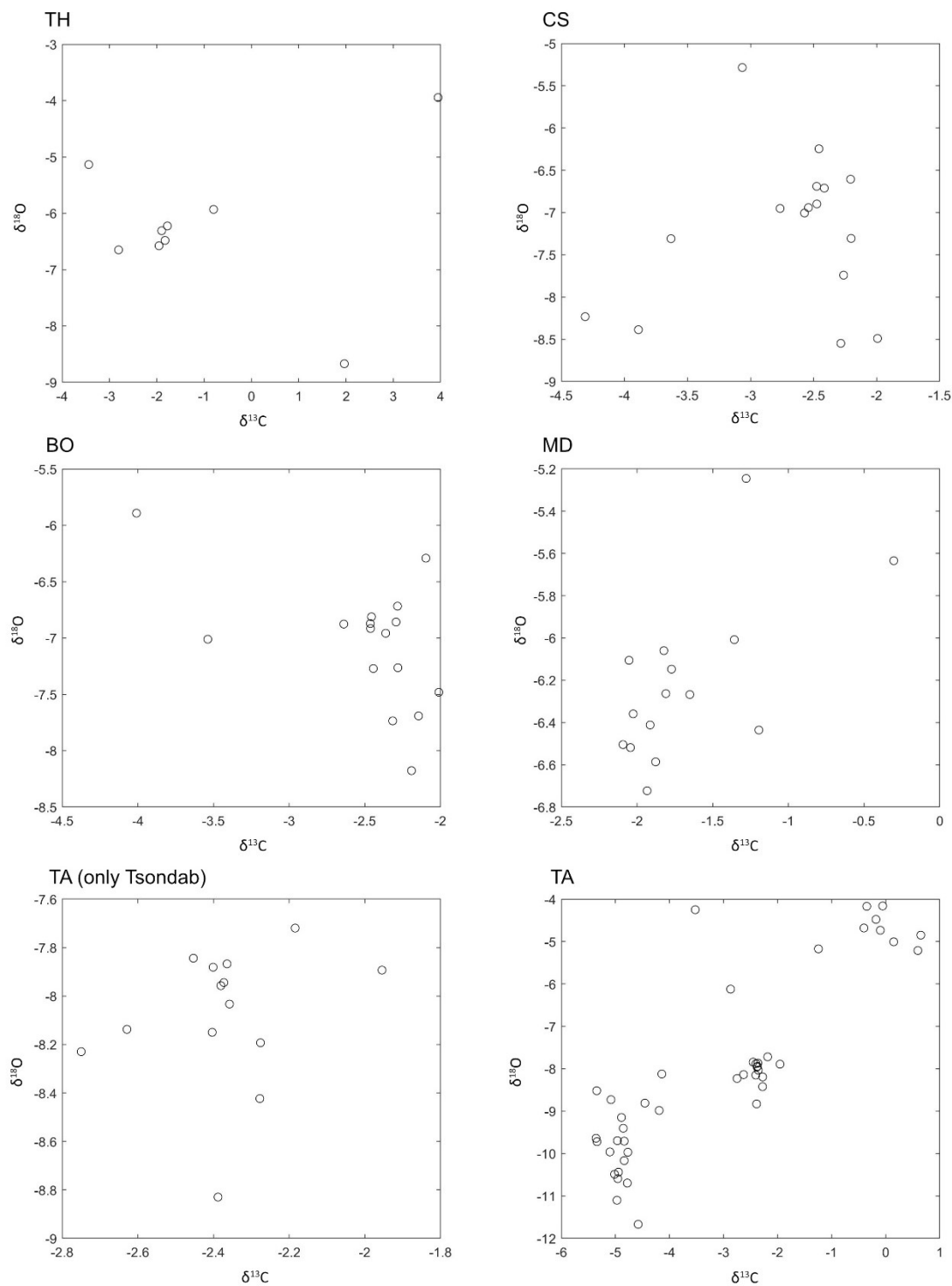
Coordinates of Named Localities

Name	Latitude	Longitude
ED	24° 07' 18.01" S, 016° 17' 11.22" E	
HD	24° 07' 16.78" S, 016° 16' 3.32" E	
TA (composite)	24° 08' 11.29" S, 016° 14' 3.22" E 24° 08' 25.51" S, 016° 13' 42.12" E	
MD (composite)	24° 06' 20.74" S, 016° 09' 45.75" E 24° 06' 20.63" S, 016° 09' 46.04" E 24° 06' 20.28" S, 016° 09' 46.73" E 24° 06' 20.07" S, 016° 09' 46.82" E 24° 06' 17.35" S, 016° 09' 49.97" E 24° 06' 13.92" S, 016° 09' 56.52" E	
CS	24° 06' 21.53" S, 016° 12' 42.32" E	
NE	24° 04' 11.80" S, 016° 18' 57.97" E	
BO	24° 04' 24.43" S, 016° 18' 44.27" E	
NW	24° 04' 15.30" S, 016° 18' 21.52" E	
NX	24° 04' 20.19" S, 016° 18' 10.97" E	
NY	24° 04' 23.61" S, 016° 18' 9.52" E	
BR	24° 05' 47.99" S, 016° 14' 32.30" E	
SR	24° 05' 36.41" S, 016° 13' 31.39" E	
TH	24° 05' 21.60" S, 016° 12' 34.64" E	
GH	24° 05' 0.90" S, 016° 11' 49.44" E	
MA	23° 54' 56.66" S, 016° 17' 39.50" E	

Supplemental Figure 2.1A. Additional measured sections of primarily the upper Blässkranz Formation and Tsondab member of the Tsabisis Formation put in context with sections from Fig. 2.3. (A) Map from Figure 2.1 with coordinates of named localities. (B) Updip sections, (C) Intermediate sections, (D) Downdip sections. Sections are positioned from updip to downdip, from left to right. Colors draw attention to related facies between sections for clarity. Green and brown colors show the upper portions of the Blässkranz Formation. The purple shales and limestone at the top of sections show the beginnings of the middle and upper members of the Tsabisis Formation, while the gray shaded facies represents the Noab Formation. ED and HD are lateral equivalents to TA and CS is a lateral equivalent to NE and BO from Fig. 2. NX and NY are immediately downdip of NW (Fig. 1.1). SR is located stratigraphically between BR and TH, with GH just downdip from TH. The SR Section shows beds of the sedimentary breccia member of the Noab Formation where the underlying Tsondab member is partly but not entirely truncated. MA section shows how the Tsondab member has completely pinched out by the downdip-most localities, where the shale-dominated downdip Blässkranz Formation is conformably overlain by the Noab Formation.



Supplemental Figure 2.2. Disrupted dolostone where the laminations have not been folded but have been brecciated into a fitted fabric.



Supplemental Figure 2.3. Cross plots of carbon and oxygen isotope values for different localities corresponding to the profiles shown in Fig. 10 (‰ VPDB).

CHAPTER 2 REFERENCES

- Adey, W. H. (1978). Coral Reef Morphogenesis: A Multidimensional Model: New data from coring and carbon-14 dating provide keys for unraveling some classical enigmas. *Science*, 202(4370), 831-837.
- Ahm, A. S. C., Bjerrum, C. J., Blättler, C. L., Swart, P. K., & Higgins, J. A. (2018). Quantifying early marine diagenesis in shallow-water carbonate sediments. *Geochimica et Cosmochimica Acta*, 236, 140-159.
- Ahr, W. M. (1973). Carbonate Ramp—Alternative to Shelf Model. *AAPG Bulletin*, 57(9), 1826-1826.
- Allen, P. A., & Hoffman, P. F. (2005). Extreme winds and waves in the aftermath of a Neoproterozoic glaciation. *Nature*, 433(7022), 123-127.
- Amos, C. L., Li, M. Z., Chiocci, F. L., La Monica, G. B., Cappucci, S., King, E. H., & Corbani, F. (2003). Origin of shore-normal channels from the shoreface of Sable Island, Canada. *Journal of Geophysical Research: Oceans*, 108(C3).
- Ashley, G. M., Southard, J. B., & Boothroyd, J. C. (1982). Deposition of climbing-ripple beds: a flume simulation. *Sedimentology*, 29(1), 67-79.
- Berra, F., & Felletti, F. (2011). Syndepositional tectonics recorded by soft-sediment deformation and liquefaction structures (continental Lower Permian sediments, Southern Alps, Northern Italy): stratigraphic significance. *Sedimentary Geology*, 235(3-4), 249-263.
- Bertrand-Sarfati, J., Flicoteaux, R., Moussine-Pouchkine, A., & Ait Kaci, A. A. (1997). Lower Cambrian apatitic stromatolites and phospharenites related to the glacio-eustatic cratonic rebound (Sahara, Algeria). *Journal of Sedimentary Research*, 67(5), 957-974.
- Bouma, A. H. (1962). Sedimentology of some flysch deposits. *Agraphic approach to facies interpretation*, 168.
- Brown, A. A., & Loucks, R. G. (1993). Influence of Sediment Type and Depositional Processes on Stratal Patterns in the Permian Basin-Margin Lamar Limestone, McKittrick Canyon, Texas: Chapter 5.
- Burchette, T. P., & Wright, V. P. (1992). Carbonate ramp depositional systems. *Sedimentary geology*, 79(1-4), 3-57.
- Catuneanu, O., Abreu, V., Bhattacharya, J. P., Blum, M. D., Dalrymple, R. W., Eriksson, P. G., ... & Winker, C. (2009). Towards the standardization of sequence stratigraphy. *Earth-Science Reviews*, 92(1-2), 1-33.
- Cheel, R. J., & Rust, B. R. (1982). Coarse grained facies of glacio-marine deposits near Ottawa, Canada. In *Research in Glacial, Glacio-Fluvial and Glacio-Lacustrine Systems. Proceedings of the 6th Guelph Symposium on Geomorphology, 1980. 1982. p 279-295, 9 fig, 22 ref.*
- Cloud, P., Wright, L. A., Williams, E. G., Diehl, P., & Walter, M. R. (1974). Giant stromatolites and associated vertical tubes from the Upper Proterozoic Noonday Dolomite, Death Valley region, eastern California. *Geological Society of America Bulletin*, 85(12), 1869-1882.
- Corkeron, M. (2007). 'Cap carbonates' and Neoproterozoic glacial successions from the Kimberley region, north-west Australia. *Sedimentology*, 54(4), 871-903.
- Corsetti, F. A., & Grotzinger, J. P. (2005). Origin and significance of tube structures in Neoproterozoic post-glacial cap carbonates: example from Noonday Dolomite, Death Valley, United States. *Palaios*, 20(4), 348-362.

- Creveling, J. R., & Mitrovica, J. X. (2014). The sea-level fingerprint of a Snowball Earth deglaciation. *Earth and Planetary Science Letters*, 399, 74-85.
- Creveling, J. R., Bergmann, K. D., & Grotzinger, J. P. (2016). Cap carbonate platform facies model, Noonday Formation, SE California. *GSA Bulletin*, 128(7-8), 1249-1269.
- Crevello, P. D., & Schlager, W. (1980). Carbonate debris sheets and turbidites, Exuma Sound, Bahamas. *Journal of Sedimentary Research*, 50(4), 1121-1147.
- Duke, W. L., Arnott, R. W. C., & Cheel, R. J. (1991). Shelf sandstones and hummocky cross-stratification: new insights on a stormy debate. *Geology*, 19(6), 625-628.
- Ezpeleta, M., Rustán, J. J., Balseiro, D., Dávila, F. M., Dahlquist, J. A., Vaccari, N. E., ... & Basei, M. (2020). Glaciomarine sequence stratigraphy in the Mississippian Río Blanco Basin, Argentina, southwestern Gondwana. Basin analysis and palaeoclimatic implications for the Late Paleozoic Ice Age during the Tournaisian. *Journal of the Geological Society*, 177(6), 1107-1128.
- Fairchild, I. J., Bao, H., Windmill, R., & Boomer, I. (2022). The Marinoan cap carbonate of Svalbard: Syngenetic marine dolomite with 17 O-anomalous carbonate-associated sulphate. *The Depositional Record*, Early-Access.
- Farrell, W. E., & Clark, J. A. (1976). On postglacial sea level. *Geophysical Journal International*, 46(3), 647-667.
- Ferronato, J. P. F., dos Santos Scherer, C. M., Drago, G. B., Rodrigues, A. G., de Souza, E. G., dos Reis, A. D., ... & Cazarin, C. L. (2021). Mixed carbonate-siliciclastic sedimentation in a mesoproterozoic storm-dominated ramp: Depositional processes and stromatolite development. *Precambrian Research*, 361, 106240.
- Field, M. E., & Roy, P. S. (1984). Offshore transport and sand-body formation; evidence from a steep, high-energy shoreface, southeastern Australia. *Journal of Sedimentary Research*, 54(4), 1292-1302.
- Fielding, C. R. (2018). Stratigraphic architecture of the Cenozoic succession in the McMurdo Sound region, Antarctica: An archive of polar palaeoenvironmental change in a failed rift setting. *Sedimentology*, 65(1), 1-61.
- Font, E., Nédélec, A., Trindade, R. I. F., & Moreau, C. (2010). Fast or slow melting of the Marinoan snowball Earth? The cap dolostone record. *Palaeogeography, Palaeoclimatology, Palaeoecology*, 295(1-2), 215-225.
- Gan, T., Zhou, G., Luo, T., Pang, K., Zhou, M., Luo, W., ... & Xiao, S. (2022). Earliest Ediacaran speleothems and their implications for terrestrial life after the Marinoan snowball Earth. *Precambrian Research*, 376, 106685.
- Goscombe, B., Foster, D. A., Gray, D., & Wade, B. (2017). Metamorphic response and crustal architecture in a classic collisional orogen: the Damara Belt, Namibia. *Gondwana Research*, 52, 80-124.
- Grammer, G. M., Ginsburg, R. N., & Harris, P. M. (1993). Timing of Deposition, Diagenesis, and Failure of Steep Carbonate Slopes in Response to a High-Amplitude/High-Frequency Fluctuation in Sea Level, Tongue of the Ocean, Bahamas: Chapter 4.
- Grammer, G. M., Eberli, G. P., Van Buchem, F. S., Stevenson, G. M., Homewood, P. W., & Eberli, G. P. (2000). Application of high-resolution sequence stratigraphy in developing an exploration and production strategy for a mixed carbonate/siliciclastic system (Carboniferous) Paradox Basin, Utah, USA. *Genetic Stratigraphy on the Exploration and Production Scales*, 29-69.

- Gray, D. R., Foster, D. A., Meert, J. G., Goscombe, B. D., Armstrong, R., Trouw, R. A. J., & Passchier, C. W. (2008). A Damara orogen perspective on the assembly of southwestern Gondwana. *Geological Society, London, Special Publications*, 294(1), 257-278.
- Grotzinger, J. P. (1986). Evolution of Early Proterozoic passive-margin carbonate platform, rocknest formation, wopmay orogen, Northwest Territories, Canada. *Journal of Sedimentary Research*, 56(6), 831-847.
- Grotzinger, J. P. (1989). Facies and evolution of Precambrian carbonate depositional systems: emergence of the modern platform archetype, In P. D. Crevello, J. L. Wilson, J. F. Sarg, J. F. Read *Controls on Carbonate Platforms and Basin Development, SEPM Special Publication 44*, (pp. 79-106).
- Grotzinger, J. P., & James, N. P. (2000). Precambrian carbonates: evolution of understanding.
- Halverson, G. P., & Shields-Zhou, G. (2011). Chemostratigraphy and the Neoproterozoic glaciations. *Geological Society, London, Memoirs*, 36(1), 51-66.
- Hanford, C. R., & Loucks, R. G. (1993). Carbonate depositional sequence and systems tracts-responses of carbonate platforms to relative sea-level changes. Chapter 1, Carbonate Sequence Stratigraphy. *American Association of Petroleum Geologists, Memoir*, 57, 3-41.
- Hartnady, C. J. H. (1978). The structural geology of the Naukluft Nappe Complex and its relationship to the Damara Orogenic Belt, South West Africa/Namibia. [Doctoral dissertation, University of Cape Town]. <http://hdl.handle.net/11427/18057>
- Hartnady, C. J. H. (1980). Geological map of the Naukluft area, *Precambrian Research Unit, University of Cape Town*.
- Higgins, J. A., & Schrag, D. P. (2003). Aftermath of a snowball Earth. *Geochemistry, Geophysics, Geosystems*, 4(3).
- Hiscott, R. N., & James, N. P. (1985). Carbonate debris flows, Cow Head Group, western Newfoundland. *Journal of Sedimentary Research*, 55(5), 735-745.
- Hoffman, P. (1974). Shallow and deepwater stromatolites in Lower Proterozoic platform-to-basin facies change, Great Slave Lake, Canada. *AAPG Bulletin*, 58(5), 856-867.
- Hoffman, P. F., & Grotzinger, J. P. (1993). Orographic precipitation, erosional unloading, and tectonic style. *Geology*, 21(3), 195-198.
- Hoffman, P. F., Kaufman, A. J., Halverson, G. P., & Schrag, D. P. (1998). A Neoproterozoic snowball earth. *science*, 281(5381), 1342-1346.
- Hoffman, P. F., & Schrag, D. P. (2002). The snowball Earth hypothesis: testing the limits of global change. *Terra nova*, 14(3), 129-155.
- Hoffman, P. F., Halverson, G. P., Domack, E. W., Husson, J. M., Higgins, J. A., & Schrag, D. P. (2007). Are basal Ediacaran (635 Ma) post-glacial “cap dolostones” diachronous?. *Earth and Planetary Science Letters*, 258(1-2), 114-131.
- Hoffman, P. F., & Li, Z. X. (2009). A palaeogeographic context for Neoproterozoic glaciation. *Palaeogeography, Palaeoclimatology, Palaeoecology*, 277(3-4), 158-172.
- Hoffman, P. F., & Macdonald, F. A. (2010). Sheet-crack cements and early regression in Marinoan (635 Ma) cap dolostones: regional benchmarks of vanishing ice-sheets?. *Earth and Planetary Science Letters*, 300(3-4), 374-384.
- Hoffman, P. F. (2011). Strange bedfellows: glacial diamictite and cap carbonate from the Marinoan (635 Ma) glaciation in Namibia. *Sedimentology*, 58(1), 57-119.
- Hoffman, P. F., Abbot, D. S., Ashkenazy, Y., Benn, D. I., Brocks, J. J., Cohen, P. A., ... & Warren, S. G. (2017). Snowball Earth climate dynamics and Cryogenian geology-geobiology. *Science Advances*, 3(11), e1600983.

- Hoffman, P. F., Halverson, G. P., Schrag, D. P., Higgins, J. A., Domack, E. W., Macdonald, F. A., ... & Nelson, L. L. (2021). Snowballs in Africa: sectioning a long-lived Neoproterozoic carbonate platform and its bathyal foreslope (NW Namibia). *Earth-Science Reviews*, 219, 103616.
- Hoffmann, K. H. (1989). New aspects of lithostratigraphic subdivision and correlation of late Proterozoic to early Cambrian rocks of the southern Damara Belt and their correlation with the central and northern Damara Belt and the Gariep Belt. *Communications of the Geological Survey of Namibia*, 5, 61-70.
- Homewood, P. W., & Eberli, G. P. (2000). *Genetic stratigraphy. On the exploration and production scales*. France.
- Hyde, W. T., Crowley, T. J., Baum, S. K., & Peltier, W. R. (2000). Neoproterozoic 'snowball Earth' simulations with a coupled climate/ice-sheet model. *Nature*, 405(6785), 425-429.
- Irie, Y., Nakada, M., Okuno, J. I., & Bao, H. (2019). Nonmonotonic postdeglacial relative sea level changes at the aftermath of Marinoan (635 Ma) snowball Earth meltdown. *Journal of Geophysical Research: Solid Earth*, 124(8), 9373-9394.
- James, N. P. (1981). Megablocks of calcified algae in the Cow Head Breccia, western Newfoundland: Vestiges of a Cambro-Ordovician platform margin. *Geological Society of America Bulletin*, 92(11), 799-811.
- James, N. P., Narbonne, G. M., & Kyser, T. K. (2001). Late Neoproterozoic cap carbonates: Mackenzie Mountains, northwestern Canada: precipitation and global glacial meltdown. *Canadian Journal of Earth Sciences*, 38(8), 1229-1262.
- Jerolmack, D. J., & Mohrig, D. (2005). Formation of Precambrian sediment ripples. *Nature*, 436(7049), E1-E1.
- Jiang, G., Kennedy, M. J., & Christie-Blick, N. (2003). Stable isotopic evidence for methane seeps in Neoproterozoic postglacial cap carbonates. *Nature*, 426(6968), 822-826.
- Jiang, G., Kennedy, M. J., Christie-Blick, N., Wu, H., & Zhang, S. (2006). Stratigraphy, sedimentary structures, and textures of the late Neoproterozoic Doushantuo cap carbonate in South China. *Journal of Sedimentary Research*, 76(7), 978-995.
- Kendall, C. G. S. C., & Schlager, W. (1981). Carbonates and relative changes in sea level. *Marine geology*, 44(1-2), 181-212.
- Kennedy, M. J. (1996). Stratigraphy, sedimentology, and isotopic geochemistry of Australian Neoproterozoic postglacial cap dolostones; deglaciation, delta 13 C excursions, and carbonate precipitation. *Journal of sedimentary Research*, 66(6), 1050-1064.
- Kennedy, M. J., Christie-Blick, N., & Sohl, L. E. (2001). Are Proterozoic cap carbonates and isotopic excursions a record of gas hydrate destabilization following Earth's coldest intervals?. *Geology*, 29(5), 443-446.
- Kennedy, M. J., & Christie-Blick, N. (2011). Condensation origin for Neoproterozoic cap carbonates during deglaciation. *Geology*, 39(4), 319-322.
- Kirschvink, Joseph L. (1992) Late Proterozoic Low-Latitude Global Glaciation: the Snowball Earth. In: J.W. Schopf, C. Klein, & D. Des Maris (eds), *The Proterozoic Biosphere: A Multidisciplinary Study*. Cambridge University Press, pp. 51-52.
- Korn, H., & Martin, H. (1959). Gravity tectonics in the Naukluft mountains of South West Africa. *Geological Society of America Bulletin*, 70(8), 1047-1078.
- Lamb, M. P., Myrow, P. M., Lukens, C., Houck, K., & Strauss, J. (2008). Deposits from wave-influenced turbidity currents: Pennsylvanian Minturn Formation, Colorado, USA. *Journal of Sedimentary Research*, 78(7), 480-498.

- Lamb, M. P., Fischer, W. W., Raub, T. D., Perron, J. T., & Myrow, P. M. (2012). Origin of giant wave ripples in snowball Earth cap carbonate. *Geology*, 40(9), 827-830.
- Liu, C., Wang, Z., & Macdonald, F. A. (2018). Sr and Mg isotope geochemistry of the basal Ediacaran cap limestone sequence of Mongolia: Implications for carbonate diagenesis, mixing of glacial meltwaters, and seawater chemistry in the aftermath of Snowball Earth. *Chemical Geology*, 491, 1-13.
- Logan, B. W. (1974). Inventory of diagenesis in Holocene-recent carbonate sediments, Shark Bay, Western Australia. In *Evolution and Diagenesis of Quaternary Carbonate Sequences, Shark Bay, Western Australia* (pp. 195-249).
- Lønne, I. (1995). Sedimentary facies and depositional architecture of ice-contact glaciomarine systems. *Sedimentary Geology*, 98(1-4), 13-43.
- Loutit, T. S., Hardenbol, J., Vail, P. R., & Baum, G. R. (1988). Condensed sections: the key to age determination and correlation of continental margin sequences. In *Sea Level Changes – An Integrated Approach, SEPM Special Publication* (n. 42).
- Lowe, D. R. (1982). Sediment gravity flows; II, Depositional models with special reference to the deposits of high-density turbidity currents. *Journal of sedimentary research*, 52(1), 279-297.
- Macdonald, F. A., Jones, D. S., & Schrag, D. P. (2009). Stratigraphic and tectonic implications of a newly discovered glacial diamictite–cap carbonate couplet in southwestern Mongolia. *Geology*, 37(2), 123-126.
- Martin, H., Porada, H., & Wittig, R. (1983). The root zone of the Naukluft Nappe Complex: geodynamic implications. In *Intracontinental Fold Belts* (pp. 679-698). Springer, Berlin, Heidelberg.
- McKenzie, D. (1978). Some remarks on the development of sedimentary basins. *Earth and Planetary science letters*, 40(1), 25-32.
- McIlreath, I., and N. James. "Facies models 13. Carbonate slopes." *Geoscience Canada* 5.4 (1978): 189-199.
- Merdith, A. S., Collins, A. S., Williams, S. E., Pisarevsky, S., Foden, J. D., Archibald, D. B., ... & Müller, R. D. (2017). A full-plate global reconstruction of the Neoproterozoic. *Gondwana Research*, 50, 84-134.
- Merdith, A. S., Williams, S. E., Collins, A. S., Tetley, M. G., Mulder, J. A., Blades, M. L., ... & Müller, R. D. (2021). Extending full-plate tectonic models into deep time: Linking the Neoproterozoic and the Phanerozoic. *Earth-Science Reviews*, 214, 103477.
- Miller, R. M. (2008). Neoproterozoic and early Palaeozoic rocks of the Damara Orogen. *The Geology of Namibia*, 2, 13-1.
- Mitchum Jr, R. M., Vail, P. R., & Thompson III, S. (1977). Seismic stratigraphy and global changes of sea level: Part 2. The depositional sequence as a basic unit for stratigraphic analysis: Section 2. Application of seismic reflection configuration to stratigraphic interpretation.
- Morris, F. K., in progress thesis. *Depositional and Structural History of the Pavian and Kudu Nappes in the Naukluft Mountains, Namibia*. Dissertation (Ph.D.), California Institute of Technology.
- Mount, J. F. (1984). Mixing of siliciclastic and carbonate sediments in shallow shelf environments. *Geology*, 12(7), 432-435.

- Mulder, T., Syvitski, J. P., Migeon, S., Faugères, J. C., & Savoye, B. (2003). Marine hyperpycnal flows: initiation, behavior and related deposits. A review. *Marine and Petroleum Geology*, 20(6-8), 861-882.
- Myrow, P. M. (1992). Bypass-zone tempestite facies model and proximity trends for an ancient muddy shoreline and shelf. *Journal of Sedimentary research*, 62(1), 99-115.
- Myrow, P. M., Tice, L., Archuleta, B., Clark, B., Taylor, J. F., & Ripperdan, R. L. (2004). Flat-pebble conglomerate: its multiple origins and relationship to metre-scale depositional cycles. *Sedimentology*, 51(5), 973-996.
- Myrow, P. M., Lukens, C., Lamb, M. P., Houck, K., & Strauss, J. (2008). Dynamics of a transgressive prodeltaic system: Implications for geography and climate within a Pennsylvanian intracratonic basin, Colorado, USA. *Journal of Sedimentary Research*, 78(8), 512-528.
- Nakada, M., & Lambeck, K. (1987). Glacial rebound and relative sea-level variations: a new appraisal. *Geophysical Journal International*, 90(1), 171-224.
- Nordsvan, A. R., Barham, M., Cox, G., Kirscher, U., & Mitchell, R. N. (2019). Major shoreline retreat and sediment starvation following Snowball Earth. *Terra Nova*, 31(6), 495-502.
- Pattison, S. A., Bruce Ainsworth, R., & Hoffman, T. A. (2007). Evidence of across-shelf transport of fine-grained sediments: turbidite-filled shelf channels in the Campanian Aberdeen Member, Book Cliffs, Utah, USA. *Sedimentology*, 54(5), 1033-1064.
- Penman, D. E., & Rooney, A. D. (2019). Coupled carbon and silica cycle perturbations during the Marinoan snowball Earth deglaciation. *Geology*, 47(4), 317-320.
- Porter, S. M., Knoll, A. H., & Affaton, P. (2004). Chemostratigraphy of Neoproterozoic cap carbonates from the Volta basin, West Africa. *Precambrian Research*, 130(1-4), 99-112.
- Powell, R. D. (1981). A model for sedimentation by tidewater glaciers. *Annals of Glaciology*, 2, 129-134.
- Powell, R. D., & Molnia, B. F. (1989). Glacimarine sedimentary processes, facies and morphology of the south-southeast Alaska shelf and fjords. *Marine Geology*, 85(2-4), 359-390.
- Prave, A. R., Hoffmann, K. H., Hegenberger, W., & Fallick, A. E. (2011). The Witvlei Group of east-central Namibia. *Geological Society, London, Memoirs*, 36(1), 211-216.
- Quinn, D. P., (2018). *Regional Structural Geology of Earth and Mars*. Dissertation (Ph.D.), California Institute of Technology. doi:10.7907/9enj-wn23.
- Read, J. F. (1985). Carbonate platform facies models. *AAPG bulletin*, 69(1), 1-21.
- Rose, C. V., & Maloof, A. C. (2010). Testing models for post-glacial 'cap dolostone' deposition: Nuccaleena Formation, South Australia. *Earth and Planetary Science Letters*, 296(3-4), 165-180.
- Rosenbaum, J., & Sheppard, S. M. F. (1986). An isotopic study of siderites, dolomites and ankerites at high temperatures. *Geochimica et cosmochimica acta*, 50(6), 1147-1150.
- Rossetti, D. D. F. (1999). Soft-sediment deformation structures in late Albian to Cenomanian deposits, São Luís Basin, northern Brazil: evidence for palaeoseismicity. *Sedimentology*, 46(6), 1065-1081.
- Schlager, W. (1981). The paradox of drowned reefs and carbonate platforms. *Geological Society of America Bulletin*, 92(4), 197-211.
- Schlager, W. (1991). Depositional bias and environmental change—important factors in sequence stratigraphy. *Sedimentary Geology*, 70(2-4), 109-130.

- Scholle, P. A. (1979). Constituents, Textures, Cements, and Porosities of Sandstones and Associated Rocks. *Amer. Assoc. Petroleum Geologists Memoir*, 28.
- Shen, W., Zhu, X., Yan, B., Qin, H., Gao, Z., & Li, F. (2021). Sequence stratigraphy of the Cryogenian Nantuo Formation in South China: Constraints on Marinoan glaciation dynamics. *Journal of Asian Earth Sciences*, 214, 104776.
- Shields, G. A., Deynoux, M., Culver, S. J., Brasier, M. D., Affaton, P., & Vandamme, D. (2007). Neoproterozoic glaciomarine and cap dolostone facies of the southwestern Taoudéni Basin (Walidiala Valley, Senegal/Guinea, NW Africa). *Comptes Rendus Geoscience*, 339(3-4), 186-199.
- Sherman, A. G., James, N. P., & Narbonne, G. M. (2000). Sedimentology of a late Mesoproterozoic muddy carbonate ramp, northern Baffin Island, Arctic Canada.
- Steckler, M. S., & Watts, A. B. (1978). Subsidence of the Atlantic-type continental margin off New York. *Earth and planetary science letters*, 41(1), 1-13.
- Southard, J. B., Lambie, J. M., Federico, D. C., Pile, H. T., & Weidman, C. R. (1990). Experiments on bed configurations in fine sands under bidirectional purely oscillatory flow, and the origin of hummocky cross-stratification. *Journal of Sedimentary Research*, 60(1), 1-17.
- Southgate, P. N., Kennard, J. M., Jackson, M. J., O'Brien, P. E., & Sexton, M. J. (1993). Reciprocal Lowstand Clastic and Highstand Carbonate Sedimentation, Subsurface Devonian Reef Complex, Canning Basin, Western Australia: Chapter 6. In *Carbonate Sequence Stratigraphy: Recent Developments and Applications* (pp. 157-179).
- Swart, P. K., Burns, S. J., & Leder, J. J. (1991). Fractionation of the stable isotopes of oxygen and carbon in carbon dioxide during the reaction of calcite with phosphoric acid as a function of temperature and technique. *Chemical Geology: Isotope Geoscience section*, 86(2), 89-96.
- Swart, P. K. (2015). The geochemistry of carbonate diagenesis: The past, present and future. *Sedimentology*, 62(5), 1233-1304.
- Trindade, R. I. F. D., Font, E., D'Agrella-Filho, M. S., Nogueira, A. C. R., & Riccomini, C. (2003). Low-latitude and multiple geomagnetic reversals in the Neoproterozoic Puga cap carbonate, Amazon craton. *Terra Nova*, 15(6), 441-446.
- Vail, P. R., Mitchum Jr, R. M., & Thompson III, S. (1977). Seismic stratigraphy and global changes of sea level: Part 3. Relative changes of sea level from Coastal Onlap: section 2. Application of seismic reflection Configuration to Stratigraphic Interpretation. In *Seismic Stratigraphy--Applications to Hydrocarbon Exploration* (pp. 63-81).
- Van Wagoner, J. C., Posamentier, H. W., Mitchum, R. M. J., Vail, P. R., Sarg, J. F., Loutit, T. S., & Hardenbol, J. (1988). An overview of the fundamentals of sequence stratigraphy and key definitions. In *Sea Level Changes – An Integrated Approach, SEPM Special Publication* (n. 42).
- Van Wagoner, J. C., Mitchum, R. M., Campion, K. M., & Rahmanian, V. D. (1990). Siliciclastic sequence stratigraphy in well logs, cores, and outcrops: concepts for high-resolution correlation of time and facies. In *Siliciclastic Sequence Stratigraphy in Well Logs, Cores, and Outcrops: Concepts for High-Resolution Correlation of Time and Facies* (pp. III-55).
- Wei, G. Y., vS Hood, A., Chen, X., Li, D., Wei, W., Wen, B., ... & Ling, H. F. (2019). Ca and Sr isotope constraints on the formation of the Marinoan cap dolostones. *Earth and Planetary Science Letters*, 511, 202-212.
- Whalen, M. T., Eberli, G. P., Van Buchem, F. S., Mountjoy, E. W., & Homewood, P. W. (2000). Bypass margins, basin-restricted wedges, and platform-to-basin correlation, Upper

- Devonian, Canadian Rocky Mountains: implications for sequence stratigraphy of carbonate platform systems. *Journal of Sedimentary Research*, 70(4), 913-936.
- Yang, J., Jansen, M. F., Macdonald, F. A., & Abbot, D. S. (2017). Persistence of a freshwater surface ocean after a snowball Earth. *Geology*, 45(7), 615-618.
- Yu, W., Algeo, T. J., Zhou, Q., Du, Y., & Wang, P. (2020). Cryogenian cap carbonate models: A review and critical assessment. *Palaeogeography, Palaeoclimatology, Palaeoecology*, 552, 109727.
- Zhou, C., Bao, H., Peng, Y., & Yuan, X. (2010). Timing the deposition of ^{17}O -depleted barite at the aftermath of Nantuo glacial meltdown in South China. *Geology*, 38(10), 903-906.
- Zurbuchen, J., & Simms, A. R. (2019). Late Holocene ice-mass changes recorded in a relative sea-level record from Joinville Island, Antarctica. *Geology*, 47(11), 1064-1068.

*Chapter 3*STRUCTURAL AND LITHOSTRATIGRAPHIC FRAMEWORK OF THE
NEOPROTEROZOIC NAUKLUFT NAPPE COMPLEX

Authors: Freya K. Morris^{a*} and John P. Grotzinger^a

^a Department of Geological and Planetary Sciences, California Institute of Technology, Pasadena, CA 91125, USA

* Corresponding Author: morrisfreya15@outlook.com

Abstract:

The Naukluft Nappe Complex (NNC) of south-central Namibia contains sedimentary rocks that record significant Neoproterozoic environmental and tectonic transitions, including Marinoan Snowball Earth glaciogenic deposits and basal-Ediacaran cap carbonates. This field study seeks to resolve the complex structural and stratigraphic relations between many of the formations of the NNC using field observations of sedimentology, stratigraphy, and structural geometries supplemented by chemostratigraphic and detrital zircon analyses. Rocks of the Northern Pavian Nappe, which includes the Marinoan-associated Blässkranz and Tsabisis formations are stratigraphically overlain by rocks assigned to the dolostone-dominated Kudu Nappe; the contact between them varies spatially between localized younger-over-older thrust faults, erosive disconformities, and progressive stratigraphic intercalation. This contrasts with prior interpretations of an exclusively tectonic contact and structural inversion of an older Kudu Nappe overlying a younger Northern Pavian Nappe. The Southern Pavian Nappe is composed of mixed carbonate-siliciclastic strata including a thick dolostone unit marked by tubestone and oolite facies. Prior work suggested correlation of this dolostone unit with the Northern Pavian cap carbonate. However, comparison of the facies, lithostratigraphic and chemostratigraphic relationships, along with structural juxtaposition by a roof thrust precludes correlation. Nor do the strata of the Southern Pavian Nappe correlate with any other units of the NNC. Rocks of the Northern Pavian and Kudu nappes can be considered a single stratigraphic succession independent of the Southern

Pavian Nappe. This combined parautochthonous succession provides a valuable Cryogenian-to-Ediacaran stratigraphic record from the northern Kalahari margin. These revisions to the stratigraphy and structure allow for a simplified nappe emplacement history of the Naukluft Nappe Complex and the displacement from its root zone.

1. Introduction

The Naukluft Nappe Complex (NNC) is a tectonic klippe in south-central Namibia composed of displaced Neoproterozoic sedimentary rocks. Rocks of the NNC are rooted in the late Ediacaran to Cambrian-age Damara Orogen, part of the broader pan-African assembly of Gondwana (Gray et al. 2008; Miller 2008; Goscombe et al. 2017; Quinn thesis; Quinn et al., in prep) following passive margin and foreland sedimentation that collectively record important global Cryogenian to early Cambrian environmental and evolutionary events (e.g. Bold et al. 2016; Xiao et al. 2016; Sui et al. 2018). Identifying strata that record early Ediacaran processes is increasingly important as it represents the time between the climatic upheavals of the Marinoan Snowball Earth (635 Ma; e.g. Hoffman et al. 2017) and the mid to late Ediacaran Gaskiers Glaciation (~580 Ma; Myrow & Kaufman 1999; Pu et al. 2016; Rooney et al. 2020) and the rise of the Ediacaran biota (~574 Ma; Rooney et al. 2020). The rocks of the NNC provide an excellent sample of this important time in Earth history.

The northern margin of the Damara orogenic belt (Congo Craton) includes well preserved Cryogenian and Ediacaran glacial and cap carbonate sedimentary successions (e.g., Hoffman et al. 2007; Hoffman 2011; Hoffman et al. 2021). The southern margin (Kalahari Craton) records the globally significant Nama Group foreland basin system, exposing excellent examples of late Ediacaran and early Cambrian ecosystems (e.g. Germs 1983; Germs & Gresse 1991; Grotzinger et al., 1995; Grotzinger et al., 2000; Wood et al., 2002; Saylor et al. 1995; Nelson et al. 2022). The NNC contains end-Cryogenian glacial deposits and overlying basal-Ediacaran cap carbonates likely deposited along the northern margin of the Kalahari Craton (~635 Ma; Hoffmann 1989; Miller 2008; Morris & Grotzinger 2023) that together record the termination of the Marinoan Snowball Earth glaciation (e.g. Kirschvink 1992; Hoffman et al. 1998; Hoffman et al. 2017). However, the stratigraphic relationships of these units to the other formations of the NNC is uncertain due to limited detailed mapping and

stratigraphic/sedimentologic studies, preventing a complete reconstruction of the Cryogenian and Ediacaran stratigraphic record along the Kalahari margin.

The NNC is composed of several allochthons that were thrust south-southeast over the Nama foreland basin of the Kalahari craton during the Damara Orogeny, with emplacement estimated at 555 Ma (Gray et al. 2008; Miller 2008; Goscombe et al. 2017; Quinn thesis; et al., in prep). The Northern Pavian Nappe includes the Remhoogte, Blässkranz, and Tsabisis formations previously interpreted as including pre-glacial, glaciogenic, and cap carbonate deposition, respectively (Hoffman et al. 1989; Miller 2008; Morris & Grotzinger 2023). The Kudu Nappe generally overlies the Northern Pavian Nappe; however, the intense shear deformation of the nappes and complex thrusting has resulted in competing interpretations for their relationship. Initial work (Korn & Martin 1959) interpreted these rocks (Pavian/Kudu) to be in true stratigraphic order, but later work (Hartnady 1978; 1980) interpreted stratigraphically older (inferred) Kudu rocks to have been thrust over younger (inferred) Northern Pavian rocks as part of a tectonic imbrication with several distinct episodes of shortening. Unpublished mapping of K. H. Hoffmann (1989; and described in Miller 2008) primarily used lithological comparison to the Samara Formation (Hakos Terrane) to suggest there is no significant tectonic dislocation between the Northern Pavian and Kudu rocks. Our work seeks to test these competing hypotheses.

Rocks of the Northern Pavian Nappe were correlated with rocks of the Southern Pavian Nappe, and both were correlated with rocks of the southernmost Zebra Nappe (Korn & Martin 1959). This correlation equates the relatively thick dolostone member of the Southern Pavian Nappe correlative to the cap carbonate of the Northern Pavian Nappe. Hartnady (1978; 1980; Miller 2008) rejected the correlation between the Northern and Southern Pavian nappes yet retained the link between the Southern Pavian Nappe and Zebra Nappe, and correlated them both with the Nama Group. However, Quinn (thesis; Quinn et al., in prep) showed that the Southern Pavian Nappe and Zebra Nappe are not equivalent, and neither can be correlated with the Nama Group. Therefore, the identity, relative age, and possible relationship to the recognized cap carbonate of the Naukluft Nappe Complex is unconstrained for the Southern Pavian Nappe strata.

The present study seeks to constrain the structure, lithofacies, and stratigraphic evolution of the nappes found in the broader NNC, placing them within tectonic evolution of the Damara Orogen and Neoproterozoic environmental history. Detailed sedimentological and stratigraphic analysis and mapping of several NNC units, complemented by chemostratigraphic and detrital zircon analyses, allows reconciliation of competing models for the relationship between the Northern Pavian, Kudu, and Southern Pavian nappes, therefore defining the extent of the Naukluft Marinoan cap carbonate succession and its transition into the early Ediacaran.

The work presented here reduces the number of tectonic nappes, and makes the term “nappe” obsolete for the “Kudu nappe” since we can show it’s in stratigraphic continuity with the Northern Pavian “nappe” rocks. Collectively the Northern Pavian and Kudu rocks constitute a single nappe. Nevertheless, we retain use of the terms “Kudu Nappe” and “Northern Pavian Nappe” because they are so ingrained in the published literature, and because the Northern Pavian/Kudu sequence is separated locally by a bedding parallel shear zone that makes their relationship parautochthonous. We use the terms “Kudu rocks”, “Northern Pavian rocks” to indicate they are not separate nappes at appropriate points in the text where we argue that that are stratigraphically intact.

2. Geologic Background

The NNC is exposed in the Naukluft Mountains of south-central Namibia. Deformation and transport of the 70 km long and 30 km wide tectonic klippe occurred during the Pan-African ~590-505 Ma Damara Orogeny (Fig. 3.1), resulting from high angle convergence of the Congo and Kalahari cratons as part of the assembly of Gondwana (Gray et al. 2008; Miller 2008; Goscombe et al. 2017). The NNC was thrust south-southeastward over the Ediacaran to Cambrian-aged Nama (e.g. Germs 1983; Germs & Gresse 1991; Saylor et al. 1995; Nelson et al. 2022) foreland (Kalahari craton) during the earlier stage of Damara cratonic collision at circa 555 Ma based on Ar-Ar muscovite ages derived from rocks along the basal décollement of the NNC (Gray et al. 2008; Goscombe et al. 2017). The root of the NNC was likely along the northern margin of the Kalahari Craton (Fig. 3.1; Hoffmann 1989; Miller 2008), yet its exact location is unclear (e.g. Viola et al. 2006) and some have even suggested

that the stratigraphy was originally deposited on the Congo Craton (Goscombe et al. 2017, Fig. 2). Tectonic displacement is estimated at ~90 km (Martin et al. 1983) or a minimum of 78 km (Hartnady 1978; see section 7). The basal décollement and its associated carbonate hosted fault rocks (termed ‘Sole Dolomite’ or ‘gritty dolomite’) have sustained interest in the elucidation of fault mechanics and lubrication over such large displacement distances (Korn & Martin 1959; Hartnady 1978; Martin et al. 1983; Viola et al. 2006; Miller 2008; Rowe et al. 2012; Fagereng et al. 2014).

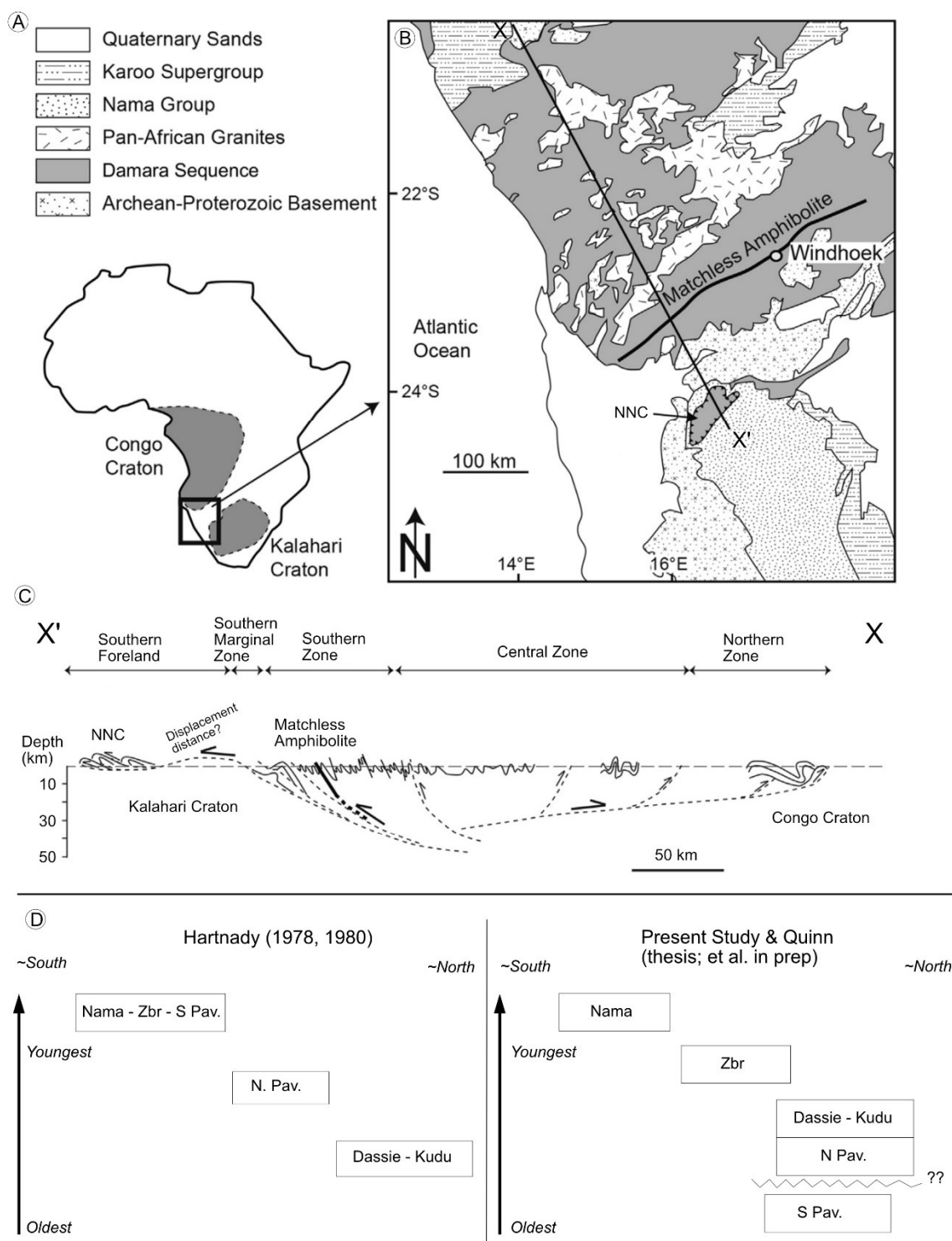


Figure 3.1. (A-C) Contextual geologic map and tectonic cross section (X-X') of the NNC within the Damara Orogen of central Namibia. Modified from Fagereng et al. (2014). (D) Schematic comparison of the temporal and spatial relationships of the nappes prior to deformation between Hartnady (1978; 1980) and the present study, along with the modified relationships for the Zebra Nappe by Quinn (thesis; et al., in prep). The relative height of the units represent their relative depositional age with

the higher units being younger than the lower. The relative depositional age for the Southern Pavian Nappe is not well constrained, but it may be the oldest unit of the NNC. The temporal gaps between the Dassie-Kudu Nappe, the Zebra Nappe, and the Nama Group are not well constrained, but their relative order is as shown (Quinn thesis; et al., in prep). See Fig. 3.4 and Quinn (thesis; et al., in prep) for cross sections showing the nappe relationships following deformation. Abbreviations – Zbr: Zebra Nappe, S Pav: Southern Pavian Nappe, N Pav: Northern Pavian Nappe.

Structural levels above the basal decollement are characterized by SSE-vergent meso-scale asymmetric folds and thrust imbricates (e.g. Fig. 3.5), within several large-scale nappe units (Korn & Martin 1959; Hartnady 1978; Hartnady 1980; Quinn thesis; et al., in prep). Vergence rotates to SW in the western Naukluft (Korn & Martin 1959; Hartnady 1978). Deformation is accompanied by lower greenschist metamorphic overprinting (Korn & Martin 1959; Hartnady 1978); fortunately, primary sedimentary fabrics are only rarely obscured. Generally, the nappes are named from lower to higher structural levels as the Zebra, Dassie, Southern Pavian, Northern Pavian, and Kudu nappes (Table 3.1; Korn & Martin 1959; Hartnady 1978; Hoffmann 1989; Quinn thesis; et al., in prep). The Zebra Nappe is a mixed carbonate-siliciclastic passive margin sequence (Table 3.1; Quinn thesis; et al., in prep), which has no clear correlation with other Naukluft rocks or those of the autochthonous Nama Group (Quinn thesis; et al., in prep). The age of the Zebra Nappe strata is broadly estimated to be early Ediacaran, prior to the initiation of Nama Group foreland deposition (Quinn thesis; et al., in prep). The Dassie Nappe is composed entirely of the mixed carbonate-siliciclastic Büllsport Formation, which contains distinctive thinly bedded intercalated phyllite and strongly rippled quartzite, and is interpreted as a southern updip equivalent of Noab Formation found in the Kudu Nappe (Korn & Martin 1959; Hartnady 1978; 1980; Martin et al. 1983; Miller 2008). The Southern Pavian Nappe (Table 3.1) has been broadly described as containing a lower unit of mixed and laterally variable shale, pebbly sandstone, dark limestone, and tan dolostone, which we assign to the Aubschlucht Formation (Hartnady 1978) up to the base of the thick, massive, gray dolostone that was correlated with parts of the Zebra Nappe by Hartnady (1978). These latter dolostones do not correlate with rocks of the Zebra Nappe (Quinn thesis; et al., in prep), and so we propose a new, descriptive term – “tubestone member” – which assign to the base of the informal Adelt formation. Conformably overlying shale, limestone, dolostone are assigned as upper members of the

Adelt formation; these rocks had previously been assigned to portions of the Tsabisis and Noab formations but our work does not support that correlation.

Structural and Stratigraphic terminology
of the Naukluft Nappe Complex

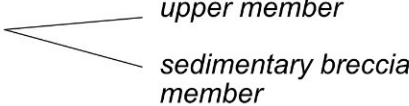
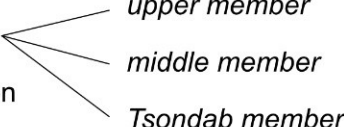
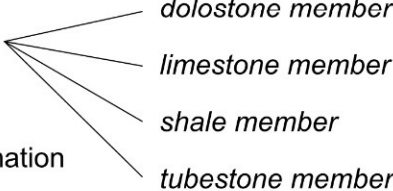
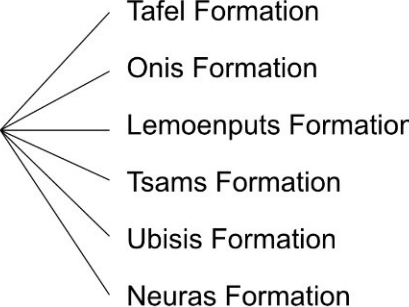
Nappes	Lithostratigraphy
Kudu Nappe	Klipbokrivier Formation*
	Noab Formation 
Northern Pavian Nappe	Tsabisis Formation 
	Blässkranz Formation
	Remhoogte Formation
Southern Pavian Nappe	Adelt formation 
	Abschlucht Formation
Dassie Nappe	Büllsport Formation
Zebra Nappe	Zebra River Group 

Table 3.1. Structural and stratigraphic terminology used in the present study. Italicized names are informal members defined in Morris & Grotzinger (2023) or the present study. The Klipbokrivier Formation marked by the asterisk (*) has been interpreted as a separate formation overlying the Noab Formation within the Kudu Nappe (Korn & Martin 1959; Hartnady 1978; Hoffmann 1989; Miller et al. 2008), but the present work questions this interpretation. The classification of the units in the Zebra Nappe follow that of Quinn (thesis; et al., in prep).

The Northern Pavian Nappe includes the Remhoogte, Blässkranz, and Tsabisis formations (Table 3.1). The Remhoogte Formation is shale dominated with minor subgreywacke and carbonate breccia (Korn & Martin 1959; Hartnady 1978), interpreted as a sedimentary *mélange* (Hartnady 1978) and deep-water turbiditic deposition (Miller 2008). The bulk of the Blässkranz Formation was described as a massive diamictite/breccia with carbonate clasts and limestones in shale (Korn & Martin 1959; Hartnady 1978; Miller 2008). Miller (2008) noted that the clast suite was dominated by dark, commonly oolitic, limestone with minor components of grey dolostone, chert, quartzite, and basement granite – the latter correlated with the Gamsberg Granite and Piksteel Granodiorite (basement in Fig. 3.1B). The upper Blässkranz contains volcanoclastic tuff interbedded with quartzite and shales (Hartnady 1978; Miller 2008). A glacial origin has been recognized for the Blässkranz via deep water mass flows and ice rafting (Miller 2008; Morris & Grotzinger 2023). The Tsabisis formation encompasses a lower white dolostone member, overlain by maroon shale and buff-orange limestone (Korn & Martin 1959; Hartnady 1978; Miller 2008). The lower dolostone member has been informally termed the Tsondab member and described in detail (Morris & Grotzinger 2023), correlated regionally and globally as a Marinoan-age (~635 Ma) cap carbonate, overlying the glaciogenic Blässkranz Formation (Hoffmann 1989; Miller 2008; Macdonald et al. 2009; Morris & Grotzinger 2023). The bulk of the overlying Kudu Nappe (Table 3.1) are rocks of the Noab Formation, consisting of thick bedded to massive dolomite, sandy dolomite, and intercalated quartzite, which occasionally show current ripples and is informally divided (Morris & Grotzinger 2023) into the stratigraphically discontinuous lower sedimentary breccia member and a laterally extensive mixed dolomite-clastic upper Noab member (Korn & Martin 1959; Hartnady 1978; Miller 2008). Also commonly included in the Kudu Nappe is the Klipbokrivier Formation, a unit dominated by shale and interbeds of carbonate breccia that has been interpreted to rest unconformably atop the Noab (Korn & Martin 1959; Hartnady 1978; Hoffmann 1989; Miller 2008). With the inverted age relationship, Hartnady (1978) correlated the Klipbokrivier Formation with the Remhoogte Formation, while Hoffmann (1989) correlated it with deep water deposits of Zebra Nappe and Nama Group.

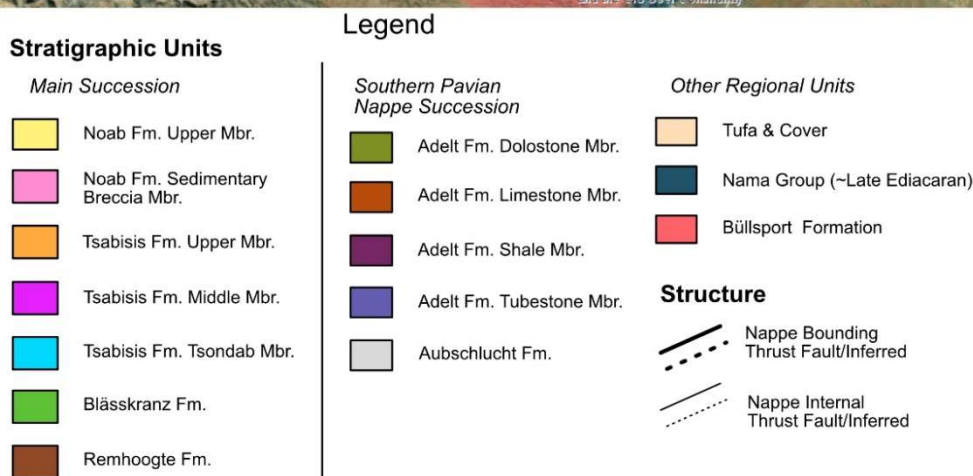
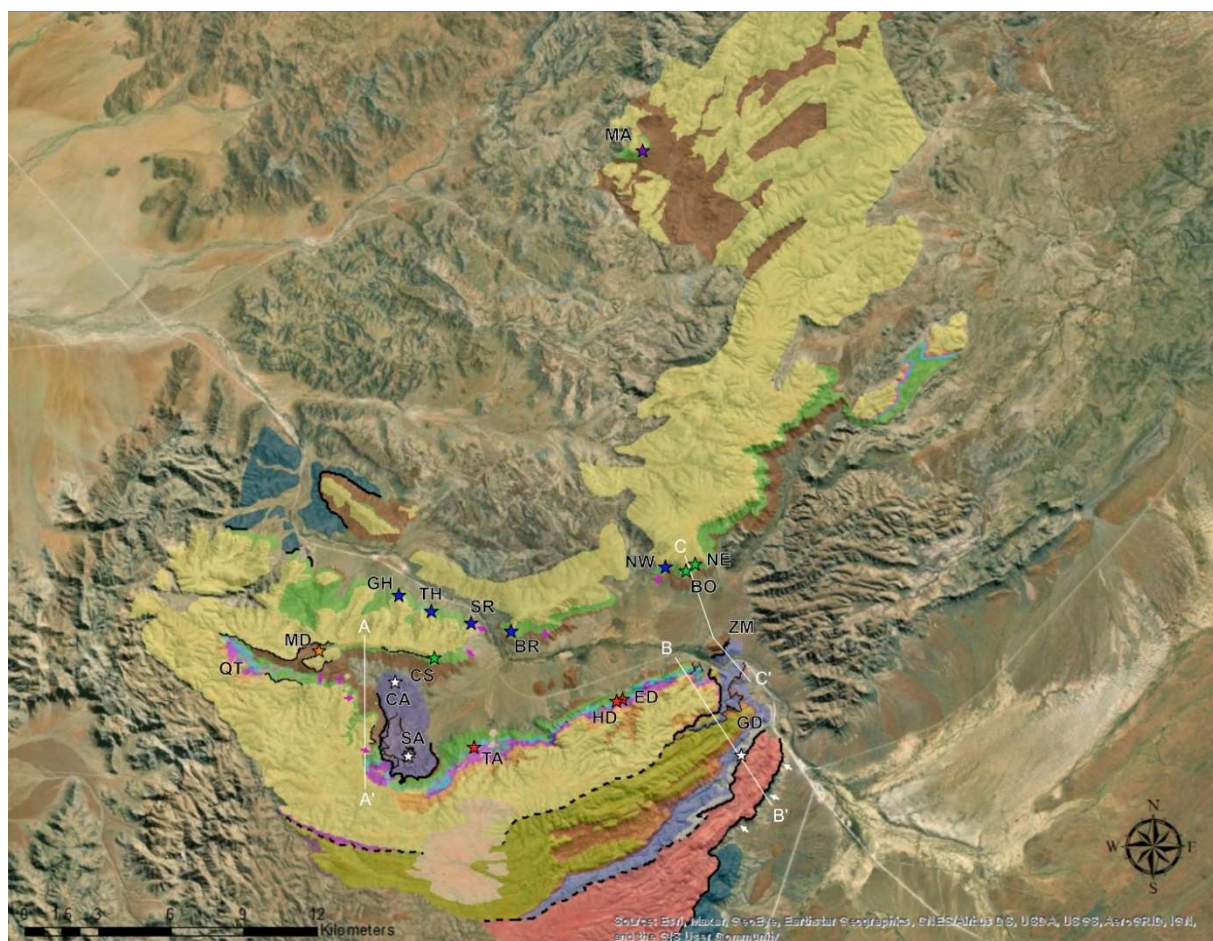
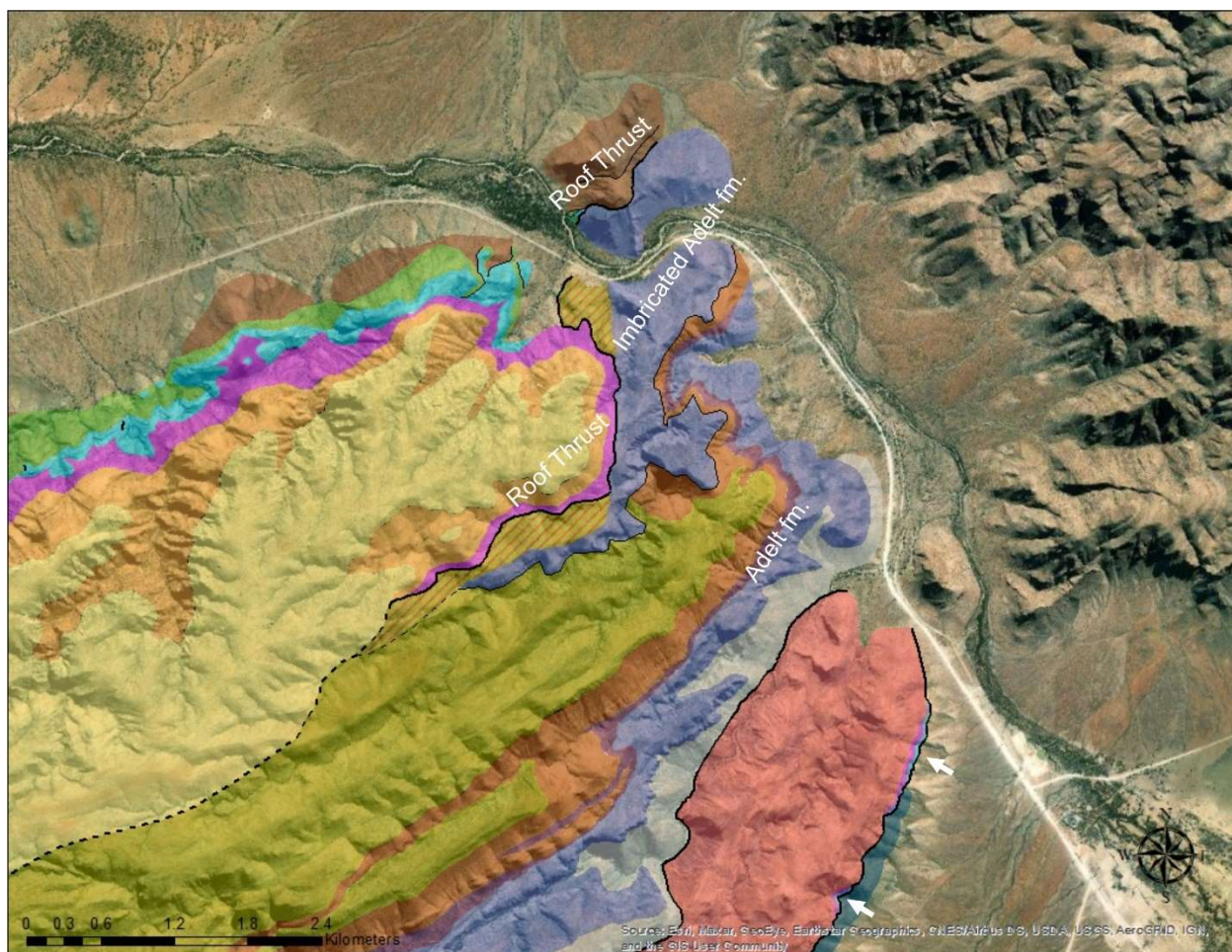


Figure 3.2. Geologic map of the study area within the Naukluft Mountains. Colored stars show the locations of the stratigraphic sections described in the text. Star colors represent the interpreted relative paleogeography for the rocks of the Northern Pavian-Kudu succession – cooler colors (purple, blue) represent more downdip localities, while hotter colors (orange, red) represent more updip localities, green represents intermediate platform positions. Representative sections are shown in Fig. 3.6; others are included in Supp. Fig. 3.2. White stars indicate the locations of the Southern Pavian Nappe sections shown in Fig. 3.6. White lines (A-A', B-B', C-C') show the profiles used with structural cross sections shown in Fig. 3.4. Given the range of shear intensities along the North

Pavian-Kudu contact, we have labeled the contact as a fault when there is evidence for tectonic truncation of underlying stratigraphic units. White arrows point to outcrops of the Tsondab member found exposed beneath the Bullsport Formation in the SE of the map. Magenta arrows point to outcrops of the laterally discontinuous sedimentary breccia member located at the base of the Noab Formation. Lithologic change within the Blässkranz Formation, coupled with structural complexities, complicate distinction between the Remhoogte Formation and Blässkranz Formation in the northernmost regions of the Naukluft Mountains. Therefore, outside of the well exposed MA locality, they are mapped together as Remhoogte Formation.

Figure 3.3. (next page) Detailed geologic maps over the GD and ZM region of the eastern field area. Symbols and lithostratigraphy colors identical to those in Fig. 3.2. White arrows point to outcrops of the Tsondab member found exposed beneath the Bullsport Formation. The thrust sheet labeled 'Imbricated Adelt fm' was previously mapped as the Noab Formation (Hartnady 1978; 1980), which was an important component of the tectonic model of out-sequence thrusting of the Northern Pavian Nappe over the Kudu Nappe. Our revised lithostratigraphy corrects the identity of this thrust sheet to that of the Adelt formation, which has a roof thrust contact with the overlying combined Northern Pavian and Kudu nappes and a thrust imbrication over another thrust sheet of the Adelt fm. to the southeast (Fig. 3.4; Fig. 3.5C; Fig. 3.11C). Additional detailed maps found in Supp. Fig. 3.1.



Stratigraphic Units

Main Succession

	Noab Fm. Upper Mbr.
	Noab Fm. Sedimentary Breccia Mbr.
	Tsabisis Fm. Upper Mbr.
	Tsabisis Fm. Middle Mbr.
	Tsabisis Fm. Tsondab Mbr.
	Blässkranz Fm.
	Remhoogte Fm.

Legend

Southern Pavian Nappe Succession

	Adelt Fm. Dolostone Mbr.
	Adelt Fm. Limestone Mbr.
	Adelt Fm. Shale Mbr.
	Adelt Fm. Tubestone Mbr.
	Abschlucht Fm.

Other Regional Units

	Tufa & Cover
	Nama Group (~Late Ediacaran)
	Büllsport Formation

Structure

	Nappe Bounding Thrust Fault/Inferred
	Nappe Internal Thrust Fault/Inferred

Structural inversion involving stratigraphically older Kudu Nappe rocks thrust over stratigraphically younger Northern Pavian Nappe rocks was proposed by Hartnady (1978; Fig. 3.1D). This interpretation was suggested by the following observations and inferences: a) clasts within the Blässkranz Formation that included oolitic dolomites, oolitic chert clasts,

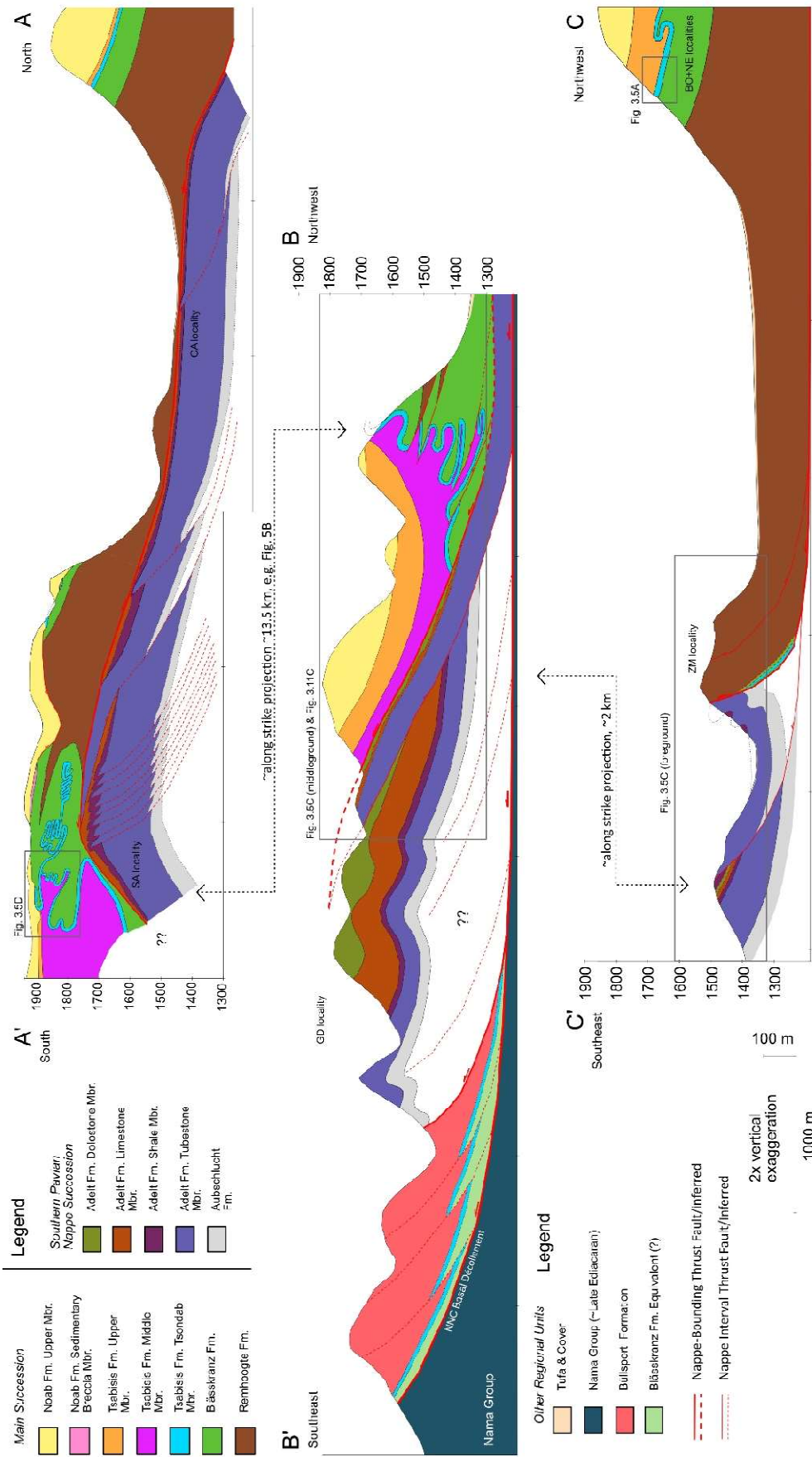
jasper fragments, and sandy dolomite, which Hartnady (1978) correlated to facies in the upper parts of the Noab and Büllsport formations, b) a ~10 m thick zone of deformed limestone marble between the Tsabisis Formation and Noab Formation, regarded as dedolomitized dolostone from the base of the Noab, and an entirely tectonic contact, c) structural relationships between the Northern Pavian and Kudu Nappes. In particular, Hartnady (1978) inferred that the Northern Pavian Nappe locally (GD and ZM localities in present study, Fig. 3.2; Fig. 3.3) is locally thrust over the Kudu Nappe, which Korn & Martin (1959) had mapped as Southern Pavian Nappe. Hartnady thus inferred a later, out-of-sequence thrusting event that deformed the earlier thrust wedge in which the Kudu Nappe had been thrust over the Northern Pavian Nappe (Fig. 3.1D).

The lithological similarity of gray dolostone (Tsondab member versus tubestone member) overlying a shale-dominated mixed *mélange* (Remhoogte-Blässkranz formations versus Aubschlucht Formation) lead Korn & Martin (1959) to interpret the northern and southern Pavian Nappes to be laterally equivalent (Table 3.1). These were then both correlated directly with the Zebra Nappe which were collectively, along with the rest of the Naukluft stratigraphy, correlated to parts of the Nama Group. Hartnady (1978) maintained correlation of the Southern Pavian Nappe with parts of the Zebra Nappe and Nama Group, but rejected the correlation via apparent lithological similarities between the dolostones and overall stratigraphic successions of the Northern Pavian and Southern Pavian nappes (Fig. 3.1D). The Southern Pavian Nappe overlies the Dassie Nappe by a thrust contact and the thick dolostone (tubestone member) is then overlain by the Kudu Nappe at a higher thrust contact (Hartnady 1978; 1980).

Five episodes of deformation were proposed resulting in a minimum southeastward displacement of 78 km (Hartnady 1978, Miller 2008). However, in most outcrops of the NNC rock fabrics record only one principal deformation phase and though there are some fabric elements that could indicate at least two episodes of deformation, such as a crenulation cleavage superimposed on earlier slaty cleavage within shales, these could also be consistent with a single deformational episode of changing boundary conditions and anisotropies in the rock (Hartnady 1978, pg. 168-169). Importantly, the five deformational episodes proposed by earlier work are defined by tectonostratigraphic relationships based on correlation of

stratigraphic units, and the assertion that all depositional unconformities were driven by tectonic processes (Hartnady 1978), rather than overprinting tectonic fabrics that might indicate differing vergence history, for example. The work of Morris and Grotzinger (2023) and Quinn (thesis; et al., in prep) indicates that unconformities in strata of the NNC may be driven by relative sea level changes unrelated to orogenic activity. Therefore, the history of deformation developed by Hartnady (1978) depends primarily on the lithostratigraphic and structural relationships between the Southern Pavian, Northern Pavian, and Kudu nappes, along with the Zebra Nappe and its correlation to the Nama Group. Quinn (thesis; et al., in prep) rejected the Zebra Nappe – Nama Group correlation and simplified the deformational history to two episodes, pending assessment of the Northern Pavian-Kudu contact, with the first episode of southward thrusting building the entire nappe wedge and a second event that directed southeast vergent structures in the Zebra Nappe, as the NNC was thrust over the Nama Group. Only two episodes of deformation would be consistent with the internal fabrics of the nappes, including those observed by Hartnady (1978). The present work in part focuses on testing Hartnady's (1978, 1980) proposed lithostratigraphic correlations and proposed tectonic contacts between the nappes to consider whether the five episodes are deformation is necessary to explain the history of the NNC or if it can be simplified.

Figure 3.4. (next page) Three structural cross sections along transects indicated in Fig. 3.2. Colors of the stratigraphic units are the same as in Fig. 3.2. Cross sections have the same vertical and lateral scales with 2x vertical exaggeration. Dashed arrows point to approximate along-strike projections of structure between A-A' and B-B' indicating the comparable folding of the Tsondab member, and between B-B' and C-C' highlighting the thrust imbrication of the Adelt formation seen along both profiles. The cross sections illustrate the larger-scale and relatively well exposed structure expressed primarily by south-vergent thrusts and asymmetric folds. At the outcrop scale zones of intense deformation, particularly within the Tsondab and tubestone members, show meter-scale folds and faults that are too small scale to illustrate in these cross sections (e.g. Fig. 3.5D). Inset boxes indicate the field pictures of the corresponding figure. Approximate locations of named localities are shown along the cross sections; the GD locality spans the entire B-B' cross section.



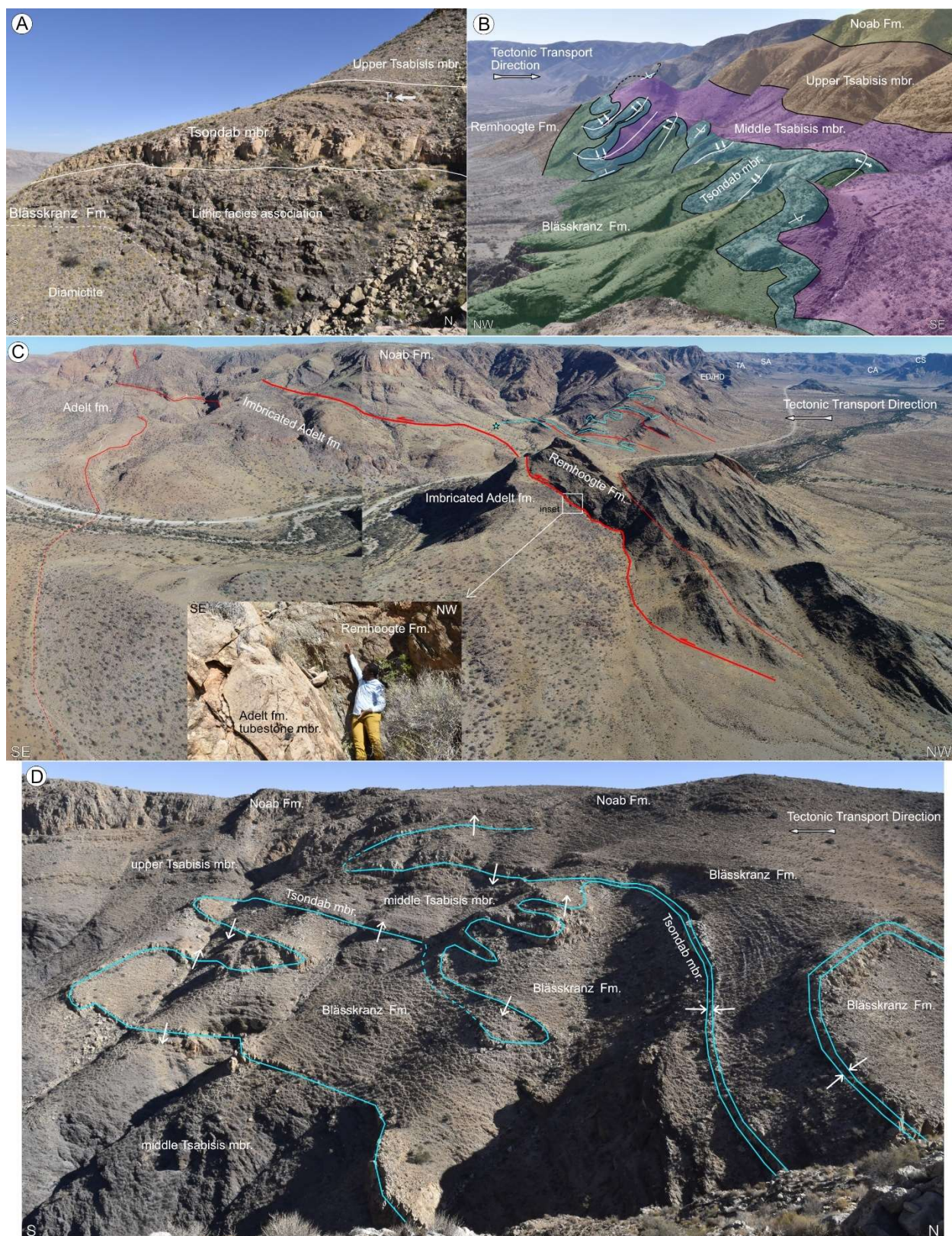


Figure 3.5. (A) Outcrop view of the buff colored Tsondab member (Tsabisis Formation) at the BO locality. Arrow points to ~2 m tall person for scale. The Blässkranz Formation shows the bedded

lithic sandstone facies overlying the smooth slopes of the more massive diamictite facies. Overlying the Blässkranz Formation is the sharp lower contact of the Tsondab member. (B) Outcrop view of the ED and HD localities (Supp. Fig. 3.1; Supp. Fig. 3.2). Representative of the structural style – the Tsondab member is often strongly folded, with tight to isoclinal angles and overturned orientations. Units colored to be consistent with Fig. 3.2. (C) View of the ZM hill in foreground (southern portion of Fig. 3.4C-C'), with inset showing the tectonic roof thrust contact (thick red line) between the light gray Adelt tubestone member and the rusty green Remhoogte Formation – this contact has a dip direction of 317°, and dip of 75°. The middleground slopes across the road show the GD outcrop (Fig. 3.4B-B') with the light blue line showing the heavily folded and thrustured Tsondab member and light blue star indicating the last exposure of the Tsondab member before cover obscures the local contact with the Adelt fm. The thinner red lines show the traces of nappe-internal thrust faults. In the upper right background, the locations of several other visible localities are labeled for context. (D) Heavily folded Tsondab member in the SA region (southern portion of Fig. 3.4A-A'), where the folded limbs of a syncline converge to isoclinal and have been subsequently folded into higher-order fold structures. The mauve colored rhythmite of the Tsondab member and overlying middle Tsabisis shales have been sheared out and appear to accumulate to the south.

3. Methods

A lithostratigraphic and structural framework was developed for the Southern Pavian Nappe, Northern Pavian Nappe, and Kudu Nappe, along with the relevant components of the peripheral Dassie Nappe. This framework is based on detailed mapping and measurement of structural features (e.g. Fig. 3.5). However, also critical was the detailed and extensive analysis of sedimentary facies and sequence stratigraphic stacking patterns to distinguish between stratigraphic and tectonic contacts and constrain feasible lateral correlations between stratigraphic units (e.g. Fig. 3.6). Mapping focused on the central portion of the Naukluft Mountains, specifically within the Büllsport, Blässkranz, and Arbeit Adelt farms, along with Farm Noab in the northern Naukluft (Supp. Fig. 1; Korn & Martin 1959; Hartnady 1980). Supplementary work was conducted in Zais (northwest), Tsabisis Oos (northeast), and Die Valle (west) farms (Korn & Martin 1959; Hartnady 1980). 25 detailed stratigraphic sections (Fig. 3.6 & Supp. Fig. 3.2) and ~1300 structural attitudes were measured across the field area; localities with stratigraphic sections are shown in Figure 3.2. Three structural cross sections were constructed (Fig. 3.4), along with the geologic map (Fig. 3.2; Fig. 3.3; Supp. Fig. 3.1), to illustrate the structural relationships between the nappes and the changes in style of deformation across the strike of the thrust wedge.

Samples for facies analysis and C and O chemostratigraphy were collected while logging stratigraphic sections. Polished slabs and 82 thin sections were used to assist in lithofacies

and diagenetic analysis. 254 samples were analyzed for carbon and oxygen isotopic values, primarily to assist with the lithostratigraphic correlation of units. Dolostone and limestone without secondary veins or obvious alteration were targeted for sampling. Carbon and oxygen isotopes were analyzed using an automated carbonate preparation device (KIEL-III) coupled to a gas-ratio mass spectrometer (Finnigan MAT 252) at the University of Arizona Environmental Isotope Laboratory. Powdered samples were reacted with dehydrated phosphoric acid under vacuum at 70°C. The data of $\delta^{13}\text{C}$ and $\delta^{18}\text{O}$ were calibrated to VPDB (Vienna Pee Dee Belemnite) and external analytical precision is ± 0.08 ‰ (1σ) for $\delta^{13}\text{C}$ and ± 0.10 (1σ) for $\delta^{18}\text{O}$. Using published correction factors (Rosenbaum & Sheppard 1986; Swart et al. 1991), 1.43414 ‰ was subtracted from the $\delta^{18}\text{O}$ values of dolomite samples to adjust for acid fractionation during analysis. No correction factors were necessary for $\delta^{13}\text{C}$ values.

Five sandstone bearing samples (described in subsection 6.2.1) were collected and analyzed for detrital zircon analysis to consider provenance and age relationships. Samples were processed and analyzed at by the Arizona LaserChron Center. Zircons are extracted and separated by standard methods of crushing and grinding, followed by a Wilfley table, heavy liquids, and a Frantz magnetic separator. Grains are then mounted with fragments or loose grains of Sri Lanka, FC-1, and R33 zircon crystals, which are used as the primary standards. Grains were polished and then imaged by back-scatter electrons, cathodoluminescence and scanning electron microscope for locating analysis pits in optimal locations. U-Pb geochronologic analyses were conducted by laser ablation inductively coupled plasma mass spectrometry (LA-ICPMS). Methods for U-Pb geochronology are described in Gehrels et al. (2006, 2008), Gehrels and Pecha (2014), Pullen et al. (2018), and Sundell et al. (2021). With an energy density of ~ 5.6 J/cm² and repetition rate of 7 Hz, laser ablation goes for ~ 15 seconds to a depth of ~ 15 microns. Following analysis, data reduction is performed with a Python decoding routine and a MATLAB program (AgeCalcML; v GGmod68e; Hartman et al. 2017). This produces ratios for common-Pb-corrected 206/238, 206/207, and 208/232, and resulting ratios of standards are compared with known values, with analyses rejected if differ from known values by more than 5%. Ages and uncertainties are calculated for unknown analyses with these ratios; a “Best Age” is determined for each analysis with the

206/238 age for < 900 Ma ages and the 206/207 age for > 900 Ma ages. Analyses are automatically filtered based on default cutoffs for uncertainty, discordance, reverse discordance, ^{204}Pb counts, ^{235}U intensity, and on-peak signal stability. For ‘Abs Fm. Congl’ sample, of the 315 U-Pb laser analyses 265 passed the standard data reduction filters to be included in the final dataset; for ‘Tsondab SS’ 140 passed out of 165, for ‘Noab Sed. Breccia’ 257 passed out of 317, for ‘Noab Sec. MA 29 m’ 277 passed out of 315, and for ‘Plateau Top SS’ 275 passed out of 315.

4. Nappe Lithostratigraphy

The stratigraphy of the Northern Pavian Nappe indicates a northward facing direction (polarity) of the depositional basin (Morris & Grotzinger 2023). The stratigraphy of the overlying Kudu and Dassie nappes appear to conform with this facing direction, but a depositional facing direction is not recognized within the Southern Pavian Nappe. The following sedimentological and stratigraphic analysis informs the lithological correlation of units between tectonic nappes and the unit contacts.

4.1 Northern Pavian Nappe Lithostratigraphy

In ascending order the Northern Pavian Nappe is composed of the Remhoogte, Blässkranz, and Tsabisis formations, with the Tsabisis Formation informally divided into the Tsondab member, middle member, and upper member (Table 3.1).

4.1.1 Remhoogte Formation

The Remhoogte Formation is predominantly composed of shale ranging in color from green to rusty brown to steel blue (Fig. 3.7A). Ductile deformation of the shale limits accurate estimation of stratigraphic thickness, but measurements show a few hundreds of meters thick, up to ~400 m. In addition to the shale, there are minor beds (cm to dm scale) of very fine to fine grained gray quartz sandstone or brown limestone. The top of the Remhoogte Formation is defined by a resistant ledge of carbonate breccia ranging from 8 to 22 meters thick, sometimes parted by a few meters of green shale, with clasts reaching up to boulder in size and varying between angular and rounded (Fig. 3.7B). In the central region of the Naukluft

the lower portion of this carbonate package tends to be a clast-supported conglomerate of largely dolomitic composition, along with minor clast components of limestone and silica both of which often show oolitic grains. The upper portion is composed of dark limestone that is typically heavily deformed but shows sheared limestone clasts with indication of partial dolomitization and silicification along with minor relatively undeformed dolostone clasts (Fig. 3.7B). In the northern portions of the Naukluft, both the limestone and dolostone portions of the resistant ledge are observed but their relative order is inconsistent. In the ~CS locality, ~15-20 meters below the carbonate breccia is a single cobble-sized granitic limestone surrounded by shales (Fig. 3.7A).

Lacking any shallow water sedimentary features, the shale-dominated Remhoogte facies represent deep water deposition with the shales accumulating as background settling of muds from suspension while the sandstone and brown limestone beds indicate deposition as fine grain turbidites (McIlreath & James 1978; Whalen et al. 2000). The thick package of carbonate breccia records higher energy deposition of a debris flow, presumably from the erosion or collapse of a proximal carbonate platform (James 1981; Lowe 1982; Hiscott & James 1985; Whalen et al. 2000). The granitic limestone is surrounded by shale that does not preserve primary lamination. This precludes us from conclusively identifying it as ice rafted debris, however, this interpretation is suggested by the extrabasinal sourcing necessary for a granitic cobble to be deposited in this unit.

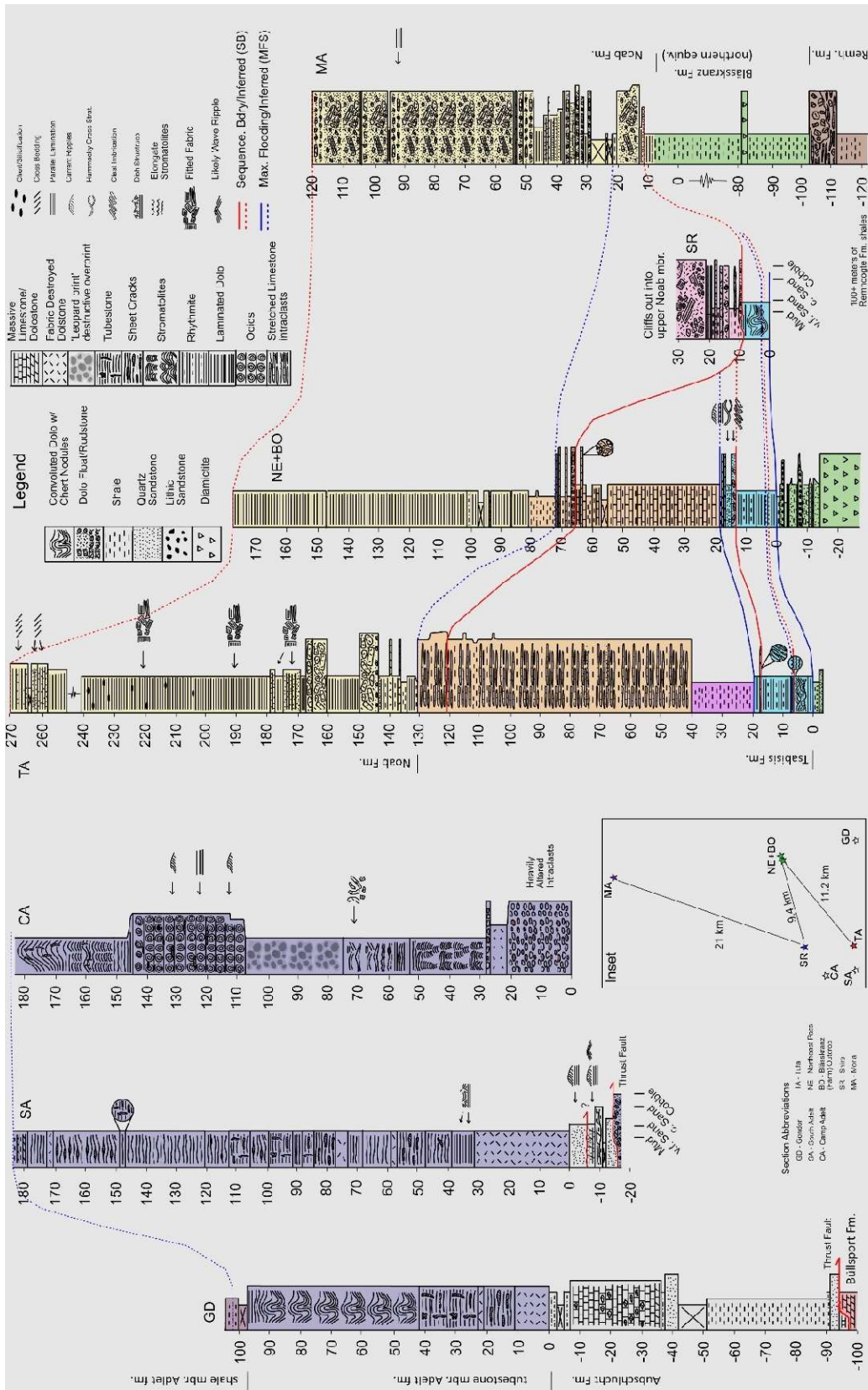


Figure 3.6. Measured stratigraphic sections, three on the right (GD, SA, CA) span the Aubschlucht Formation and tubestone member of the Adelt formation, along with the beginning of the upper shale member of the Southern Pavian Nappe. The four on the right show parts of the Remhoogte, Blässkranz, Tsabisis and Noab formations, all part of the Northern Pavian and Kudu Nappes. Sections are positioned from updip (left) to downdip (right). As considered in the text, the Southern Pavian units do not appear to represent an updip equivalent to the Northern Pavian or Kudu nappe stratigraphy. Colors of the stratigraphic units are the same as Fig. 3.2, with red and blue lines respectively representing sequence boundaries and maximum flooding surfaces. Inset shows positions and distances between the sections. NE+BO is a composite section between the two closely spaced localities (~0.5 km) – the Blässkranz Formation below 0 meters, and Tsabisis Formation between 19 and 27 meters from the BO locality as these portions are not well exposed at NE, the rest of the NE+BO composite section is based on the NE locality.

4.1.2 Blässkranz Formation

The Blässkranz Formation, approximately 80 m thick, is dominated by a diamictite facies consisting of matrix-supported and very poorly-sorted clasts ranging from coarse sand to boulder in size. Clasts are dominated by tan dolostone and gray limestone with abundant clasts of ooid grainstone. Rare quartzite and granitic clasts also are present. The Blässkranz Formation sharply overlies the Remhoogte Formation, and its base is characterized by several meters of medium to gravel-sized quartz sandstone, intercalated and intermixed with green shale and diamictite clasts. In updip locations (TA, NE+BO in Fig. 3.2 & Fig. 3.6) the upper portion of the Blässkranz Formation is distinguished by an intercalated succession of lithic pebbly sandstone, quartz sandstone, and shale, which contains outsized rock fragments and uncommon interbeds of the diamictite facies (for more details see Morris & Grotzinger 2023).

The diamictite facies records the till of a glacial grounding line and/or resedimented debris flows of till characteristic of ice-contact submarine fans (Powell 1981; Lowe 1982; Lønne 1995; Shen et al. 2021; Morris & Grotzinger 2023). The predominance of carbonate clast composition suggests subglacial erosion of a carbonate platform, though its provenance is unknown. Similarly, the quartzite and granitic clasts indicates glacial erosion of extrabasinal cratonic sources.

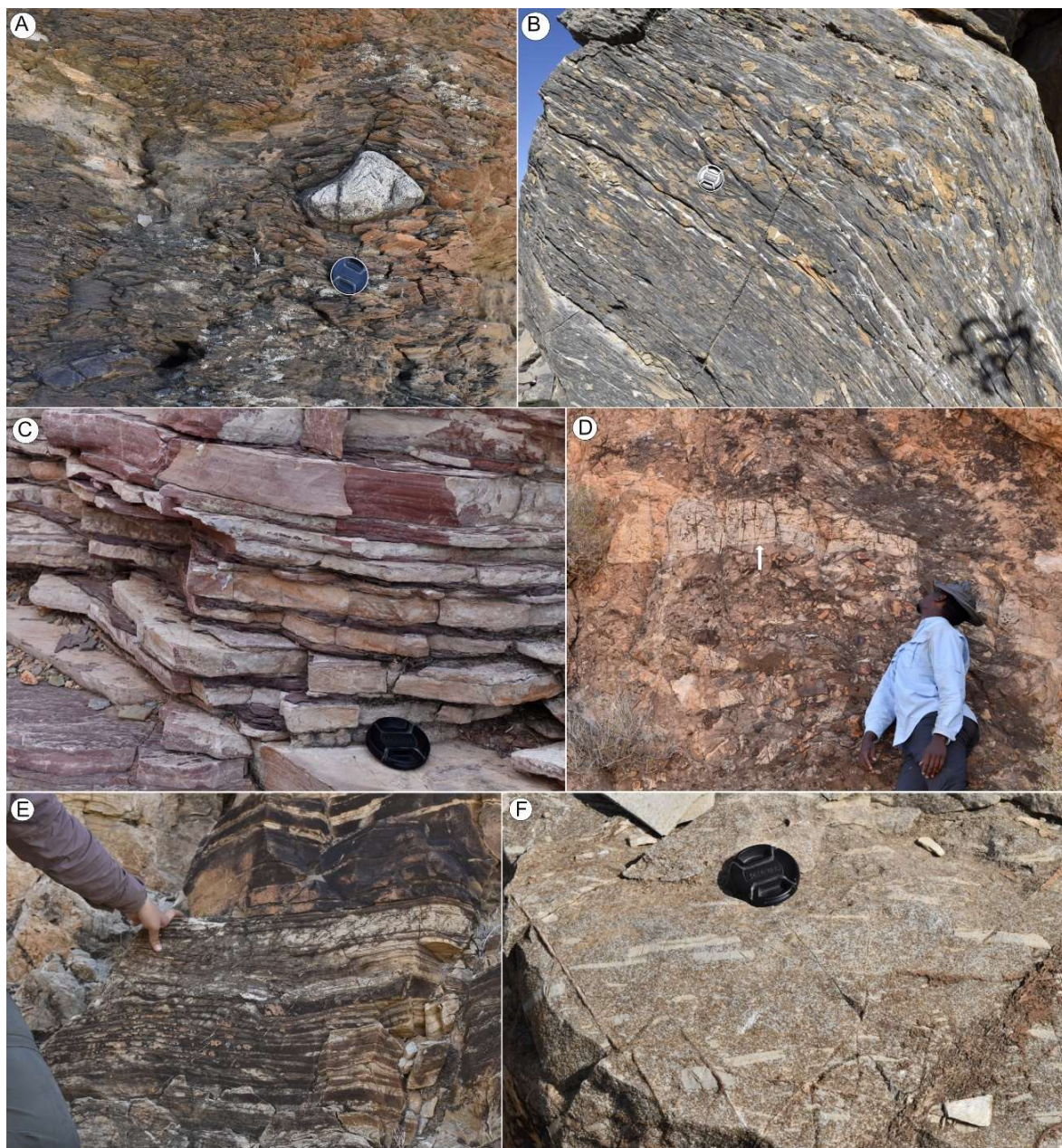


Figure 3.7. (A) Representative cleaved shale of the Remhoogte Formation with granitic limestone, which may have been tectonically flattened, ~15-20 meters below the top of the formation. Lens cap is 5.5 cm in diameter. (B) Top of Remhoogte Formation carbonate breccia at MA locality – ductile deformation of dark limestone with flattened clasts of more competent tan dolostone. Lens cap is 5.5 cm in diameter. (C) Rhythmite facies consists of mauve dolostone beds parted by laminae of maroon shale. Lens cap is 5.5 cm in diameter. (D) Sedimentary breccia facies with up to meter-scale angular blocks of light-toned laminated dolostone and silicified oolite. This locality has breccia abruptly overlying diamictite of the Blässkranz Formation. Arrow points to the center of a clast that reaches ~2 meters in length. This locality is ~1.5 km to the west-northwest of the BR locality (24° 05' 34.44" S, 016° 15' 20.95" E; Supp. Fig. 1F). (E) Thinly to thickly interbedded laminated dolostone and coarse sandstone of northern Noab Formation (MA locality). (F) Flat pebble and angular intraclasts of laminated dolostone within a matrix of coarse to very coarse quartz sands of northern Noab Formation (MA locality). Lens cap is 5.5 cm in diameter.

4.1.3 Tsabisis Formation, Tsondab member

Abruptly overlying the Blässkranz Formation is the Tsondab member of the Tsabisis Formation, a cream to mauve colored dolostone unit up to 21 meters thick (Fig. 3.2; Fig. 3.6; Supp. Fig. 1; Supp. Fig. 2). In downdip localities Blässkranz diamictite transitions into a sandy dolostone containing outsized clasts of both carbonate and granite composition overlain by laminated dolostone. In the northernmost (downdip) locality (Fig. 3.2, MA) the Blässkranz Formation is overlain by the sandy dolostone succession of the Noab Formation; the Tsabisis Formation is absent (Fig. 3.10C). The lower part of the Tsondab Member is dominated by the laminated dolostone, but in the updip areas contains a laterally persistent succession of stromatolites (Fig. 3.6, TA). The laminated dolostone is overlain by mauve colored carbonate-shale rhythmite (Fig. 3.7C). Near the top of the Tsondab member lenses of tabular intraclast conglomerate occur in association with lenses of hummocky cross stratified brown quartz sandstone. These facies transition into the middle Tsabisis member in the updip localities, suggesting backstepping of the local carbonate source. See Morris and Grotzinger (2023) for more details.

The Tsondab member of the Tsabisis Formation represents a carbonate ramp whose facies distributions reflect changing sea level and variations in siliciclastic influx (Morris & Grotzinger 2023). The transition from the backstepping sandstones of the uppermost Blässkranz Formation through the sandy and laminated basal dolostone facies represents a transgression with a retreat of the siliciclastic clastic source. The overlying facies of the Tsondab member indicate two distinct intervals of regression (sequence boundaries, Fig. 3.6; Morris & Grotzinger 2023).

4.1.4 Tsabisis Formation, middle member

The middle member of the Tsabisis Formation is composed of maroon shale with rare interlaminae of pale green shale. Extensive ductile deformation of the shale makes estimates of stratigraphic thickness difficult, with lateral thickness variations due to nearby tight to isoclinal folding of the Tsondab Member resulting in localized thicknesses of hundreds of meters (Fig. 3.4, A-A' & B-B'; Fig. 3.5B). Yet, considering the average of

several transects in areas of varying levels of deformation, for stratigraphic purposes we estimate the upper bound of the middle Tsabisis member's thickness to be approximately 20 meters. The middle member of the Tsabisis Formation is limited to updip localities (Fig. 3.2, GD, ED, TA, QT) and appears to pinch out completely by intermediate localities (MD, NE, BO, CS) as the dolostone of the Tsondab Member is directly overlain by the upper member limestone.

The shales of the middle member of the Tsabisis Formation were deposited by background settling from hypopycnal plumes or fine-grained turbidites in deep waters (Morris & Grotzinger 2023). The maroon versus pale green colors of the shale reflects oxidation state of the mudstone either during deposition or, more likely, by later diagenesis (e.g. Myrow 1990).

4.1.5 Tsabisis Formation, upper member

The upper member of the Tsabisis Formation is composed primarily of pale orange to maroon colored limestone, commonly interbedded with dark shale. Intraclasts of limestone, and rarely dolostone, are especially common in the updip localities (Fig. 3.2, TA; Fig. 3.6) and range in size from cm to meter-scale in diameter (Fig. 3.10A). Common internal folding of upper member limestones suggests that the unit's thickness has been locally modified, but in updip regions (TA) it's measured thickness is ~100 meters. It depositionally thins to 20 – 50 meters by the intermediate localities (CS, NE, BO), and pinches out completely by the downdip locations (SR, BR, TH, GH). The lower contact with the middle Tsabisis member is conformable showing progressive intercalation of the shale with limestone beds of increasing thickness (Fig. 3.2 & Fig. 3.6, TA locality).

Alternating fine-grained limestone and shale deposition represents mixed carbonate-siliciclastic sedimentation in a distal deep-water slope setting (Morris & Grotzinger 2023). The coarse intraclast deposits likely represent sediment gravity flows triggered by storms and/or slope failure. The finer grained carbonate and shale deposition shows lower energy allochthonous sedimentation by gravitational settling or turbidites from updip sources.

4.3 Kudu Nappe Lithostratigraphy

The Kudu Nappe is composed of the Noab Formation which we informally divided into the lower sedimentary breccia member and the upper member (Table 3.1). Previous work had suggested that the Klipbokrivier Formation overlies the Noab Formation, but this was via stratigraphic correlation that our work does not support. The Noab Formation defines the topographically highest level of the Naukluft mountains with no evidence of being overlain by younger Ediacaran strata, although it is possible that remnants of Permian rocks may be scattered across the top of the plateau (section 6.2; Hartnady 1980).

4.3.1 Noab Formation, sedimentary breccia member

The sedimentary breccia member of the Noab Formation is a laterally discontinuous unit that frequently incises the Tsabisis and even the upper Blässkranz formations, locally reaching at least 15 meters in thickness (Fig. 3.2; Fig. 3.6, SR; Supp. Fig. 3.2, SR) and structurally conforming with the rest of the overlying Noab Formation. The unit consists of clasts derived from the erosion of older strata that are both matrix and clast supported and range from centimeters to meters in diameter (Fig. 3.7D). Clasts include laminated dolostone, cream and mauve colored rhythmite, silicified oolite, massive gray dolostone, and rare clasts of quartzite and granite. See Morris and Grotzinger (2023) for further details.

This facies is interpreted as a set of stacked or amalgamated debris flows deposited following incision and reworking of underlying stratigraphic units (Morris & Grotzinger 2023). Clasts were emplaced through remobilization of the underlying Tsabisis and Blässkranz formations, perhaps triggered by base level fall across a carbonate platform during a lowstand, though the extent of relative sea level change remains unclear given the lack of evidence for subaerial exposure.

4.3.2 Noab Formation, upper member

The upper member of the Noab Formation, which makes up the majority of the formation, is comprised of sandy dolostone. This unit weathers to form conspicuous cliffs and forms the uppermost plateau that rims the northern two thirds of the Naukluft Mountains. Being the uppermost unit, the thickness estimate of 130 meters is a lower bound. In southern locations the Noab Formation (south of GH) is predominantly composed of finely laminated dolostone

with minor components of silt to medium sized intermixed quartz grains, with cross bedding in the upper parts of the formation (Fig. 3.6, TA) and cm to dm-scale intraclasts, commonly showing fitted fabrics (Fig. 3.6, TA). In the more northern locations (Fig. 3.2, MA), the grain size of the quartz sands increases, ranging between medium to very coarse sand and the proportion of quartz greatly increases (MA locality in Fig. 3.2 & Fig. 3.6). Quartz sandstone with planar lamination and rare cross bedding occurs in northern localities (Fig. 3.7E) but also forms the sand matrix of dolostone intraclasts beds (Fig. 3.7F). Beds of maroon or green shale are intermittently intercalated with the other lithologies, particularly in the lower portions of the Noab Formation. See Morris and Grotzinger (2023) for additional details.

The laminated fine-grained carbonates are likely derived from an updip carbonate source (McIlreath & James 1978; James 1981; Grotzinger 1986) and deposited below wave base via hypopycnal plumes or fine grained turbidites (e.g. Creveling et al. 2016). The breccia intraclasts, with common fitted fabrics, are indicative of local remobilization of the *in situ* laminated dolostone into debris flows (Lowe 1982; Grotzinger 1986). These features suggest a deep-water slope environment where the debris flows may be triggered by gravitational instability (McIlreath & James 1978; Whalen et al. 2000). The upper Noab member shows similar slope deposition to the upper Tsabisis member, but with dolostone and a higher proportion of siliciclastic silts and sands that may indicate further highstand progradation of the siliciclastic source into the platform (Whalen et al. 2000).

4.4 Klipbokrivier Formation

The stratigraphy mapped as the Klipbokrivier Formation by previous workers (Korn & Martin 1959; Hartnady 1978; 1980) was investigated within the northern Noab Farm region. It is primarily composed of dark shale and carbonate breccia beds that are indistinguishable from the Remhoogte Formation in the same region. In the well-preserved MA location (Fig. 3.2), an upward succession of dark green shale is overlain by a ~9 meter bed of limestone and dolostone breccia, this is followed by 20 meters of shale, then two meters of diamictite with carbonate clasts, succeeded by several 10s of meters of shale before there is a progressive stratigraphic contact with the sandy dolostone base of the Noab Formation (Fig. 3.2; Fig. 3.6; Fig. 3.10C). This outcrop has previously been mapped as the Klipbokrivier

Formation that has been overthrust by the Noab Formation (Hartnady 1978; 1980), however, it appears to simply be the northern equivalents of the Remhoogte and Blässkranz (with more limited diamictite deposition) stratigraphically overlain by the Noab Formation with the Tsabisis Formation absent, marking a pinchout of those facies (Fig. 3.10C). We also found elsewhere in the Noab Farm area that previously mapped thrust contacts (Hartnady 1978; 1980; Hoffmann 1989) are gradual stratigraphic transitions between the northern equivalents of the Remhoogte and Blässkranz formations with the Noab Formation. Furthermore, there is no evidence of the Klipbokrivier Formation overlying the top of the Noab as might be predicted if the Klipbokrivier was stratigraphically younger than the Noab. Within the Noab Farm region, the Northern Pavian and Kudu nappe stratigraphy of the northern Naukluft can be fully accounted for by a stratigraphic succession of the northern extensions of the Remhoogte, Blässkranz, and Noab formations with no need for the Klipbokrivier Formation to exist as a shale unit overlying the Noab Formation within the Kudu Nappe.

4.5 Dassie Nappe Lithostratigraphy

The Dassie Nappe is composed entirely of the Büllsport Formation.

4.5.1 Büllsport Formation

The Büllsport Formation, ~200-300 meters thick (Korn & Martin 1959), is composed of variably interbedded buff-orange to mauve limestone, maroon shale, and tan dolostone. It also contains laterally discontinuous lenses of gray fine grained quartz sandstone finely interbedded with maroon shale, showing mud cracks, wave ripples, current ripples, and cross bedding. The facies of the Büllsport Formation broadly suggests a mixed carbonate-siliciclastic platform that, at least occasionally, shallowed to the fair-weather wave base recorded by the wave ripples, or even became subaerially exposed. In the southeast range front of the Naukluft Mountains, the Büllsport Formation is found to overlie an outcrop of the Tsondab member of the Tsabisis Formation (Fig. 3.4B-B'). Though the quality of exposure was limited, it appears that the contact between the Tsondab member and Büllsport Formation is stratigraphic, which would support previous inferences (Korn & Martin 1959; Hartnady 1978) that the Büllsport Formation is a southern stratigraphic equivalent to the

Noab Formation. The sedimentologic contrast between the two correlative units suggests the Büllsport was deposited in a more depositionally updip paleogeographic position.

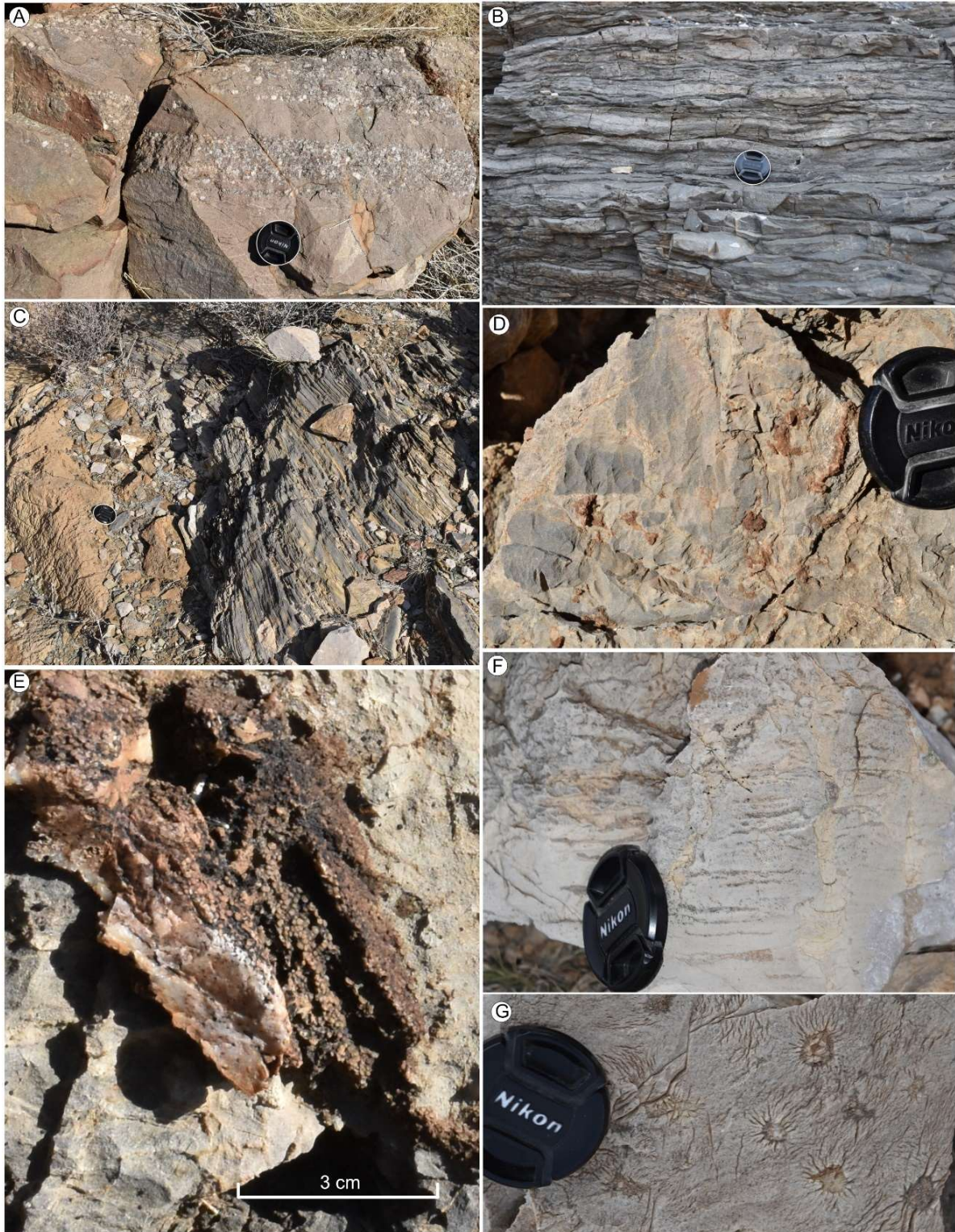


Figure 3.8. (A) Quartz sandstone and pebble conglomerate of Aubschlucht Formation in GD area. Lens cap is 5.5 cm in diameter. (B) Thin lenticular beds of fine grained sandstone beds of Aubschlucht Formation in SA area. Lens cap is 5.5 cm in diameter. (C) Dark limestone of Aubschlucht Formation on right, abruptly overlying the tan dolostone of the Büllsport Formation by a thrust fault (GD area). Lens cap is 5.5 cm in diameter. (D) Dark gray dolostone intraclast facies of the lower portions of the tubestone member, Adelt formation. Lens cap is 5.5 cm in diameter. (E) Coarse grained silicified ooid grainstone. Ooids are present in surrounding gray dolostone; their identification is enhanced by silicification. Lower tubestone member of Adelt formation. Lens cap is 5.5 cm in diameter. (F) Cross sectional view of tubestone facies. Internal fill of fine dolostone sediment. Lens cap is 5.5 cm in diameter. (G) Plan view of tubestone facies. Lens cap is 5.5 cm in diameter.

4.6 Southern Pavian Nappe Lithostratigraphy

The Southern Pavian Nappe is composed of the lower Aubschlucht Formation and the overlying Adelt formation. The Adelt formation is informally divided, in ascending order, into the tubestone, shale, limestone, and dolostone members (Table 3.1).

4.6.1 Aubschlucht Formation

The Aubschlucht Formation, up to 90 meters thick, is the lithologically heterogeneous and laterally variable unit that underlies the Adelt formation at the base of the Southern Pavian Nappe (Fig. 3.6). Quartz sandstones are the most distinctive facies of the Aubschlucht Formation. In the SA region, sandstones are greenish gray in color, very fine to fine grained, in successive meter-thick intervals of thin lenticular beds with current ripples and parallel laminations (Fig. 3.6; Fig. 3.8B). The GD region quartz sandstones are fine sand to pebble clast-supported conglomerate with a gray to rusty brown color, a minor component of feldspar grains (~5%), and thin to very thick bedding (Fig. 3.8A). Interbedded in varying proportions is dark green shale, gray to brown siltstones, sometimes sandy tan dolostone, and dark limestone (Fig. 3.6; Fig. 3.8C). Wave ripples are observed in the sandy tan dolostone (Fig. 3.6). Transitions between the sandy tan dolostones and dark limestones are often gradual with lenses of the two lithologies intimately intercalated.

The formation broadly represents a mixed carbonate-siliciclastic platform that at least occasionally shallowed to wave base and had influxes of quartz grains up to pebble in size, suggesting that it was relatively proximal to a shoreline and may have been intermittently fluvial.

4.6.2 Adelt formation, tubestone member

The informally defined Adelt formation, up to ~200-300 meters thick, has 4 members. The most distinctive member is the lowermost gray-colored tubestone member which is 97 meters thick at the GD locality (Fig. 3.6), while at the SA and CA localities is 170-180 meters thick. However, internal thrust faults are common in the CA-SA region (Fig. 3.4A-A'; Supp. Fig. 1C) and fabric destructive recrystallization of the dolostone can make their identification challenging, therefore structural repetition may be present, and true stratigraphic thickness may be less than what is documented there. The SA and GD localities have loosely similar successions (Fig. 3.2; Fig. 3.6). In some outcrops, when traced laterally, the massive highly recrystallized dolostone shows the primary facies to be coarse grained ooid grainstone (Fig. 3.8E), which is only visible when preserved by local silicification, and a dark gray dolostone intraclast facies, typically clast supported (Fig. 3.8D). Above this ambiguous strata is a facies of laminated dolostone, with common laminae-parallel sheet cracks filled with dolomitic spar. This is broadly succeeded by laminated dolostone that contains both sheet cracks and cm-scale spar- or sediment (10-30 microns)-filled tubes (tubestone) (Fig. 3.8F, G; *sensu* Cloud et al. 1974; Corsetti & Grotzinger 2005; Bosak et al. 2013). Tubestone facies have not been observed in any other units of the NNC. The GD locality shows a simple succession of dolostone passing upward from sheet cracks to sheet cracks and tubestone, while the SA has multiple iterations of both facies associations (potential thrust repetitions). In both cases the upper portions of the Adelt formation is dominated by laminated dolostone, sometimes showing convolute bedding (Fig. 3.9A); its upper contact is conformable and marked by interbedding with the overlying shale member of the Adelt Formation (Fig. 3.9B). The CA locality (Fig. 3.2; Fig. 3.6) lacks an exposed upper contact and its upper half shows a succession of (largely silicified) ooid grainstone, followed by meters-scale domal stromatolitic mounds with internal cm-scale stromatolites and tubestone interbedded with laminated dolostone containing sheet cracks. However, unlike the GD and SA localities the ooid and tubestone facies are underlain by ~100 meters of dolostone containing cm-scale domal stromatolites, intraclast conglomerates, and a series of unusual diagenetic textures (Fig. 3.6).

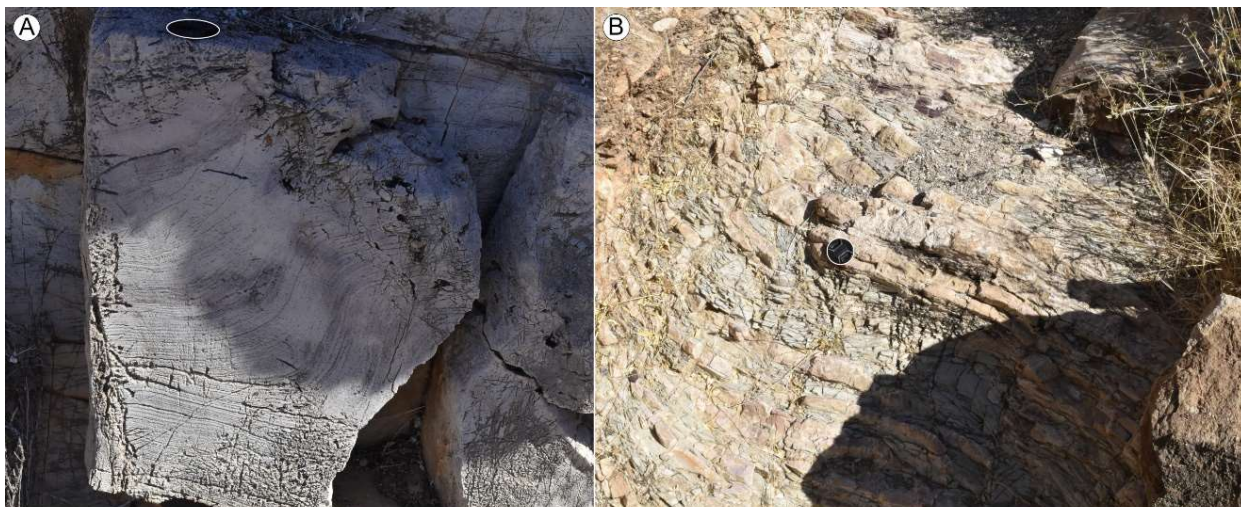


Figure 3.9. (A) Convoluted dolostone lamination, tubestone member of Adelt formation. Lens cap is 5.5 cm in diameter. (B) Upper contact of tubestone member dolostone conformably intercalated with the overlying Adelt formation shale member. Note how most of the shale is pale green in color and intercalations with the tan dolostone tend to be ~5-20 cm thick. Lens cap is 5.5 cm in diameter.

The ooid grainstone, stromatolite, and tubestone facies are all indicative of a relatively shallow water carbonate platform (e.g. Bathurst 1972; Cloud et al. 1974; Hoffman 1974; Logan 1974; Sumner & Grotzinger 1993; Sherman et al. 2000; Corsetti & Grotzinger 2005; Bosak et al. 2013; Trower et al. 2017), and assuming the ooids are *in situ* the need for regular agitation for their development implies deposition above fair-weather wave base. The convoluted laminae in the upper portions of the GD and SA section indicate soft sediment deformation of finely laminated, fine grained carbonate sediment. Though not diagnostic of a particular water depth, finely laminated sediment suggests settling of fines from suspension in quiet waters and soft sediment deformation is often facilitated by steeper slopes that could provide the gravitational instability deformation. If so, the convoluted laminated dolostone could represent a transition to deeper waters in the upper parts of the tubestone member of the Adelt formation, which would be consistent with the backstepping of the local carbonate source and transition to shales at its upper contact. Therefore, there could be a general trend of increasing water depth recorded by the tubestone member.

4.6.3 Adelt formation, upper members

The tubestone member of the Adelt Formation is overlain by three other members, each on the order of a few tens of meters in thickness, that were not measured in detail but will be

summarized here. In ascending order, they are the shale member, limestone member, and dolostone member. The shale member is composed of siliciclastic mudstone generally maroon or pale green in color. It has a conformable contact with the underlying tubestone member where 5-20 cm interbeds of shale intercalate with ~5 cm beds of tan to mauve colored dolostone (Fig. 3.9B). This shale member passes conformably into the overlying buff-orange to pale green limestone member. The limestone does not have distinguishable internal textures and transitions upward into a tan to gray colored dolostone member. This upper dolostone is predominantly either planar laminated or massively bedded. The dolostone tends to contain a small component of fine to coarse sized quartz sands and frequently shows silica veins cross cutting the primary laminations. Some portions of the dolostone unit shows extensive veins and possible interlamination of pale white limestone.

The stratigraphy of the Adelt Formation units above the tubestone member broadly records a shallow marine, mixed carbonate-siliciclastic platform environment. Despite some similarities to members of the Tsabisis and Noab formations there are substantial differences to suggest that these are stratigraphically distinct. Most notably, the greater thickness of the shale/carbonate interbeds, and high proportion pale green color for the shale overlying the tubestone member are both distinctly different from the Tsondab member rhythmite and its transition to maroon shale of the middle Tsabisis member, which is remarkably consistent in scale and color throughout the field area. Meanwhile the limestone and upper dolostone units of the Adelt formation lack any indication of intraclasts. Additionally, the style of silica and limestone veins that are common within the upper dolostone member are not found within the potentially analogous Noab Formation.

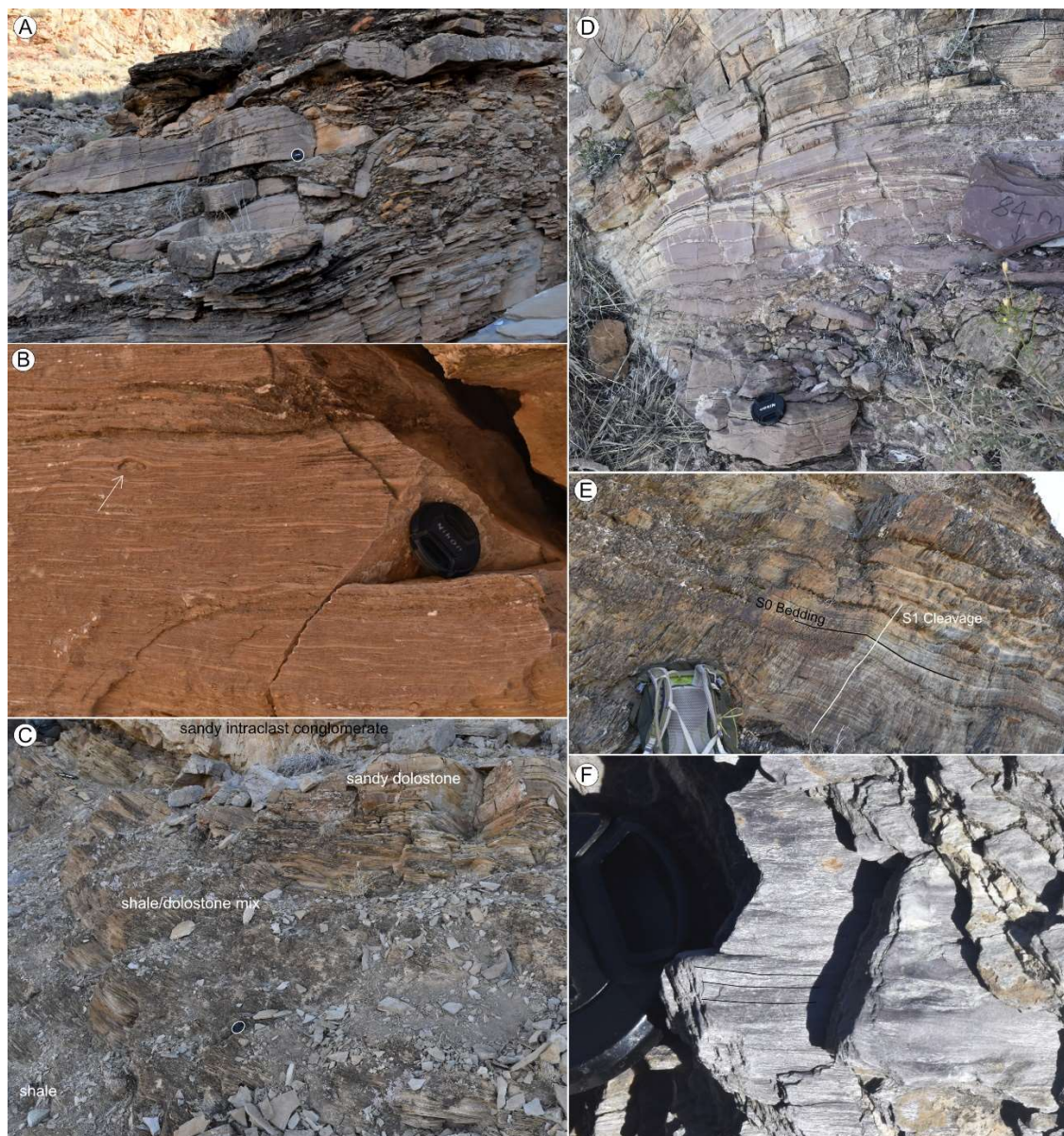


Figure 3.10. (A) Upper Tsabisis member with relatively undeformed angular limestone intraclasts at the NE locality. Lens cap is 5.5 cm in diameter. (B) Upper Tsabisis member with intensely flattened and elongated (oblate ellipsoid) limestone intraclasts at the TA locality. Arrow points to a relatively undeformed dolostone clast. Lens cap is 5.5 cm in diameter. (C) Contact of the Noab Formation at the MA locality stratigraphically overlying shales that are interpreted as the northern equivalents to the Blässkranz Formation. Lighter colors in the shales show progressively increasing proportion of fine dolostone sediment. Lens cap is 5.5 cm in diameter. (D) Conformable contact between the maroon shale/siltstone of upper Tsabisis member with the gray laminated dolostone of the Noab Formation. BO locality. Lens cap is 5.5 cm in diameter. (E) Slaty, penetrative cleavage of the shale found in the Remhoogte Formation in the central portion of the field area (Fig. 3.2, ~between HD and BR localities). Primary bedding (S0) is annotated in black (dip direction of 09°, and dip of 06°), cleavage (S1) is annotated in white (dip direction of 332°, and dip of 48). Backpack for scale. (F) Mineral extension lineations in the shale of the middle Tsabisis member. Annotations illustrate the direction of the fabric, which parallels the orientations of fold axes in the area (Fig. 3.2 & Supp. Fig. 1A, QT).

5. Structural Expression

5.1 Faults

The NNC is characterized by thrust faults developed at a variety of scales that presumably relate and connect at depth to the basal NNC décollement (Fig. 3.4; *sensu* Boyer & Elliott 1982). Nappe-bounding thrusts are directly observed with steep northwestward dips between the Dassie and Southern Pavian nappes (Fig. 3.2, GD; Fig. 3.3; Fig. 3.4B-B') and between the Southern Pavian and Northern Pavian nappes (Fig. 3.2, ZM; Fig. 3.3; Fig. 3.4C-C'; Fig. 3.5C). The latter thrust is covered further west but can be inferred by the juxtaposition of Southern Pavian and Northern Pavian units in the GD area (Fig. 3.4B-B'; Fig. 3.5C) and the SA/CA area (Fig. 3.4A-A'). At the southeast end of the Naukluft Mountains the Büllsport Formation overlies the Tsondab member (Fig. 3.3; Fig. 3.4B-B') which supports the inference that the Dassie and Kudu nappes are laterally correlative (Korn & Martin 1959; Hartnady 1978) with the Northern Pavian Nappe stratigraphically and structurally underlying both (Fig. 3.1D). Therefore, with the Southern Pavian Nappe thrust over the Dassie Nappe, bounded by a roof thrust with the Northern Pavian-Kudu nappes (Fig. 3.4; Fig. 3.5C), and coupled with the absence of stratigraphic correlation between the Northern Pavian and Southern Pavian nappe (section 4; subsection 7.2), it suggests that rocks of the Southern Pavian Nappe originated from a lower structural level beneath rocks of the Northern Pavian Nappe (Fig. 3.1D; Fig. 3.4). The traces of the nappe-bounding thrust faults are difficult to distinguish across the poorly exposed south-central plateau of the Naukluft Mountains (Fig. 3.2), but the prominent structures of the Northern Pavian Nappe (subsection 5.3 below) are consistent with a south-southeast vergence of the thrust faults, with an arcuate east-west curvature resulting from differential displacements of the convergent structures (as noted in Korn & Martin 1959). Within the nappes thrust faults accommodate tectonic shortening and tend to dip north/northwestward with frequent imbrication observed, especially in the brittlely deformed dolostone units, which can result in fault-bend-folds (Fig. 3.4). Thrust imbricate displacements vary, with an imbrication of the Adelt formation (Fig. 3.4, especially B-B') showing an exposed displacement of at least a kilometer (Fig. 3.11C).

5.2 Kudu Nappe Basal Contact

The thick dolomitic Noab Formation is the most structurally competent unit in the NNC, with folds showing open to closed angles and common internal thrust faults accommodating strain (thrust sheets on 10s of meters scale, offsets up to 100s of meters). The Noab Formation of the Kudu Nappe and the underlying units of the Northern Pavian Nappe collectively experienced southward directed simple shear with strain being concentrated along the rheological transition from the upper shales and limestones of the Tsabisis Formation to the more competent Noab Formation. This created a variably thick shear zone with southward directed, ~bedding parallel transport that varies laterally in intensity and can locally thin, in extreme examples, to form features approaching discontinuous thrust faults (*sensu* Ramsay et al. 1983; Fig. 3.2; Fig. 3.4A-A'). Therefore, local excisement by younger-over-older thrust faults (*sensu* Billings 1933; Morley 1988; Axen & Wernicke et al. 1990; Pace 2014) results in the Noab Formation abruptly overlying parts of the Remhoogte, Blässkranz, or Tsabisis formations (Fig. 3.4A-A'). Meanwhile, in other localities where shear deformation did not narrow to the same level of intensity, stratigraphic contacts are discernable (BO in Fig. 3.4C-C'; Fig. 3.6; Fig. 3.10C, D). Many locations show progressive (conformable) stratigraphic contacts, illustrated by gradual transition from shales and limestone to dolostone via beds of either intraclasts or finely laminated carbonates, intercalated with shale (Fig. 3.6; Fig. 3.10C, D). Other locations display erosive contacts (disconformity), typically with the sedimentary breccia member of the Noab Formation downcutting into the underlying strata and remobilizing clasts of the older units (Fig. 3.2; Fig. 3.6, SR; Fig. 3.7D), and suggesting a sequence boundary with incised valley development at the contact. Limestone intraclasts near the contact in the upper Tsabisis member locally show extreme flattening (subsection 5.5; Fig. 3.6, TA; Fig. 3.10B), but in other localities the limestone clasts show relatively undeformed angular shapes (Fig. 3.6, NE+BO; Fig. 3.10A). This indicates that the intensity of the shear zone between the Northern Pavian Nappe and Kudu Nappe varies widely and though it does locally thin into thrust faults, in most locations the contacts between the Noab Formation and the underlying units is stratigraphic. We have not observed any example of out-of-sequence thrusting of the Northern Pavian Nappe over the Kudu Nappe (Fig. 3.3). Therefore, the Northern Pavian and Kudu nappes can be considered parautochthonous – in that there was some bedding parallel tectonic transport, but, relative to the scale of the NNC, there was no major stratigraphic displacement and the combined sequence of Northern

Pavian/Kudu rocks can effectively be considered a single nappe. This is a principal conclusion of our work.



Figure 3.11. (A) Measured cleavage poles for the present study ($n=324$) with contours indicate overall southward vergence with a slight average southeastward preference. (B) Representative fold in the ED/HD area (Fig. 3.4) of a large overturned anticline of the buff Tsondab member with dark

diamictite, shale, and sandstone in the core of the fold. Approximate trace of northwest dipping axial plane annotated, consistent with the cleavage of part (A) and a single episode of deformation. (C) Thrust imbrication of the Adelt Formation (Southern Pavian Nappe) in the GD location, also shown in the upper left background of Fig. 3.5C and in Fig. 3.4B-B'. Thinner red line represents the internal imbrication of the Southern Pavian Nappe while the thicker red line shows the nappe-bounding roof thrust between the Southern Pavian and Northern Pavian nappes. Displacement across the Adelt Formation imbrication reaches at least 1 km.

5.3 Folds

Folds throughout the Naukluft tend to be asymmetrical with south-southeast vergence. Depending on the rheology and thickness of the units, fold angles range from open to isoclinal, and many show recumbent orientations. Fault-bend folds are common, while others indicate development by simple shear expressed in alternating units of substantially different rheology (Fig. 3.4). Projecting along strike, folds are broadly harmonic on ~1-2 km scales, but vary in exact style across the thrust belt (e.g. Tsondab member in Fig. 3.4 A-A' versus B-B'). Strain in the Tsondab member is largely accommodated by well exposed folds – the cream and mauve colored decameter-scale competent dolostone becomes heavily folded between the incompetent dark colored Blässkranz diamictite below and the maroon-colored shale of the middle Tsabisis member above. Tsondab member folds commonly reach tight to isoclinal interlimb angles, are consistently asymmetrical, and frequently recumbent (Fig. 3.4; Fig. 3.5B-D; Fig. 3.11B). Axial planes range from steep to horizontal with dips generally to the north – the arcuate east-west curvature of the NNC resulting in northeastward dipping axial surfaces in the western Tsondab exposures (Fig. 3.2, QT, SA; Supp. Fig. 1A), northward dipping axial surfaces in the central outcrops (Fig. 3.2, TA; Supp. Fig. 1D) and northwestward dipping axial surfaces in the eastern Tsondab (Fig. 3.2, ED/HD, GD; Fig. 3.4; Fig. 3.11B; Supp. Fig. 1E). Locally in the SA region, the Tsondab member is folded into an isoclinal syncline where upper mauve colored rhythmite of the Tsondab member and shale of the middle Tsabisis member has been sheared out and the syncline has been subsequently folded into higher order fold structures (Fig. 3.4A-A'; Fig. 3.5D). This is potentially the result of the high density of thrust imbrications in the underlying Southern Pavian Nappe, thickening the Adelt formation and causing a narrowing of the Northern Pavian-Kudu shear zone (Fig. 3.4A-A'). Strain is accommodated in the relatively ductile limestone of the upper Tsabisis member by extensive internal recumbent folding of tight to isoclinal internal angles with hinge lines paralleling those of the underlying Tsondab member. The overlying Noab

Formation, along with the Aubschlucht and Adelt formations, are more competent such that strain is accommodated primarily by thrust faults, but these units also show folds with open to close angles indicating vergence consistent with the broader structural fabrics.

5.4 Cleavage

A slaty mineral cleavage is common in the shale-dominated units, while the carbonate stratigraphy commonly shows a spaced dissolution cleavage (cm-dm scale spacing). Cleavage attitudes (S_1 , where S_0 is stratigraphic bedding) are broadly coplanar with local fault orientations and axial fold planes showing southward vergence (Fig. 3.10E; Fig. 3.11A, B), with the arcuate curvature of the NNC resulting in northeastward dipping cleavage in the western Tsondab exposures (Fig. 3.2, QT, CS) and northwestward dipping cleavages in the eastern Tsondab (Fig. 3.2, ED/HD, GD, ZM; Fig. 3.11A, B). Dips within the central Naukluft valley (Fig. 3.2) tend to be relatively shallow in the northern portions ($\sim 30^\circ$; CS, BR, BO, NE) and generally steepen to the south ($\sim 60^\circ$) up to the Northern Pavian and Southern Pavian nappe fault contact (Fig. 3.2, ZM; Fig. 3.3; Fig. 3.4; Fig. 3.5C). In the Remhoogte Formation and middle Tsabisis member cleavage tends to be spaced on cm to sub-mm (down to ~ 100 microns) scales with general slaty planar morphology (Fig. 3.10E). Cleavage within the Blässkranz Formation tends to be on similar scales but with anastomosing cleavage shapes due to interference caused by the diamictite clasts within the shale matrix (*sensu* Powell 1979; Engelder 1985). Crenulation cleavage is uncommon and poorly developed within the study areas, both in outcrop and thin section. However, prior work has found some examples, primarily in the northernmost portions of the Remhoogte Formation (Hartnady 1978), which have orientations consistent with south to southeastward directed S_2 deformation.

5.5 Stretching and Flattening Fabrics

Mineral extension lineations are found within the shale of the middle Tsabisis member (Fig. 3.10F) with extension approximately parallel to local fold axes. The relatively ductile limestone clasts of the top of the Remhoogte Formation, the diamictites and conglomerates of the Blässkranz Formation, and the intraclasts of upper Tsabisis member commonly show intense strain accommodation with flattened and elongate shapes (oblate ellipsoid) in

directions consistent with local cleavage and fold vergence. Aspect ratios of the strained clasts reach up to ~40:1 (Fig. 3.10B; initial dimensions are variable given that relatively undeformed intraclasts are commonly elongate, e.g. Fig. 3.10A).

5.6 Deformational History

The stratigraphy of the NNC was variably strained depending on the rheology of the stratigraphic units resulting in highly inhomogeneous deformation in response to simple shear tectonic stresses directed in a south to southeastward direction. The structural (section 5.1) and stratigraphic context (section 4; subsection 7.2) of the Southern Pavian Nappe indicate that it was thrust over the Dassie Nappe from a lower structural level, with a roof thrust contact with the overlying Northern Pavian-Kudu Nappe (Fig. 3.4). The structural fabrics present in the NNC as documented in the present study are consistent with a single episode of deformation with variations in structural attitude related to the east-west arcuate curvature of the NNC, where vergence in the eastern end of the NNC is directed southeastward, in the central region of the NNC is directed southward, and in the western end of the NNC is directed southwestward. Faults and folds are consistent with this deformation style with cleavage and stretching fabrics co-aligned to the larger structures. Previous work suggested up to two episodes of deformation are indicated within the NNC given the crenulation cleavage found of the northern portions of the Remhoogte Formation (Hartnady 1978) and changing directions of deformation in the Zebra Nappe (Quinn thesis; et al., in prep). The deformation described here is consistent with recording the first of these two deformation episodes, directed south-southeastward, with the second more eastward directed deformation phase (Quinn thesis; et al., in prep) not readily discernible in these units of the central Naukluft.

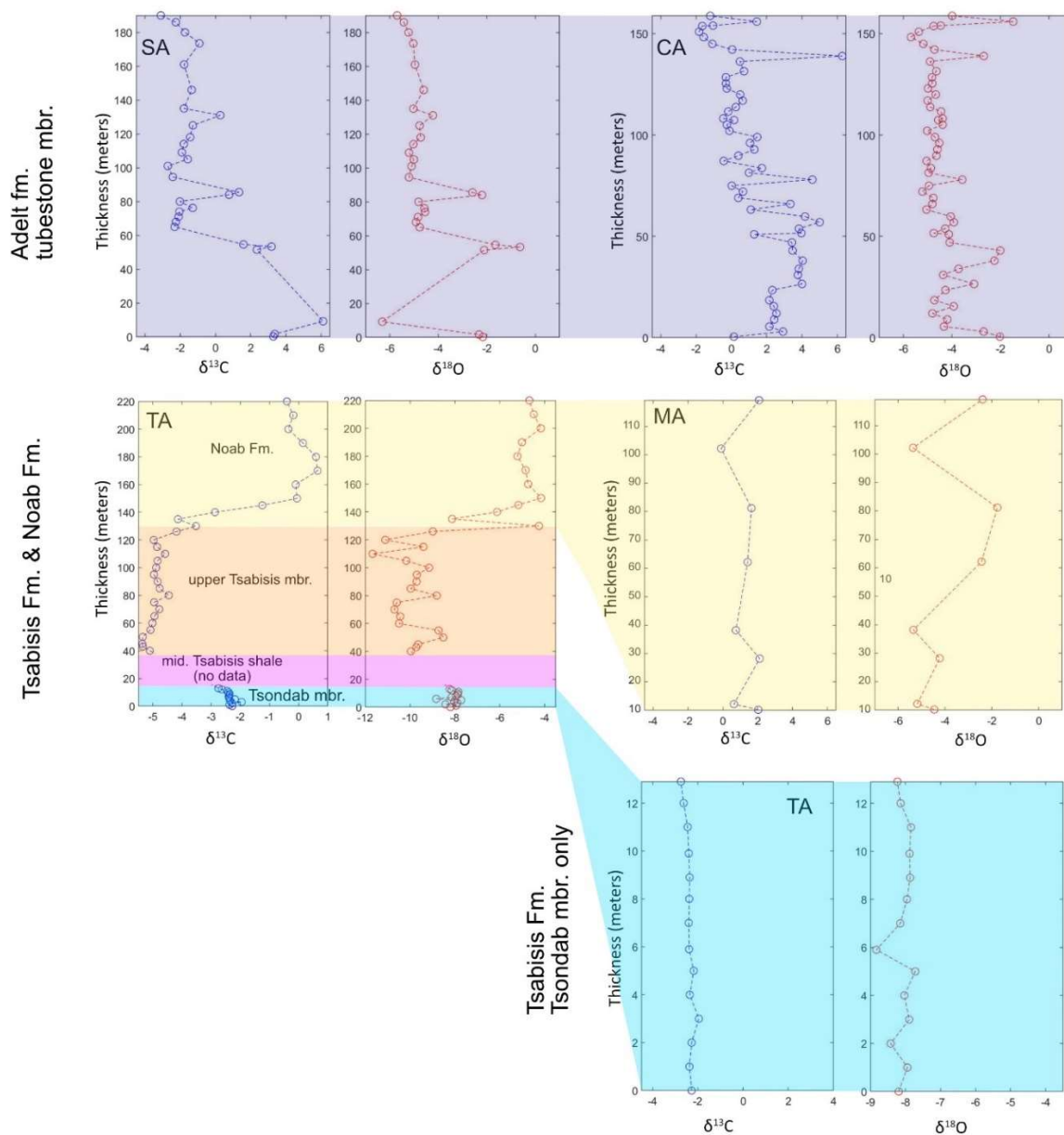


Figure 3.12. Carbon and oxygen isotope profiles for different localities (‰ VPDB; data in Supp. Table 3.1). Vertical scales correspond to the stratigraphic thickness shown in the sections of Fig. 3.6 (Supp. Fig. 3.2). Shaded colors of the stratigraphic units are the same as in Fig. 3.2 and Fig. 3.6. The SA and CA profiles show the values for the tubestone member of the Adelt formation. The complete TA profile shows the Tsondab member at its base, along with the overlying upper Tsabasis member (40 - 130 meters) and the Noab Formation (130 - 220 meters). The SA and CA $\delta^{13}\text{C}$ profiles are relatively positive and trend to more negative values upward, while the TA examples of the Tsondab member $\delta^{13}\text{C}$ profile is consistently negative (~ -2 ‰). Values in the upper Tsabasis member decline to ~ -5 ‰ before rise to 0-1 ‰ in the Noab Formation. The differences in magnitude and trends suggests the tubestone member cannot be correlated with these other carbonate units of the NNC. See Supp. Fig. 3.3 for cross plots of $\delta^{13}\text{C}$ and $\delta^{18}\text{O}$.

6. Geochemistry

6.1 Carbon and Oxygen Isotope Geochemistry

The $\delta^{13}\text{C}$ and $\delta^{18}\text{O}$ carbonate chemostratigraphy for the Tsabisis and Noab formations, and tubestone member of the Adelt formation are shown in Fig. 3.12 (data in Supp. Table 3.1). Four profiles correspond to the respective stratigraphic columns of these units from Fig. 3.6. Samples were collected every ~3-10 meters for the larger sections encompassing a broader range of stratigraphy. In addition, more tightly spaced data sets were collected for sections of the Tsondab member at TA, with samples every ~1 meter. Profiles of the Tsondab member show the bulk $\delta^{13}\text{C}$ values centered around -2 ± 0.6 ‰ (for additional examples see Morris & Grotzinger 2023). In the overlying upper Tsabisis member limestone $\delta^{13}\text{C}$ values decline to approximately -5 ‰, then values rise in the Noab Formation to about $+0.1 \pm 0.6$ ‰ in the TA profile. At the MA locality the Noab Formation is similar, with average $\delta^{13}\text{C}$ values of $\sim +1.3 \pm 1$ ‰ and does not show a particular trend in values. The two tubestone member localities show wide scatter but broadly a similar trend of progressively more negative values upward through the section, starting at $\sim +2-4$ ‰ and ending around ~ -2 ‰. Cross-plots of $\delta^{18}\text{O}$ and $\delta^{13}\text{C}$ (Supp. Fig. 3.3) of the CA, MA, and Tsondab only TA sections lack correlation, whereas the SA and overall TA sections do you show positive correlation. This suggests that while the Tsondab member appears to retain primary signals, at least locally, parts of the upper Tsabisis member, Noab Formation, and tubestone member of the Adelt formation may have experienced diagenetic overprinting (Swart 2015; Ahm et al. 2018).

For these analyses we presume that temporal correlations can be made with $\delta^{18}\text{O}$ and $\delta^{13}\text{C}$ profiles as indicators of marine dissolved inorganic carbon isotopic composition or coeval post-depositional processes. The $\delta^{13}\text{C}$ values of the Tsondab member show steady and consistent trends within profiles and between localities (Morris & Grotzinger 2023). The relatively negative plateau of $\delta^{13}\text{C}$ values is broadly consistent with Marinoan cap carbonates found elsewhere (e.g. Hoffman et al. 1998; Kennedy 1996; James et al. 2001; Jiang et al. 2003; Porter et al. 2004; Liu et al. 2018; Yu et al. 2020) and support the recognition of the Tsondab member as a basal-Ediacaran cap carbonate (Morris & Grotzinger 2023). The $\delta^{13}\text{C}$ profiles of the tubestone member of the Adelt formation generally show relatively positive

values and significantly more scatter than those of the Tsondab member (Fig. 3.12; Morris & Grotzinger 2023). The upper portions of the SA profile approach negative values close to that of the Tsondab member, yet, with the transgressive base of the Tsondab member, correlating the tubestone member as an updip shelf equivalent would be inconsistent with the positive $\delta^{13}\text{C}$ values found in the lower portions of the tubestone member (SA and CA profiles). Additionally, cross-plots of $\delta^{18}\text{O}$ and $\delta^{13}\text{C}$ (Supp. Fig. 3.3) for the SA profile shows a strong positive correlation, indicating that significant diagenetic alteration could have lowered the measured $\delta^{13}\text{C}$ values. Therefore, the $\delta^{13}\text{C}$ profiles of the tubestone member of the Adelt formation are not consistent with the geochemical values or trends within the Tsondab member or other Marinoan cap carbonates, even though the presence of the tubestone facies suggests that these rocks could be Marinoan in age. The Adelt formation profiles also do not appear to have recognizable similarities to the upper Tsabisis member limestones or Noab Formation. Diagenetic processes may have overprinted these latter units as well, but given the data we have with the sites that appear to be minimally altered, by their lack of positive correlation between $\delta^{18}\text{O}$ and $\delta^{13}\text{C}$, (CA, MA, TA Tsondab), $\delta^{13}\text{C}$ and $\delta^{18}\text{O}$ carbonate chemostratigraphy does not support the correlation of the Adelt formation with any other studied units of the Naukluft Mountains.

6.2 Detrital Zircon

6.2.1 Sample Context

The ‘Abs Fm. Congl’ sample was collected from the quartz dominated sandstone and conglomerate of the Aubschlucht Formation in the GD area, approximately 750 m to the southwest of the GD stratigraphic column marked in Fig. 3.2 (bed shown in Fig. 3.8A). Laterally coarsening to up to pebble grain size the sample was collected at a stratigraphic level ~comparable to -40 meters on the GD column (Fig. 3.6). The ‘Tsondab SS’ sample was collected from the fine grained sandstone of the upper Tsondab member, at a laterally equivalent to 14-16 meters on the NE+BO column (Fig. 3.2; Fig. 3.6). The ‘Noab, Sed. Breccia’ sample was collected from the matrix-supported breccia of the sedimentary breccia member, at a laterally equivalent to 9-15 meters on the SR column (Fig. 3.2; Fig. 3.6). The ‘Noab MA 29 m’ sample was collected from the coarse sandstone-tabular intraclast bed at

29 meters in the MA column (Fig. 3.2; Fig. 3.6; Fig. 3.7H). The ‘Plateau Top SS’ sample was collected from a coarse sand to cobble sized conglomerate-breccia that unconformably overlies the Noab Formation on the poorly exposed plateau of the Naukluft (‘cover’ south of TA locality, Fig. 3.2). It is composed primarily of quartz with no indication of carbonate intraclasts or fine-grained carbonate matrix, suggesting it is a significantly younger unit that unconformably covers the Noab without local remobilization of the overlying dolostone or carbonate precipitation.

6.2.2 Bulk Zircon Results

All five samples have analyses clustering in two peaks indicating Mesoproterozoic and Paleoproterozoic ages, along with a small set of Archean zircons (Fig. 3.13; Supp. Table 3.2). The Mesoproterozoic peaks are centered between 1110-1130 Ma for all samples except for the Tsondab SS, which has an older peak centered at 1347 Ma (Fig. 3.13). The Paleoproterozoic peaks are all centered between 1750-1900 Ma. The maximum depositional age (MDA, the oldest a sample can be) is based conservatively on the youngest cluster of ages, rather than the youngest individual grain, which may be compromised by Pb-loss or contamination (Dickinson & Gehrels 2009). The age of the youngest cluster is determined by the weighted mean age of the youngest cluster that has at least three ages which overlap at the 2σ level. With this criteria, the MDA of the Abs. Fm. Congl., Tsondab SS, and Noab Sed. Breccia are all between ~1040-1110 Ma. The Noab MA 29 m has a younger MDA cluster at 680 Ma.

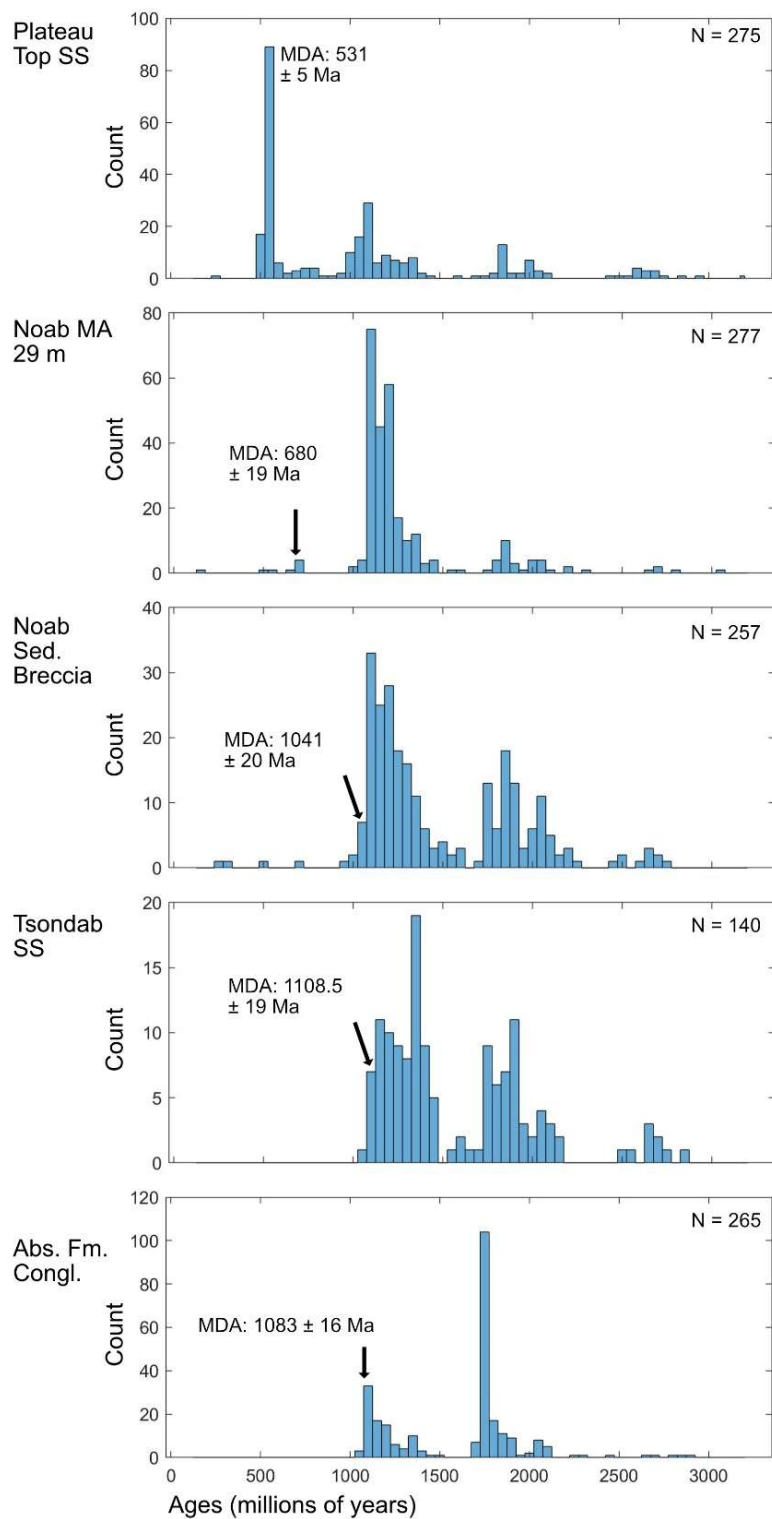


Figure 3.13. Detrital zircon age distributions for five samples. MDA (maximum depositional age) labeled for each sample, which is based on the youngest cluster of ages. Number of analyzed zircons (N) are those that passed the standard data reduction filters to be included in the final dataset.

The MDA of these lower four samples is consistent with our expectations from regional lithostratigraphic correlations (Fig. 3.13; Hoffmann 1989; Miller 2008) that the Aubschucht, Tsabisis, and Noab formations are Neoproterozoic in age. However, without younger conclusive age clusters, the detrital zircon ages provide limited additional constraints to these units, given that the Tsabisis Formation has been interpreted as a Marinoan age (~635 Ma) cap carbonate succession (Hoffmann 1989; Miller 2008; Hoffman et al. 2017; Morris & Grotzinger 2023). The Plateau Top SS is the outlier with a large cluster of ages that peaks at 536 Ma, with an MDA of 531 Ma. These ages are consistent with zircons derived from the Pan-African Damara Orogeny (~590-505 Ma, Gray et al. 2008; Foster et al. 2015; Anderson et al. 2016; Goscombe et al. 2017; Zieger et al. 2020). Along with the observation that the Plateau Top SS overlies the Noab Formation unconformably, the ages may suggest that these quartz sandstones were deposited at some point after the deformation and emplacement of the NNC (estimated at ~555 Ma, Gray et al. 2008; Goscombe et al. 2017).

The distribution and abundance of zircon ages differs between the Kalahari and Congo cratons, allowing for the distinction of provenance (Foster et al. 2015). The relative scarcity of ages in the Abs. Fm. Congl., Tsondab SS, Noab Sed. Breccia, and Noab MA 29 m samples between 1000-1050 Ma and predominance of Mesoproterozoic ages between 1100-1350 Ma is consistent with sediment sourced from the Kalahari Craton without significant input from the Congo Craton (Foster et al. 2015; Anderson et al. 2018). The Plateau Top SS then has a broader age distribution that could be a result of both Kalahari and Congo craton provenance. These observations, along with a northward facing direction of the Cryogenian-Ediacaran platform (Morris & Grotzinger 2023) and similar zircon distributions from the Zebra Nappe strata (Quinn thesis; et al., in prep) indicate that the Neoproterozoic units of the NNC were deposited along the northern margin of the Kalahari Craton, not the Congo Craton (consistent with suggestions from Hartnady 1978; Martin et al. 1983; Hoffmann 1989; Miller 2008; in contrast with Goscombe et al. 2017, Fig. 2). It also suggests that through the deposition of the Southern Pavian, Northern Pavian, and Kudu nappe stratigraphy, the Congo Craton was not proximal enough to the Kalahari margin to provide a significant source of siliciclastic sediment.

6.2.3 Detrital Zircon Outliers

There are several outlier ages significantly younger than the respective MDA of the sample (Fig. 3.13), particularly with the Noab Sed Breccia and Noab MA 29 m samples, along with one outlier in the Plateau Top SS. Ages significantly younger than ~500 Ma for the two Noab Formation samples (167, 268, 284 Ma) are inconsistent with the relatively well constrained geologic context, indicating that they are either the result of Pb loss producing younger ages or contamination in the field with dust containing younger zircons, potentially related to other Permian-aged zircons found in Namibia from an ambiguous Gondwanan volcanic source (Rubidge et al. 2013; McKay et al. 2015; Zieger et al. 2020). The three ages comparable to the Damara Orogeny (496, 517, 557 Ma) within the Noab Formation could have the potential to suggest a late Ediacaran to Cambrian age for the Noab Formation. However, with the limited number of analyses, $^{206}\text{Pb}/^{207}\text{Pb}$ vs $^{206}\text{Pb}/^{238}\text{U}$ discordance for the 496 Ma analysis, U concentrations and U/Th ratio differences between the 517 and 557 Ma analyses (suggesting they are from different sources; Supp. Table 3.2), and the deviance of this age estimation from existing lithostratigraphic and tectonic models (Hoffmann 1989; Saylor et al. 1995; Gray et al. 2008; Miller 2008; Goscombe et al. 2017; Nelson et al. 2022; Quinn thesis; et al., in prep) indicates that such a hypothesis is unlikely. Future additional detrital zircon datasets and detailed analyses of diagenetic alteration would facilitate a conclusive distinction of the age models. The Permian outlier age for the Plateau Top SS sample (251 Ma) could be consistent with substantially later Phanerozoic deposition of this sandstone over the Noab Formation (Zieger et al. 2020) but may also represent contamination.

7. Discussion

7.1 Revisions to Naukluft Tectonostratigraphy

The results of the present study suggest an alternative hypothesis to earlier inferences that the contact between the Northern Pavian Nappe and Kudu Nappe is uniformly a thrust fault and that the Kudu Nappe represents an older unit that has been thrust over a younger Northern Pavian Nappe (in contrast to Hartnady 1978; 1980; consistent with Korn & Martin 1959). Mapping presented here shows that the broad ~bedding parallel shear zone between the two

nappes does locally thin to concentrate strain in thrust faults (*sensu* Ramsay 1983; Fig. 3.2; Supp. Fig. 3.1). However, there are many examples of stratigraphic contacts – both depositionally continuous as well as erosionally scoured – between the Northern Pavian Nappe and Kudu Nappe (Fig. 3.2; Fig. 3.3; Fig. 3.6; Fig. 3.10C, D) indicating a contiguous stratigraphic succession between the nappes that has not been inverted. Another key aspect of the structural model of Hartnady (1978; 1980) relied on the interpretation in the GD area of the Northern Pavian Nappe locally thrust over the Kudu Nappe (Fig. 3.3). However, by identification and lithologic correlation of the tubestone facies we show that this dolostone-dominated thrust sheet is the tubestone member of the Adelt formation and not the Noab Formation (Fig. 3.3; Fig. 3.4 B-B' & C-C'; comparable instead to how it is mapped by Korn & Martin 1959), so this discounts the Northern Pavian Nappe having been thrust over the Kudu Nappe. Additionally, we reject the interpretation that clasts of oolite, chert/jasper, and sandy dolostone found in the Blässkranz Formation indicate that it represents the erosion of an older Noab Formation. The only example of *in situ* ooids facies within the Naukluft are in the tubestone member of the Adelt formation (Fig. 3.6; Fig. 3.8E). The only oolites in the Noab Formation are clasts of silicified oolite in the sedimentary breccia member, analogous to the limestone oolite clasts of the underlying Blässkranz Formation that the sedimentary breccia member incises into; suggesting that they are remobilized and silicified clasts sourced from the Blässkranz Formation into the sedimentary breccia member. No examples of *in situ* oolite were found in the Noab Formation. Parts of the Noab Formation are notable for the high proportion of coarse quartz grains intermixed with dolostone (Fig. 3.7E, F), yet sandy dolostone in general, along with chert/jasper, are not diagnostic facies of the Noab Formation.

The Northern Pavian Nappe was also mapped in detail, especially the members of the Tsabisis Formation, at higher resolution (1:10,000 versus 1:100,000; e.g. Fig. 3.3 & Supp. Fig. 3.1) than previous workers (Korn & Martin 1959; Hartnady 1978; 1980). This allowed for the identification of proximal (depositionally updip) versus distal (depositionally downdip) facies gradients within the Tsondab member (Fig. 3.2; Supp. Fig. 3.1) that proved critical for the detailed stratigraphic interpretation of this Marinoan cap carbonate (Fig. 3.6; Supp. Fig. 3.2; Morris & Grotzinger 2023). Associated mapping of the basal Noab Formation

identified incised valley fill deposits of the sedimentary breccia member that allowed determination of the degree of stratigraphic downcutting of the underlying units (Fig. 3.2). Along similar lines, the northernmost MA outcrop shows the basal contact of the Noab Formation to be stratigraphic and that the Tsondab member has completely pinched out stratigraphically by these northern localities (Fig. 3.6; Fig. 3.10D). Finally, in the northern region (Farm Noab) we found no stratigraphic or structural reason to distinguish the Klipbokrivier Formation as a unit that overlies the Noab Formation within the Kudu Nappe (subsection 4.4). In summary, the present study shows that the lithostratigraphy of the Remhoogte, Blässkranz, Tsabisis and Noab formations can be explained by a deformed but parautochthonous stratigraphic succession of a single Northern Pavian-Kudu Nappe – a conclusion that simplifies the NNC structural evolution as well (section 7.4).

7.2 Stratigraphic Relationships and Evolution

More precise tectonostratigraphic characterization of the major stratigraphic units found in the NNC, with a particular interest in contextualizing the early Ediacaran rocks, including the Marinoan cap carbonate (Hoffmann 1989; Miller 2008; Morris & Grotzinger 2023) provides a point for further refinement of Neoproterozoic history, specifically recording much of the climate transition resulting from the termination of a Snowball Earth (e.g. Hoffman et al. 1998; Hoffman & Schrag 2002; Halverson & Shields-Zhou 2011; Hoffman et al. 2017). As described above, we have shown that the relationship between the Northern Pavian Nappe and Kudu Nappe does not involve major structural inversion (Hartnady 1978, D₂; Fig. 3.1D). The contact varies laterally between progressive conformable transition, development of incised valleys associated with erosive disconformities, and localized younger-over-older thrust faults to form a single Northern Pavian-Kudu Nappe whose internal contact is parautochthonous. Additionally, the Remhoogte-Blässkranz contact may represent a glacially-related erosional disconformity. However, there is no indication that the unconformity represents syn-depositional deformation, as proposed for the D₁ episode by Hartnady (1978). Therefore, the depositional evolution of the basin recorded by the Northern Pavian Nappe continues with the overlying, younger Noab Formation of the Kudu Nappe uninterrupted by episodes of syndepositional tectonic translation and deformation.

The Southern Pavian Nappe was originally correlated with the Northern Pavian Nappe, along with a tentative correlation to the Zebra Nappe (Korn & Martin 1959). Later work disagreed with a correlation between the Pavian nappes but maintained that the Southern Pavian Nappe correlates to the Zebra Nappe and Nama Group (Hartnady 1978; 1980), which has been subsequently rejected by lithological comparison (Quinn thesis, Quinn et al., in prep). Therefore, the stratigraphic context of the Southern Pavian Nappe has not been well constrained. A potential correlation with the Northern Pavian Nappe (Korn & Martin 1959), would have important implications for the interpretation of the Naukluft cap carbonate record, with the distinctive tubestone member as an updip shelf equivalent to the thinner distal carbonate ramp deposits of the Tsondab member. This could be especially appealing given that tubestone is a relatively rare carbonate facies in the rock record and is most commonly associated with Neoproterozoic cap carbonates (Cloud et al. 1974; Corsetti & Grotzinger 2005; Bosak et al. 2013; Hoffman et al. 2017). However, our facies and stratigraphic analysis shows that there is no indication of transitional facies or stratal geometries that would be expected for a shelf to ramp transition (Fig. 3.6). If the tubestone member was a updip shelf equivalent to deeper-water Tsondab member ramp deposits, then the two sequence boundaries observed in the Tsondab member should correlate and be evident in the higher elevation tubestone member shelf, likely as substantial subaerial exposure surfaces and/or incised valleys (Fig. 3.6). Yet, there is no indication of even a single subaerial exposure surface, incised valley, or any other evidence for a sequence boundary within the tubestone member of the Adelt formation (Fig. 3.6). Additionally, the most diagnostic facies of both units are not found within the other - tubestone, *in situ* ooids, and meter-scale stromatolitic mounds are found only in the tubestone member (Fig. 3.8), while the small-scale elongate stromatolites and the finely intercalated mauve rhythmite is limited to the Tsondab member (Fig. 3.7). Similarly, while the diamictites of the Blässkranz Formation suggest a glaciogenic origin, the Aubschlucht Formation underlying the tubestone member lacks any indication of glaciogenic erosion or deposition. These stratigraphic distinctions pair with the observations of structural juxtaposition (section 5; Fig. 3.4; Fig. 3.5C) and lack of geochemical correlation (section 6.1; Fig. 3.12), to show that the units of the Southern Pavian Nappe are not stratigraphic-basin equivalents to any units of the Northern-Pavian-Kudu Nappe.

As a result, we can consider the combined units of the Northern Pavian-Kudu Nappe as a single depositional succession independent of the Southern Pavian Nappe that provides a valuable Cryogenian and Ediacaran stratigraphic record from the northern Kalahari margin (section 6.2). The Northern Pavian-Kudu combined basin history begins with the Remhoogte Formation representing extended deep-water deposition prior to the glaciation represented by the Blässkranz Formation. The initiation of regional glaciation might be represented by the basal coarse sandstones and diamictite in the Blässkranz Formation. However, it is also possible that the first encroachment of regional glaciation is recorded earlier in the uppermost Remhoogte Formation where the upper succession of carbonate breccia could be the distal record of glacial erosion of a nearby carbonate platform and the granitic limestone cobble in the underlying shales could suggest early ice rafted debris. The diamictite that constitutes the majority of the Blässkranz Formation represents proximal glacial deposition, though because of its massive bedding the portions of the diamictite that constitute regional glacial initiation, deposition during the Marinoan glacial epoch, or the deglaciation remains poorly constrained. The intercalated lithic and quartz sandstones of the uppermost Blässkranz Formation indicate backstepping and retreat of the glacial influence, representing a portion of the deglaciation (Morris & Grotzinger 2023). The Tsondab member records a carbonate ramp experiencing changing sea levels and fluxes of siliciclastics, including two sequence boundaries represented shallowing in the lower stromatolite succession and the upper storm influenced deposits (Fig. 3.6; Morris & Grotzinger 2023). The carbonate source transgresses at the top of the Tsondab member leading to the deep-water shale of the middle Tsabisis member, overlain by mixed carbonate-siliciclastic slope deposition of the Tsabisis member limestones (Fig. 3.6). Frequently downcutting into the underlying units the sedimentary breccia member of the Noab Formation represent large scale remobilization likely by slope failure and/or base level fall. The rest of the upper Noab member largely represents deep-water mixed carbonate-siliciclastic slope deposition with likely northward progradation. The Büllsport Formation of the Dassie Nappe may represent a shallower, updip equivalent to the Noab Formation.

7.3 Identity of the Southern Pavian Nappe

The Southern Pavian Nappe represents an unusual stratigraphic succession with no clear equivalents within the Naukluft Nappe Complex (subsection 7.2; Quinn thesis; et al., in prep) and poorly constrained age (Fig. 3.13). These rocks are likely Proterozoic in age given the lack of body or trace fossils, the widespread distribution of tubestone and stromatolite facies (Cloud et al. 1974; Corsetti & Grotzinger 2005; Bosak et al. 2013), and lack of detrital zircons younger than 1 Ga (Fig. 3.13, Abs. Fm. Congl.). Assuming the Aubschlucht Formation does stratigraphically underlie the Adelt formation, the depositional history of the Southern Pavian Nappe begins with a marginal-marine mixed carbonate-siliciclastic platform that may record intermittent terrestrial/fluvial deposition. Subsequent deposition of the tubestone member suggests a transgression of the shoreline given the scarcity of siliciclastic sediments within the thick dolostone unit.

Though the units of the Southern Pavian Nappe are not intra-basinal stratigraphic equivalents of the Northern Pavian Nappe (subsection 7.2), it is possible that the tubestone member could represent a different Marinoan-age cap carbonate disconformably overlying a pre-glacial Aubschlucht Formation. This could be viable given the thickness of the siliciclastic-poor dolostone that could be showing a large deglacial transgression (Hoffman et al. 2017; Nordsvan et al. 2019) and distinctive tubestone facies which are most commonly associated with Marinoan cap carbonates (Cloud et al. 1974; Corsetti & Grotzinger 2005; Bosak et al. 2013). This would make for an unusual combination of facies, as oolite is not typically found in Neoproterozoic cap carbonates. Along with the lack of underlying glacial evidence, tight absolute age constraints, or the typical chemostratigraphic signature of Neoproterozoic cap carbonates (e.g. Hoffman et al. 1998; Kennedy 1996; James et al. 2001; Jiang et al. 2003; Porter et al. 2004; Liu et al. 2018; Yu et al. 2020) any such connection is speculative. Another possibility is that the units of the Southern Pavian Nappe represent older units stratigraphically underlying the Northern Pavian-Kudu succession within the same basin (Fig. 3.1D). This would be consistent with its lower structural position within Naukluft Nappe Complex and could suggest it is the source of the variety of oolitic grainstone intraclasts found throughout the Northern Pavian and Kudu Nappes (though intraclasts of tubestone have not been observed). Regardless, with the unusual combination of tubestone

and ooid facies the tubestone member of the Adelt formation is an unusual Precambrian dolostone unit.

If units of the Southern Pavian Nappe could be correlated with a Marinoan cap carbonate it might be more comparable with the Buschmannsklippe Formation of the Witvlei Group in east-central Namibia (Hoffmann 1989; Prave et al. 2011). There the Bildah Member has been recognized as a cap carbonate by the lithofacies, stratigraphic position, and characteristic $\delta^{13}\text{C}$ chemostratigraphy. The Bildah Member is also relatively thick (typically ~40-60 m), shows tubestone facies, and lacks a conformable basal contact with glaciogenic strata, instead unconformably overlying non-glacial units (Prave et al. 2011). Whether or not ooid facies can be observed within the Bildah Member could help test this correlation. Otherwise, previous workers (Hartnady 1978) have suggested that the Aubschlucht and Adelt formations correspond to pre-Nama Kamtsas Formation and the Nama Group Kuibis Formation, respectively. However, these correlations relied on a Southern Pavian Nappe connection to the Zebra Nappe, which was then correlated with the Nama group, both of which have since been rejected (Quinn thesis; et al., in prep).

7.4 Nappe Relationships and Development

The units defined within the Northern Pavian and Kudu nappes moved together tectonically with shearing along their contact attributed to lithology-related differences in rheology. South to southeastward directed shear resulted in a variety of structural features expressing inhomogeneous deformation, including localized younger-over-older thrust faults (Fig. 3.2; Fig. 3.4; *sensu* Billings 1933; Ramsay et al. 1983; Morley 1988; Axen & Wernicke et al. 1990; Pace 2014). The Dassie Nappe represents a similar and likely lateral equivalent stratigraphy to that within the Kudu Nappe. The Southern Pavian Nappe is an independent stratigraphic and structural unit that was tectonically emplaced from a lower structural level, ramped upward to thrust over the Dassie Nappe, bounded by a roof thrust contact with the Northern Pavian–Kudu Nappe, and internally imbricated by large-scale thrust faults in the direction of tectonic transport (Fig. 3.4). Its structural, and therefore potential stratigraphic position, below the Northern Pavian-Kudu Nappe could suggest it is an older unit than the other formations of the NNC (consistent with detrital zircon results, Fig. 3.13).

Recognizing the above relationships of the combined Northern Pavian-Kudu Nappe and the stratigraphic development within it, we are able to further simplify the structural model for how the Naukluft Nappe Complex developed and consider the basis for the 78 km minimum estimate of nappe displacement (Hartnady 1978). Hartnady (1978) proposed a five step deformational model defined largely by unconformity relationships between lithostratigraphic units of different nappes. Steps D₁ and D₂ depended on Northern Pavian-Kudu structural inversion, interpreted to include the southward directed emplacement of the Northern Pavian Nappe and the subsequent thrusting of the Kudu and Dassie Nappe over the Northern Pavian Nappe. Displacement from this was estimated by shifting the leading edge of the Kudu and Dassie nappes northward beyond the exposed limits of the Remhoogte Formation. D₃ was to reflect southward directed dismemberment of the Kudu and Dassie nappes along with re-imbrication of Kudu-Northern Pavian Nappe complex and incorporation of a portion of the Zebra Nappe stratigraphy as the Southern Pavian Nappe. This deformation and displacement estimate was based on a combination of internal shortening calculations within the eastern Dassie Nappe and the structural relationships and lithostratigraphic correlations of the Southern Pavian Nappe with the Kudu, Dassie, and Zebra Nappes (Fig. 3.3). D₄ involved NE-SW folding of the Zebra Nappe (followed by unconformable deposition of an additional unit atop the Zebra Nappe), while D₅ represented the emplacement of the entire Naukluft Nappe Complex atop the sole dolomite. The combined displacement vector for the D₄ and D₅ episodes was based on the correlation of the Zebra Nappe with the underlying Nama Group and therefore the rigid-body displacement past the northwestern occurrences of the Nama Group. Quinn's work (thesis; et al., in prep) revised the tectonostratigraphy of the Zebra Nappe, simplifying the tectonic contacts, finding a lack of disconformities within the Zebra Nappe, and showing that it cannot be correlated with the Nama Group.

With our rejection of Northern Pavian-Kudu thrust inversion model of Hartnady (1978) we concur with the regional comparisons to other Namibian basins (Hoffmann 1989; Miller 2008), and we can therefore build upon Quinn (thesis; et al., in prep) to further simplify the deformational model. With the lack of evidence for syn-depositional deformation at the Remhoogte-Blässkranz contact (D₁, Hartnady 1978), the rejection of the Northern Pavian-

Kudu thrust inversion (D₂, Hartnady (1978), and correction of the lithostratigraphy and contacts in the GD area (Fig. 3.3) along with the lack of correlation of the Southern Pavian Nappes with the Northern Pavian Nappe, Zebra Nappe, or Nama Group (D₃, Hartnady 1978; Quinn thesis; et al., in prep), the broader deformation associated with emplacement of the Naukluft Nappe Complex can be collapsed into two episodes. The entire nappe stack was built in the first episode of southward thrusting, then a second episode of eastward thrusting developed the southeastward vergent structures within parts of the Zebra Nappe, and potentially parts of the Remhoogte Formation (Hartnady 1978), and emplaced the entire nappe complex over the Nama Group (Quinn thesis; et al., in prep). This simplification of the deformation and rejection of the former lithostratigraphic relationships undermines the estimation of large-scale tectonic displacements and the quantitative minimum displacement estimate of 78 km towards the southeast cannot be substantiated (Hartnady 1978).

The other quantitative displacement estimate of 90 km (Martin et al. 1983) relied on the correlation with the lower Damara Duruchaus Formation (of the Nosib Group, present limits of basin located 80-90 km to the north-northeast), as the basal Sole Dolomite of the Naukluft Nappe Complex was interpreted to be a mylonitic sludge containing a hot saline fluid derived from the evaporite beds of the Duruchaus Formation. However, a sedimentary origin for the basal décollement has been questioned with a tectonic co-seismic origin since advanced (Münch 1978; Viola et al. 2006, Rowe et al. 2012). This suggests that there may be no viable quantitative estimate for Naukluft Nappe Complex displacement. Association with the southern region of the Damara Belt is still expected given regional correlations, Kalahari Craton detrital zircon provenance, and the direction and timing of displacement (subsection 6.2; Hoffmann 1989; Miller 2008 Gray et al. 2008; Goscombe et al. 2017; Quinn thesis; et al., in prep). Yet the displacement distance may be significantly less than the 78 km minimum estimated by Hartnady (1978) and future work will be needed to better constrain the root location and exact tectonic context of Naukluft Nappe Complex within the Damara Orogen.

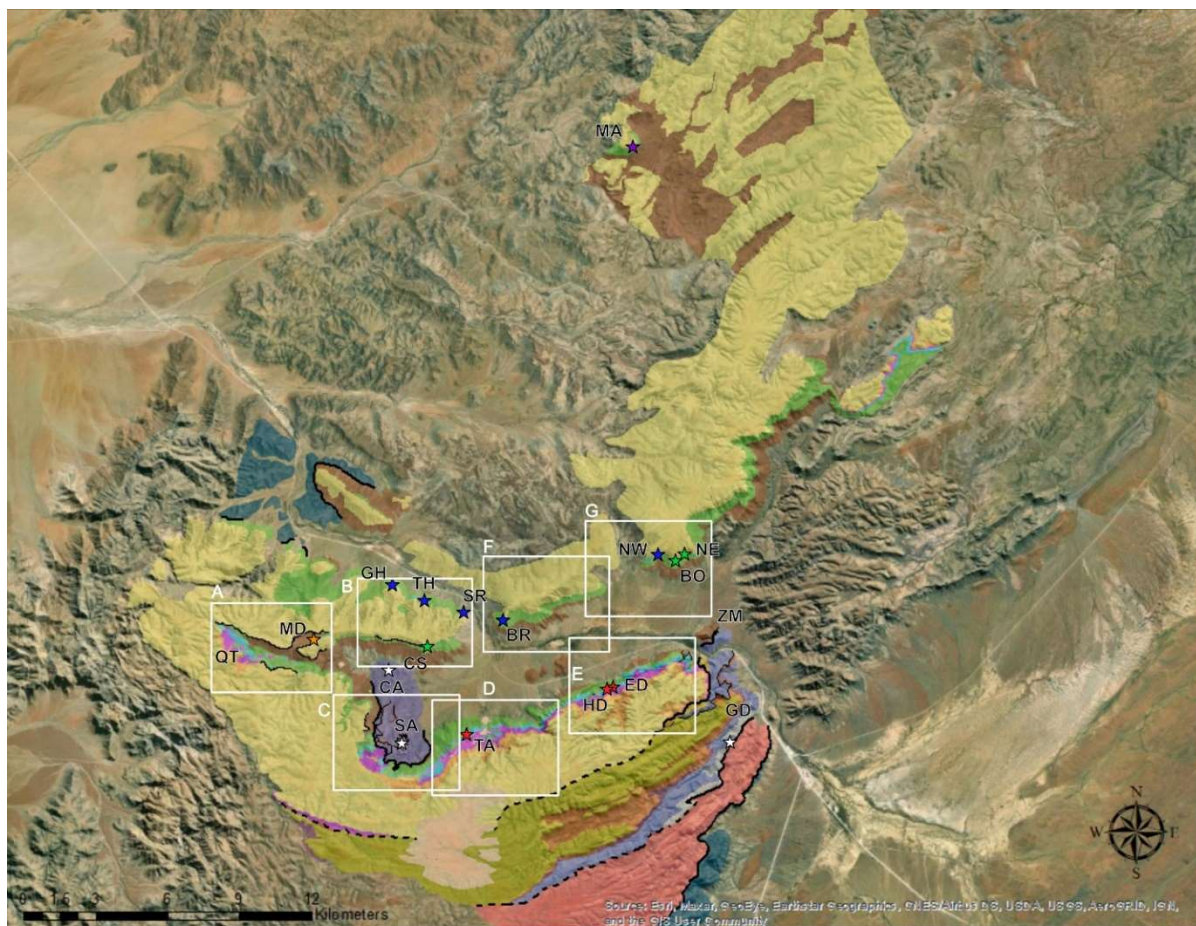
Chapter 3 supplementary data tables can be found at:

<https://doi.org/10.22002/hsdw4-6mz33>

Supplemental Table 3.1. Table for all $\delta^{13}\text{C}$ and $\delta^{18}\text{O}$ values shown in Fig. 3.12 and Supp. Fig. 3.3.

Supplemental Table 3.2. Table for all detrital zircon analytical geochronology values shown in Fig. 3.13. See text for explanation of methods and analysis.

Chapter 3 Supplemental Figures:



Stratigraphic Units

Main Succession

	Noab Fm. Upper Mbr.
	Noab Fm. Sedimentary Breccia Mbr.
	Tsabisis Fm. Upper Mbr.
	Tsabisis Fm. Middle Mbr.
	Tsabisis Fm. Tsondab Mbr.
	Blässkranz Fm.
	Remhoogte Fm.

Legend

Southern Pavian Nappe Succession

	Adelt Fm. Dolostone Mbr.
	Adelt Fm. Limestone Mbr.
	Adelt Fm. Shale Mbr.
	Adelt Fm. Tubestone Mbr.
	Aabschlucht Fm.

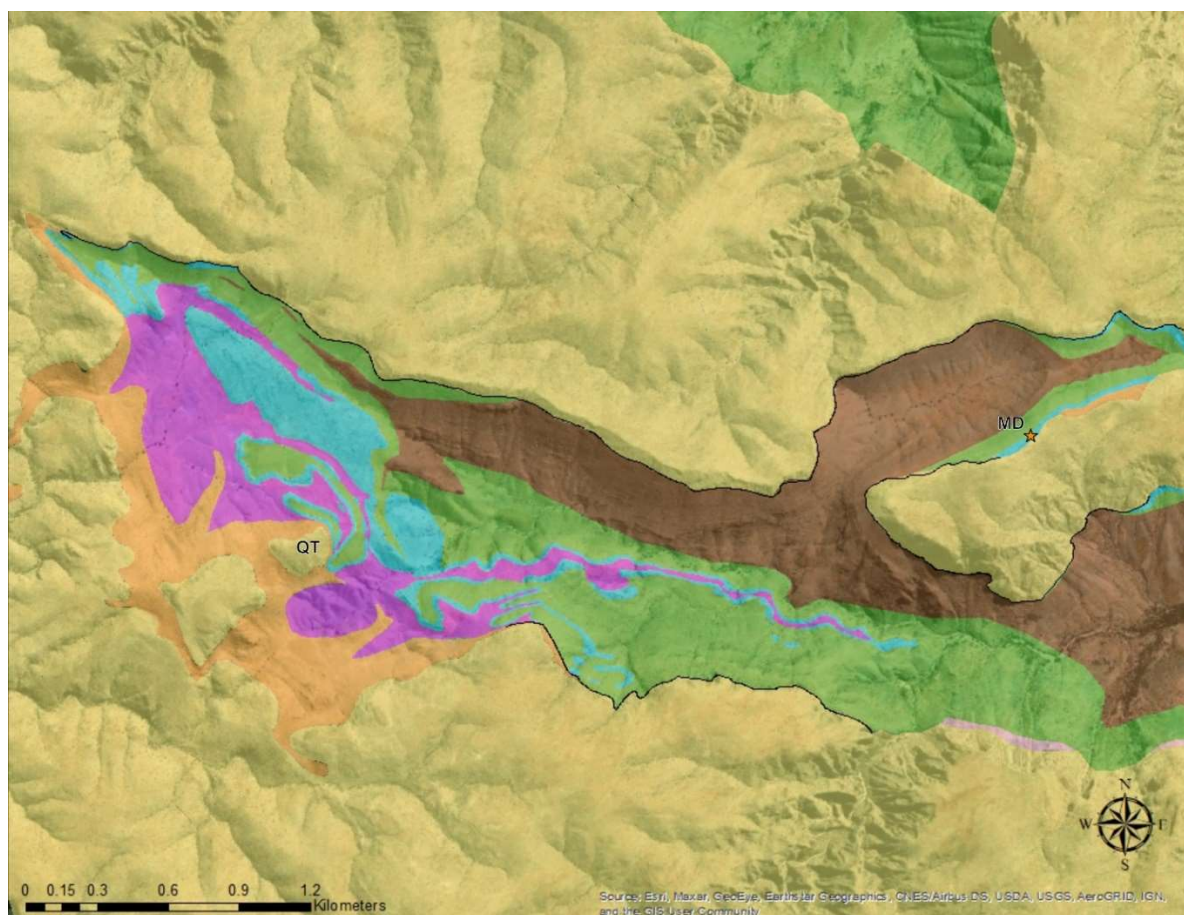
Other Regional Units

	Tufa & Cover
	Nama Group (~Late Ediacaran)
	Büllsport Formation

Structure

	Nappe Bounding Thrust Fault/Inferred
	Nappe Internal Thrust Fault/Inferred

Supplemental Figure 3.1. White boxes show the locations of the following map views. Boxes A, B, and C roughly correspond to the Arbeit Adelt farm boundaries (now part of the Namib-Naukluft National Park). D, E, F, and G roughly correspond to the Blässkranz farm. The GD locality is primarily within the Büllsport farm. The MD localities is within the Noab farm.



Stratigraphic Units

Main Succession

- Noab Fm. Upper Mbr.
- Noab Fm. Sedimentary Breccia Mbr.
- Tsabisis Fm. Upper Mbr.
- Tsabisis Fm. Middle Mbr.
- Tsabisis Fm. Tsondab Mbr.
- Blässkranz Fm.
- Remhoogte Fm.

Legend

Southern Pavian Nappe Succession

- Adelt Fm. Dolostone Mbr.
- Adelt Fm. Limestone Mbr.
- Adelt Fm. Shale Mbr.
- Adelt Fm. Tubestone Mbr.
- Aubschlucht Fm.

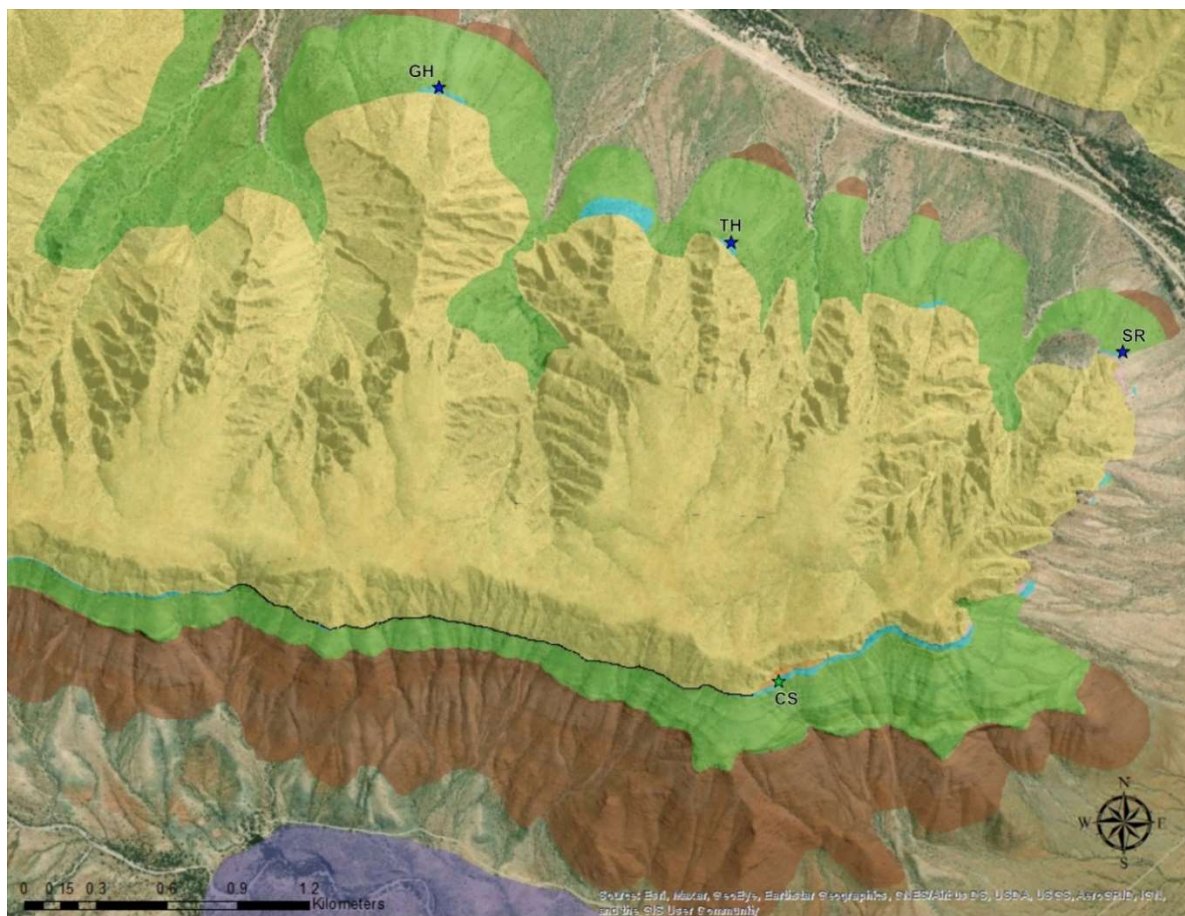
Other Regional Units

- Tufa & Cover
- Nama Group (~Late Ediacaran)
- Büllsport Formation

Structure

- Nappe Bounding Thrust Fault/Inferred
- Nappe Internal Thrust Fault/Inferred

Supplemental Figure 3.1A. Extensive folded of the Tsondab member in the QT area. Stratigraphically, the Tsabisis Formation in the QT area is similar to that shown in for the TA locality. The MD locality is one of the best preserved outcrops of the Tsondab member in the Naukluft and shows lateral transition of facies from those shown in the updip TA localities to more intermediate platform positions (Supp. Fig. 2).



Stratigraphic Units

Main Succession

- Noab Fm. Upper Mbr.
- Noab Fm. Sedimentary Breccia Mbr.
- Tsabisis Fm. Upper Mbr.
- Tsabisis Fm. Middle Mbr.
- Tsabisis Fm. Tsondab Mbr.
- Blässkranz Fm.
- Remhoogte Fm.

Legend

Southern Pavian Nappe Succession

- Adelt Fm. Dolostone Mbr.
- Adelt Fm. Limestone Mbr.
- Adelt Fm. Shale Mbr.
- Adelt Fm. Tubestone Mbr.
- Aubschlucht Fm.

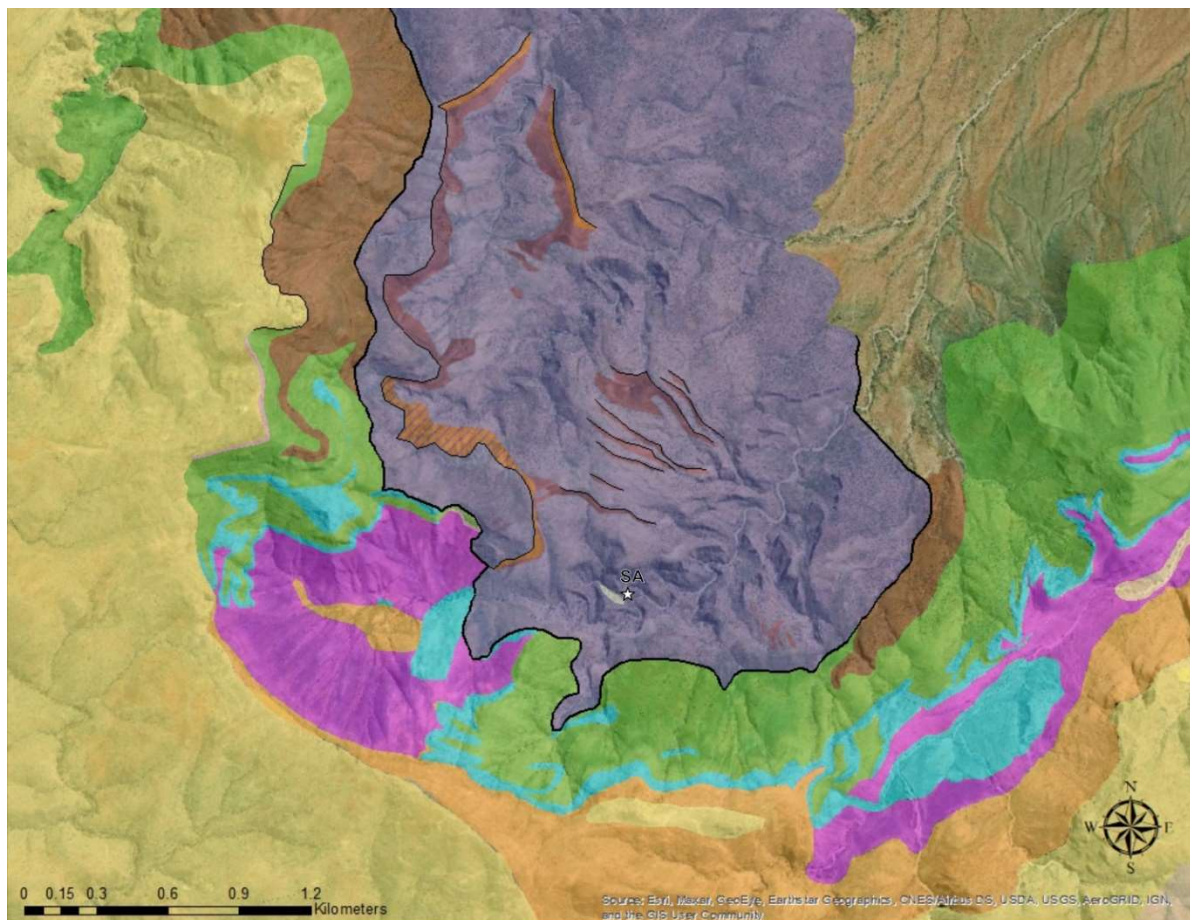
Other Regional Units

- Tufa & Cover
- Nama Group (~Late Ediacaran)
- Büllsport Formation

Structure

- Nappe Bounding Thrust Fault/Inferred
- Nappe Internal Thrust Fault/Inferred

Supplemental Figure 3.1B. Difficult to find outcrops of the Tsondab member mapped below the Noab Formation in this area provided immediate and downdip platform exposes with critical stratigraphic information (Supp. Fig. 2; Morris & Grotzinger 2023).



Stratigraphic Units

Main Succession

- Noab Fm. Upper Mbr.
- Noab Fm. Sedimentary Breccia Mbr.
- Tsabisis Fm. Upper Mbr.
- Tsabisis Fm. Middle Mbr.
- Tsabisis Fm. Tsondab Mbr.
- Blässkranz Fm.
- Remhoogte Fm.

Legend

Southern Pavian Nappe Succession

- Adelt Fm. Dolostone Mbr.
- Adelt Fm. Limestone Mbr.
- Adelt Fm. Shale Mbr.
- Adelt Fm. Tubestone Mbr.
- Aabschlucht Fm.

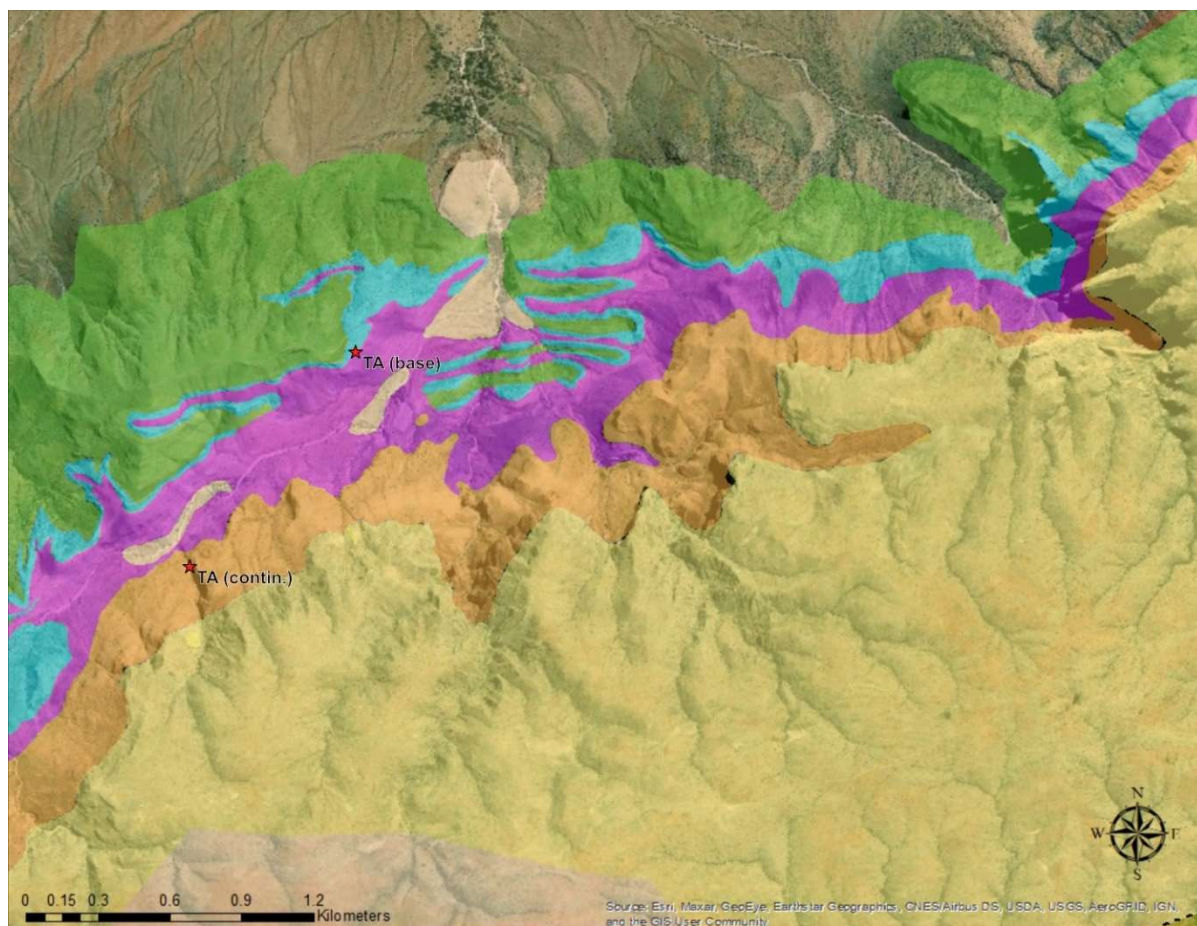
Other Regional Units

- Tufa & Cover
- Nama Group (~Late Ediacaran)
- Büllsport Formation

Structure

- Nappe Bounding Thrust Fault/Inferred
- Nappe Internal Thrust Fault/Inferred

Supplemental Figure 3.1C. Structurally complex region shows internal imbrication of the Adelt formation and exclusively tectonic contacts between the Southern Pavian and Northern Pavian nappe units.



Stratigraphic Units

Main Succession

- Noab Fm. Upper Mbr.
- Noab Fm. Sedimentary Breccia Mbr.
- Tsabisis Fm. Upper Mbr.
- Tsabisis Fm. Middle Mbr.
- Tsabisis Fm. Tsondab Mbr.
- Blässkranz Fm.
- Remhoogte Fm.

Legend

Southern Pavian Nappe Succession

- Adelt Fm. Dolostone Mbr.
- Adelt Fm. Limestone Mbr.
- Adelt Fm. Shale Mbr.
- Adelt Fm. Tubestone Mbr.
- Aabschlucht Fm.

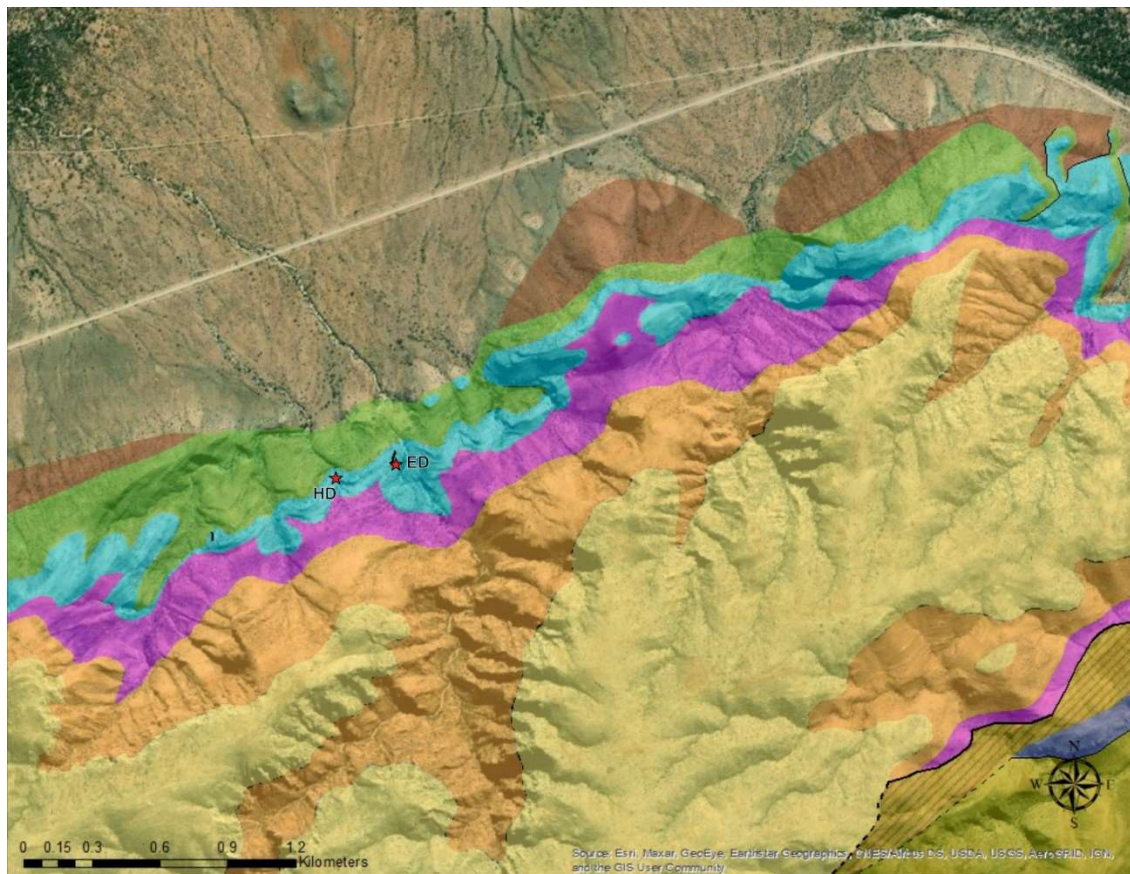
Other Regional Units

- Tufa & Cover
- Nama Group (~Late Ediacaran)
- Büllsport Formation

Structure

- Nappe Bounding Thrust Fault/Inferred
- Nappe Internal Thrust Fault/Inferred

Supplemental Figure 3.1D. Heavily folded exposes for the Tsabisis Formation provided the stratigraphy measured for the TA locality, which continued from the Tsondab member to the plateau top of the Noab Formation.



Stratigraphic Units

- Main Succession*
- Noab Fm. Upper Mbr.
 - Noab Fm. Sedimentary Breccia Mbr.
 - Tsabisis Fm. Upper Mbr.
 - Tsabisis Fm. Middle Mbr.
 - Tsabisis Fm. Tsondab Mbr.
 - Blässkranz Fm.
 - Remhoogte Fm.

Legend

- Southern Pavian Nappe Succession*
- Adelt Fm. Dolostone Mbr.
 - Adelt Fm. Limestone Mbr.
 - Adelt Fm. Shale Mbr.
 - Adelt Fm. Tubestone Mbr.
 - Aubschlucht Fm.
- Other Regional Units*
- Tufa & Cover
 - Nama Group (~Late Ediacaran)
 - Büllsport Formation
- Structure**
- Nappe Bounding Thrust Fault/Inferred
 - Nappe Internal Thrust Fault/Inferred

Supplemental Figure 3.1E. Well exposed folds of the Tsabisis Formation shown in Fig. 3.5B.



Stratigraphic Units

Main Succession

- Noab Fm. Upper Mbr.
- Noab Fm. Sedimentary Breccia Mbr.
- Tsabisis Fm. Upper Mbr.
- Tsabisis Fm. Middle Mbr.
- Tsabisis Fm. Tsondab Mbr.
- Blässkranz Fm.
- Remhoogte Fm.

Legend

Southern Pavian Nappe Succession

- Adelt Fm. Dolostone Mbr.
- Adelt Fm. Limestone Mbr.
- Adelt Fm. Shale Mbr.
- Adelt Fm. Tubestone Mbr.
- Aabschlucht Fm.

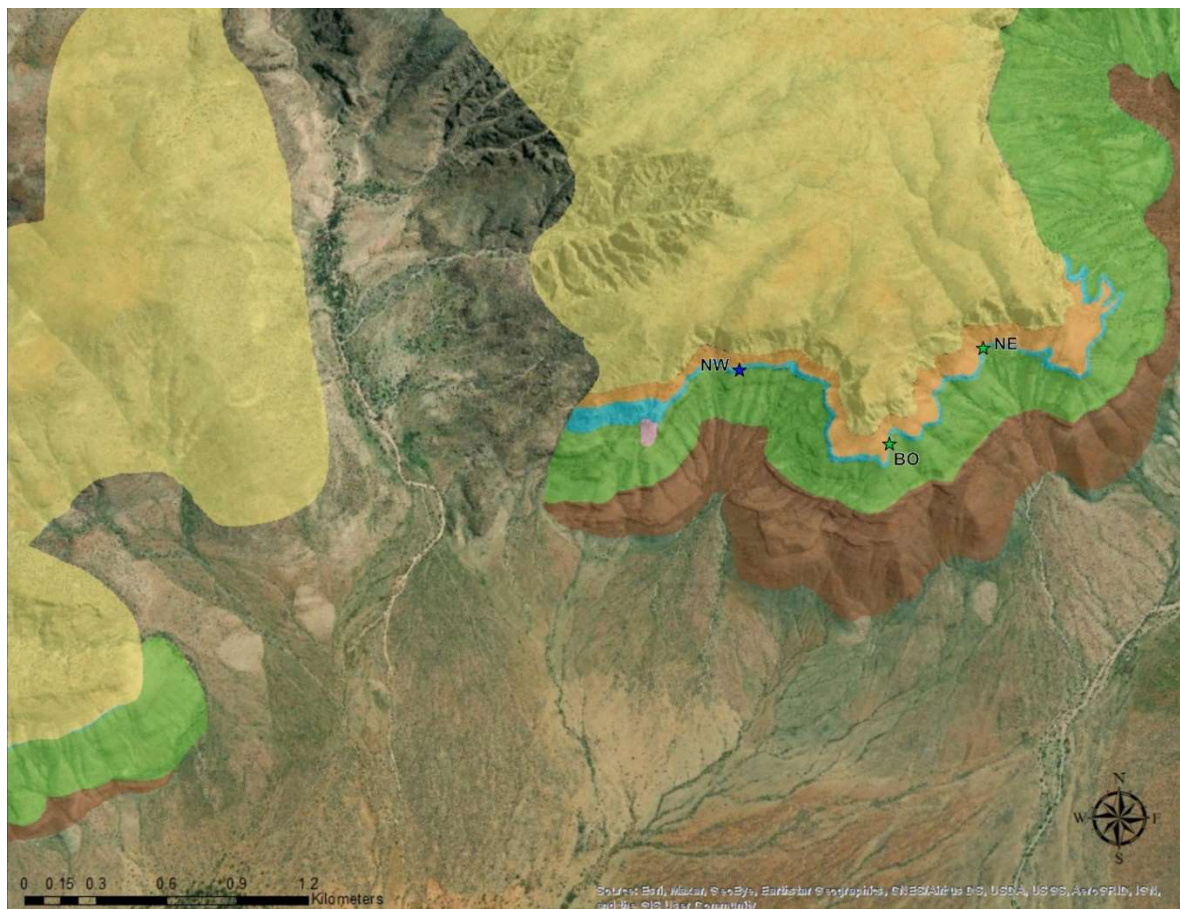
Other Regional Units

- Tufa & Cover
- Nama Group (~Late Ediacaran)
- Büllsport Formation

Structure

- Nappe Bounding Thrust Fault/Inferred
- Nappe Internal Thrust Fault/Inferred

Supplemental Figure 3.1F. Eastward of the BR outcrop of the Tsondab member, much of the base of the Noab Formation shows exposures of the sedimentary breccia member.



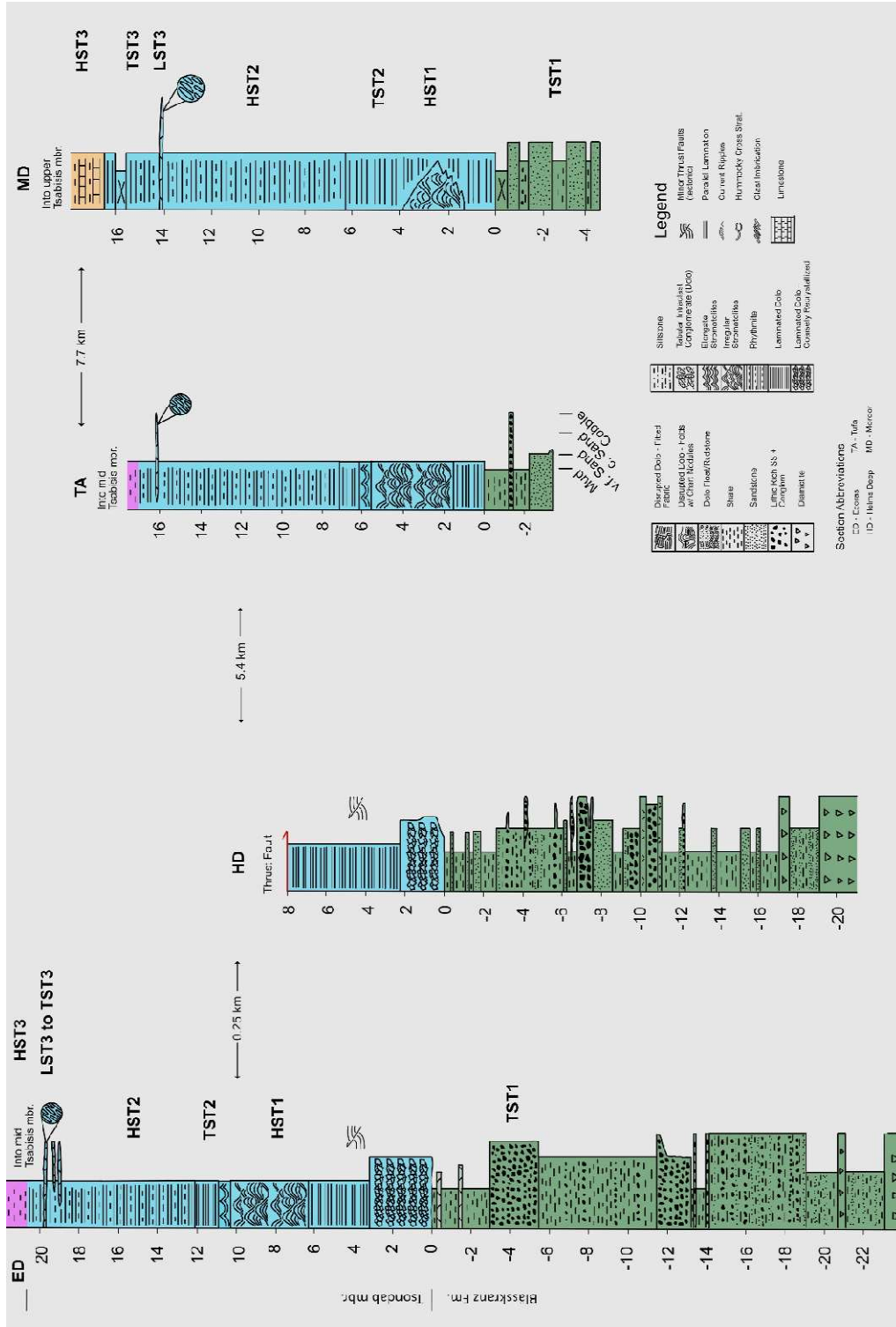
Stratigraphic Units

- Main Succession*
- Noab Fm. Upper Mbr.
 - Noab Fm. Sedimentary Breccia Mbr.
 - Tsabisis Fm. Upper Mbr.
 - Tsabisis Fm. Middle Mbr.
 - Tsabisis Fm. Tsondab Mbr.
 - Blässkranz Fm.
 - Remhoogte Fm.

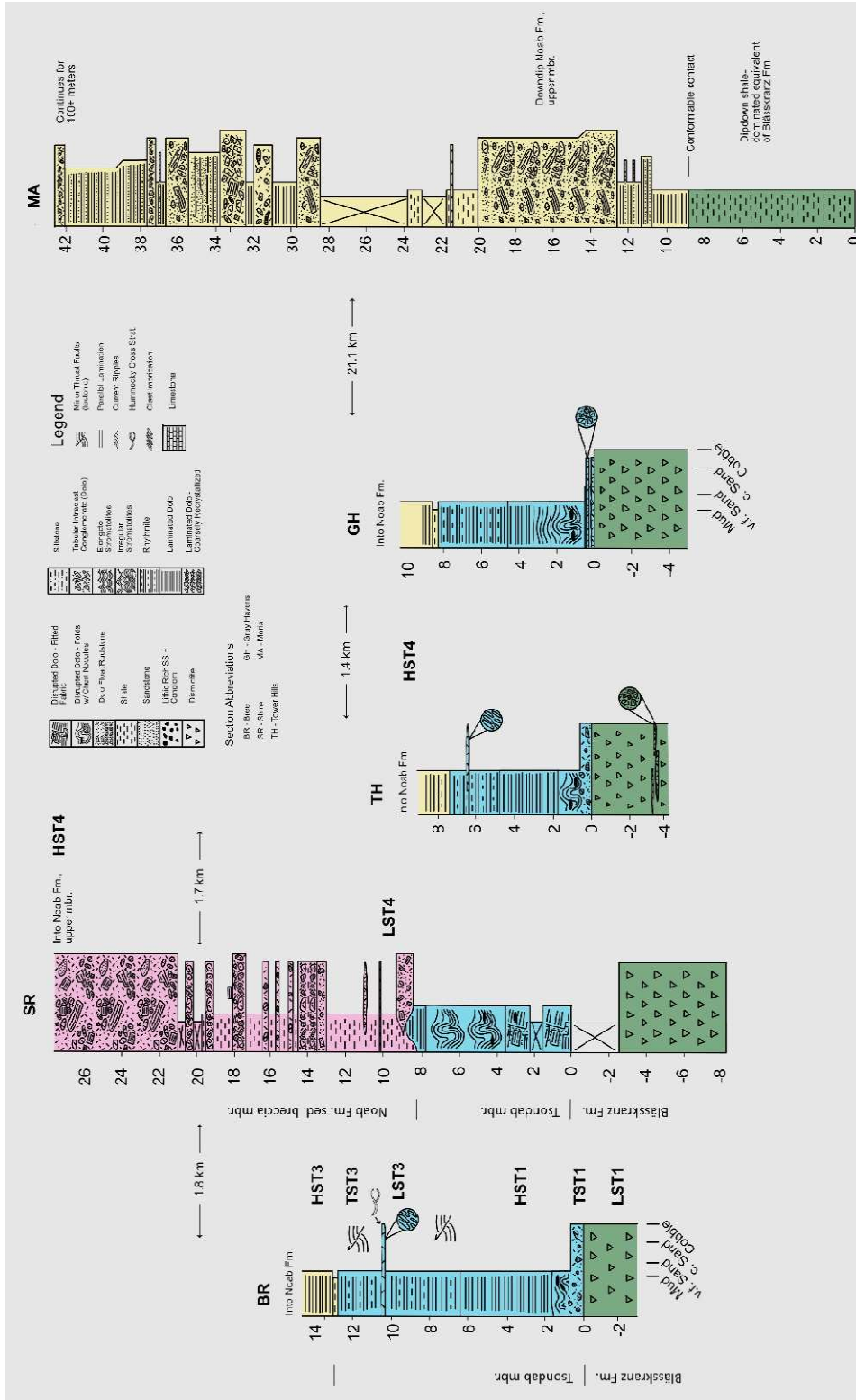
Legend

- Southern Pavian Nappe Succession*
- Adelt Fm. Dolostone Mbr.
 - Adelt Fm. Limestone Mbr.
 - Adelt Fm. Shale Mbr.
 - Adelt Fm. Tubestone Mbr.
 - Aabschlucht Fm.
- Other Regional Units*
- Tufa & Cover
 - Nama Group (~Late Ediacaran)
 - Büllsport Formation
- Structure**
- Nappe Bounding Thrust Fault/Inferred
 - Nappe Internal Thrust Fault/Inferred

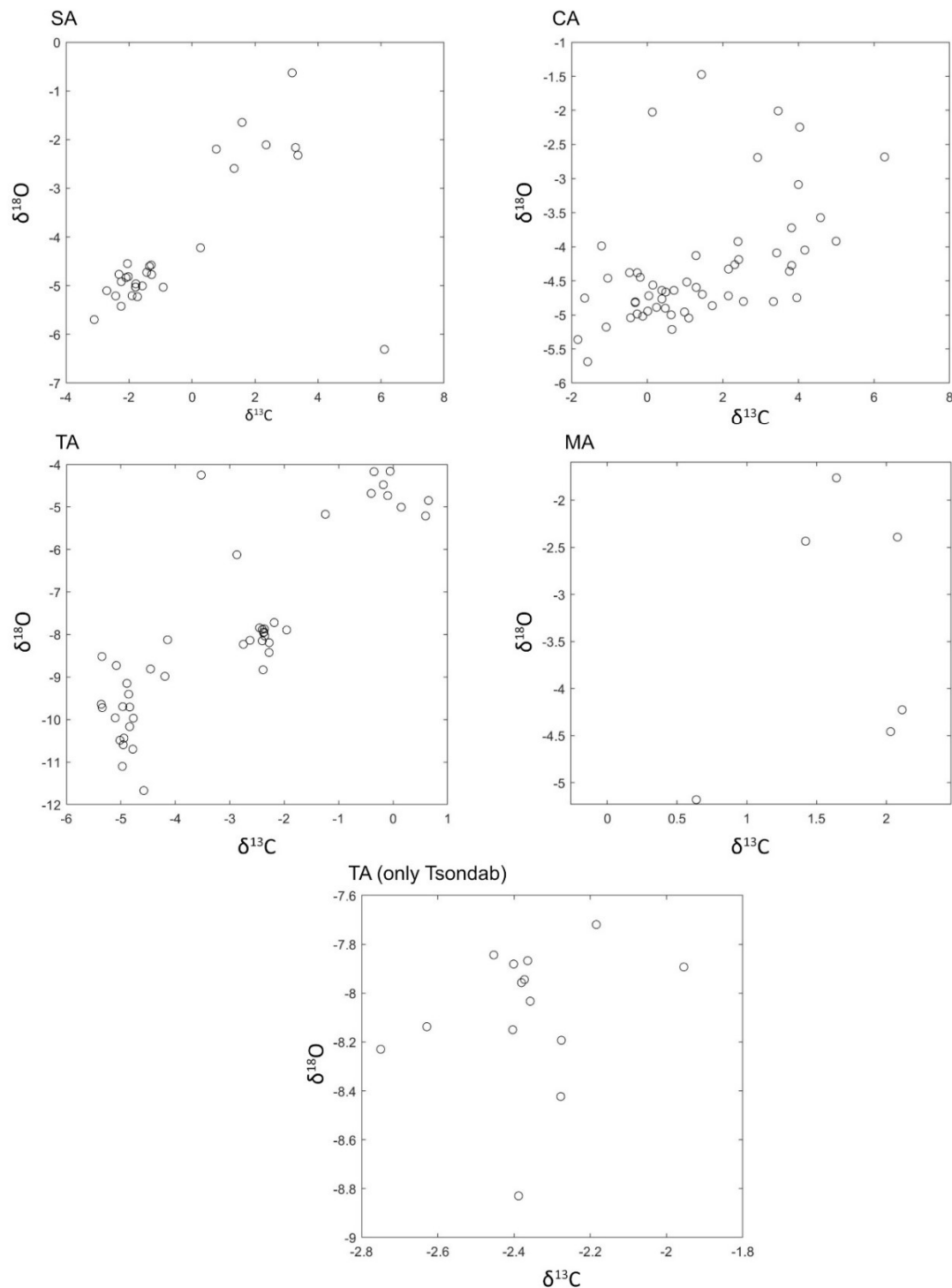
Supplemental Figure 3.1G. Well exposed stratigraphic exposures from the Remhoogte Formation to the plateau top of the Noab Formation.



Supplemental Figure 3.2B.



Supplemental Figure 3.2D.



Supplemental Figure 3.3. Cross plots of carbon and oxygen isotope values for different localities corresponding to the profiles shown in Fig. 3.13 (‰ VPDB). The SA and full TA profiles show positive correlations between $\delta^{13}\text{C}$ and $\delta^{18}\text{O}$, suggesting they may have experienced significant diagenetic alteration. See text for discussion.

CHAPTER 3 REFERENCES

- Ahm, A. S. C., Bjerrum, C. J., Blättler, C. L., Swart, P. K., & Higgins, J. A. (2018). Quantifying early marine diagenesis in shallow-water carbonate sediments. *Geochimica et Cosmochimica Acta*, 236, 140-159.
- Andersen, T., Kristoffersen, M., & Elburg, M. A. (2016). How far can we trust provenance and crustal evolution information from detrital zircons? A South African case study. *Gondwana Research*, 34, 129-148.
- Andersen, T., Elburg, M. A., van Niekerk, H. S., & Ueckermann, H. (2018). Successive sedimentary recycling regimes in southwestern Gondwana: Evidence from detrital zircons in Neoproterozoic to Cambrian sedimentary rocks in southern Africa. *Earth-Science Reviews*, 181, 43-60.
- Axen, G. J., Wernicke, B. P., Skelly, M. F., & Taylor, W. J. (1990). Mesozoic and Cenozoic tectonics of the Sevier thrust belt in the Virgin River Valley area, southern Nevada.
- Bathurst, R. G. (1972). *Carbonate sediments and their diagenesis*. Elsevier.
- Billings, M. P. (1933). Thrusting younger rocks over older. *American Journal of Science*, 5(146), 140-165.
- Bosak, T., Mariotti, G., MacDonald, F. A., Perron, J. T., & Pruss, S. B. (2013). Microbial sedimentology of stromatolites in Neoproterozoic cap carbonates. *The Paleontological Society Papers*, 19, 51-76.
- Boyer, S. E., & Elliott, D. (1982). Thrust systems. *Aapg Bulletin*, 66(9), 1196-1230.
- Bold, U., Smith, E. F., Rooney, A. D., Bowring, S. A., Buchwaldt, R., Dudás, F. Ö., ... & Macdonald, F. A. (2016). Neoproterozoic stratigraphy of the Zavkhan terrane of Mongolia: The backbone for Cryogenian and early Ediacaran chemostratigraphic records. *American Journal of Science*, 316(1), 1-63.
- Cloud, P., Wright, L. A., Williams, E. G., Diehl, P., & Walter, M. R. (1974). Giant stromatolites and associated vertical tubes from the Upper Proterozoic Noonday Dolomite, Death Valley region, eastern California. *Geological Society of America Bulletin*, 85(12), 1869-1882.
- Corsetti, F. A., & Grotzinger, J. P. (2005). Origin and significance of tube structures in Neoproterozoic post-glacial cap carbonates: example from Noonday Dolomite, Death Valley, United States. *Palaios*, 20(4), 348-362.
- Creveling, J. R., Bergmann, K. D., & Grotzinger, J. P. (2016). Cap carbonate platform facies model, Noonday Formation, SE California. *GSA Bulletin*, 128(7-8), 1249-1269.
- Dickinson, W. R., & Gehrels, G. E. (2009). Use of U–Pb ages of detrital zircons to infer maximum depositional ages of strata: a test against a Colorado Plateau Mesozoic database. *Earth and Planetary Science Letters*, 288(1-2), 115-125.
- Engelder, T., & Marshak, S. (1985). Disjunctive cleavage formed at shallow depths in sedimentary rocks. *Journal of Structural Geology*, 7(3-4), 327-343.
- Fagereng, Å., Smith, Z., Rowe, C. D., Makhubu, B., & Sylvester, F. Y. (2014). Stress, strain, and fault behavior at a thrust ramp: Insights from the Naukluft thrust, Namibia. *Journal of Structural Geology*, 58, 95-107.
- Foster, D. A., Goscombe, B. D., Newstead, B., Mapani, B., Mueller, P. A., Gregory, L. C., & Muvangua, E. (2015). U–Pb age and Lu–Hf isotopic data of detrital zircons from the

- Neoproterozoic Damara Sequence: Implications for Congo and Kalahari before Gondwana. *Gondwana Research*, 28(1), 179-190.
- Gehrels, G., Valencia, V., & Pullen, A. (2006). Detrital zircon geochronology by laser-ablation multicollector ICPMS at the Arizona LaserChron Center. *The Paleontological Society Papers*, 12, 67-76.
- Gehrels, G.E., Valencia, V., Ruiz, J. (2008). Enhanced precision, accuracy, efficiency, and spatial resolution of U-Pb ages by laser ablation–multicollector–inductively coupled plasma–mass spectrometry: *Geochemistry, Geophysics, Geosystems*, v. 9, Q03017, doi:10.1029/2007GC001805.
- Gehrels, G. and Pecha, M. (2014). Detrital zircon U-Pb geochronology and Hf isotope geochemistry of Paleozoic and Triassic passive margin strata of western North America: *Geosphere*, v. 10 (1), p. 49-65.
- Germis, G. J. B. (1983). Implications of a sedimentary facies and depositional environmental analysis of the Nama Group in South West Africa/Namibia.
- Germis, GJB* & Gresse, P. (1991). The foreland basin of the Damara and Gariep orogens in Namaqualand and southern Namibia: stratigraphic correlations and basin dynamics. *South African Journal of Geology*, 94(2), 159-169.
- Goscombe, B., Foster, D. A., Gray, D., & Wade, B. (2017). Metamorphic response and crustal architecture in a classic collisional orogen: the Damara Belt, Namibia. *Gondwana Research*, 52, 80-124.
- Gray, D. (1977). Morphologic classification of crenulation cleavage. *The Journal of Geology*, 85(2), 229-235.
- Gray, D. R., Foster, D. A., Meert, J. G., Goscombe, B. D., Armstrong, R., Trouw, R. A. J., & Passchier, C. W. (2008). A Damara orogen perspective on the assembly of southwestern Gondwana. *Geological Society, London, Special Publications*, 294(1), 257-278.
- Grotzinger, J. P. (1986). Evolution of Early Proterozoic passive-margin carbonate platform, rocknest formation, wopmay orogen, Northwest Territories, Canada. *Journal of Sedimentary Research*, 56(6), 831-847.
- Grotzinger, J. P., Bowring, S. A., Saylor, B. Z., & Kaufman, A. J. (1995). Biostratigraphic and geochronologic constraints on early animal evolution. *Science*, 270(5236), 598-604.
- Grotzinger, J. P., Watters, W. A., & Knoll, A. H. (2000). Calcified metazoans in thrombolite-stromatolite reefs of the terminal Proterozoic Nama Group, Namibia. *Paleobiology*, 26(3), 334-359.
- Halverson, G. P., & Shields-Zhou, G. (2011). Chemostratigraphy and the Neoproterozoic glaciations. *Geological Society, London, Memoirs*, 36(1), 51-66.
- Hartman, J., Franks, R., Gehrels, G., Hourigan, J., and Wenig, P. 2017, Decoding files from a Thermo Element ICP Mass Spectrometer: Archiv.org (ark:/13960/t3jx4rd3b)
- Hartnady, C. J. H. (1978). The structural geology of the Naukluft Nappe Complex and its relationship to the Damara Orogenic Belt, South West Africa/Namibia. [Doctoral dissertation, University of Cape Town]. <http://hdl.handle.net/11427/18057>
- Hartnady, C. J. H. (1980). Geological map of the Naukluft area, *Precambrian Research Unit, University of Cape Town*.
- Hiscott, R. N., & James, N. P. (1985). Carbonate debris flows, Cow Head Group, western Newfoundland. *Journal of Sedimentary Research*, 55(5), 735-745.
- Hoffman, P. (1974). Shallow and deepwater stromatolites in Lower Proterozoic platform–to–basin facies change, Great Slave Lake, Canada. *AAPG Bulletin*, 58(5), 856-867.

- Hoffmann, K. H. (1989). New aspects of lithostratigraphic subdivision and correlation of late Proterozoic to early Cambrian rocks of the southern Damara Belt and their correlation with the central and northern Damara Belt and the Gariiep Belt.
- Hoffman, P. F., Kaufman, A. J., Halverson, G. P., & Schrag, D. P. (1998). A Neoproterozoic snowball earth. *science*, 281(5381), 1342-1346.
- Hoffman, P. F., & Schrag, D. P. (2002). The snowball Earth hypothesis: testing the limits of global change. *Terra nova*, 14(3), 129-155.
- Hoffman, P. F., Halverson, G. P., Domack, E. W., Husson, J. M., Higgins, J. A., & Schrag, D. P. (2007). Are basal Ediacaran (635 Ma) post-glacial “cap dolostones” diachronous?. *Earth and Planetary Science Letters*, 258(1-2), 114-131.
- Hoffman, P. F. (2011). Strange bedfellows: glacial diamictite and cap carbonate from the Marinoan (635 Ma) glaciation in Namibia. *Sedimentology*, 58(1), 57-119.
- Hoffman, P. F., Abbot, D. S., Ashkenazy, Y., Benn, D. I., Brocks, J. J., Cohen, P. A., ... & Warren, S. G. (2017). Snowball Earth climate dynamics and Cryogenian geology-geobiology. *Science Advances*, 3(11), e1600983.
- Hoffman, P. F., Halverson, G. P., Schrag, D. P., Higgins, J. A., Domack, E. W., Macdonald, F. A., ... & Nelson, L. L. (2021). Snowballs in Africa: sectioning a long-lived Neoproterozoic carbonate platform and its bathyal foreslope (NW Namibia). *Earth-Science Reviews*, 219, 103616.
- James, N. P. (1981). Megablocks of calcified algae in the Cow Head Breccia, western Newfoundland: Vestiges of a Cambro-Ordovician platform margin. *Geological Society of America Bulletin*, 92(11), 799-811.
- James, N. P., Narbonne, G. M., & Kyser, T. K. (2001). Late Neoproterozoic cap carbonates: Mackenzie Mountains, northwestern Canada: precipitation and global glacial meltdown. *Canadian Journal of Earth Sciences*, 38(8), 1229-1262.
- Jiang, G., Kennedy, M. J., & Christie-Blick, N. (2003). Stable isotopic evidence for methane seeps in Neoproterozoic postglacial cap carbonates. *Nature*, 426(6968), 822-826.
- Kennedy, M. J. (1996). Stratigraphy, sedimentology, and isotopic geochemistry of Australian Neoproterozoic postglacial cap dolostones; deglaciation, delta 13 C excursions, and carbonate precipitation. *Journal of sedimentary Research*, 66(6), 1050-1064.
- Kirschvink, Joseph L. (1992) Late Proterozoic Low-Latitude Global Glaciation: the Snowball Earth. In: J.W. Schopf, C. Klein, & D. Des Maris (eds), *The Proterozoic Biosphere: A Multidisciplinary Study*. Cambridge University Press, pp. 51-52.
- Korn, H., & Martin, H. (1959). Gravity tectonics in the Naukluft mountains of South West Africa. *Geological Society of America Bulletin*, 70(8), 1047-1078.
- Liu, C., Wang, Z., & Macdonald, F. A. (2018). Sr and Mg isotope geochemistry of the basal Ediacaran cap limestone sequence of Mongolia: Implications for carbonate diagenesis, mixing of glacial meltwaters, and seawater chemistry in the aftermath of Snowball Earth. *Chemical Geology*, 491, 1-13.
- Logan, B. W. (1974). Inventory of diagenesis in Holocene-recent carbonate sediments, Shark Bay, Western Australia. In *Evolution and Diagenesis of Quaternary Carbonate Sequences, Shark Bay, Western Australia* (pp. 195-249).
- Lønne, I. (1995). Sedimentary facies and depositional architecture of ice-contact glaciomarine systems. *Sedimentary Geology*, 98(1-4), 13-43.

- Lowe, D. R. (1982). Sediment gravity flows; II, Depositional models with special reference to the deposits of high-density turbidity currents. *Journal of sedimentary research*, 52(1), 279-297.
- Macdonald, F. A., Jones, D. S., & Schrag, D. P. (2009). Stratigraphic and tectonic implications of a newly discovered glacial diamictite–cap carbonate couplet in southwestern Mongolia. *Geology*, 37(2), 123-126.
- Martin, H., Porada, H., & Wittig, R. (1983). The root zone of the Naukluft Nappe Complex: geodynamic implications. In *Intracontinental Fold Belts: Case Studies in the Variscan Belt of Europe and the Damara Belt in Namibia* (pp. 679-698). Springer Berlin Heidelberg.
- McKay, M. P., Weislogel, A. L., Fildani, A., Brunt, R. L., Hodgson, D. M., & Flint, S. S. (2015). U-PB zircon tuff geochronology from the Karoo Basin, South Africa: implications of zircon recycling on stratigraphic age controls. *International Geology Review*, 57(4), 393-410.
- McIlreath, I., and N. James. "Facies models 13. Carbonate slopes." *Geoscience Canada* 5.4 (1978): 189-199.
- Miller, R. M. (2008). Neoproterozoic and early Palaeozoic rocks of the Damara Orogen. *The geology of Namibia*, 2, 13-1.
- Morris, F. K., & Grotzinger, J. P. (2023). Facies and stratigraphy of the basal Ediacaran cap carbonate, Naukluft Mountains, Namibia. *Precambrian Research*, 394, 107113.
- Morley, C. K. (1988). Out-of-sequence thrusts. *Tectonics*, 7(3), 539-561.
- Münch, H. G. (1978). Das Schmiermittel an der Basis der Naukluft-Decke, Südwestafrika. *Zeitschrift der Deutschen Geologischen Gesellschaft*, 7-31.
- Myrow, P. M. (1990). A new graph for understanding colors of mudrocks and shales. *Journal of Geological Education*, 38(1), 16-20.
- Myrow, P. M., & Kaufman, A. J. (1999). A newly discovered cap carbonate above Varanger-age glacial deposits in Newfoundland, Canada. *Journal of Sedimentary Research*, 69(3), 784-793.
- Nelson, L. L., Ramezani, J., Almond, J. E., Darroch, S. A., Taylor, W. L., Brenner, D. C., ... & Smith, E. F. (2022). Pushing the boundary: a calibrated Ediacaran-Cambrian stratigraphic record from the Nama Group in northwestern Republic of South Africa. *Earth and Planetary Science Letters*, 580, 117396.
- Pace, P., Domenica, A. D., & Calamita, F. (2014). Summit low-angle faults in the Central Apennines of Italy: Younger-on-older thrusts or rotated normal faults? Constraints for defining the tectonic style of thrust belts. *Tectonics*, 33(5), 756-785.
- Porter, S. M., Knoll, A. H., & Affaton, P. (2004). Chemostratigraphy of Neoproterozoic cap carbonates from the Volta basin, West Africa. *Precambrian Research*, 130(1-4), 99-112.
- Powell, C. M. (1979). A morphological classification of rock cleavage. *Tectonophysics*, 58(1-2), 21-34.
- Powell, R. D. (1981). A model for sedimentation by tidewater glaciers. *Annals of Glaciology*, 2, 129-134.
- Prave, A. R., Hoffmann, K. H., Hegenberger, W., & Fallick, A. E. (2011). The Witvlei Group of east-central Namibia. *Geological Society, London, Memoirs*, 36(1), 211-216.
- Pu, J. P., Bowring, S. A., Ramezani, J., Myrow, P., Raub, T. D., Landing, E., ... & Macdonald, F. A. (2016). Dodging snowballs: Geochronology of the Gaskiers glaciation and the first appearance of the Ediacaran biota. *Geology*, 44(11), 955-958.
- Pullen, A., Ibanez-Mejia, M., Gehrels, G., Giesler, D., and Pecha, M., 2018, Optimization of a Laser Ablation-Single Collector-Inductively Coupled Plasma-Mass Spectrometer (Thermo

- Element 2) for Accurate, Precise, and Efficient Zircon U-Th-Pb Geochronology: *Geochemistry, Geophysics, Geosystems*, v. 19 (10), p. 3689-3705. <https://doi.org/10.1029/2018GC007889>
- Quinn, D. P., (2018). *Regional Structural Geology of Earth and Mars*. Dissertation (Ph.D.), California Institute of Technology. doi:10.7907/9enj-wn23.
- Quinn, D. P., (in prep). *Tectonostratigraphy of the Zebra Nappe, a structurally displaced Ediacaran passive margin in the southern Naukluft Mountains, Namibia*. *Gondwana Research*.
- Ramsay, J. G., Casey, M., & Kligfield, R. (1983). Role of shear in development of the Helvetic fold-thrust belt of Switzerland. *Geology*, 11(8), 439-442.
- Rooney, A. D., Cantine, M. D., Bergmann, K. D., Gómez-Pérez, I., Al Baloushi, B., Boag, T. H., ... & Strauss, J. V. (2020). Calibrating the coevolution of Ediacaran life and environment. *Proceedings of the National Academy of Sciences*, 117(29), 16824-16830.
- Rosenbaum, J., & Sheppard, S. M. F. (1986). An isotopic study of siderites, dolomites and ankerites at high temperatures. *Geochimica et cosmochimica acta*, 50(6), 1147-1150.
- Rowe, C. D., Fagereng, Å., Miller, J. A., & Mapani, B. (2012). Signature of coseismic decarbonation in dolomitic fault rocks of the Naukluft Thrust, Namibia. *Earth and Planetary Science Letters*, 333, 200-210.
- Rubidge, B. S., Erwin, D. H., Ramezani, J., Bowring, S. A., & de Klerk, W. J. (2013). High-precision temporal calibration of Late Permian vertebrate biostratigraphy: U-Pb zircon constraints from the Karoo Supergroup, South Africa. *Geology*, 41(3), 363-366.
- Saylor, B. Z., Grotzinger, J. P., & Germs, G. J. (1995). Sequence stratigraphy and sedimentology of the Neoproterozoic Kuibis and Schwarzrand subgroups (Nama Group), southwestern Namibia. *Precambrian Research*, 73(1-4), 153-171
- Shen, W., Zhu, X., Yan, B., Qin, H., Gao, Z., & Li, F. (2021). Sequence stratigraphy of the Cryogenian Nantuo Formation in South China: Constraints on Marinoan glaciation dynamics. *Journal of Asian Earth Sciences*, 214, 104776.
- Sherman, A. G., James, N. P., & Narbonne, G. M. (2000). Sedimentology of a late Mesoproterozoic muddy carbonate ramp, northern Baffin Island, Arctic Canada.
- Sui, Y., Huang, C., Zhang, R., Wang, Z., Ogg, J., & Kemp, D. B. (2018). Astronomical time scale for the lower Doushantuo Formation of early Ediacaran, South China. *Science bulletin*, 63(22), 1485-1494.
- Sumner, D. Y., & Grotzinger, J. P. (1993). Numerical modeling of ooid size and the problem of Neoproterozoic giant ooids. *Journal of Sedimentary Research*, 63(5), 974-982.
- Sundell, K.E., Gehrels, G.E., and Pecha, M.E., 2021, Rapid U-Pb Geochronology by Laser Ablation Multi-Collector: *Geostandards and Geoanalytical Research*, v. 45 (1), p. 37-57. doi.org/10.1111/ggr.12355
- Swart, P. K., Burns, S. J., & Leder, J. J. (1991). Fractionation of the stable isotopes of oxygen and carbon in carbon dioxide during the reaction of calcite with phosphoric acid as a function of temperature and technique. *Chemical Geology: Isotope Geoscience section*, 86(2), 89-96.
- Swart, P. K. (2015). The geochemistry of carbonate diagenesis: The past, present and future. *Sedimentology*, 62(5), 1233-1304.
- Viola, G., Mancktelow, N. S., & Miller, J. A. (2006). Cyclic frictional-viscous slip oscillations along the base of an advancing nappe complex: Insights into brittle-ductile nappe emplacement mechanisms from the Naukluft Nappe Complex, central Namibia. *Tectonics*, 25(3).

- Whalen, M. T., Eberli, G. P., Van Buchem, F. S., Mountjoy, E. W., & Homewood, P. W. (2000). Bypass margins, basin-restricted wedges, and platform-to-basin correlation, Upper Devonian, Canadian Rocky Mountains: implications for sequence stratigraphy of carbonate platform systems. *Journal of Sedimentary Research*, 70(4), 913-936.
- Wood, R. A., Grotzinger, J. P., & Dickson, J. A. D. (2002). Proterozoic modular biomineralized metazoan from the Nama Group, Namibia. *Science*, 296(5577), 2383-2386.
- Xiao, S., Narbonne, G. M., Zhou, C., Laflamme, M., Grazhdankin, D. V., Moczydlowska-Vidal, M., & Cui, H. (2016). Towards an Ediacaran time scale: problems, protocols, and prospects. *Episodes Journal of International Geoscience*, 39(4), 540-555.
- Yu, W., Algeo, T. J., Zhou, Q., Du, Y., & Wang, P. (2020). Cryogenian cap carbonate models: A review and critical assessment. *Palaeogeography, Palaeoclimatology, Palaeoecology*, 552, 109727.
- Zieger, J., Harazim, S., Hofmann, M., Gärtner, A., Gerdes, A., Marko, L., & Linnemann, U. (2020). Mesozoic deposits of SW Gondwana (Namibia): unravelling Gondwanan sedimentary dispersion drivers by detrital zircon. *International Journal of Earth Sciences*, 109, 1683-1704.

*Chapter 4***MELTING THE MARINOAN SNOWBALL EARTH: THE IMPACT OF DEGLACIATION DURATION ON THE SEA-LEVEL HISTORY OF CONTINENTAL MARGINS**

Authors: Freya K. Morris ^{a*}, Tamara Pico ^b, Jessica R. Creveling ^c, John Grotzinger ^a

^a *Department of Geological and Planetary Sciences, California Institute of Technology, Pasadena, CA 91125, USA*

^b *Department of Earth and Planetary Sciences, UC Santa Cruz, Santa Cruz, CA 95064, USA*

^c *College of Earth, Ocean, and Atmospheric Sciences, Oregon State University, Corvallis, OR 97331*

* *Corresponding Author: morrisfreya15@outlook.com*

Abstract: The termination of the Marinoan Snowball Earth (~635 Ma) represents a significant transition in Earth's climate. Cap carbonate strata, and underlying glaciogenic deposits, record global deglaciation and preserve diverse sea-level histories representing the intersection of global mean sea-level rise with regional forcings of glacial isostatic adjustment and sedimentation. Cap carbonate outcrops in the Naukluft Mountains of central Namibia record two intervals of sea-level rise and fall. This unexpected deglacial pattern motivates our exploration of complex sea level histories driven by glacial isostatic adjustment. We modeled sea level change accounting for glacial isostatic adjustment in response to a reconstructed globally synchronous and continuous Marinoan deglaciation to explore how the duration of deglaciation impacts the range of resulting sea-level histories across continental margins. Short snowball deglaciation durations, on the order of ~2 kyr, result in exclusive sea-level rise, or sea-level rise followed by sea-level fall but cannot drive two distinct phases of sea-level fall. However, these processes with longer duration snowball deglaciations, of ~10-30 kyr, can drive two distinct intervals of sea-level rise and fall across much of the width of a continental margin, consistent with the stratal patterns observed in Naukluft Mountains cap carbonate succession. Our spatially varying sea-level predictions resulting from longer duration deglaciations may be applicable in interpreting stratal patterns of other enigmatic cap carbonate successions. Furthermore, this work underlines the need for better constraints on the areal distribution and volume of Marinoan ice sheets, including

improved understanding of plausible deglacial durations using updated global climate models.

1. Introduction

The termination of the Marinoan Snowball glacial epoch (635 Ma) was one of the most significant climate transitions in Earth history (e.g. Kirschvink 1992; Hoffman et al. 1998; Hoffman et al. 2017). Global deglaciation caused hundreds of meters of global mean sea-level rise from the melting of ice sheets (Hoffman et al. 2007; Hoffman 2011). Basal-Ediacaran cap carbonates (~635 Ma) overlie terminal Marinoan glaciogenic strata and together constitute the primary sedimentary record of the changes in sea-level, climate, and ocean chemistry associated with deglaciation (e.g. Hoffman & Schrag 2002; Halverson & Shields-Zhou 2011; Hoffman et al. 2017; Wei et al. 2019; Fig. 4.1A). Yet, the local changes in sea-level recorded within cap carbonate stratal patterns across continental margins show a range of patterns, likely driven by the intersection of global mean sea-level with regionally dependent mechanisms of sea-level change. One variable controlling regional sea-level is the duration of deglaciation, where different timescales of melting result in different patterns of glacial isostatic adjustment (GIA; Creveling & Mitrovica 2014). The duration of deglaciation can change patterns of sea-level change along continental margins, and therefore be recorded within the stratigraphic record of cap carbonates and their underlying glaciogenic deposits.

Most previous work on globally distributed cap carbonates concluded that stratal patterns recorded only sea-level rise (transgression, Fig. 4.1C purple line; Kennedy 1996; Macdonald et al. 2009; Hoffman & Halverson 2011), early sea-level fall followed by later sea-level rise (regression-transgression, Fig. 4.1C red line; Hoffman & Macdonald 2010; Hoffman 2011), or early sea-level rise followed by subsequent sea-level fall – culminating in subaerial exposure -- at the top of the cap carbonate sequence (Fig. 4.1C blue line; Summa 1993; Bertrand-Sarfati 1997; Shields et al. 2007; Zhou et al. 2010; Creveling et al. 2016; Gan et al. 2022). Recent work in the Naukluft Mountains of Namibia (Fig. 4.1A; Morris & Grotzinger 2023), report an example of terminal glaciogenic and cap carbonate strata that record two distinct intervals of sea-level rise and fall (Fig. 4.1B; initial transgression, regression, second transgression, and a second regression; sea-level fluctuations up to ~10s of meters). Previous

GIA modeling has shown that a single, continuous Snowball deglaciation can produce diverse and divergent sea-level trajectories around the Ediacaran globe (Creveling and Mitrovica, 2014; Irie et al., 2019), yet these studies did not capture the two depositional sequence stratal architecture observed in the Naukluft Mountains (Fig. 4.1). Here we ask whether this geological observation (two episodes of sea level rise and fall) might represent perturbations to sea level by glacial isostatic adjustment on the timescale of thousands of years instead of longer-term tectonics and sedimentation that act on the order of 100s of kyr (e.g. Schlager 1981).

Regional sea-level change associated with Marinoan deglaciation was driven largely by a combination of global mean sea-level rise and glacial isostatic adjustment. Glacial isostatic adjustment results in complex spatio-temporal patterns of sea-level change, as the solid Earth responds to changes in ice and ocean loading through crustal deformation, in addition to perturbations to the Earth's gravitational field and Earth's rotation axis (Milne & Mitrovica 2002). Previous work cataloged a variety of (non-monotonic) patterns in local sea-level arising from modeled Marinoan deglaciation of varying deglacial duration for various paleogeographic locations proximal and distal to ice margins (Creveling & Mitrovica 2014) and with increasingly complex continental margin geometry (Irie et al. 2019). However, the spatial distribution of sea-level change along shore-perpendicular transects of continental margins has not been exhaustively explored for a range of deglacial durations, an important vantage given the spatial distribution of cap carbonate outcrops across expansive platforms (e.g. Kennedy et al. 2001; Zhou et al. 2010; Hoffman 2011; Creveling et al. 2016; Morris & Grotzinger 2023). At any given location, the timing, rate, and sign of glacial isostatic adjustment-induced sea-level change will rely on the duration of ice sheet melting and solid Earth rheology, in addition to conventional controls on accommodation space (such as sediment accumulation and tectonic subsidence; e.g. Schlager 1981).

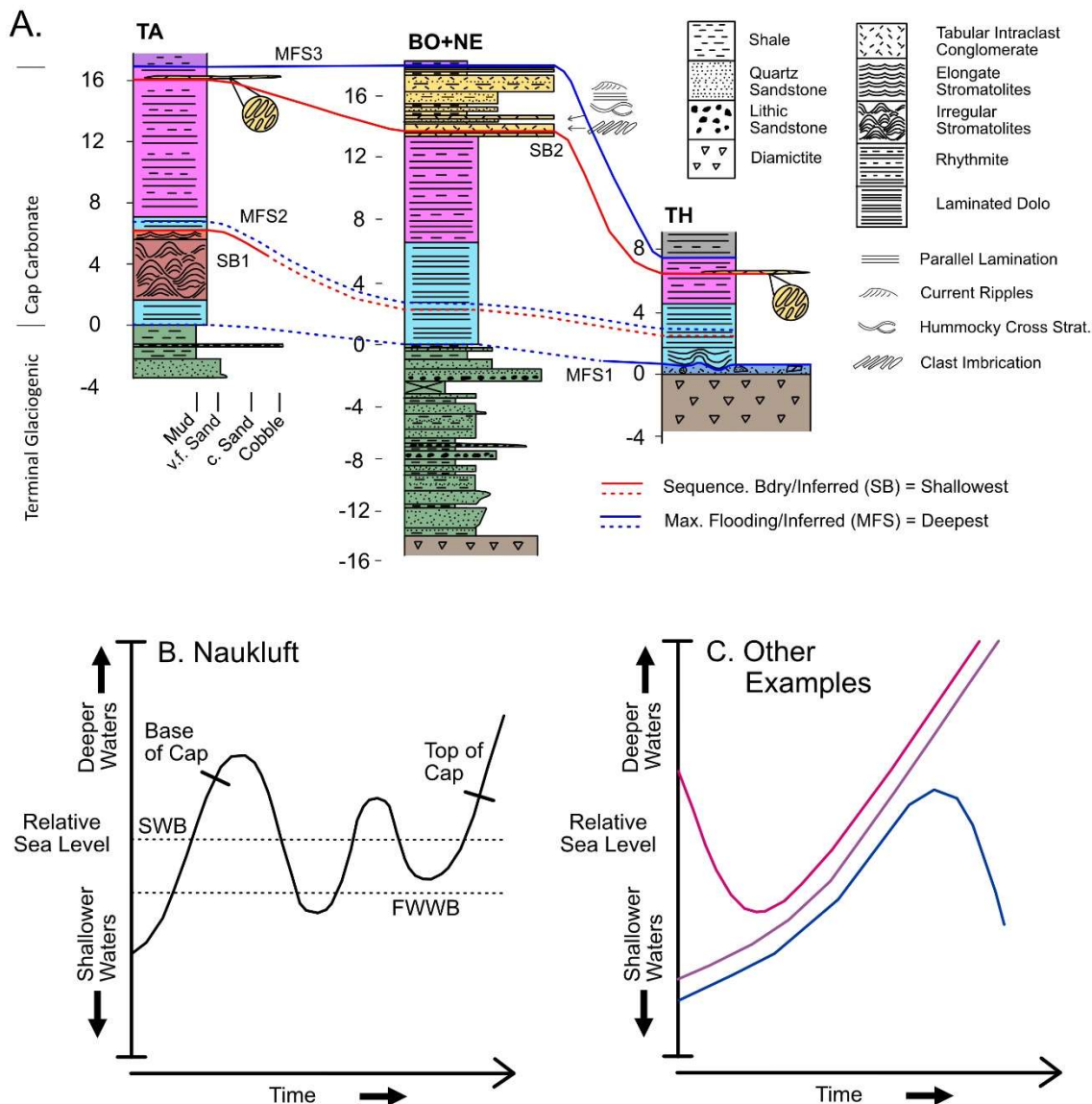


Figure 1. Examples of the terminal Marinoan sea-level history in the geologic record. A) Simplified stratigraphic columns for the terminal glaciogenic deposits (upper Blässkranz Formation) and overlying cap carbonate (Tsondab member of Tsabisis Formation) of the Naukluft Mountains (Namibia). Maximum flooding surfaces indicate time of deepest water depths (maximum transgression), sequence boundaries indicate time of shallowest water depths (maximum regression). This cap carbonate includes two sequence boundaries. Modified from Morris & Grotzinger (2023). B) Qualitative relative sea-level history inferred from Naukluft geologic record. The span of cap deposition begins with the downdip localities, which initiate deposition earlier than updip sites as glaciers retreat inland. Because of continuing thermal subsidence, sedimentary systems will generally deepen without significant sedimentation or external forcings, therefore it is the two distinct intervals of sea-level fall that motivate our additional exploration. FWWB – fair weather wave base, SWB – storm wave base. From Morris & Grotzinger (2023). C) Other commonly reported relative sea-level histories for terminal Marinoan deposits. See text for references.

The duration of deglaciation is poorly constrained as resolution limitations have prevented direct radiometric geochronology and, despite various efforts to estimate the duration of cap carbonate deposition, the relative timing of the cap carbonate deposition and deglaciation remains uncertain (Trindade et al. 2003; Hoffman et al. 2007; 2011; 2017; Font et al. 2010; Hoffman & Macdonald 2010; Kennedy & Christie-Blick 2011; Yang et al. 2017; Nordsvan et al. 2019; Fairchild et al. 2022). The only direct quantitative estimate for the duration of the Marinoan deglaciation is based on the limited global climate model simulations of Hyde et al. (2000), which predicted a timespan of ~ 2 kyr or less. By qualitative comparison to Quaternary analogues, Hoffman et al. (2007) speculated that the duration may have lasted up to 10 kyr. Nevertheless, given the need for additional parameter space exploration with more recent estimates of ice sheet dynamics (e.g. de Boer et al. 2017), paleogeographies (Merdith et al. 2017; 2021), and greenhouse gas concentrations (e.g. Bao et al. 2008; 2009; Cao & Bao 2013; Abbot et al. 2013; Ohenmueller et al. 2014; Hoffman et al. 2017) in global climate models for the Marinoan deglaciation, the timescale of ice sheet melting remains poorly constrained. Meanwhile, estimates for the timescale of cap carbonate deposition ranges from extremely short ~ 2 kyr (by coupling to above deglacial duration; Hoffman & Schrag 2002; Hoffman et al. 2007; Hoffman & Macdonald 2010; Hoffman 2011), to the scale of a few 10s of kyr (by coupling to ocean mixing timescale; Yang et al. 2017; Hoffman et al. 2017), up to several 100s of kyr (by paleomagnetic reversal evidence; Trindade et al. 2003; Font et al. 2010; Nordsvan et al. 2019). Distinguishing the mechanisms that drive the sea-level changes observed in cap carbonate successions may provide ways to better constrain the duration of cap carbonate deposition.

We seek to explore the uncertainty on the duration of Marinoan deglaciation and its impact on shoreline-perpendicular spatial patterns applicable to the geographic scale and distribution of cap carbonate stratal patterns across continental margins. Therefore, for the scope of the present study, we explore variable timescales of global deglaciation from 2 to 50 kyr where, given the resolution of the geologic record, melting will be approximated as globally synchronous and continuous (no hiatuses or reversals in melting) across all continental ice sheets (considered in Creveling & Mitrovica 2014; Irie et al. 2019; Morris & Grotzinger 2023). We investigate how different durations of deglaciation impact shoreline-

perpendicular sea-level patterns and how these model results compare with the spatially varying sea-level history recorded in the Naukluft Mountains and in other globally-distributed cap carbonate successions (Fig. 4.1).

2. Model Set-Up

Our model uses the recently available paleogeographic reconstructions of Merdith et al. (2021) at 600 Ma and 680 M (Fig. 4.2A; Fig. 4.9A). We followed the method described in Creveling & Mitrovica (2014) to construct an initial topography based on modern mean topographic/bathymetric values. From a peak elevation of 850 m in continental interiors, topography decreases linearly over 350 km to the shoreline, drops to -150 m within 80 km of the shoreline, falls to -2000 m over the next 30 km it and to -3800 m over the following 300 km, where it continues at that depth for the abyssal plain.

The ice histories for both paleogeographies (600 Ma and 680 Ma) include ice sheets over all major continents at the first time step (Fig. 4.2A; Fig. 4.9A). The plan-view shape of these ice sheets are simple ellipses broadly fit over the shape of the continents. The distribution of ice thickness of all ice sheets throughout the deglaciations is based on a parabolic equilibrium thickness profile (Patterson 1969; 1994). For syn-deglacial time steps, ice sheet margins retreat such that the total global ice volume declines linearly (Fig. 4.3C), resulting in a total global mean (eustatic) sea level rise of 800 m over the full deglaciation. We later explored the sensitivity of our results to other retreat rates (Suppl. Fig. 4.1). Through the syn-deglacial phase, ice sheets melted synchronously globally, as was considered in Creveling & Mitrovica (2014) and Irie et al. (2019). We varied the duration of the deglacial phase, which include 2, 5, 10, 15, 20, 30, and 50 kyr deglaciations. The model assumes that the ice sheets were in isostatic equilibrium prior to the start of deglaciation – though there may have been minor changes in ice sheet distribution during the Snowball epoch (duration of several million years) their timing and magnitude is poorly constrained, and were likely small in scale relative to the terminal deglaciation (e.g. Benn et al. 2015; Hoffman et al. 2017).

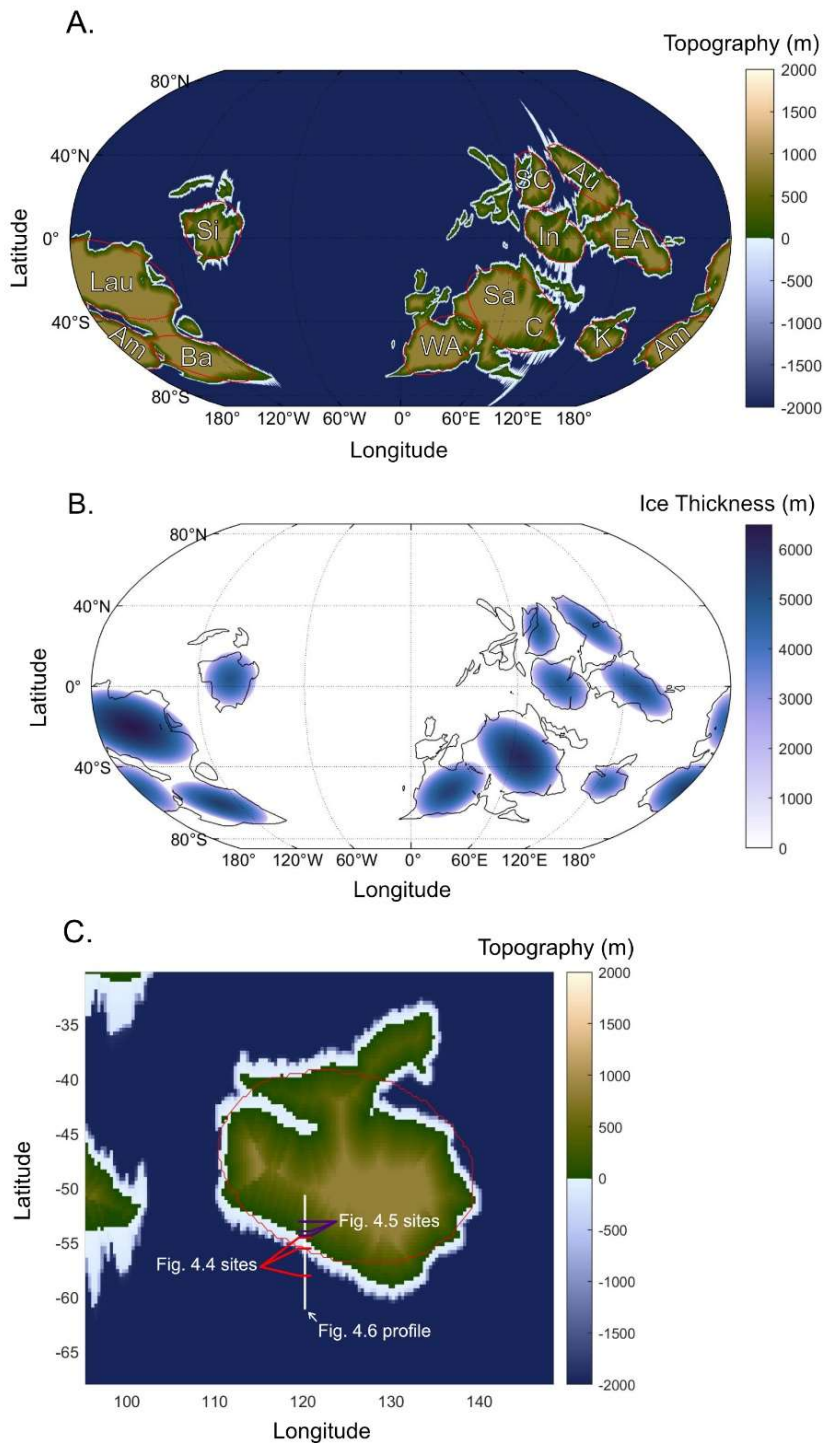


Figure 4.2. Paleogeography and maximum ice sheet distribution for the 600 Ma paleogeography (Merdith et al. 2021), used in figures 4.3, 4.4, 4.5, 4.6, 4.7, and 8 A) Global paleogeography with red outlines showing the maximum extent of the ice sheets upon the major continental cratons. Craton abbreviations: K – Kalahari, Am – Amazonia, Au – Australia, Ba – Baltica, C – Congo, East Antarctic (Mawson), In – India, Lau – Laurentia, Sa – Sahara, SC – South China (Cathaysia), and Si – Siberia. B) Global ice thickness and extents at the start of the model, prior to deglaciation. Black contours show the outline of the continental cratons. C) Paleogeography and maximum ice sheet distribution

of the Kalahari Craton. North-south white line shows the cross-margin profile shown in Fig. 4.6, while the red dashes show the locations of the individual sites explored in Fig. 4.4 and the purple dashes show locations the sites explored in Fig. 4.5.

Modeling predictions are based on a gravitationally self-consistent treatment of post-glacial sea-level change developed to compute the sea-level response to the Plio-Pleistocene ice-age cycles (Mitrovica & Milne 2003; Kendall et al. 2005). The model accounts for the time-varying shorelines associated with local changes in sea-level and the extent of grounded, marine-based ice as well as the impact on sea-level of perturbations in Earth's rotation. Calculations employ the pseudo-spectral algorithm discussed by Kendall et al. (2005) with a truncation at spherical harmonic degree 256. These calculations incorporate viscoelastic deformation of a spherically symmetric Earth in which the elastic and density structure are given by the seismic model PREM (Dziewonski & Anderson 1981). Following Creveling and Mitrovica (2014), we adopt a radial viscosity structure characterized by a 70 km thick elastic lithosphere, upper mantle viscosity of 5×10^{20} Pa s, and lower mantle viscosity of 5×10^{21} Pa s, consistent with far-field Holocene sea level records (Lambeck et al. 1998; Mitrovica & Forte 2004). We also performed simulations using an alternate earth model (VM2; ~ 95 km lithospheric thickness, $\sim 5 \times 10^{20}$ Pa s and 3×10^{21} Pa s, lower and upper mantle viscosity, respectively; (Supp. Fig. 4.2; Peltier & Fairbanks 2006). These values provide a reasonable span of lithospheric and mantle estimates, with possible changes going back to the Neoproterozoic likely only decreasing mantle viscosity and lithospheric thickness (e.g. Grotzinger & Royden 1990), which could result in more pronounced GIA effects.

3. Results

We began by modeling sea-level change using the 600 Ma paleogeography (Fig. 4.2A) and a deglacial ice history (Fig. 4.2B) where all ice sheets melted within 2 kyr, as inferred from the global climate model in Hyde et al. (2000). Figure 4.3 shows the total sea-level change 10 kyr after the end of the 2 kyr duration deglaciation ($t = 12$ kyr). Over the interiors of formerly glaciated continents, relative sea-level falls by up to 880 meters. Far away from the ice sheets, the far-field oceans experience a sea-level rise (global average ~ 800 meters; Fig. 4.3C). Along the continental margins of formerly glaciated continents, there is a gradient in

sea-level change, where sea-level falls within the interior and sea-level rises along the continental periphery.

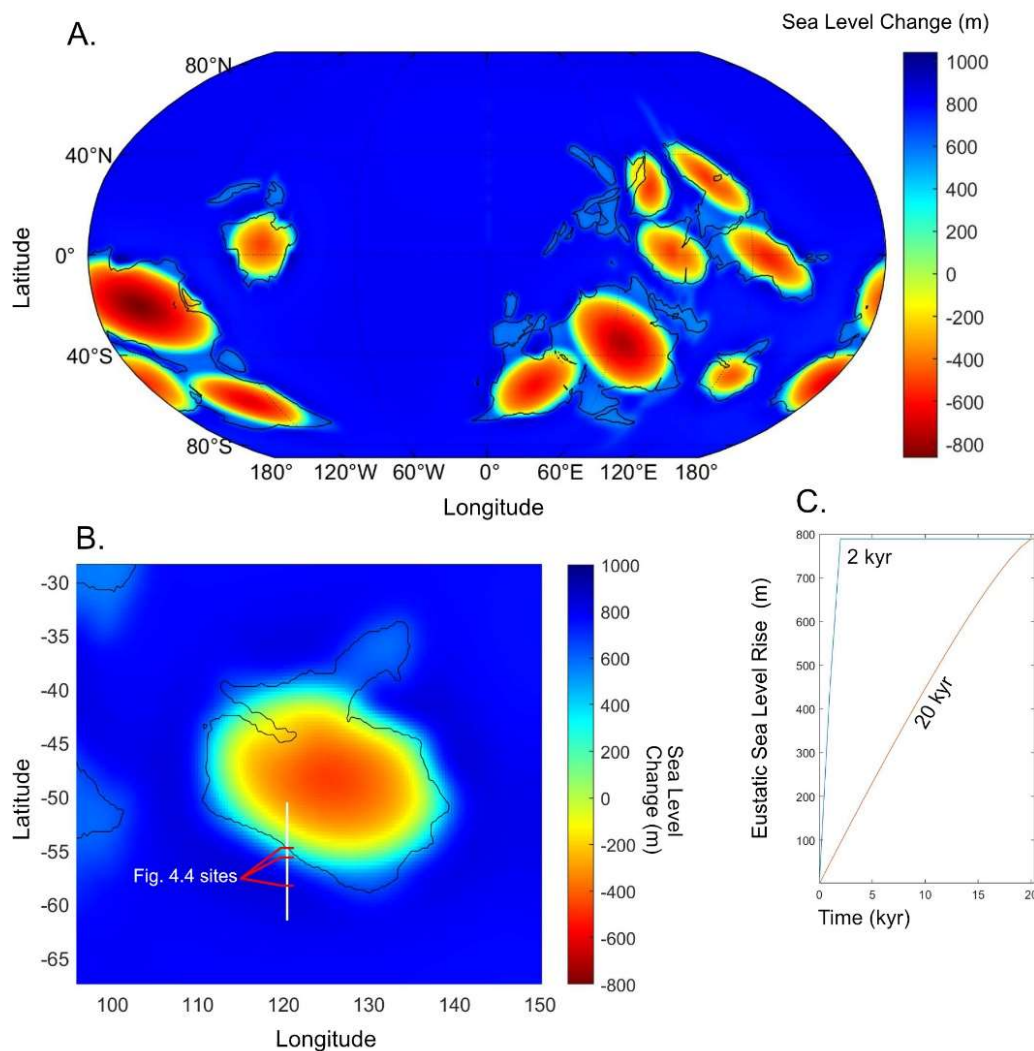


Figure 4.3. A) Global map of relative sea level change 10 kyr since the end of deglaciation ($t = 12$ kyr) with a 2 kyr long deglaciation. Black contours show the outline of the continental cratons. B) Same as A for the Kalahari Craton. North-south-oriented white line shows the cross-margin profile shown in Fig. 4.6, while the red dashes show the locations of the individual sites in Fig. 4.4. C) Eustatic sea level rise over the 2 kyr deglaciation (blue) and 20 kyr deglaciation (orange).

To explore the time history of sea-level across a platform-perpendicular transect akin to the study area of the Naukluft Mountains, Namibia, we plotted relative sea-level at three representative sites across the southwestern margin of the modeled Kalahari Craton (Fig. 4.2C; Fig. 4.4). The most proximal site (Fig 4.4A) is predicted to experience a relative sea-level rise from 0 to 2 kyr (syn-deglacial), followed by a relative sea-level fall and still stand.

At the intermediate site, relative sea-level rises from 0 to 9 kyr, followed by a smaller magnitude relative sea-level fall. In contrast, the distal site only experiences a relative sea-level rise followed by standstill.

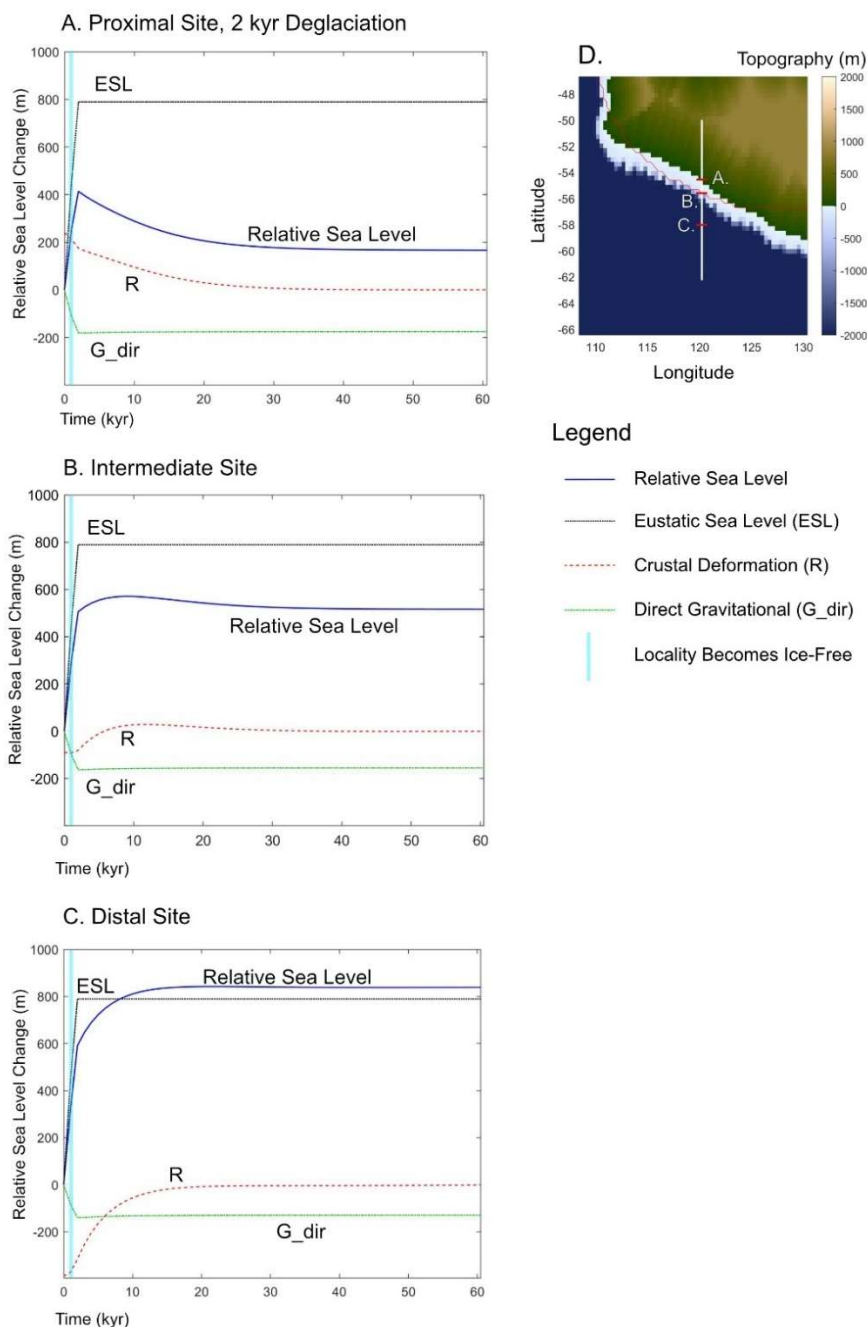


Figure 4.4. Curves showing the relative sea level history across space (solid blue line). Additionally, we show the three key components that make up the deglacial sea level history – global mean (eustatic) sea level (dotted black, ESL), the direct gravitational attraction between ice sheets and the oceans (dot-dash green, G_{dir}), and crustal deformation (dashed red, R). Blue triangles point to when the locality becomes ice free. All plots are across the Kalahari margin with the 600 Ma

paleogeography with a 2 kyr deglaciation (Fig. 4.2, Fig. 4.3). A) Proximal site with lat/long of -54.4° , 120° , which is the location of the initial shoreline. B) Intermediate site with lat/long of -55.6° , 120° , which is the location of the maximum ice margin. C) Distal site with lat/long of -58° , 120° . D) Localities of A-C shown by red dashes.

To understand what drives the sea-level pattern across this transect, we decomposed relative sea-level into its constituent components, which include global mean eustatic sea-level (Fig. 4.4 ESL, black) and glacial isostatic adjustment (Fig. 4.4). There are two main controls on relative sea-level due to glacial isostatic adjustment: crustal deformation (Fig. 4.4 R, red) and the direct gravitational attraction between ice sheets and the oceans (Fig. 4.4 G_dir, green). Relative sea-level at the distal site is largely dominated by the eustatic sea-level signal supplemented by the crustal subsidence (Fig. 4.4C), whereas the relative sea-level at the proximal site is dominated by the crustal deformation component (Fig. 4.4A). The proximal site experiences crustal rebound as ice sheets unload the solid Earth, which drives a relative sea-level fall. The formerly uplifted peripheral bulge of the ice sheet subsides as the ice unloads (red line; Fig. 4.4C), and results in small sea level fall in the far-field due to the redistribution of the oceans into area formerly uplifted by the peripheral bulge.

We next considered how shore-perpendicular sea-level patterns are impacted by deglaciation duration. We performed GIA simulations using a range of ice histories characterized by deglacial durations from 2 to 50 kyr (Fig. 4.5; 4.6; 4.7; 4.8). Changing the deglaciation duration results in more complex relative sea-level histories across the continental margin with a shift in which sites show signals representative of spatially variable patterns (Fig. 4.5). For a deglacial duration of 20 kyr, the intermediate site records two episodes of sea-level rise and fall (Fig. 4.5B). Similar patterns are found between the inland proximal site (Fig. 4.5A), where crustal rebound is dominant and the distal site (Fig. 4.5C) where sea-level is dominated by rising eustatic sea-level. Within this spatial region spanning proximal to distal sites (Fig. 4.5A to C), these fluctuating sea-level patterns diverge from the simpler patterns observed on the Kalahari margin for the 2 kyr deglacial (Fig. 4.4). More inland than the proximal site shown (Fig. 4.5A), the second interval of sea-level change is lost and the pattern instead shows a single sea-level rise followed by sea-level fall (analogous to Fig. 4.4A). Further oceanward from the distal site (Fig. 4.5C), the first episode of sea-level fluctuation is not

detectable and the pattern shows a large sea-level rise followed by a late fall, and in the most distal peripheral localities only sea-level rise is recorded (analogous to Fig. 4.4C).

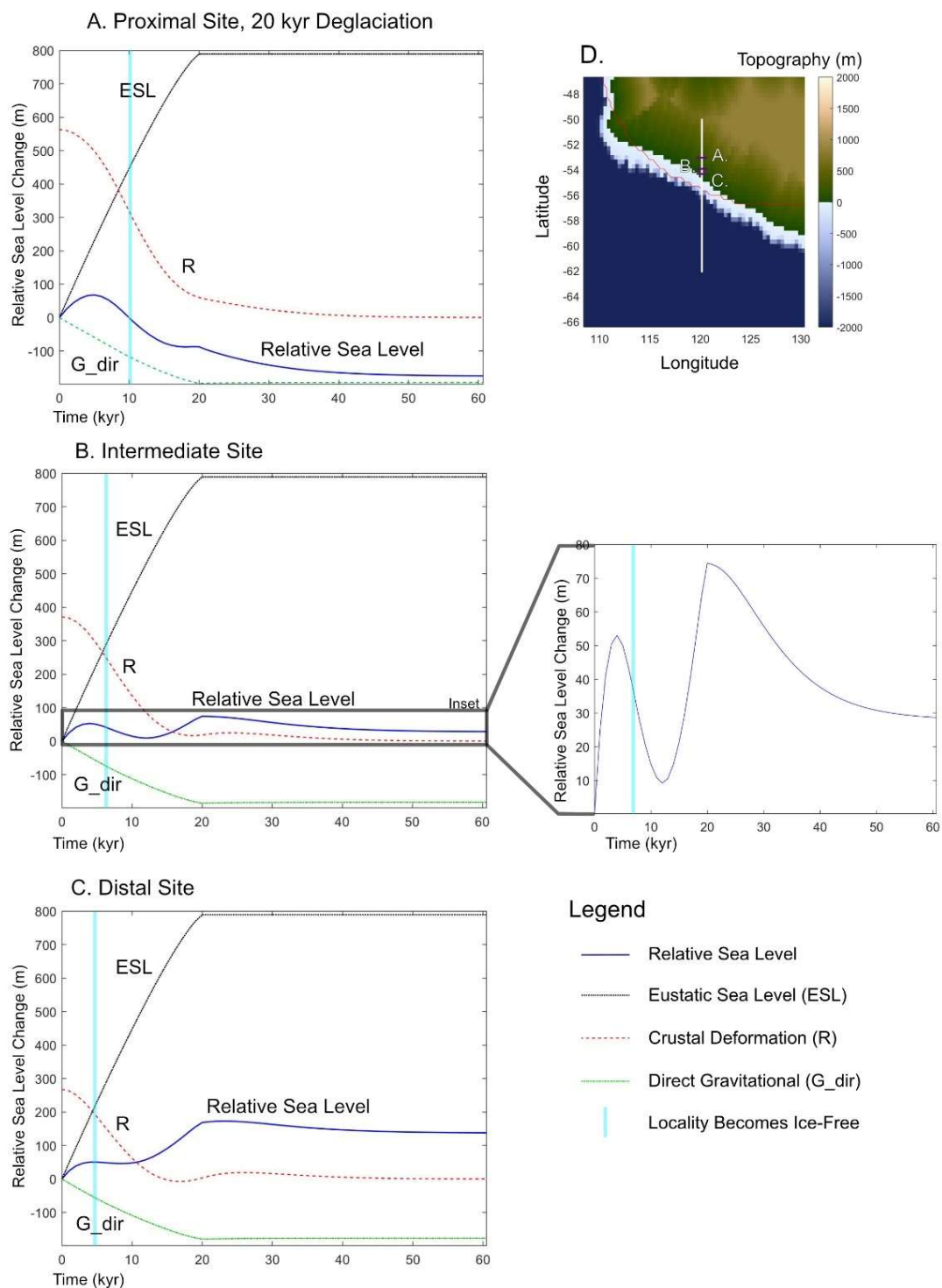


Figure 4.5. Relative sea level history (solid blue line), global mean (eustatic) sea level (ESL; dotted black), the direct gravitational attraction (dot-dash green, G_dir), and crustal deformation (dashed

red, R) for 20 kyr deglaciation. Blue triangles point to when the locality becomes ice free. A) Proximal site with a lat/long of -53° , 120° . B) Intermediate site with a lat/long of -53.9° , 120° . C) Distal site with a lat/long of -54.3° , 120° . D) Locations of A-C shown by purple dashes. E) Intermediate site inset of only the relative sea-level.

To illustrate these complex sea-level patterns across the modeled Kalahari continental marginal-platform, we created time-stratigraphic diagrams (*sensu* Wheeler, 1957; 1964) that depict relative sea-level change through time and space for both the 2 kyr (Fig. 4.6A) and 20 kyr (Fig. 4.6B) modeled deglaciations. For the 2 kyr deglaciation, areas inland of the maximum ice extent have relative sea-level histories characterized by rapid sea-level rise (densely spaced contours between 0 and 2 kyr), followed by a sea-level fall. In contrast, for the 20 kyr deglaciation there is a more complex, spatially varying sea-level pattern across the margin. The more distal areas ($> -54.4^{\circ}$ latitude) show a continuous sea-level rise during the deglaciation (followed by post-deglacial fall out to $\sim 55^{\circ}$ latitude, and post-deglacial rise further in the periphery e.g. -58° latitude), while the most inland regions ($< -53.1^{\circ}$ latitude) show a sea-level rise followed by a sea-level fall. Between these regions is an area that experiences two intervals of sea-level rise and fall. This pattern is most prominent at the intermediate site (Fig. 4.5B) while the phases of sea-level fall are more muted at the distal site (Fig. 4.5C).

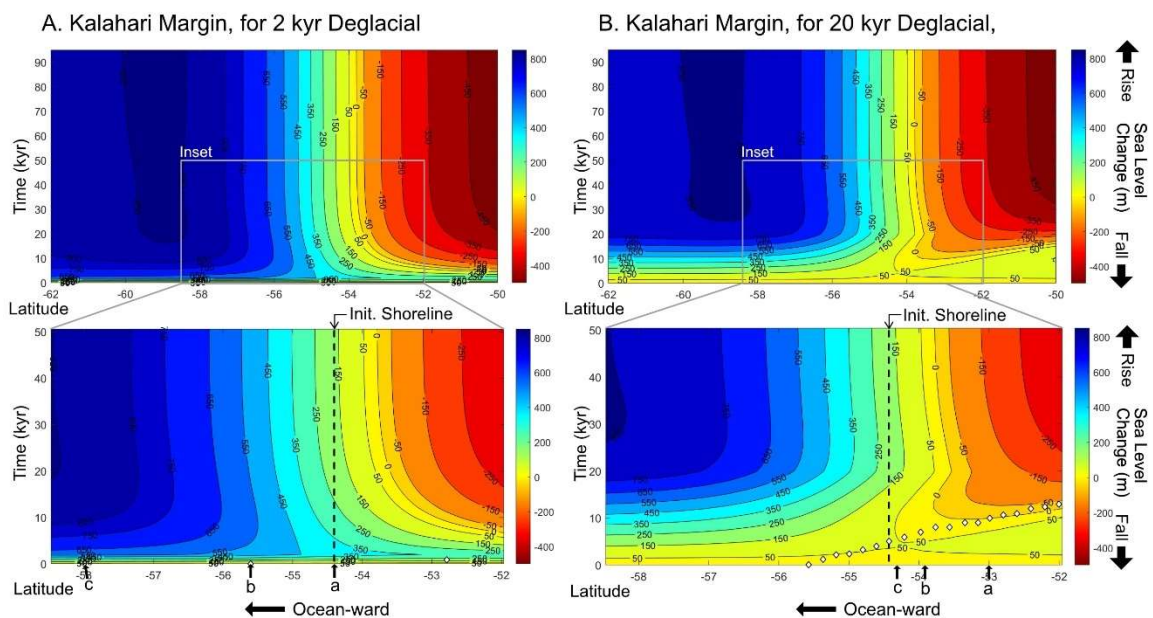


Figure 4.6. Wheeler style diagrams showing sea level patterns through time across the Kalahari margin (600 Ma paleogeography). The x-axis shows latitude along a profile at 120° longitude (white line; Fig. 4.2C). Colored contours show relative sea level change. Gray inset boxes show zoomed in versions of continental margin. White diamonds indicate the location of the retreating ice margin through time and the black dashed lines show the initial shoreline. A) Wheeler for the 2 kyr deglaciation. The black arrows with ‘a, b, c’ correspond to sites A-C from Fig. 4.4. B) Wheeler for the 20 kyr deglaciation. The black arrows with ‘a, b, c’ correspond to sites A-C from Fig. 4.5.

Complex sea-level histories characterized by two intervals of sea-level rise and fall are observed in all deglacial durations between 10 and 30 kyr (Fig. 4.7). For durations less than ~10 kyr, there is only a single peak in relative sea-level. Durations longer than ~30 kyr (Fig. 4.7, 50 kyr curve) can record two intervals of sea-level rise, but the rate of the second sea-level fall approaches ~1 m/kyr, which, in the Neoproterozoic geologic record, would likely become indistinguishable. From the Wheeler-style diagrams for deglacial durations from 10 – 50 kyr (Fig. 4.8), our modeling indicates that as the deglacial duration increases, the continental margin region featuring two intervals of sea-level rise and fall expands in both the inland and seaward directions.

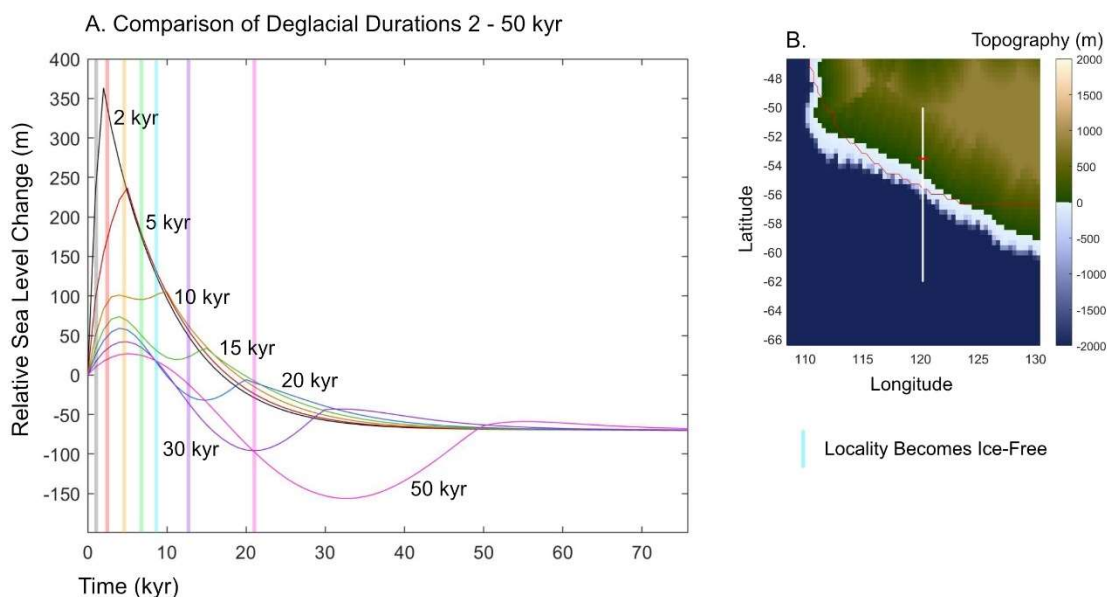


Figure 4.7. A) Relative sea level history at a single site (-53.5° , 120°) for the deglacial durations of 2, 5, 10, 15, 20, 30, and 50 kyr. B) Location of the illustrated site in A.

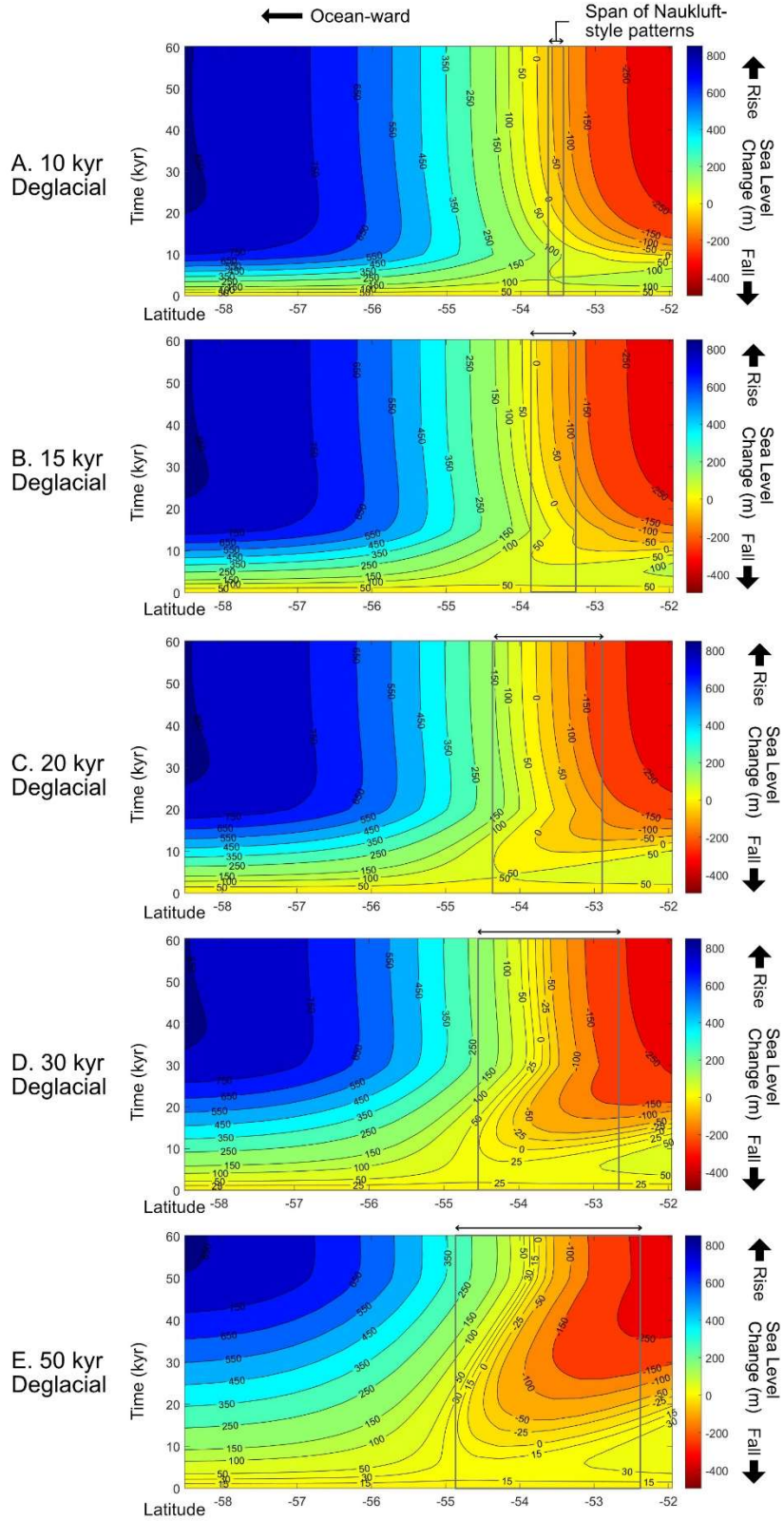


Figure 4.8. Wheeler diagrams, as in Fig. 4.5, showing deglacial durations of (A) 10, (B) 15, (C) 20, (D) 30, and (E) 50 kyr. The gray boxes show the approximate spatial extent of the Naukluft-style sea level pattern that shows two episodes of sea level rise and fall.

4. Discussion

While the focus of our study was to test the impact of different deglacial durations on margin-perpendicular sea-level records, we also explored the sensitivity for a particular deglacial duration to different rates of ice sheet melting (linear vs parabolic ESL change, Supp. Fig. 4.1E), Earth model rheology, continental margin configurations, and paleogeographic reconstruction. Varying the ice sheet melting rate (from linear to parabolic) and Earth model modifies the relative magnitudes and timing of sea-level changes but results in similar overall patterns, including multiple episodes of sea-level rise and fall (Suppl. Fig. 4.1, 4.2). We found the illustrated patterns of multiple sea-level rise and falls to be robust between the 600 Ma and 680 Ma paleogeographies (Fig. 4.9) and across the margins of different continents (Supp. Fig. 4.3). For example, analogous sites along the Kalahari margin in the 680 Ma paleogeography (Fig. 4.9) show very similar patterns of sea-level change with only minor differences in relative magnitude (for both short and long deglacial durations). Therefore, across most continental margins, where the sea-level record is most likely to be recorded in stratigraphy, we can expect sea-level patterns that vary spatially over only a few 10's of km (Fig. 4.6; 4.8) and depend primarily on the proximity to regional ice masses and the duration of the deglaciation. Deglaciations shorter than ~10 kyr (Fig. 4.6A; Fig. 7) show either exclusively sea-level rise (distal; Fig. 4.4C) or sea-level rise followed by fall (proximal; Fig. 4.4A, B). Deglacial durations between 10 and 30 kyr (when the Maxwell relaxation time is comparable to the deglacial duration; e.g. Peltier 1974) show these same patterns in more distal or proximal sites, but also have a spatial zone in between that records two intervals of sea-level rise and fall (Fig. 4.8). The spatial distribution of sea-level histories dominated by post-deglacial peripheral bulge subsidence is found only in sites more distal than the maximum ice margin (Fig. 4.4; 4.5; 4.6), in contrast to the suggestion of Hoffman et al. (2017) that peripheral bulge subsidence could be a mechanism for continued post-deglacial sea-level rise for 60 kyr along continental margins with typical cap carbonate deposits. Indeed, our models show that GIA effects would become geologically indistinguishable as the rate of sea-level rise along the peripheral bulge (Fig. 4.4C) decayed

below the rate of average carbonate platform sedimentation (~ 1 m/kyr) and passive margin tectonic subsidence (~ 0.1 m/kyr) within 20 kyr of the end of deglaciation (Adey 1978; McKenzie 1978; Steckler & Watts 1978; Schlager 1981; Hoffman & Schrag 2002).

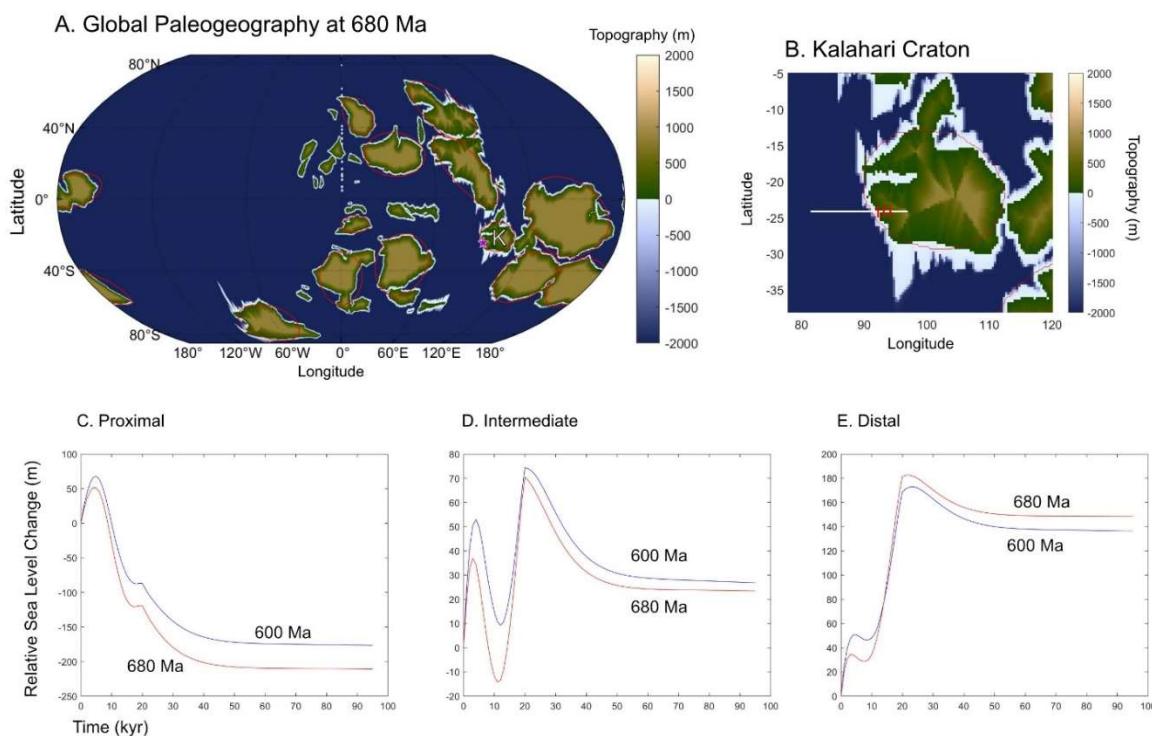


Figure 4.9. A) Global paleogeography with red outlines showing the maximum extent of the ice sheets upon the major continental cratons for the 680 Ma paleogeography (Merdith et al. 2021). The Kalahari Craton is labeled (K), with a purple star along the investigated margin. B) Paleogeography and ice sheet extent for the Kalahari Craton. East-west white line shows the cross-margin profile explored, with the red dashes showing the locations of the individual sites shown in C-E. Relative sea level curve of 20 kyr deglaciation for 600 Ma paleogeography (blue) and an analogous proximal site with the 680 paleogeography (red) at C) proximal site D) intermediate site E) distal site.

Our exploration of deglacial sea-level patterns is inspired by the unusual sea-level pattern found associated with the cap carbonate of the Naukluft Mountains (Fig. 4.1; Morris & Grotzinger 2023), where initial sea-level rise is followed by two distinct episodes of relative sea-level fall (sequence boundaries) within the terminal glaciogenic deposits and cap carbonate. Two depositional models have been previously proposed (Morris & Grotzinger 2023) that could potentially account for this sea-level pattern. These invoke either regionally asynchronous deglaciation that drives an irregular relative sea level history pattern or a synchronous deglacial model where the first sea-level fall is driven by crustal rebound (R) and the second sea-level rise and fall results from longer-term conventional controls on

accommodation space (sedimentation and tectonic subsidence). Regionally asynchronous deglaciation, with irregular patterns of hiatuses and/or reversals in ice sheet melting, have the potential to create a variety of sea-level patterns. However, the range of permutations are extremely wide in this case as nearly any pattern of sea-level change could be created with a sufficiently complex ice melting history. Therefore, we consider simpler ways to explain the Naukluft sea-level pattern (Fig. 4.1) entirely by deglacial mechanisms, within the constraint of a synchronous and continuous deglaciation.

We have shown that 2 kyr-duration deglaciations can produce a range of sea-level patterns, but cannot drive two distinct intervals of sea-level rise and fall (Fig. 4.4; Fig. 4.6A; Fig. 4.7). However, with longer deglacial duration (~10-30 kyr), globally synchronous, continuous deglaciations can drive two distinct cycles of sea-level rise and fall across much of the width of continental margins (Fig. 4.5; Fig. 4.6B; Fig. 4.8; Fig. 4.9). For much of the early stages of longer-duration deglaciations (e.g. 20 kyr, Fig. 4.5; Fig. 4.6B), the continental margins are still covered by ice sheets. As a result, the initial sea-level rise to earliest portion of the first sea-level fall predicted at the intermediate site (Fig. 4.5B) are contemporaneous with persistent glaciation, while the distal site had become ice-free approximately at the end of the first sea-level rise (Fig. 4.5C). This prediction is broadly consistent with the Naukluft geologic record, with updip outcrops (e.g. TA locality in Fig. 4.1A; Morris & Grotzinger 2023) showing the first sea-level rise entirely recorded in the terminal glaciogenic deposits and the cap carbonate beginning with the first relative sea-level fall (following the maximum flooding surface; analogous to Fig. 4.5B). The downdip outcrops (e.g. TH locality in Fig. 4.1A; Morris & Grotzinger 2023) record the end of the initial sea-level rise continuing through the basal cap carbonate dolostone intermixed with glacially sourced siliciclastics (analogous to Fig. 4.5C). Additionally, downdip-most outcrops of the Naukluft show only one phase of sea-level fall near the top of the cap carbonate (e.g. TH locality in Fig. 4.1A; Morris & Grotzinger 2023), this could be consistent with the more distal sites where the magnitude of the first sea-level fall wanes and the sea-level pattern is dominated by sea-level rise followed by a single late fall (Fig. 4.5C, Fig. 4.6B). The distance between the exposed updip and downdip outcrops in the Naukluft is on the order of ~10 km (without the tectonic shortening, Morris & Grotzinger 2023). Though a shorter distance than that between the end-

member model results (~44.4 km; Fig. 4.5B vs. Fig. 4.5C; Fig. 4.6), differences in sea-level patterns can be substantial on ~10 km scales and the outcrops of the Naukluft could be showing either side of a threshold where the first sea-level fall becomes too small to be recorded in the sedimentary facies.

Other cap carbonate successions around the world show a range of interpreted sea-level patterns including simple sea-level rise (transgression, Fig. 4.1C purple; Kennedy 1996; Macdonald et al. 2009; Hoffman & Halverson 2011), early sea-level rise followed by later relative sea-level fall (transgression-regression, Fig. 4.1C blue; Bertrand-Sarfati 1997; Shields et al. 2007; Zhou et al. 2010; Creveling et al. 2016; Gan et al. 2022), and early sea-level fall followed by later sea-level rise (regression-transgression, Fig. 4.1C red; Hoffman & Macdonald 2010; Hoffman 2011). The longer deglacial durations explored in this study may be able to offer a general model to explain the sea-level records at these sites. Histories that are, at least locally, ice-free throughout a simple sea-level rise or sea-level rise followed by fall are predicted for a 20 kyr deglaciation for sites that are more distal than the marginal zone of Naukluft-style sea-level patterns found along most continents, where the large sea-level rise is followed by post-deglacial fall or continued rise depending on proximity and size of the ice sheet (Fig. 4.5, Fig. 4.6B; Supp. Fig. 4.3). Meanwhile, along the margins of the largest continental ice sheets (Supp. Fig. 4.3, Congo), the 20 kyr deglaciation shows sea-level patterns in relatively distal sites where the initial sea-level rise and the second sea-level fall of a Naukluft-style pattern are subtle enough that they may not be distinguishable in the geologic record (with the initial sea-level rise likely occurring while the site is still glaciated; Supp. Fig. 4.3, Congo). At these sites, the dominant signals that would be recorded in the stratigraphic record would show an early sea-level fall followed by a sea-level rise (e.g. site L; Supp. Fig. 4.3; *sensu* Hoffman & Macdonald 2010; Hoffman 2011).

The different mechanisms that account for the deglacial sea-level changes could also provide constraints on the time interval that cap carbonate stratigraphy represents (meters to decameters thick, Fig. 4.1A). Average rates of the longer-term conventional controls on accommodation space (Morris & Grotzinger 2023) could be consistent with cap carbonate deposition timescales of a few 10s to 100s of kyr (given average ~1 m/kyr carbonate platform sedimentation, up to ~0.1 m/kyr tectonic subsidence; Adey 1978; McKenzie 1978; Steckler

& Watts 1978; Schlager 1981; Hoffman & Schrag 2002), and paleomagnetic reversal studies of certain cap carbonates have proposed estimates of ~a few 100s of kyr (Trindade et al. 2003; Font et al. 2010) that could be accounted for by sediment starvation resulting from major landward shoreline migration and slow deposition (Nordsvan et al. 2019). If both intervals of sea-level rise and fall are directly driven by deglacial mechanisms of a long duration deglaciation (e.g. 20 kyr in Fig. 4.5) the timespan between when the intermediate and distal sites become ice-free (to allow for cap carbonate deposition) and when the second sea-level fall has largely decayed (Fig. 4.5, ~35 kyr) suggests the cap carbonate represents ~25-30 kyr. Nevertheless, the possibility of regionally asynchronous melting (Hoffman & Macdonald 2010; Hoffman 2011; Hoffman et al. 2021), could change any predictions for the duration of deglaciation by modeling sea-level patterns.

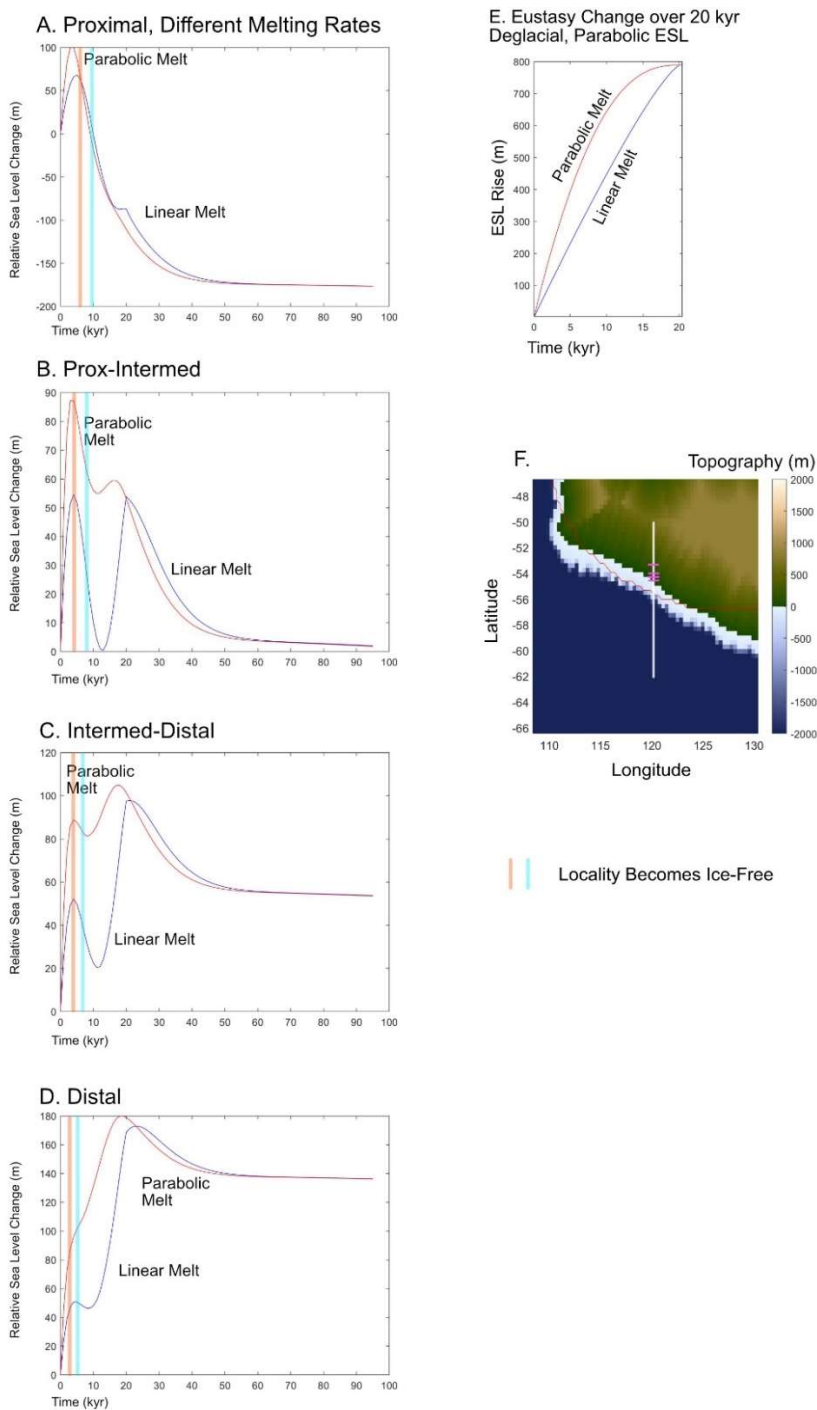
Our modeling highlights that refining the duration of the Marinoan deglaciation can constrain the mechanisms that control stratigraphic sea-level records. Future work constraining ice sheet distribution preceding and during deglaciation would improve the ice loading histories for Marinoan GIA sea-level predictions. Moreover, further climate modeling is needed to test the possible range of deglacial duration and explore the synchronicity of melting, which to date has been limited to the global climate model simulations of Hyde et al. (2000). Including inputs on the broader parameter range of ice sheet dynamics with friction coefficients, ice flow rheology, the buttressing of ice shelves, and feedbacks of marine terminating ice sheets (e.g. de Boer et al. 2017), as well as revisions of Neoproterozoic paleogeography (Merdith et al. 2017; 2021) and more recent estimates of greenhouse gas concentrations (e.g. Bao et al. 2008; 2009; Cao & Bao 2013; Abbot et al. 2013; Ohenmueller et al. 2014; Hoffman et al. 2017), should allow future higher resolution coupled ice sheet and atmosphere models to explore the possibility of a >2 kyr duration deglaciation as investigated in this sea-level modeling effort.

5. Conclusions

In this study we explored the range of sea-level patterns that may result from the deglaciation of the Marinoan Snowball Earth to consider whether the two intervals sea-level rise and fall recorded in the Naukluft Mountains of Namibia (Fig. 4.1; Morris & Grotzinger 2023) can be

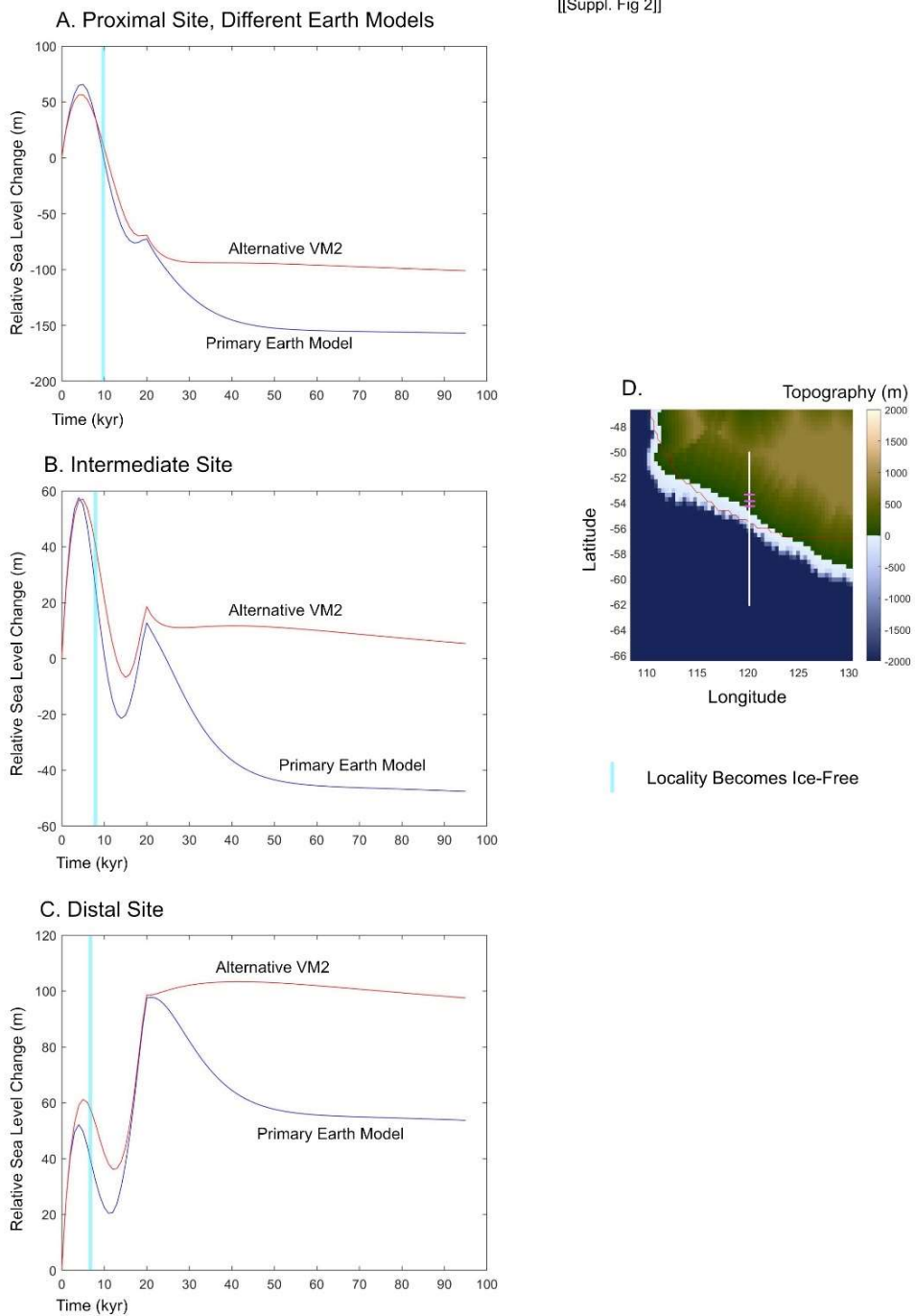
accounted for by the mechanisms of glacial isostatic adjustment. Using shoreline-perpendicular transects to illustrate the spatial variability across continental margins, the present work showed that for synchronous and continuous histories of deglaciation, short durations of ice-sheet melting (~2 kyr) produces a spatially variable range of sea-level patterns but cannot explain the Naukluft sea-level pattern. Yet, longer deglacial durations (~10-30 kyr) can produce two intervals of sea-level rise and fall across much of the width of a continental margin, consistent with the terminal Marinoan deposits of the Naukluft. The sea-level patterns resulting from longer deglaciations may be applicable to other cap carbonate successions around the world and have potential for providing estimates on the timescale of cap carbonate deposition. This work highlights the importance of future research to constrain the ice history and the feasibility of longer duration climate transitions for the Snowball Earth deglaciation.

Chapter 4 Supplementary Figures

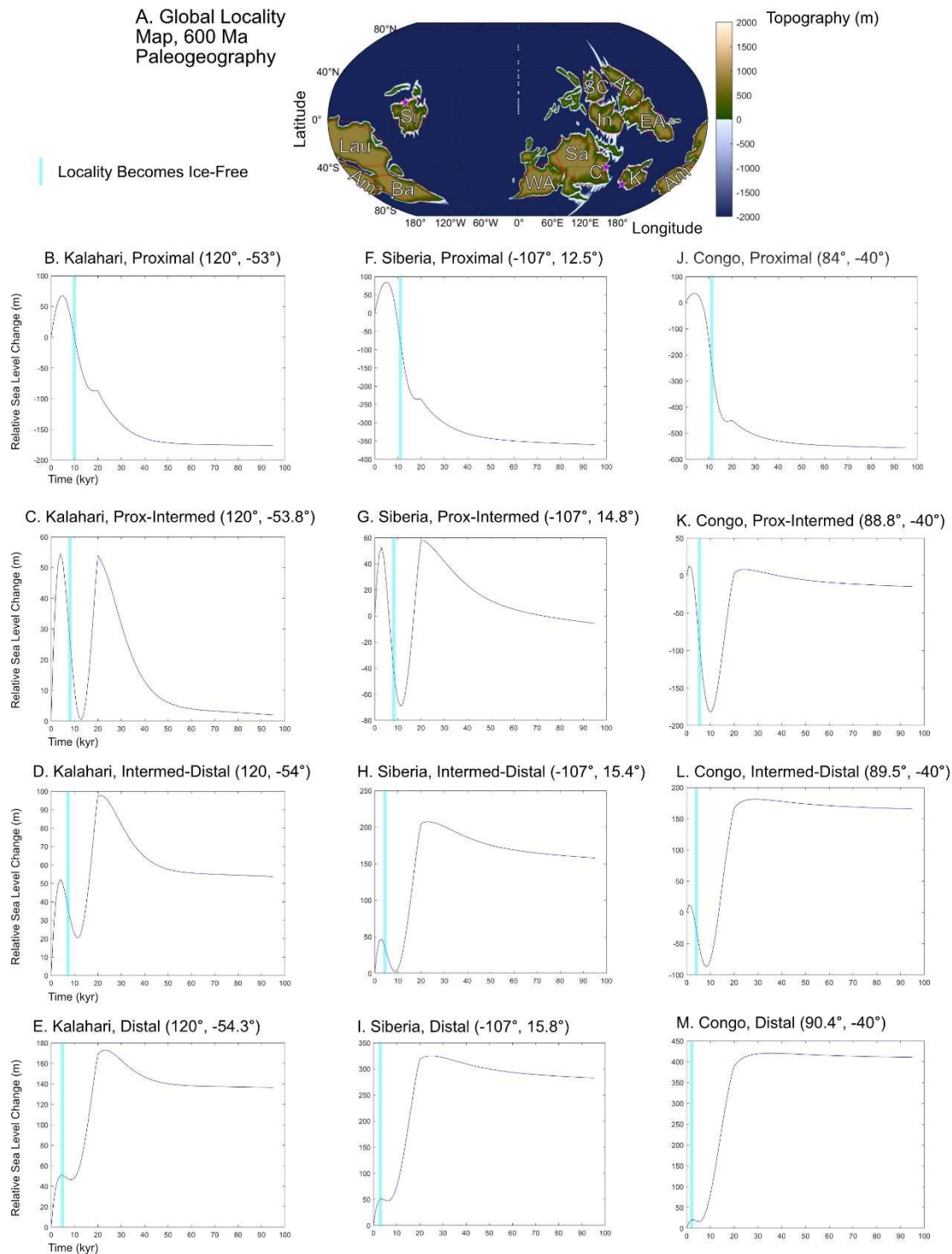


Supplemental Figure 4.1. Illustration of sensitivity to different rates of ice sheet melting. Main figures all had ice sheet radii decrease at a \sqrt{t} rate, resulting in an approximately linear decrease in global ice volume, and therefore a linear increase in global mean sea level (Fig. 4.2C). Here we show deglaciation where ice sheet radii were decreased linearly, resulting in a parabolic curve of global mean sea level rise (E). A) Shows the comparison for a proximal site (-53° , 120°), B) for a site between proximal and intermediate (-53.8° , 120°), C) for a site between intermediate and distal (-54° , 120°), for a distal site (-54.3° , 120°). F) Shows the locations of these sites across the Kalahari Margin.

[[Suppl. Fig 2]]



Supplemental Figure 4.2. Illustration of sensitivity to different Earth models (lithospheric thickness and mantle viscosity), comparing the primary Earth model used in all other figures with the “VM2” Earth Model. A) Shows the comparison for a proximal site (-53° , 120°), B) for a site between proximal and intermediate (-53.8° , 120°), C) for a site between intermediate and distal (-54° , 120°), for a distal site (-54.3° , 120°). D) Shows the locations of these sites across the Kalahari Margin.



Supplemental Figure 4.3. Illustration of sensitivity to different continental margins within the 600 Ma global paleogeography (A) by comparing analogous locations along the southwestern Kalahari margin (B-E), the northern Siberian margin (F-I), and eastern Congo craton margin (J-M).

CHAPTER 4 REFERENCES

- Abbot, D. S., Voigt, A., Li, D., Hir, G. L., Pierrehumbert, R. T., Branson, M., ... & B. Koll, D. D. (2013). Robust elements of Snowball Earth atmospheric circulation and oases for life. *Journal of Geophysical Research: Atmospheres*, 118(12), 6017-6027.
- Adey, W. H. (1978). Coral Reef Morphogenesis: A Multidimensional Model: New data from coring and carbon-14 dating provide keys for unraveling some classical enigmas. *Science*, 202(4370), 831-837.
- Bao, H., Lyons, J. R., & Zhou, C. (2008). Triple oxygen isotope evidence for elevated CO₂ levels after a Neoproterozoic glaciation. *Nature*, 453(7194), 504-506.
- Bao, H., Fairchild, I. J., Wynn, P. M., & Spötl, C. (2009). Stretching the envelope of past surface environments: Neoproterozoic glacial lakes from Svalbard. *Science*, 323(5910), 119-122.
- Benn, D. I., Le Hir, G., Bao, H., Donnadieu, Y., Dumas, C., Fleming, E. J., ... & Fairchild, I. J. (2015). Orbitally forced ice sheet fluctuations during the Marinoan Snowball Earth glaciation. *Nature Geoscience*, 8(9), 704-707.
- Bertrand-Sarfati, J., Flicoteaux, R., Moussine-Pouchkine, A., & Ait Kaci, A. A. (1997). Lower Cambrian apatitic stromatolites and phospharenites related to the glacio-eustatic cratonic rebound (Sahara, Algeria). *Journal of Sedimentary Research*, 67(5), 957-974.
- de Boer, B., Stocchi, P., Whitehouse, P. L., & van de Wal, R. S. (2017). Current state and future perspectives on coupled ice-sheet–sea-level modelling. *Quaternary Science Reviews*, 169, 13-28.
- Cao, X., & Bao, H. (2013). Dynamic model constraints on oxygen-17 depletion in atmospheric O₂ after a snowball Earth. *Proceedings of the National Academy of Sciences*, 110(36), 14546-14550.
- Castleman, B. A., Schlegel, N. J., Caron, L., Larour, E., & Khazendar, A. (2022). Derivation of bedrock topography measurement requirements for the reduction of uncertainty in ice-sheet model projections of Thwaites Glacier. *The Cryosphere*, 16(3), 761-778.
- Creveling, J. R., & Mitrovica, J. X. (2014). The sea-level fingerprint of a Snowball Earth deglaciation. *Earth and Planetary Science Letters*, 399, 74-85.
- Creveling, J. R., Bergmann, K. D., & Grotzinger, J. P. (2016). Cap carbonate platform facies model, Noonday Formation, SE California. *GSA Bulletin*, 128(7-8), 1249-1269.
- Dziewonski, A. M., & Anderson, D. L. (1981). Preliminary reference Earth model. *Physics of the earth and planetary interiors*, 25(4), 297-356.
- Fairchild, I. J., Bao, H., Windmill, R., & Boomer, I. (2022). The Marinoan cap carbonate of Svalbard: Syngenetic marine dolomite with 17 O-anomalous carbonate-associated sulphate. *The Depositional Record*, Early-Access.
- Font, E., Nédélec, A., Trindade, R. I. F., & Moreau, C. (2010). Fast or slow melting of the Marinoan snowball Earth? The cap dolostone record. *Palaeogeography, Palaeoclimatology, Palaeoecology*, 295(1-2), 215-225.
- Gan, T., Zhou, G., Luo, T., Pang, K., Zhou, M., Luo, W., ... & Xiao, S. (2022). Earliest Ediacaran speleothems and their implications for terrestrial life after the Marinoan snowball Earth. *Precambrian Research*, 376, 106685.
- Grotzinger, J., & Royden, L. (1990). Elastic strength of the Slave craton at 1.9 Gyr and implications for the thermal evolution of the continents. *Nature*, 347(6288), 64-66.

- Halverson, G. P., & Shields-Zhou, G. (2011). Chemostratigraphy and the Neoproterozoic glaciations. *Geological Society, London, Memoirs*, 36(1), 51-66.
- Hoffman, P. F., Kaufman, A. J., Halverson, G. P., & Schrag, D. P. (1998). A Neoproterozoic snowball earth. *Science*, 281(5381), 1342-1346.
- Hoffman, P. F., & Schrag, D. P. (2002). The snowball Earth hypothesis: testing the limits of global change. *Terra nova*, 14(3), 129-155.
- Hoffman, P. F., Halverson, G. P., Domack, E. W., Husson, J. M., Higgins, J. A., & Schrag, D. P. (2007). Are basal Ediacaran (635 Ma) post-glacial “cap dolostones” diachronous?. *Earth and Planetary Science Letters*, 258(1-2), 114-131.
- Hoffman, P. F., & Macdonald, F. A. (2010). Sheet-crack cements and early regression in Marinoan (635 Ma) cap dolostones: regional benchmarks of vanishing ice-sheets?. *Earth and Planetary Science Letters*, 300(3-4), 374-384.
- Hoffman, P. F. (2011). Strange bedfellows: glacial diamictite and cap carbonate from the Marinoan (635 Ma) glaciation in Namibia. *Sedimentology*, 58(1), 57-119.
- Hoffman, P. F., & Halverson, G. P. (2011). Chapter 36 Neoproterozoic glacial record in the Mackenzie Mountains, northern Canadian Cordillera. *Geological Society, London, Memoirs*, 36(1), 397-412.
- Hoffman, P. F., Abbot, D. S., Ashkenazy, Y., Benn, D. I., Brocks, J. J., Cohen, P. A., ... & Warren, S. G. (2017). Snowball Earth climate dynamics and Cryogenian geology-geobiology. *Science Advances*, 3(11), e1600983.
- Hoffman, P. F., Halverson, G. P., Schrag, D. P., Higgins, J. A., Domack, E. W., Macdonald, F. A., ... & Nelson, L. L. (2021). Snowballs in Africa: sectioning a long-lived Neoproterozoic carbonate platform and its bathyal foreslope (NW Namibia). *Earth-Science Reviews*, 219, 103616.
- Hyde, W. T., Crowley, T. J., Baum, S. K., & Peltier, W. R. (2000). Neoproterozoic ‘snowball Earth’ simulations with a coupled climate/ice-sheet model. *Nature*, 405(6785), 425-429.
- Irie, Y., Nakada, M., Okuno, J. I., & Bao, H. (2019). Nonmonotonic postdeglacial relative sea level changes at the aftermath of Marinoan (635 Ma) snowball Earth meltdown. *Journal of Geophysical Research: Solid Earth*, 124(8), 9373-9394.
- Kennedy, M. J. (1996). Stratigraphy, sedimentology, and isotopic geochemistry of Australian Neoproterozoic postglacial cap dolostones; deglaciation, delta 13 C excursions, and carbonate precipitation. *Journal of sedimentary Research*, 66(6), 1050-1064.
- Kendall, R. A., Mitrovica, J. X., & Milne, G. A. (2005). On post-glacial sea level—II. Numerical formulation and comparative results on spherically symmetric models. *Geophysical Journal International*, 161(3), 679-706.
- Kennedy, M. J., & Christie-Blick, N. (2011). Condensation origin for Neoproterozoic cap carbonates during deglaciation. *Geology*, 39(4), 319-322.
- Kirschvink, Joseph L. (1992) Late Proterozoic Low-Latitude Global Glaciation: the Snowball Earth. In: J.W. Schopf, C. Klein, & D. Des Maris (eds), *The Proterozoic Biosphere: A Multidisciplinary Study*. Cambridge University Press, pp. 51-52.
- Lambeck, K., Smither, C., & Johnston, P. (1998). Sea-level change, glacial rebound and mantle viscosity for northern Europe. *Geophysical Journal International*, 134(1), 102-144.
- Lecavalier, B. S., Milne, G. A., Simpson, M. J., Wake, L., Huybrechts, P., Tarasov, L., ... & Larsen, N. K. (2014). A model of Greenland ice sheet deglaciation constrained by observations of relative sea-level and ice extent. *Quaternary Science Reviews*, 102, 54-84.

- Macdonald, F. A., Jones, D. S., & Schrag, D. P. (2009). Stratigraphic and tectonic implications of a newly discovered glacial diamictite–cap carbonate couplet in southwestern Mongolia. *Geology*, *37*(2), 123-126.
- McKenzie, D. (1978). Some remarks on the development of sedimentary basins. *Earth and Planetary science letters*, *40*(1), 25-32.
- Merdith, A. S., Collins, A. S., Williams, S. E., Pisarevsky, S., Foden, J. D., Archibald, D. B., ... & Müller, R. D. (2017). A full-plate global reconstruction of the Neoproterozoic. *Gondwana Research*, *50*, 84-134.
- Merdith, A. S., Williams, S. E., Collins, A. S., Tetley, M. G., Mulder, J. A., Blades, M. L., ... & Müller, R. D. (2021). Extending full-plate tectonic models into deep time: Linking the Neoproterozoic and the Phanerozoic. *Earth-Science Reviews*, *214*, 103477.
- Mitrovica, J. X., & Milne, G. A. (2002). On the origin of late Holocene sea-level highstands within equatorial ocean basins. *Quaternary Science Reviews*, *21*(20-22), 2179-2190.
- Mitrovica, J. X., & Milne, G. A. (2003). On post-glacial sea level: I. General theory. *Geophysical Journal International*, *154*(2), 253-267.
- Mitrovica, J. X., & Forte, A. M. (2004). A new inference of mantle viscosity based upon joint inversion of convection and glacial isostatic adjustment data. *Earth and Planetary Science Letters*, *225*(1-2), 177-189.
- Morris, F. K., & Grotzinger, J. P. (2023). Facies and stratigraphy of the basal Ediacaran cap carbonate, Naukluft Mountains, Namibia. *Precambrian Research*, *394*, 107113.
- Nordsvan, A. R., Barham, M., Cox, G., Kirscher, U., & Mitchell, R. N. (2019). Major shoreline retreat and sediment starvation following Snowball Earth. *Terra Nova*, *31*(6), 495-502.
- Ohnemueller, F., Prave, A. R., Fallick, A. E., & Kasemann, S. A. (2014). Ocean acidification in the aftermath of the Marinoan glaciation. *Geology*, *42*(12), 1103-1106.
- Paterson, W. S. B. (1969). *The physics of glaciers*. Oxford: Pergamon Press.
- Paterson, W. S. B. (1994). *The physics of glaciers*. Oxford: Pergamon.
- Peltier, W. R. (1974). The impulse response of a Maxwell Earth. *Reviews of Geophysics*, *12*(4), 649-669.
- Peltier, W. R., & Fairbanks, R. G. (2006). Global glacial ice volume and Last Glacial Maximum duration from an extended Barbados sea level record. *Quaternary Science Reviews*, *25*(23-24), 3322-3337.
- Schlager, W. (1981). The paradox of drowned reefs and carbonate platforms. *Geological Society of America Bulletin*, *92*(4), 197-211.
- Shields, G. A., Deynoux, M., Culver, S. J., Brasier, M. D., Affaton, P., & Vandamme, D. (2007). Neoproterozoic glaciomarine and cap dolostone facies of the southwestern Taoudéni Basin (Walidiala Valley, Senegal/Guinea, NW Africa). *Comptes Rendus Geoscience*, *339*(3-4), 186-199.
- Steckler, M. S., & Watts, A. B. (1978). Subsidence of the Atlantic-type continental margin off New York. *Earth and planetary science letters*, *41*(1), 1-13.
- Summa, C. L., Southard, J. B., & Grotzinger, J. P. (1993). Distinctive cross-stratification in amalgamated storm event beds: Neoproterozoic upper Johnnie Formation, eastern California. In *Geological Society of America Abstracts with Programs* (Vol. 25, No. 6, p. 67).
- Trindade, R. I. F. D., Font, E., D'Agrella-Filho, M. S., Nogueira, A. C. R., & Riccomini, C. (2003). Low-latitude and multiple geomagnetic reversals in the Neoproterozoic Puga cap carbonate, Amazon craton. *Terra Nova*, *15*(6), 441-446.

- Wei, G. Y., vS Hood, A., Chen, X., Li, D., Wei, W., Wen, B., ... & Ling, H. F. (2019). Ca and Sr isotope constraints on the formation of the Marinoan cap dolostones. *Earth and Planetary Science Letters*, 511, 202-212.
- Wheeler, H. E., & Murray, H. H. (1957). Base-level control patterns in cyclothemic sedimentation. *AAPG Bulletin*, 41(9), 1985-2011.
- Wheeler, H. E. (1964). Baselevel, lithosphere surface, and time-stratigraphy. *Geological Society of America Bulletin*, 75(7), 599-610.
- Yang, J., Jansen, M. F., Macdonald, F. A., & Abbot, D. S. (2017). Persistence of a freshwater surface ocean after a snowball Earth. *Geology*, 45(7), 615-618.
- Zhou, C., Bao, H., Peng, Y., & Yuan, X. (2010). Timing the deposition of ^{17}O -depleted barite at the aftermath of Nantuo glacial meltdown in South China. *Geology*, 38(10), 903-90.